2020

# MICROFILTRATION MEMBRANE PORE FUNCTIONALIZATION APPROACHES FOR CHLORO-ORGANIC REMEDIATION TO HEAVY METAL SORPTION

Mohammad Saiful Islam
*University of Kentucky*, saiful1948@gmail.com
Author ORCID Identifier:
https://orcid.org/0000-0001-6234-953X
Digital Object Identifier: https://doi.org/10.13023/etd.2020.303

STUDENT AGREEMENT:

I represent that my thesis or dissertation and abstract are my original work. Proper attribution has been given to all outside sources. I understand that I am solely responsible for obtaining any needed copyright permissions. I have obtained needed written permission statement(s) from the owner(s) of each third-party copyrighted matter to be included in my work, allowing electronic distribution (if such use is not permitted by the fair use doctrine) which will be submitted to UKnowledge as Additional File.

I hereby grant to The University of Kentucky and its agents the irrevocable, non-exclusive, and royalty-free license to archive and make accessible my work in whole or in part in all forms of media, now or hereafter known. I agree that the document mentioned above may be made available immediately for worldwide access unless an embargo applies.

I retain all other ownership rights to the copyright of my work. I also retain the right to use in future works (such as articles or books) all or part of my work. I understand that I am free to register the copyright to my work.

REVIEW, APPROVAL AND ACCEPTANCE

The document mentioned above has been reviewed and accepted by the student's advisor, on behalf of the advisory committee, and by the Director of Graduate Studies (DGS), on behalf of the program; we verify that this is the final, approved version of the student's thesis including all changes required by the advisory committee. The undersigned agree to abide by the statements above.

Mohammad Saiful Islam, Student

Dr. Dibakar Bhattacharyya, Major Professor

Dr. Steve Rankin, Director of Graduate Studies

# MICROFILTRATION MEMBRANE PORE FUNCTIONALIZATION APPROACHES FOR CHLORO-ORGANIC REMEDIATION TO HEAVY METAL SORPTION

---

DISSERTATION

---

A dissertation submitted in partial fulfillment of the
requirements for the degree of Doctor of Philosophy in the
College of Engineering
at the University of Kentucky


By

Mohammad Saiful Islam

Lexington, Kentucky

Director: Dr. Dibakar Bhattacharyya, Professor of Chemical Engineering

Lexington, Kentucky


2020



ORCID ID: https://orcid.org/0000-0001-6234-953X

ABSTRACT OF DISSERTATION

# MICROFILTRATION MEMBRANE PORE FUNCTIONALIZATION APPROACHES FOR CHLORO-ORGANIC REMEDIATION TO HEAVY METAL SORPTION


Microfiltration polyvinylidene fluoride (PVDF) membranes have distinct advantage for open structure in terms of high internal surface area and ease of access in the pore domain. Functionalization of PVDF membranes with different functional groups (-COOH, -OH, -SH) enables responsive (pH, temperature) properties to membrane, tuning of effective pore size, controlling permeate flux. PVDF microfiltration membrane functionalization with suitable responsive polymer such as poly acrylic acid (PAA) to incorporate carboxyl (-COOH) group enables further modification of functionalized PAA-PVDF membranes for different application ranging from catalysis, bio reactor to heavy metal sorption platform. As a catalytic reactor bed, this PAA-PVDF membranes are very desirable platform for in-situ synthesis of catalytic nanoparticles for conducting a wide range of reactions. As a bio reactor, PAA-PVDF membrane with a net charge have been used to electrostatically immobilize enzymes for conducting catalytic reactions. Functionalization of PVDF membrane also allow for the development of high capacity heavy metal sorbents by modifying existing functional groups (-COOH) to other functional groups (-SH) to adsorb heavy metal cations from contaminated water.

Hydrophilic polymers with carboxylic (-COOH) groups are studied in different functionalization processes especially in preparation of responsive (pH) membranes. To understand the role of membrane pore polymerization condition on the properties of functionalized membrane a systematic study has been conducted, specifically, the effects of polymerization on the membrane mass gain, water permeability, Pd-Fe nanoparticle (NP) loading, of pore functionalized polyvinylidene fluoride (PVDF) membranes. In this study, monomer (acrylic acid (AA)) and cross-linker (N, N′- methylene-bis (acrylamide)) concentrations were varied from 10 to 20 wt% of polymer solution and 0.5-2 mol% of monomer concentration, respectively. Results showed that responsive behavior of membrane could be tuned in terms of water permeability over a range of 270-1 $Lm^{-2}$ $h^{-1}$ $bar^{-1}$, which is a function of water pH. The NP size on the membrane surface was found in the range of 16-23 nm. NP loading was found to vary from 0.21 to 0.94 mg per $cm^2$ of membrane area depending on the variation of available carboxyl groups in membrane pore domain.

The NPs functionalized membranes were then tested as a platform for the degradation of 3,3',4,4',5-pentachlorobiphenyl (PCB 126) and understand the effect of NP loading of the rate of degradation of PCB 126. The observed batch reaction rate ($K_{obs}$) for PCB 126 degradation for per mg of catalyst loading was found 0.08-0.1 $h^{-1}$. Degradation

study in convective flow mode shows 98.6% PCB 126 is degraded at a residence time of 46.2 s. The corresponding surface area normalized reaction rate ($K_{sa}$) is found about two times higher than $K_{sa}$ of batch degradation; suggesting elimination of the effect of diffusion resistance for degradation of PCB 126 in convective flow mode operation.

A layer-by-layer approach to immobilize laccase enzyme into PAA functionalized PVDF microfiltration membranes for degradation of 2,4,6-trichlorophenol (TCP) from water was demonstrated to offer bioinspired remediation. Over 80% of the initial TCP was degraded at optimum flow rate under an applied air pressure of about 0.7 bar or lower. This corresponds to degrading a substantial amount of the initial substrate in only 36 seconds residence time, which in a batch reaction take hours. This, in fact, demonstrates an energy efficient flow through system with potential large-scale applications. Comparison of the stability of the enzyme in solution phase vs. immobilized on membrane phase showed a loss of some 65% of enzyme activity in the solution phase after 22 days, whereas the membrane-bound enzyme lost only a negligible percentage of activity in comparable time span. Finally, the membrane was exposed to rigorous cycles of TCP degradation trials to study its reusability. The primary results reveal a loss of only 14% of the initial activity after four cycles of use in a period of 25 days, demonstrating its potential to reuse. Regeneration of the functionalized membrane was also validated by dislodging the immobilized enzyme followed by immobilization of fresh enzyme on to the membrane.

A multi-enzyme functionalized membrane reactor for bioconversion of lignin model compound involving enzymatic catalysis was also developed. Layer-by-layer approach was used to immobilize three different enzymes (glucose oxidase, peroxidase and laccase) into pH-responsive membranes. This novel membrane reactor couples the in-situ generation of hydrogen peroxide (by glucose oxidase) to oxidative conversion of a lignin model compound, guaiacylglycerol-B-guaiacylether (GGE). Preliminary investigation of the efficacy of these functional membranes towards GGE degradation is demonstrated under convective flow mode. Over 90% of the initial feed could be degraded with the multienzyme immobilized membranes at a residence time of approximately 22 seconds. GGE conversion product analysis revealed formation of oligomeric oxidation products with peroxidase, which might be potential hazard to membrane bioreactors. These oxidation products could be further degraded by laccase enzymes in the multi-enzymatic membranes explaining the potential of multienzyme membrane reactors. The multi-enzyme incorporated membrane reactors were active for about a month time of storage at 4 $^{o}$C, and retention of activity was demonstrated after repetitive use.

Further, PAA functionalized PVDF membranes are immobilized with thiol (-SH) groups for metal sorption from industrial effluent water. The sorption capacity of mercury for CysM immobilized membrane is 2446 mg/g PAA and the efficiency of Hg removal is 99.1±0.1% respectively from synthetic water. For 1300 minutes CysM-PAA-PVDF membrane is used to remove $Hg^{2+}$ cations from effluent water. The adsorption efficiency in this long-term study is around 97%. In presence of $Ca^{2+}$ cations adsorption efficiency

drops to 82% for CysM-PAA-PVDF membrane and to 40% for Cys-PAA-PVDF membrane. A mathematical model on heavy metal adsorption by thiol (-SH) functionalized membrane was developed to predict experimental results over a wide range of operating conditions. These diverse functional approaches of microfiltration membranes and its application towards water remediation offer superior performance over traditional treatment process thus anticipates immediate industrial application.

Finally, hollow Fe-Pd nanoparticles were synthesized for the application towards degradation of chlorinated compounds. This fabricated Fe hollow spheres have 2.6 times higher surface area and 4.28 times pore volume compare to commercial Fe catalyst. Initial investigation reveals in presence of palladium, these prepared hollow NPs can completely degrade polychlorinated biphenyl (PCB-1) anticipating future potential for water remediation application.

KEYWORDS: Microfiltration PVDF Membrane, Nanoparticles, Catalytic Membrane Reactor, Enzyme Immobilized Membrane, Thiol Functionalized Membrane, Hollow Nanoparticles

Mohammad Saiful Islam

*(Name of Student)*

05/12/2020

Date

# MICROFILTRATION MEMBRANE PORE FUNCTIONALIZATION APPROACHES FOR CHLORO-ORGANIC REMEDIATION TO HEAVY METAL SORPTION

By

Mohammad Saiful Islam

Dr. Dibakar Bhattacharyya
Director of Dissertation

Dr. Steve Rankin
Director of Graduate Studies

05/12/2020
Date

DEDICATION

To *my beloved family and friends*

## ACKNOWLEDGMENTS

I take immense pleasure to express my sincere gratitude towards my research advisor, Professor Dibakar Bhattacharyya (DB). Thank you. The guidance you provided over the past five years, which I am pretty sure will have an ever-lasting impact on my scientific abilities and will continue to help me grow as a researcher. Your unfathomable passion for the field of membrane science and the chemical engineering profession is very inspiring and has helped me a lot to stay motivated over the past five years. Discussing research with you has always been a great pleasure. I am always amazed with your vast knowledge and the critical inputs provided by you during research discussions. Thank you for providing resources and opportunities to pursue research ideas of my interest and for always encouraging me to attend conferences and meetings with collaborators. You made me feel like a family by inviting me to numerous celebrations and for sharing life lessons over the past couple of years. You and Gale (a very kind and brave person) always support us like your child. I will forever be in-debt of the affection and will cherish the great memories.

I would like to thank Professor Lindell Ormsbee, Professor Steve Rankin, Professor Beth S. Guiton to serve in my defense committee and to provide ideas that guided and challenged my thinking. To Dr. Ormsbee, I am really amazed by the vast knowledge you have regarding hazardous waste sites and treatment processes. Your encouragement to treat superfund site water using the membranes we prepared in Dr. DB's lab always gave me the pleasure as an engineer to implement the lab research to a test site. To Dr. Rankin, I think in our department I visited your lab so frequently in last five years next to my own lab. Sometimes for using instruments and sometimes for a short chat with graduate students. Syed, Arif, and Yuxin, all are Ph.D.'s now. To Dr. Beth, you are the only professor in University of Kentucky, whose research publication I follow on regular basis. Your cool and exciting research published in very high impact journals, really inspired me a lot. I visited your lab few times to discuss my work with your graduate student Ahamed. Thank you, Professor Mark Meier for serving as my outsider examiner.

I would like to thank Dr. Evan Hatakeyama of Chevron Corporation, one of our research collaborators who helped me to improve the quality of the work presented in this dissertation. Thank you, Dr. Hatakeyama, for considering the field application perspective

of our in-house fabricated membrane to treat wastewater streams, as well as, for the cordial feedback on the research paper.

Faculties at the University of Kentucky have been very helpful in sharing resources and ideas. It created a friendly and welcoming work environment, which has greatly facilitated overall research atmosphere. Thank you, Dr. Barbara Knutson, Dr. Tate Tsang, Dr. Bradley Berron, Dr. Dibakar Bhattacharyya, Dr. Isabel Escobar and Dr. Yang-Tse Cheng for your wonderful lectures in graduate classes. Special thanks to Dr. Zach Hilt, Dr. Steve Rankin, and Dr. Doo Young Kim, for letting me use instruments in their research labs. Special thanks to Dr. Grulke, who is no longer with us, continues to inspire by his example. Small talks in the elevator and across the campus with Dr. Grulke, which were often accompanied with laughter will always be cherished. I also enjoyed brief talks in elevator and seventh floor with Dr. Fuqian Yang, which boost my motivation for research.

Research facilities at the University of Kentucky provided great help with the characterization of materials and analytical assistance. My sincere thanks to Dr. John Balk, Dr. Dali Qian, Dr. Nicolas Briot and Dr. Azin Akbari at the Electron Microscopy Center (EMC) for providing support with material characterization. It is one of the best research facilities I have come across. Thank you all for helping me understand the working procedure of few advanced characterization tools at the EMC. Environmental Research and Training Laboratory (ERTL) provided immense analytical help during various stages of my research. I am thankful to John May and Megan Combs for their assistance and sharing of insights on analyzing different constituents from water using various analytical instruments. John May, I feel privileged to work with you. Your in-depth understanding of the working of instruments at ERTL amazed me.

I would like to convey my special gratitude to all the staffs at the Department of Chemical Engineering at University of Kentucky. Thank you, Bruce Cole, Marlene Spurlock, Joshua Duruttya, Amy Terry, Paula McGee, Melissia Witt, and Chelsea Hansing for the assistance you all provided and not letting tedious paperwork come in the way of our research. You all pushed us to carry through during our graduate studies. You all keep us updated. You all are amazing. Thank you, Nick Cprek, for your help with assembling experimental setups and lab supports. Thank you, Nancy Miller for supporting us to clean

the lab during yearly inspection and providing us empty glass bottles for keeping waste chemicals. It was a pleasure to have Dr. Thomas Dziubla and Dr. Steve Rankin as DGS. Your support to graduate students and MACE has helped a lot in creating a pleasant working atmosphere for the graduate students in the department. I would also like to acknowledge the support provided over the past couple of years by the department chairs: Dr. Douglas Kalika and Dr. Thomas Dziubla.

From Fall 2015, I have had the pleasure of working with a great team of lab mates on 7$^{th}$ floor of FPAT building at University of Kentucky. I would like specially thank Dr. Rupam Sarma. It is great to have you as a lab mate. First three years in Dr. DB's lab you played a significant role to keep me working. Thank you for keeping me in all your research projects. I really miss the discussion apart from research with you in lab. Dr. Andrew Colburn, I feel lucky to have you as a lab mate and discussing everything with you. I am grateful and want to thank Dr. Sebastian Hernandez, Dr. Priyesh Wagh, Dr. Sneha Chede, Dr. Michael Detisch, Dr. Hongyi Wan (Derek), Dr. Ashish Aher, Anthony Saad, John Cravens, Nathan Puckett, Madison Sloan, Conor Sprick, Francisco Leniz, Ufuoma Kara, Spencer T. Schwab, Dr. Xiaobo Dong (Max), Joyner Eke, and Dr. Yuxia. You guys are amazing, and I will cherish the memories with you all. I will miss you all.

During my research at the University of Kentucky, I had the privilege to work and mentor some of the bright undergraduate students. Their curiosity and persistence towards research helped me to keep my motivation. I directly mentored Christopher Fugate and Ronald J. Vogler. These two are awesome students. I also partially mentored Samuel Thompson and Madison Kearschner. I know they will do great in their future. I also want to thank Fox Thrope, Victoria Claus, Mariah Bezold, Trisha Nickerson, Rollie Mills, Paul Lee and Phillip Sandman for their sincere effort towards research. Without the presence of undergraduate students in labs, graduate research will be so routine work.

It is my honor to be a member of our UK Superfund center. This center is not just about the research about health and environmental protection issues but also involves lots of community engagements. Thank you, Dr. Bernhard Henning and Dr. Zack Hilt for the suggestions regarding my career and research. I really liked the yearly one to one meeting with you two. I would also like to thank Jennifer Moore and Emily Raine Koyagi to save us from all the paper works.

It was a great opportunity for me that I along with Dr. Hongyi Wan (Derek) had the privilege to take our test unit to an actual hazardous waste site at Louisville, KY. Thanks for the collaboration with Arcadis US Inc, especially to the practical suggestions from Dr. Matthew Schnobrich and Todd Brooks. Thanks, Lucy Pacholik and Tahiya Tarannum for the sampling on-site and the economic estimation.

I would like to express my gratitude to my parents Mohammad Shafiq Ullah and Jobeda Begum who raise me up and support me for my education. I want to thank my sister Dr. Sabrina Shafiq and my brother Dr. Faisal Mahmud for their encouragement throughout my life. Special thanks to my wife Samira Islam, who carried with me during this challenging time of our life. Even you finished all the CFA exams in 2016, you sacrificed your career for me during my graduate studies. My special thanks to my only daughter Subhana Islam for understanding that I have a defense exam. Both my wife and daughter were so supportive during last two months when we all have to stay at home from COVID-19. Without their support I was not able to finish this dissertation on time. It is my pleasure that my family is always on my side. I am indebted forever for all the sacrifices my family members did for me to walk though this stage of my life. Thank you.

I would like to acknowledge research funding agencies. This research was funded by the NIEHS Superfund program (Grant no: PE42ES007380), NSF-EPSCoR (Grant no: 1355438) and Chevron Corporation. Special thanks to Nanostone Water, Solecta, and DOW Filmtec for providing commercial membranes to conduct the research.

.

## TABLE OF CONTENTS

## LIST OF TABLES

## LIST OF FIGURES

# CHAPTER 1. INTRODUCTION

## 1.1 Membrane Technology for Sustainable Water Treatment

Water is one of the most precious resource for life in this planet and is becoming scarce and contaminated [1-3]. Population growth, industrialization and climate change constitute an expanding list of stressors to water resources that exacerbate global water scarcity [1, 4]. In both developing and industrialized nations, a growing number of contaminants are entering water supplies from human activity, from traditional compounds such as heavy metals and distillates to emerging micropollutants [2-5].These constant contamination of water sources strongly affects energy and food production, industrial output, and the quality of our environment [1-3].

Treatment of industrial process water has become a major challenge and such wastewaters are characterized by a high level of total dissolved solids, and a high fouling potential [1-2]. These wastewaters are therefore difficult to treat [3-4]. Furthermore, potential new regulations may require zero liquid discharge for industrial wastewaters [1]. In addition, resource recovery will be an integral part of wastewater treatment in the coming decades. This will necessitate the development of lower-cost, energy-efficient, efficacious technologies for the treatment of waste and contaminated water from source to point-of-use are needed, without further stressing the environment or endangering human health by the treatment itself [1-4]. Fortunately, a recent surge of activity in water treatment research offers hope in mitigating the impact of impaired waters around the world [2]. Conventional methods of water disinfection, decontamination and desalination can address many of these problems with quality and supply [1]. However, these treatment methods are often chemically, energetically and operationally intensive, focused on large systems, and thus require considerable infusion of capital, engineering expertise and infrastructure, all of which precludes their use in much of the world [1-4].

Membrane-based treatment technologies play a key role in water treatment and purification [6-10]. These technologies produce water of superior quality, are less sensitive to feed quality fluctuations, more energy efficient and have a much smaller footprint compared with conventional water treatment technologies [1, 11-12].

## 1.2 Membrane, Membrane Classification and Transport Mechanism

Membranes are thin barriers that permit selective mass transport and form the basis of several separation processes typically driven by gradients in pressure, electric potential, concentration or temperature [8]. With the advantages of modularity, scalability, compactness and high energy efficiency, membrane separations have become pervasive in applications related to energy, water, food, biotechnology and chemical processing [4, 8]. Major applications include water treatment and desalination, natural gas purification, production of nitrogen from air, bioprocessing, solvent- and petrochemical-based separations and, production of ultrapure water [4, 8]. Beyond separations, membranes find use in fuel cells, drug delivery, bio or chemical sensors, therapeutic procedures, tissue repair, production of pharmaceuticals and energy harvesting from mixing processes [4, 8].

Membrane processes can be classified into different categories, based on different criteria including membrane configuration, type of membrane materials, driving force, separation mechanism, and size range of constituents removed [13]. The latter is dictated by the membrane's pore size or molecular weight cut-off (MWCO). Four main membrane types are commonly used to treat wastewater to potable standards and are classified in order of decreasing pore size [13]. As the pores get smaller the processes need more driving force. The technologies are often classified as low pressure (MF, UF) and high pressure (NF, RO) [13]. A schematic diagram summarizing the most important constituents rejected by each membrane type is shown in **Figure 1.1** [13]. Since a larger driven force is needed for the membranes with smaller pores, MF/UF membranes have been widely used in the wastewater treatment processes to save energy and cost [1, 13].

Membranes achieve selective transport through a variety of mechanisms operative over different length scales [7-8]. **Figure 1.2** shows a schematic of length-scale dependence of membrane transport mechanisms [8]. At the smallest scale, dense polymeric membranes (without defined pores), such as reverse osmosis membranes for water desalination and many gas separation membranes, operate by a solution-diffusion mechanism [8]. Here, selectivity results from differences in species solubilities and diffusivities in the membrane material; solubility depends on the molecular structure, membrane porosity and chemical affinity, whereas diffusivity is governed by thermally activated rearrangements of the polymer chains that strongly favor size-dependent diffusion of smaller molecules [8]. When

selectivity is governed by diffusion alone (as in many polymeric gas separation membranes, a more permeable material typically provides less selectivity and results in a trade-off between permeability and selectivity known as the Robeson limit in the context of gas separations [7-8]. Overcoming this trade-off requires incorporation of additional mechanisms such as chemical affinity or molecular sieving, where smaller molecules pass through while larger ones are sterically impeded [7-8]. Due to the small free volume available, gas transport in membranes with pore diameters just beyond the molecular size is governed by phenomena such as diffusion, surface adsorption and condensation of gas molecules in the membrane pores [7-8]. In pores that are much larger than molecular size but smaller than the gas mean free path, gas transport is governed by Knudsen diffusion, where molecules with lower molecular mass travel faster and have higher permeance [7-8].

In liquid environments, transport in pores that are larger than molecules or ions is influenced by differences in species diffusivity, steric effects, chemical affinity and electrostatic interactions, including surface charge and dielectric effects [7-8]. When the pore size is below ~2 nm, transport of water is also influenced by hydrogen bonding and structuring of water molecules, which depends on the pore geometry and functional groups [8]. The effect of pore functional groups on water flow tends to be modest, with hydrophilic groups (for example, -OH, Mo, -N) reported to enhance permeation of water by up to twofold by attracting water molecules to the pore, compared with hydrophobic groups (for example, -H), which can present an entropic barrier to transport [6-8]. Transport of hydrated ions across atomically thin pores is influenced by electrostatic interactions, coordination with functional groups or charges at pore edges, and steric exclusion of the ion hydration shell [6-8]. Pore functionalization can radically alter ionic transport, especially if the pore is smaller than the size of the hydrated ion [6-8]. Charged or partially charged functional groups along the pore edge can lower the energy barrier for ions of opposite charge and increase the barrier for ions of like charge, leading to cation/anion selectivity [7-8]. Although transport in membranes is complex, a thin selective layer with precisely controlled pores and chemical functionality could yields high permeance and high selectivity [8]. **Figure 1.3** shows relationship of membrane structure with selective layer thickness for different kind of membranes [8].

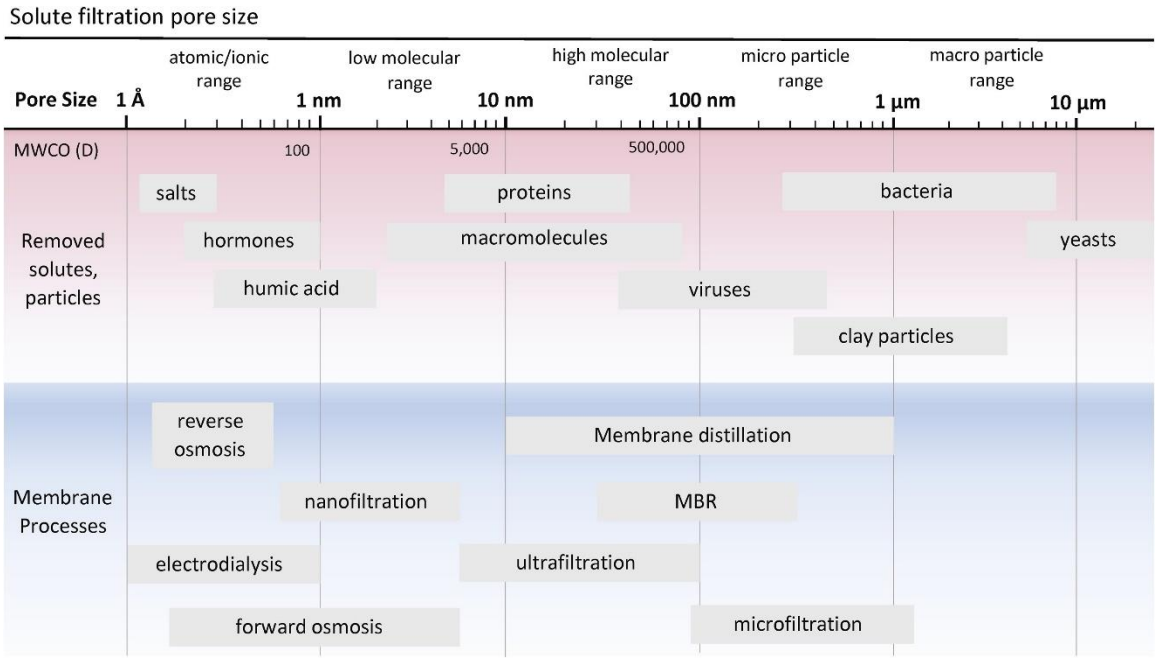


**Figure 1.1** Membrane separation processes, pore sizes, molecular weight cut-off (MWCO) and examples of sizes of solutes and particles. (Figure was adapted with permission from Progress in Polymer Science, Warsinger et al., 2018).

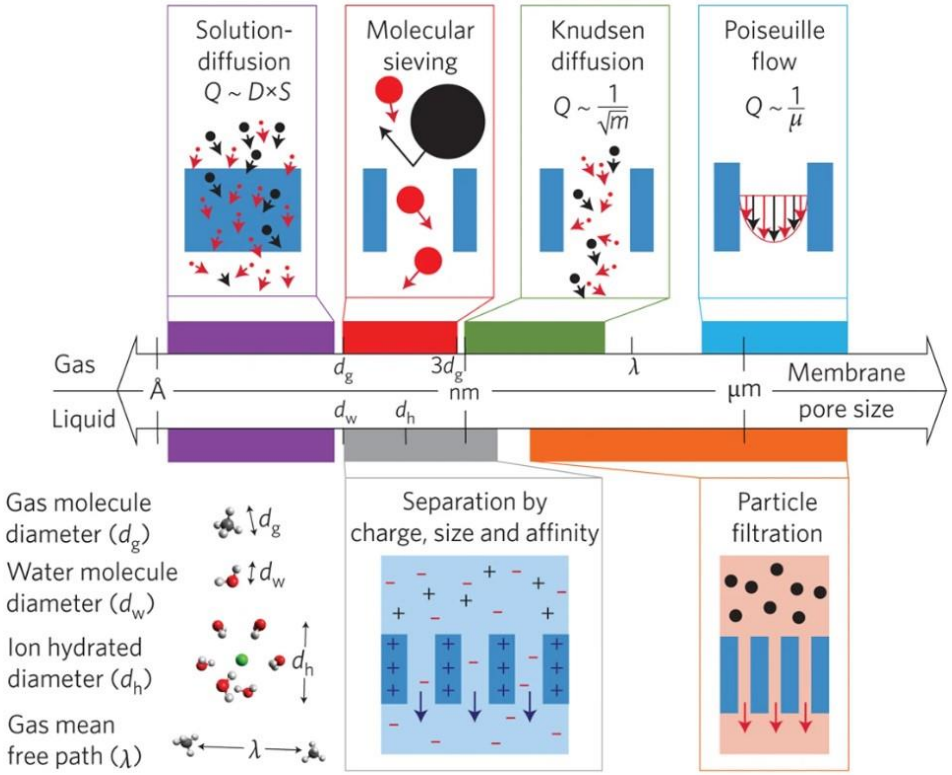


**Figure 1.2** Length-scale dependence of membrane transport mechanisms. Relative scales of gas and water molecules, hydrated ions and gas mean free path are depicted on bottom left. Q, flux; D, diffusivity; S, sorption coefficient; m, molecular mass; µ, viscosity. (Figure was adapted with permission from Nature Nanotechnology, Wang et al., 2017).

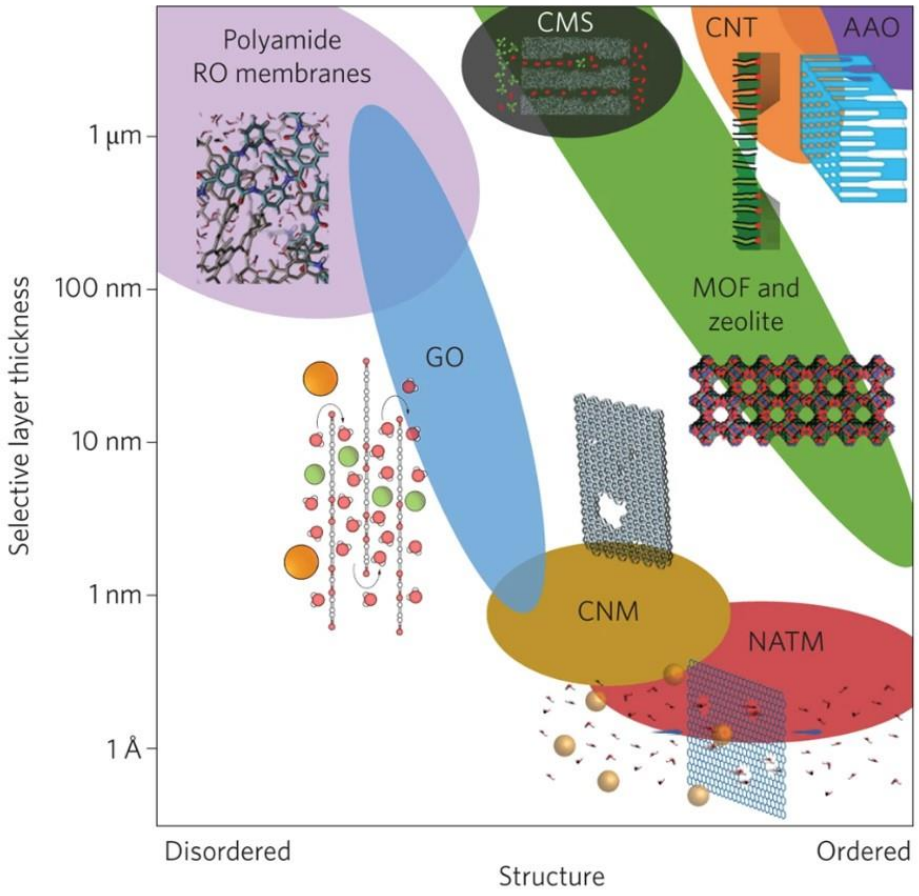


**Figure 1.3** Membrane structure–thickness map with some illustrative examples. From left to right, the structures change from disordered to ordered (Figure was adapted with permission from Nature Nanotechnology, Wang et al., 2017).

## 1.3 Pore Functionalization Approaches of Microfiltration Membranes

Several polymers are used for making membranes. Among them a select few have emerged as leading choices for the synthesis of MF/UF membrane for their versatile application [13]. Two main design considerations such as **i)** membrane material properties and, **ii)** membrane formation mechanisms drive the fabrication of membrane technologies [13-14]. Driving factors for material choice include pore size distribution, wetting susceptibility, porosity, mechanical strength, cost, polymer flexibility, fouling resistance, stability, durability and, chemical resistance [13-14]. The latter may include resistance to pH, oxidants, and chlorination [13-14]. Other desirable properties that also relate to the fabrication itself include low tortuosity and surface properties that influence rejection (e.g., surface charge) [13]. Additional characteristics may influence performance as well, such as improved regeneration/fouling recovery, which results from many things including low surface roughness, poorly adhering materials, and resistance to cleaning agents [13]. Warsinger et al. reported conventional materials for the fabrication of MF/UF membranes are summarized in **Table 1.1** [13]. Among those materials PVDF polymer has emerged as one of the potential candidates for making MF/UF membrane due to their broad pore size distribution, wide pH range of operation and very much stable in harsh operation condition.

It is promising to utilize and modify PVDF membrane pores with functional groups to obtain special separation and reaction functions. Many studies have been reported on functionalizing the MF membrane pores with -OH, $-NH_2$, $-SO_3H$, -COOH, or $-CONH_2$ groups by using chemical modification, polymerization, and layer by layer assembly (LBL) methods [6, 15-21]. The functionalized membrane has been studied for various applications such as heavy metal removal, bioreaction, and catalysis [15, 20-28]. The advantages of using PVDF functionalized porous membrane are high mass transfer capacity, low operating pressure due to the open structure and many versatile applications [15, 21-24, 29-30]. **Figure 1.4** shows a schematic of PVDF microfiltration membrane functionalization with suitable polymer such as poly acrylic acid (PAA) to incorporate carboxyl (-COOH) group and further modification of functionalized membranes for different application ranging from catalysis, bio reactor to heavy metal adsorption platform.

As a catalytic reactor bed, support materials such as PVDF after functionalization with suitable responsive polymers are very desirable platform for in-situ synthesis of

catalytic nanoparticles for conducting a wide range of reactions [6, 15]. Due to their high surface area to volume ratio, large amounts of catalyst can be loaded onto a relatively small volume of materials. Since many catalysts are derived from heavy metals, the same responsive materials used to capture heavy metal ions for their synthesis and immobilization [6]. This membrane platform containing immobilized catalysts can be operated under convective flow, thereby significantly reducing the mass transfer limitation [6, 15, 26].

As a bio reactor, membrane with a net charge have been used to electrostatically immobilize enzymes for conducting catalytic reactions [6, 21, 31]. Although enzyme immobilization generally lowers activity, the use of free enzyme in the homogeneous phase is restricted due to lower stability and product inhibition [6]. Methods for enzyme immobilization include covalent, site-directed and electrostatic attachment [6]. Layer-by-layer assembly technique commonly used by intercalation of positive and negative polyelectrolytes, is a powerful, versatile and, simple method for assembling supramolecular structures [6, 21]. These structures exhibit negative and positive charges, which allow for incorporation of a variety of materials in particular, enzymes [6, 21]. Though a LbL assembly consisting of multiple layers of polyelectrolytes is an excellent platform for enzyme immobilization, covalent attachment of the first layer may be necessary in order to impart greater stability to the assembly. Poly(allylamine-hydrochloride) (PAH), Poly (L-lysine hydrochloride) (PLL) are well known polyelectrolytes used for this purpose [6].

Functionalization of PVDF membrane materials also allow for the development of high capacity heavy metal adsorbents [6, 22-24]. Unlike charged based exclusion, where separation occurs due to the electrostatic repulsive force between fixed ionizable groups and permeating co-ions in solution, adsorption mechanism such as ion exchange, chelation etc. are due to the attraction of the counterion to the immobilized polyelectrolyte [6]. Ion exchange is driven by electroneutrality, such that a divalent counterion requires two binding sites for metal capture [6].

**Table 1.1** Typical materials used for fabrication of MF/UF membranes (Table was adapted and modified with the permission from Progress in Polymer Science, Warsinger et al., 2018).

| Material | Most Common Use | Advantages | Disadvantages |
|---|---|---|---|
| Polysulfone (PSU) | MF/UF | Good mechanical strength, Chemically resistant pH Range: 1-13 Chlorine Resistance: Good | |
| Polyether Sulfone (PES) | MF/UF | Rigid, compaction resistant, Very permeable pH Range: 1-13 Chlorine Resistance: Good | |
| Polyacrylonitrile (PAN) | MF/UF | Oxidant tolerant, Narrow pore size distribution | |
| Polyvinylidiene Fluoride (PVDF) | MF/UF | Very oxidant tolerant, pH Range: 2-11 Chlorine Resistance: Fair | Broader pore size distribution |
| Polyethylene (PE) | MF/UF (Uncommon) | High resistance to organic solvents, low cost, oxidant tolerant | Poor thermal properties, Weaker fouling resistance Chlorine Resistance: Poor |
| Polypropylene (PP) | MF/UF (Uncommon) | High resistance to organic solvents, Decent mechanical strength pH Range: 2-11 | Low fouling resistance, Not oxidant tolerant Chlorine Resistance: Poor |
| Polyvinyl Chloride (PVC) | MF/UF (Occasionally) | | Poor thermal stability, Not oxidant tolerant |
| Cellulose Acetate (CA) | RO, MF/UF | Renewable source pH Range: 5-8.5 Chlorine Resistance: Good | Low permeability (RO) |
| Polyamide (PA) | RO (TFC active layer), NF, MF/UF (Occasionally) | Small pores, Excellent rejection, selectivity pH Range: 1-13 | Relatively impermeable/dense Chlorine Resistance: Poor |

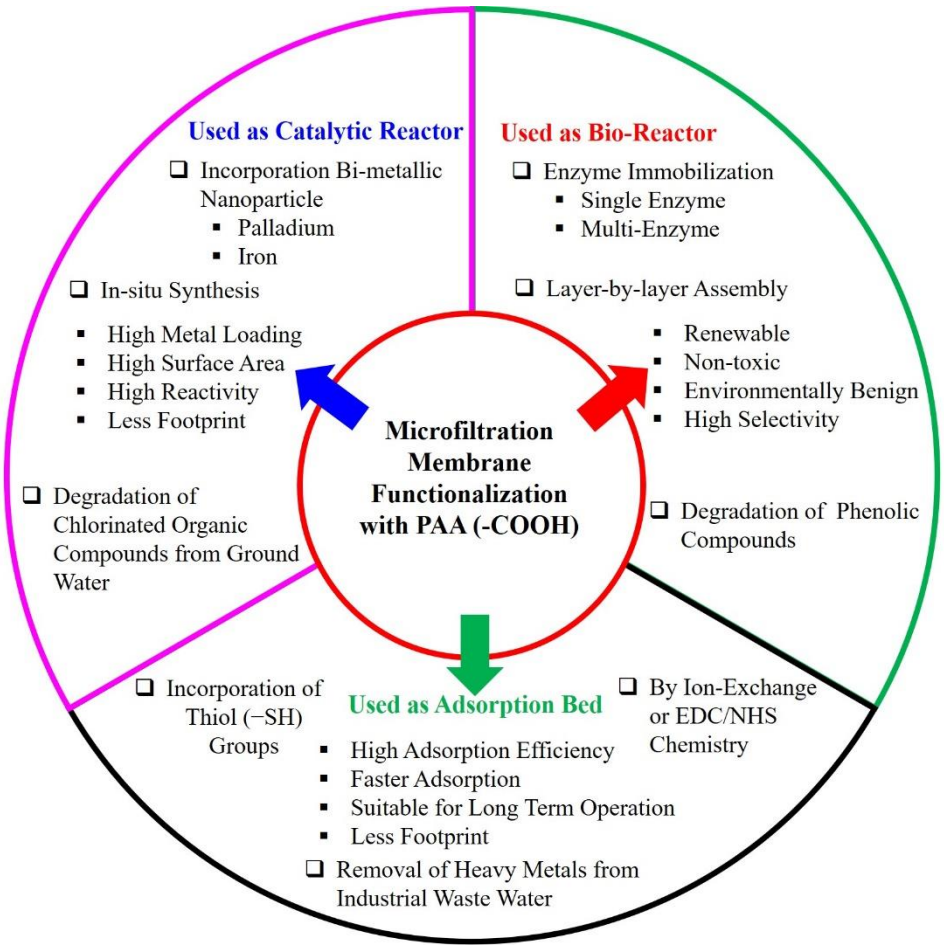


**Figure 1.4** A schematic of PVDF microfiltration membrane functionalization with PAA (-COOH) group and further modification of functionalized membranes for different application ranging from catalysis, bio reactor to heavy metal adsorption platform.

## 1.4 Functionalization of PVDF Microfiltration Membrane with PAA

Functionalization of PVDF base membrane by incorporation of suitable functional groups will enable further modification of the membrane platform [6]. These functional groups are mostly chosen from stimuli responsive polymers [6]. Such stimuli responsive polymers are generally used as the building blocks for responsive membranes [6, 32-33]. Stimuli responsive membranes exploit the interplay between the pore structure and changes in the conformation/polarity/reactivity of responsive polymers of functional groups in the membrane bulk or on its surfaces [6, 32-33].

Incorporation of suitable responsive groups may be classified as in-situ or post synthesis [6]. In the former method, the group is part of one of the monomers used to form the membrane. In the latter method, the membrane polymer is synthesized and then a reactive group present is functionalized prior to membrane casting [6]. Using in-situ method, the monomer containing the responsive group and other co-monomers used as cross-linker are co-polymerized and the copolymers are fabricated into the desired membrane [6]. This in-situ polymerization and concurrent cross-linking results a high degree of ionization groups in the membrane pore structure [6, 32-33].

Poly(acrylic acid) (PAA), poly(methacrylic acid) (PMAA), poly(vinylpyridine), poly(L-glutamic acid) etc. are well known pH responsive polymers [6]. Among them, poly(acrylic acid) (PAA) and poly(methacrylic acid) (PMAA) have been wildly used as hydrogel [6, 32, 34-35]. The side chains, with carboxyl groups (-COOH), of PAA and PMAA can lose protons at neutral or base solution (when pH > pKa of polymers) [6, 32]. This makes carboxyl groups convert to anion $-COO^-$, which can be used to capture metal cations [32]. Therefore, PAA functionalized PVDF membranes along with novel ion-exchange and in-situ reduction processes for Pd-Fe particle incorporation have been reported for the treatment of chlorinated organic compounds [28, 36-39]. Carboxylate groups from PAA can ion-exchange with metal cations and the captured metal cations can be converted to metallic nanoparticles (in-situ) through adding reducing agent ($NaBH_4$) [15, 28, 35-36, 39]. These carboxylate groups also prevent the leaching of produced metal ion (i.e., recapture by ion exchange) and nanoparticle aggregation [40]. Tunable membrane pores can be achieved by changing environmental pH through ionization of carboxylate groups from PAA [32-33].

## 1.5 Incorporation of Bi-metallic Nanoparticles in Membrane Pore Domain for Remediation of Chlorinated Organics

Chlorinated organic compounds (COCs) are a serious concern as environmental pollutants due to their high toxicity, chemical stability and presence in soils, sediments as well as in different water sources [17, 36, 41]. Nano scale zero valent iron (nZVI) and iron based bimetallic NPs have been intensively studied for the degradation of COCs into less toxic or nontoxic products [42-49]. The addition of a second metal such as Pt, Pd, Au, Ag, Ni, Cu, Zn with Fe will enhance the catalytic activity for dechlorination [50-52]. Among these metals, Pd is well known and the most studied catalyst for hydro-dechlorination of COCs due to its noble nature [15, 53]. When bimetallic Pd-Fe is used in COCs degradation in water, Fe acts as an electron source and Pd as a catalyst. Once, hydrogen is produced from nZVI due to its corrosion in water, it is activated by Pd to form highly reactive hydrogen radicals. These hydrogen radicals then serve as effective electron donors for dechlorination of COCs, whether Pd is coated on nZVI or is present as separate NPs [54].

Incorporation of these reactive NPs in membrane results as a suitable platform for water remediation and antifouling application. Different methods for in situ preparation of nanoparticle-based membrane systems for water remediation are well documented in literature [48]. Synthesis of Fe, Pd-Fe, Ni-Fe, and iron oxide immobilized in polyvinylidene fluoride/poly (acrylic acid) (PVDF-PAA) membranes for use in the degradation of COCs was reported in previous studies [20, 55-57]. These functionalized membranes have been used as porous supporting materials to control NPs aggregation, to capture dissolved metal ions, and to perform batch and convective flow degradation studies of COCs through the associate membrane pores. **Figure 1.5** shows a schematic of pore functionalized Pd-Fe nanoparticle incorporated PAA-PVDF membrane is degrading PCBs to less toxic biphenyl. Further, reaction mechanism and reaction pathway via electron transfer is also demonstrated in **Figure 1.5**.

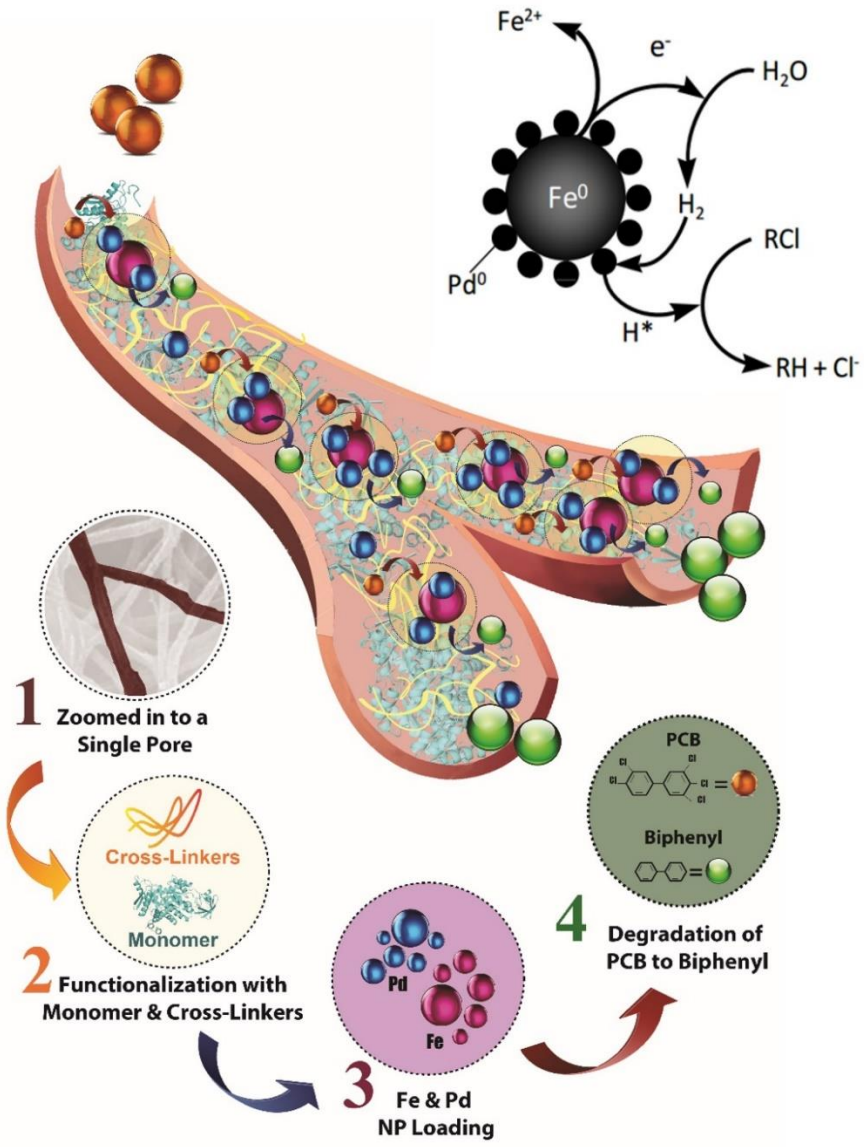


$$Fe^0 + 2H_2O \rightarrow Fe^{2+} + H_2 + 2OH^-$$

$$H_2 \xrightarrow{Pd} 2H\bullet \qquad \text{Extremely Reactive}$$

$$PCBs + 2nH\bullet \rightarrow Biphynyl + nH^+ + nCl^-$$

$$2Fe^0 + O_2 + 4H^+ \rightarrow 2Fe^{2+} + 2H_2O$$

**Figure 1.5** A schematic of pore functionalized Pd-Fe nanoparticle incorporated PAA-PVDF membrane. This membrane reactor platform is degrading PCBs to less toxic biphenyl. The reaction mechanism and reaction pathway via electron transfer is also demonstrated.

## 1.6 Immobilization of Enzymes on PAA Functionalized Microfiltration Membrane for Degradation of Chloro-Organics

Introduction of functional polymers into the membrane pores enables deliberate immobilization of biological molecules such as enzymes within the polymer matrix, thus allowing catalytic remediation of toxic organics in water. Apart from providing enhanced stability, reusability and ease of handling, immobilization of enzymes onto membranes increases their practical utility by coupling them with immediate separation of the products in a flow-through system thereby minimizing inhibition of enzyme activity [58-59].

Chlorinated organic compounds such as chlorophenols are a class of persistent environmental pollutants which have been extensively used as wood preservatives and for pesticide formulation over the years [60]. These chlorinated organic compounds have a long history as threats to human health. Various chloro-organics, such as, 2,4,6-trichlorophenol (TCP), have immense health impact, and is widely detected in ground water and soil [61-62]. Existing remediation techniques degrade the chloro-organics by both physical and chemical methods [63-64]. In contrast, bioremediation is accomplished using enzymes which are environmentally benign, renewable and non-toxic [65-66]. Furthermore, enzymes are highly selective natural biocatalysts that accelerate reactions with extreme efficacy and selectivity. However, enzymes have had limited industrial application due to their lack of long-term operational stability, intricate recovery and poor re-usability. Fortunately, these limitations can often be overcome by immobilizing them on suitable matrices such as functionalized membrane [67-68].

Laccase has long been used in the paper industry for its lignolytic activity, and also gained attention for its ability to degrade phenolic and other compounds in contaminated effluents [69-73]. Combining promising activity of laccase with the versatile tunable behavior of polyacrylate polymers will allow to fabricate bioinspired membranes for dechlorination of polychlorophenols. The hypothesis is that under convective flow the reactants can rapidly access the active sites and the metabolized products leave the membrane and hence the enzyme active sites immediately after the reaction, eliminating unnecessary deterioration of the enzyme activity.

To this end the immobilization of laccase on polyacrylic acid (PAA) functionalized polyvinylidene fluoride (PVDF) microfiltration membranes following a layer-by-layer

(LBL) assembly technique is reported in this study [74-76]. A general believe is that, unlike enzymes entrapped in matrix, covalent binding usually leads to higher stability due to increased enzyme-support attachment, however, reduces enzyme activity due to changes in the enzyme's native structure [31, 77-80]. LBL assembly offers such entrapment with an oppositely charged polyelectrolyte within the membrane domain without deteriorating the core structure. It helps to retain the enzyme activity without compromising on the stability aspect. Moreover past studies have shown that it is possible to reload the enzyme when necessary [21]. **Figure 1.6** shows a schematic of laccase immobilization in membrane platforms through layer-by layer approach. PAA-PVDF membrane with an electrostatically immobilized layer of PAH and subsequent laccase immobilization enables dechlorination of polychlorophenols.

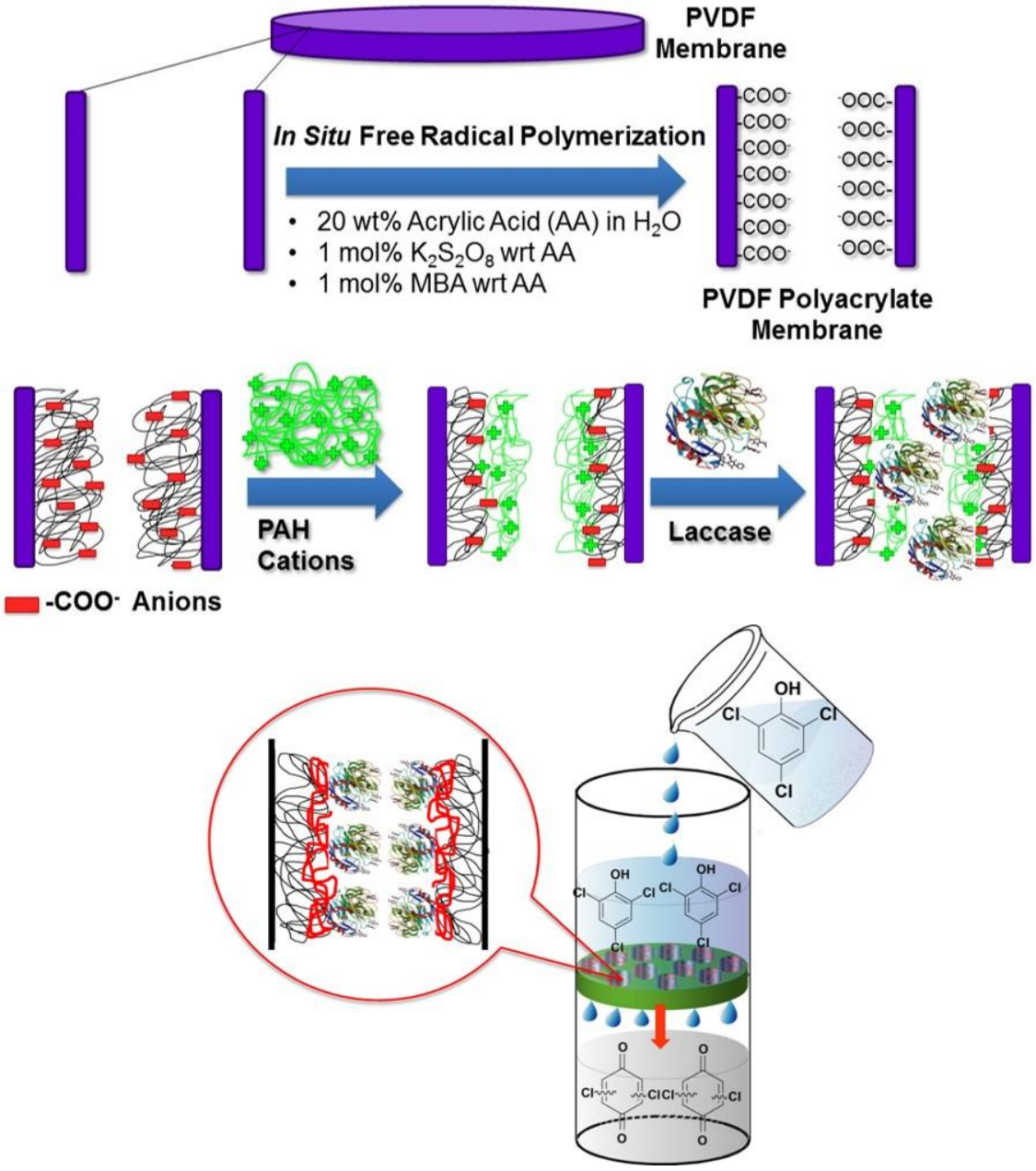


**Figure 1.6** Schematic of laccase immobilization in membrane platforms through layer-by layer approach. PAA-PVDF membrane with an electrostatically immobilized layer of PAH and subsequent laccase immobilization enables dechlorination of polychlorophenols. (In the scheme 'with respect to' is abbreviated as 'wrt').

## 1.7 Multi-Enzyme immobilization on PAA-PVDF Membrane for Transformation of Lignin Model Compound

Synthetic membranes provide a versatile platform for immobilization of bio-catalysts (enzymes) thereby overcoming the inadequacies of soluble enzymes such as instability, difficult recovery, trouble of handling and non-reusability [58-59]. Enzymatic reactions, on the other hand, encourage emerging technology incorporating multienzyme systems, making catalytic strategies operative and sophisticated [81-83]. Immobilized multi-enzymatic systems that exploit the selectivity of biocatalysts have been developed from time to time [65-66]. In this respect, pore functionalized membranes with porous support and functional polymer matrices may be an ideal platform for multiple enzyme immobilization and thus developing bioreactors for enzymatic reactions [67-68].

Lignocellulosic feedstocks have received continuous attention as renewable biomass for generation of biofuels and fine chemicals [84]. In particular, the highly abundant polymer, lignin, deserves more attention than only getting used for low value applications such as low grade fuel [85]. Plenty of research have been conducted that report ways to exploit the prospective of lignin as a resource for value added chemicals [84, 86-87]. However, practical utility is far ahead owing to the challenges involved during lignin depolymerization. Most of the methods reported for lignin valorisation, such as pyrolysis, catalytic oxidation and/or hydrolysis under supercritical conditions etc., are either energy-consuming or environmentally unfavorable [88]. In nature, lignin is degraded by a pool of extracellular ligninolytic enzymes such as peroxidases and laccases over a period of many years [89]. One of the novel approaches to mimic natural ways of lignin depolymerization is involving multi enzymatic reactions and is worth considering.

Membrane based multienzyme systems can be constructed by carrying out sequential deposition onto the membrane pores. The layer-by-layer (LbL) adsorption technique is a general and versatile tool for the controlled fabrication of surfaces and pores by the consecutive deposition of alternatively charged polyelectrolytes [74-76]. Efforts have been made to fabricate multienzyme surfaces through LbL techniques for bioprocessing applications [31, 77-80].

Recent interest in enzymatic methods for the lignin biodegradation has focused on using enzymes such as peroxidases, laccase, phenol oxidases etc [90-93]. Peroxidases and

laccases constitute an interesting tool for the development of alternative oxidative processes for lignin degradation due to their low substrate specificity and relatively wide pH of action [69-73, 94-96]. The exploitation of their potentiality is prevented, especially in the case of peroxidases, by their low stability. Although there are quite a few reports on the use of peroxidase for lignin oxidative process [97], horseradish peroxidase (HRP) has been shown to catalyse spontaneous polymerization of a variety of aromatic compounds [98-99]. Such undesired polymeric by-products have to be filtered out of the reactor solution in order to avoid poisoning of the biocatalysts. On the other hand, in the case of membrane bioreactors such polymeric products need to be avoided to circumvent clogging and fouling of the membrane. One such technique is to use multi enzyme system to convert such poly/oligomeric products formed by peroxidases to simpler ones.

A composite membrane with horseradish peroxidase (HRP) and laccase immobilized on it via the LbL technique and its performance towards degradation of a lignin model compound is reported in this study. The hypothesis is that by the use of such multienzyme immobilized membrane system, any unnecessary by-products can simultaneously be converted to small molecules thereby prohibiting membrane fouling as well as enzyme inhibition. In essence, the HRP enzyme partially degrades/modifies the substrate (Guaiacylglycerol-β-guaiacylether) to oligomeric unit which is then degraded by laccase to monomeric units. As peroxidase enzyme needs hydrogen peroxide as one of the substrate, glucose oxidase (GO) was incorporated as a third enzyme for the in situ generation of hydrogen peroxide. Alternatively, for membranes with only laccase and HRP on it, hydrogen peroxide was added to the feed. The main objective of this study is to understand the activity of such multi enzyme functionalized membranes towards degradation of an aromatic phenolic lignin model compound, specifically Guaiacylglycerol-β-guaiacylether (GGE). **Figure 1.7** demonstrates a schematic of degradation events of the lignin model compound GGE by multi-enzymatic reactions.

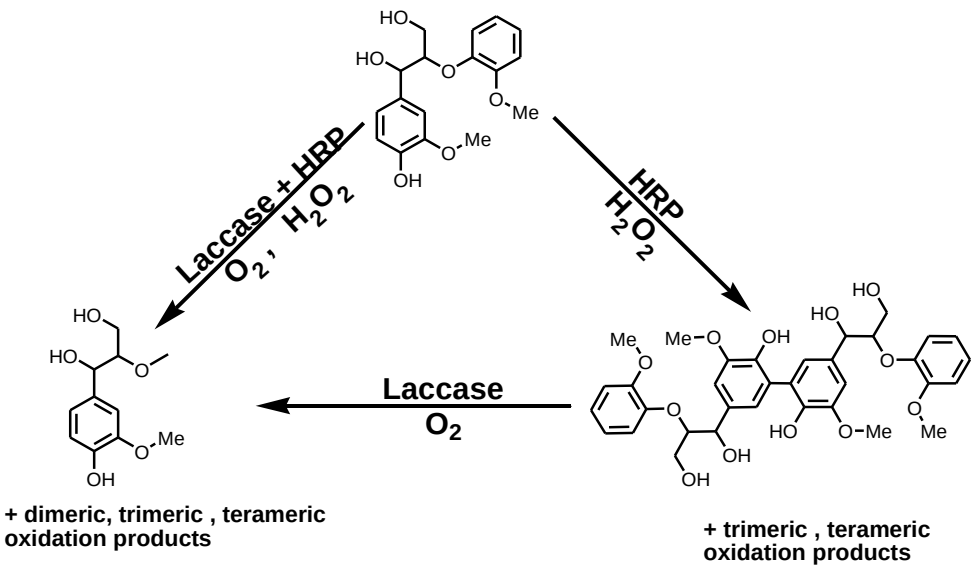


**Figure 1.7** Schematic of degradation events of the lignin model compound GGE by multi-enzymatic reactions.

## 1.8 Thiol Functionalizes Membrane for Heavy Metal Removal from Water

Functionalization of PVDF membrane with suitable responsive (pH, temperature) polymer allows to incorporate charged groups (-COOH, -OH) in membrane pore domain and tuning of pore size and flux [19, 100]. Carboxyl groups incorporated in PVDF membranes can be replaced by thiol (-SH) groups by either ion-exchange (IE) or by activated through ethyl(dimethylaminopropyl) carbodiimide/N-Hydroxysuccinimide (EDC/NHS) coupling [101-104]. The NHS-$O^-$ functional groups formed during this process can subsequently be substituted by thiol containing amines (organic compounds containing a basic nitrogen atom with a lone pair of electrons, e.g., R-$NH_2$). The resulting thiol membranes are expected to effectively absorb ionic mercury from water because of the strong propensity of thiols to bond with ionic mercury to form mercury-sulfur complexes [105-107]. The application could be further extended to capture other metals such as nickel, gold, arsenic from wastewater.

The affinity between mercury ions and sulfur is well-known. HgS may be present in geologic formations and enter wastewater streams as HgS particles or may be formed in an industrial facility by the reaction between ionic $Hg^{2+}$ and sulfur. HgS formation and precipitation can occur in the wastewater stream or can take place elsewhere in a facility and migrate to the wastewater. Organic compounds present in soils, natural waters, sediments, and living beings containing thiol (–SH) groups can complex mercury or form mercury-thiol species ($Hg(SR)_x$) through physicochemical sorption, ion exchange, and ligand-induced oxidative complexation [108]. In the aqueous phase, the soft lewis acids $Ag^+$ and $Hg^{2+}$ prefer complexation with the soft base $SH^-$ over reactions with hard bases such as $Br^-$, $Cl^-$, and $OH^-$. The mercury-sulfur complex is poorly soluble and very resilient, which allows for effective removal of ionic dissolved mercury species using sulfur groups [25, 105-106].

Cysteine ($C_3H_7NO_2S$, (Cys)), an amino acid that contains a thiol functional group, is known to interact strongly with mercury ions, affecting the metabolism and nucleic acids in the body [107]. Various studies, including some from this group, have used immobilized derivatives of cysteine and poly-thiol compounds onto polyelectrolytes, taking advantage of the Hg/Ag–thiol affinity for removal of $Hg^{2+}$ and $Ag^+$ [22-25]. Another amino compound with similar characteristics is cysteamine or β-Mercaptoethylamine ($C_2H_7NS$ (CysM)).

One industrial application of CysM is as a chelating agent to support gold and silver in biosensors and membranes [109-110]. The main difference between Cys and the less studied CysM is the absence of a carboxyl group in CysM. This could theoretically make CysM a more effective alternative to remove heavy metals from wastewater because relatively high concentrations of other cations ($Ca^{2+}$, $Mg^{2+}$) in wastewater may react with the carboxyl group due to their higher reactivity compare to heavy metal cations ($Hg^{2+}$, $Ag^{+}$) and cause steric hindrance for $Hg^{2+}$- $SH^{-}$ interaction.

Mercury (Hg) can be present as dissolved, elemental, or solid (e.g., nanoparticle HgS) species in wastewater streams from various industries, including industrial wastewater treatment plants, oil refineries, and ore extraction operations from mining industries. Mercury species present in industrial wastewaters are typically dominated by HgS nanoparticles and soluble $Hg^{2+}$ complexes [108, 111]. Discharge of wastewaters with elevated concentrations of mercury and other heavy metals can potentially impact aquatic life and the food chain [112-114]. Depending on site-specific conditions such as mercury speciation, geochemical conditions, and the presence of labile organic matter, certain mercury species deposited in sediments can be methylated over time and potentially accumulate in benthic organisms and fish to levels of concern [115]. Development of processes for effective, sustained, and cost-effective removal of dissolved Hg, elemental Hg, and nanoparticulate HgS from various wastewaters has been a challenge to scientist and the engineering community [116-118]. A variety of physical and/or chemical treatment processes have been proposed and developed for removal of particle-bound and dissolved Hg species from wastewater [105, 119-121]. The effectiveness of physical separation of particle bound Hg through methods such as filtration, flotation, centrifugation, or gravity settling is typically a function of particle size and/or specific gravity. Technologies for removal of dissolved Hg species from wastewater include ion exchange, activated carbon absorption, precipitation, electrodeposition, selective liquid-liquid extraction, and membrane separation [25, 122-130].

The physical and chemical composition and characteristics of wastewater can be complex. The performance efficiencies of most treatment technologies highly depends on the water source (sediment, surface water, ground water or industrial effluent water) and water composition, including mercury speciation and concentration, water quality

parameters such as pH, redox potential, ionic composition, ionic strength, and the presence of DOM and dispersed oil [131]. Removal of mercury and other heavy metals can be associated with several of these parameters. Among the treatment processes to remove dissolved Hg from wastewater, membrane-based separation is not well explored despite offering high treatment capacities, relatively small footprints, and long-term stability suitable for full scale operation for industrial applications [57, 101]. Removing mercury from wastewater compared to synthetic water can be challenging because the complexity of the water matrix can significantly impact the solids removal and adsorption performance of a treatment process. In addition, long term application of filtration and adsorption processes for removal of heavy metals can alter the performance of the treatment process over time. Few literature studies have evaluated mercury removal from real wastewater [131]. **Figure 1.8** is showing a schematic of thiol functionalized membrane adsorbing mercury from water.

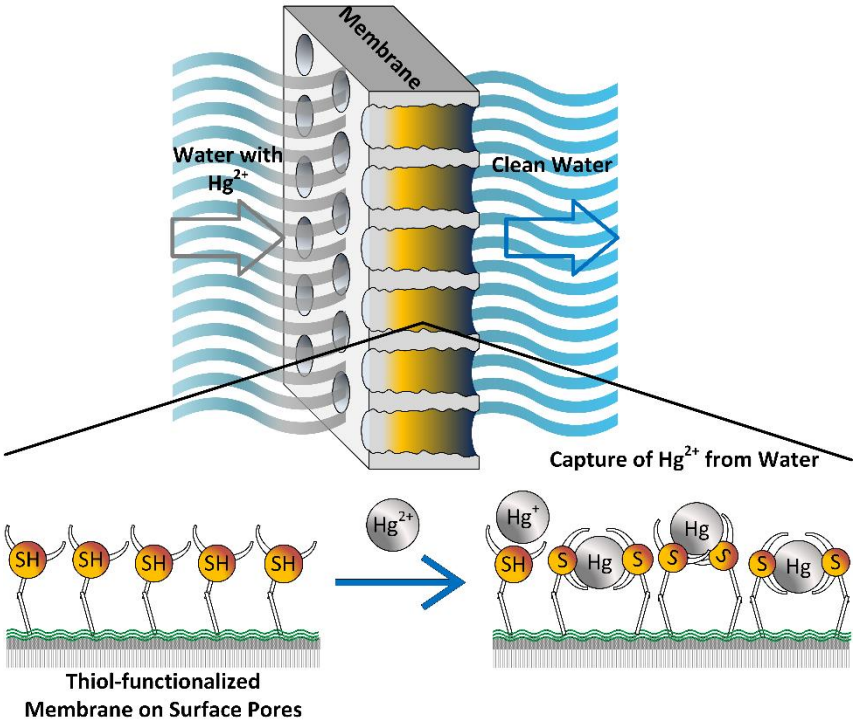


**Figure 1.8** A schematic of thiol functionalized membrane adsorbing mercury from water.

## 1.9 Next Generation Hollow Nanoparticles for Chloro-Organics Degradation

Hollow micro-/nanostructured metal oxide, which represent a class of materials with the unique properties of high porous structures, high surface area, inner hollow architecture and low density have attracted great attention in last several years [132-141]. These materials find potential application in photonics, catalysis, sensors, drug delivery, energy conversion, light weight fillers, adsorptive materials and storage systems because of their unique and improved properties [132-133, 136-137, 142-145]. To date, notable progress was made on the synthesis of hollow structures. Several chemical and physicochemical approaches such as template methods, the Kirkendall effect, Ostwald ripening, self-assembly techniques and spray drying method was reported [132-133, 137]. Among these, template-assisted methods, was most effective way to produce uniform hollow structures. Template methods are based on the formation of a core-shell structure by coating a desired material or its precursor on the surface of the template, followed by removal of the template by an appropriate technique [133, 137]. Methods using hard templates are most commonly used due to their effectiveness in the production of uniform hollow structures and applicability towards a large variety of materials [133, 137]. However, the procedure is expensive and requires additional steps during the synthesis as well as removal of templates; also, the hollow architecture may break during removal of the template [132-133, 137]. Thus, challenge remains to demonstrate simplified procedure to make hollow structures.

Recent studies demonstrated that hollow micro-/nano hierarchically structured materials exhibit enhanced properties compared to their bulk counterparts for water treatment application [135]. As a result, continuous efforts are being made on the preparation of complex iron oxide nanostructures assembled from low-dimensional building blocks [135]. Among them, sphere shaped hollow structures with permeable shells and high surface area have emerged as an attractive material for water treatment application [132, 135]. In this context a simplified hydrothermal approach for the synthesis of hollow iron oxide and palladium-iron oxide is demonstrated as a platform for chloroorganic degradation.

# CHAPTER 2. RESEARCH OBJECTIVES

The overall objective of this research is to assess different pore functionalization approaches of microfiltration membrane for the application of chloro-organic remediation to heavy metal sorption. To achieve this goal, PVDF microfiltration membrane was initially functionalized with polyacrylic acid (PAA) polymer to incorporate carboxylic acid (-COOH) group in membrane pores. This PAA-PVDF membrane was then investigated for three different pore functionalization approaches for water treatment application. Initially, **i)** incorporation of bimetallic (Pd-Fe) nanoparticles by in-situ synthesis for the remediation of chlorinated organic compounds (COCs); then, **ii)** incorporation of enzymes by layer-by-layer (LBL) assembly towards degradation of polychloro-organics; and finally, **iii)** thiol (-SH) functionalized PVDF membranes for heavy metal sorption from water. The detail goals of these diverse approached pore functionalized membranes towards application of water remediation are mentioned below.

Nanoparticle incorporated PAA-PVDF membrane as a catalytic reactor bed:

The main purpose of this study is to investigate the effects of monomer (M) and cross-linker (X) concentrations on the performance of pore functionalized pH responsive membranes for water-based dechlorinations applications, using 3,3',4,4',5-pentachlorobiphenyl (PCB 126) as a model compound.

The specific objectives of this work are:

- To functionalize PVDF membranes using different combinations in concentrations of PAA as a monomer, M (wt.%), and (N, N′- methylenebis (acrylamide)) (MBA) as a cross-linker, X (mol%).
- To study the variation of responsive behavior of PAA-PVDF membrane and understand its effects on mass gain, water permeability, Pd-Fe NPs size and metal loading.
- To depict the details of Pd-Fe-PAA-PVDF membranes and nanoparticles by TGA, contact angle measurement, surface zeta potential, XRD, SEM, XPS, FIB, TEM and other characterization techniques.
- To investigate the reaction kinetics of Pd-Fe NPs through the reduction of PCB 126. A Schematic of details of specific objectives are portrayed in **Figure 2.1**.

Enzyme Immobilized PAA-PVDF membrane as a bio reactor:

There two primary objectives for the enzyme immobilized PAA-PVDF membrane to be used as membrane bio reactor. **i)** To understand the activity of laccase-functionalized membranes towards degradation of polychloro-organics, specifically, 2,4,6-trichlorophenol. **ii)** To understand the activity of multi-enzyme functionalized membranes towards degradation of an aromatic phenolic lignin model compound, specifically guaiacylglycerol-β-guaiacylether (GGE).

Within these contexts, specific goals are:

- To fabricate functionalized membrane by alternating attachment of cationic and anionic polyelectrolytes via the LBL technique and characterize the functional domain.
- To compare the stability and reactivity of the immobilized enzyme to those of the free enzyme.
- To evaluate the long-term performance of the laccase-functionalized membranes towards degradation of 2,4,6-trichlorophenol in water under convective flow conditions.
- To immobilize multi-enzyme on PAA-PVDF membrane by alternating attachment of cationic and anionic polyelectrolytes via the LBL technique and characterize the functional domain,
- To evaluate the long-term performance of the multi-enzyme functionalized membranes towards degradation of lignin models in water under convective flow conditions.

Thiol incorporated PAA-PVDF membrane as heavy metal adsorption bed:

The overall goal of this work is to synthesize thiol functionalized PVDF membranes for removal of heavy metal specifically mercury from water.

Specific aims of this work are:

- To prepare and characterize cysteine (Cys) and cysteamine (CysM) (thiol precursors) functionalized PVDF membranes.
- To evaluate the efficacy of cysteamine (CysM) functionalized membrane for removal of $Hg^{2+}$ from synthetic water.

- For the treatment of industrial wastewater by cysteamine (CysM) functionalized membrane to establish a process to remove both HgS nanoparticle and dissolved $Hg^{2+}$ from wastewater.
- To evaluate the impact of cations in the wastewater on mercury removal by thiol functionalized membranes.
- To assess the performance of the thiol membrane for long-term mercury adsorption.
- To develop and validate a mathematical model to predict the performance of a thiol membrane for heavy metal adsorption.

Finally, a new kind of hollow (Fe and Pd-Fe) nanoparticles are synthesized for the application towards degradation of chlorinated organic compounds (COC) specifically 2-Chlorobiphenyl PCB-1.

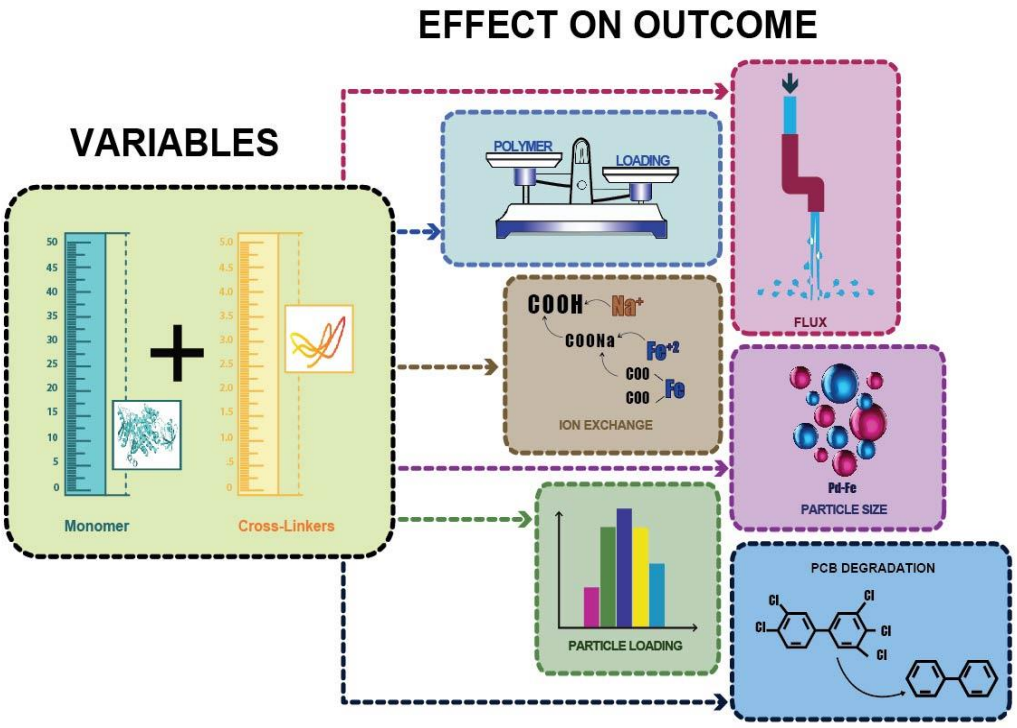


**Figure 2.1** Graphical illustration depicting the specific aims of nanoparticle incorporated PAA-PVDF membrane catalytic reactor bed. Block diagrams are represented by correlation of inputs (monomer and cross-linker concentrations) in left side and output variables (mass gain, water permeability), Ion exchange capacity, Fe metal loading and Pd-Fe nanoparticle size distribution and dechlorination of PCB 126 to biphenyl) in right side.

# CHAPTER 3. EXPERIMENTAL AND ANALYTICAL METHODS

## 3.1 Overview

This chapter discusses all the materials, methods and instruments used in the synthesis, characterization and experiments conducted for all the research projects for this dissertation. Details synthesis of Pd-Fe bimetallic nanoparticles incorporated membranes, single and multi-enzyme immobilized membranes and thiol incorporated microfiltration membranes have been discussed. Finally, Fe and Pd-Fe hollow nanoparticles preparation techniques also mentioned.

## 3.2 Materials

All chemicals used during the laboratory-scale membrane functionalization and the other studies were reagent grade and used without further purification. Full scale PVDF microfiltration membranes (PV700, pore diameter of 250-400 nm, thickness around 172 ± 5 µm and porosity around 38~46%) were obtained from Nanostone Water, Inc.

For synthesis and experiments conducted for Pd-Fe NPs incorporated PAA functionalized PVDF membranes the chemicals used are acrylic acid (AA, 98%), N, N′-methylenebis (acrylamide) (MBA, 99%) and sodium borohydride (98%) were received from ACROS ORGANICS. Potassium persulfate (KPS, >99%) was procured from EM SCIENCE. Potassium tetrachloropalladate (II) (99%) was purchased from STREM Chemicals. Naphthalene_$d_8$ (99 atom% D) was purchased from Sigma-Aldrich. Sodium hydroxide (0.1 N), sulfuric acid (0.5 M), hydrochloric acid (0.1 N), hexanes (>99%) and ferrous chloride tetrahydrate (>99%) were obtained from Fisher Scientific. 3,3',4,4',5-pentachlorobiphenyl (PCB 126) (>97%, neat) and biphenyl (>97%, neat) along with their analytical solution (100 ppm in hexane) were acquired from Ultra Scientific. Ethyl alcohol and methanol were bought from EMD Millipore Corporation. Sodium chloride (99%) was purchased from Alfa Aesar.

For synthesis and experiments conducted for laccase immobilized PAA-PVDF membranes the chemicals used are 2,4,6-trichlorophenol (TCP, 98%), ammonium persulfate (APS, >98%) and the enzyme laccase from *Trametes versicolor* (powder, light brown, ≥0.5 U/mg) were purchased from Sigma Aldrich. Poly(allylamine-hydrochloride)

(PAH) was obtained from Acros, New Jersey, NJ, USA. Bradford reagent was obtained from VWR.

In addition, for synthesis and experiments conducted for multi-enzyme immobilized polymeric membrane reactor are guaiacylglycerol-β-guaiacylether (GGE) and the enzymes Glucose Oxidase (GO) and Horseradish Peroxidase (HRP) were purchased from Sigma Aldrich.

For synthesis and experiments conducted for thiol (-SH) functionalized membranes the chemicals used are Fluoraldehyde™ o-Phthaldialdehyde Reagent solution, (Product Number (PN): 26025) (Thermo Scientific, Rockford, IL, USA), sodium hydroxide (NaOH) solution (1.0 N), (PN: BDH7222) (VWR Analytical, USA), sodium chloride (NaCl) salt, PN: BDH9286 (VWR Chemicals, Ohio, USA), calcium chloride ($CaCl_2$) salt, ACS Grade, PN: BDH9224, (VWR International, PA, USA), sulfuric acid ($H_2SO_4$) solution (1.0 N), PN: BDH7232 (VWR Analytical, USA), Nitric acid 68,0 - 70,0%, AR Select® ACS for trace metal analysis, (Macron Fine Chemicals, Center Valley, PA, USA). Ethanol, 99.5%, (PN: EX0276-3) (EMD Millipore Corporation, USA), ammonium persulfate ($(NH_4)_2S_2O_8$), 98+% (Acros Organic, Geel, Belgium), N-(3-Dimethylaminopropyl)-N′-ethylcarbodiimide hydrochloride (EDC), ≥ 98.0% (Sigma-Aldrich, St Louis, MO, USA), and N-hydroxysucinimide (NHS), ($C_4H_5NO_3$), >98.0% (TCI, Tokyo, Japan). Cysteamine hydrochloride (MEA), ≥ 98.0% (Sigma-Aldrich, St Louis, MO, USA), L-Cysteine Hydrochloride; Monohydrate (Cys), ($C_3H_7NO_2.HCl.H_2O$), PN: C-6852 (Sigma-Aldrich, St Louis, MO, USA). Mercury (II) nitrate hydrate ($Hg(NO_3)_2 \cdot xH_2O$, x= 1-2), ACS 98.0% (Alfa Aesar, Ward Hill, MA, USA). Silver Nitrate ($AgNO_3$), Crystal, 99.8-100.5% (PN: JT3429-04), (J. T. Baker, Phillipsburg, NJ, USA).

Finally, for synthesis of Fe and Pd-Fe hollow nanoparticles the chemicals used are D-(+)-Glucose, min 99.5%, SIGMA-ALDRICH, Inc., St. Louis, MO, USA and Ferrous ammonium sulfate hexahydrate ($(NH_4)_2.Fe(SO_4)_2.6H_2O$), M = 392.14 g/mol, assay 98.5-101.5, Billerica, MA, USA.

### 3.3 Functionalization of PVDF Membranes with PAA

Lab scale PVDF membranes were functionalized via an in-situ polymerization method, as reported before [57, 146]. Before functionalization, membranes were soaked in methanol for 5 to 10 minutes to remove dirt, clean the pores and increase the hydrophilicity of the surface [147]. After that a mixture of monomer solution (pH = 5.5~5.6) of AA (10~20 wt.% aqueous solution) with MBA as the cross-linker (0.5~2.0 mol% of AA), and KPS as an initiator (1.0 mol% of AA) was passed through the membrane under vacuum (0.14~0.16 bar vacuum) [87]. The solution was passed 3~4 times through the top surface of the membrane and once through the back of the membrane to confirm a homogenous polymerization across the pores. The membranes were then baked at 70~75 °C for 1~1.5 hrs under $N_2$ atmosphere or vacuum. This allows functionalization of the membrane via a thermal initialized polymerization of AA inside the PVDF membrane pores. After that, functionalized membranes were washed thoroughly with deionized ultrafiltered (DIUF) water to eliminate any unreacted constituents and then dried for 30 minutes at around 50~55 °C. Finally, the membranes were weighed to confirm polymerization through mass gain. In **Figure 3.1** a step by step process of the functionalization of the PVDF membrane, the Pd-Fe NP loading, and the degradation of PCB 126 solution using a Pd-Fe-PAA-PVDF membrane is depicted.

In order to study the effects of M and X concentrations, six different batches of functionalized membranes were prepared. M concentration was varied from 10 to 20 wt.% of solution, and X concentration was varied from 0.5 to 2 mol% of monomer concentration. In our previous studies we have taken monomer concentration to vary from 10 to 20 wt.% with 1 mol% of cross-linker concentration [26, 28, 39, 57]. However, in those studies we have not addressed the effect that M and X have on mass gain, permeability (A), metal loading, NP size and degradation of COCs (in this case, PCB 126) besides membrane characterizations. In this study, we have extended the variation of cross-linker concentration in the range of 0.5 to 2 mol% of monomer concentration. For all the prepared batches of membrane, the initiator (KPS), concentration was kept constant to 1 mol% of M concentration in polymer solution. In **Table 3.1** the matrix of chemicals used for preparing different batches of pore functionalized membranes to evaluate the effect of monomer and cross-linker concentration variation is shown.

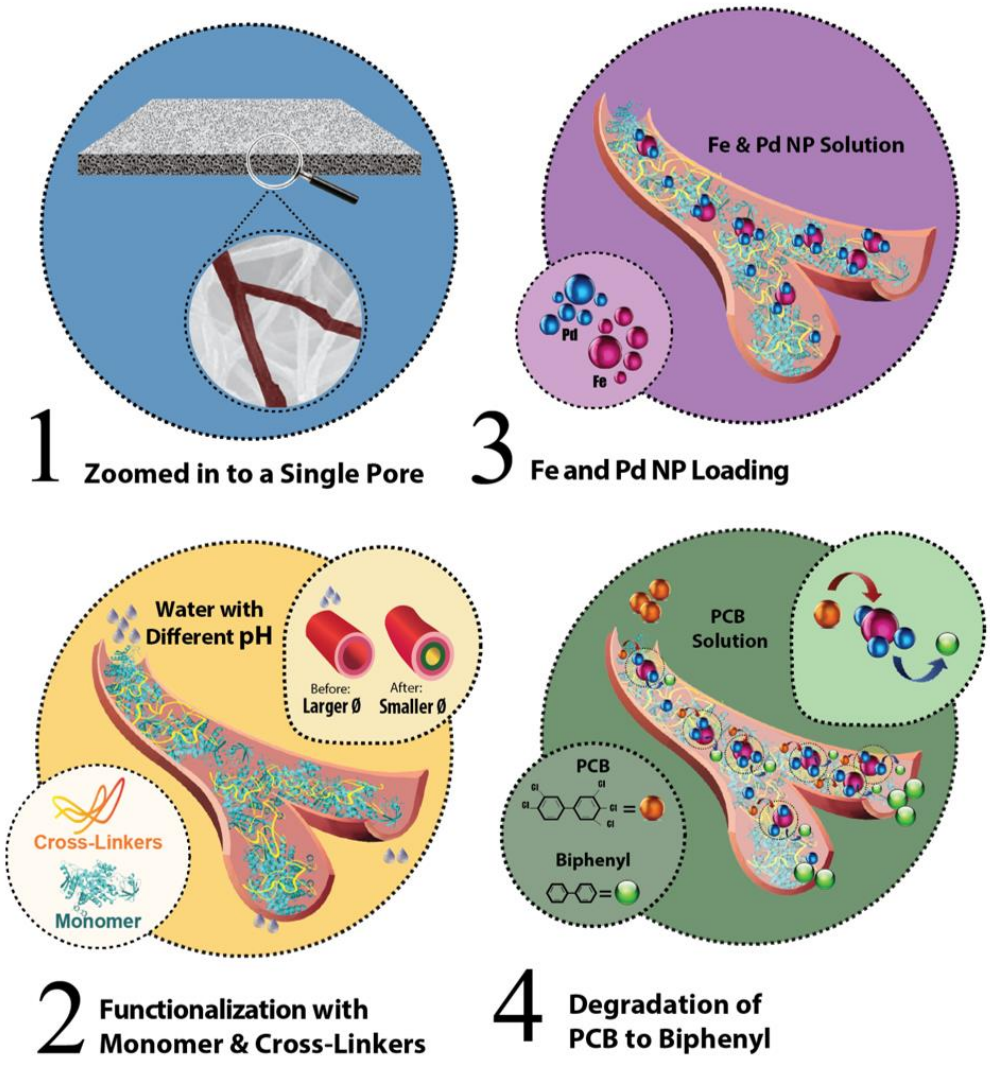


**Figure 3.1** Schematic representation of step by step functionalization of the PVDF membrane and its use as a platform for PCB 126 degradation. **(1)** A zoomed image of PVDF pore is shown, **(2)** In situ polymerization of membrane pores using monomer (acrylic acid (AA)) and cross-linker (N, N′- methylenebis (acrylamide) (MBA)). This causes the pore size to shrink and swell in different pH environment making it a pH responsive membrane, **(3)** Fe and Pd NPs are loaded inside the pores using a double ion exchange process by convective flow, **(4)** Degradation of the PCB 126 solution to biphenyl using Pd-Fe-PAA-PVDF membrane.

**Table 3.1** Matrix of polymeric solution used for making different batches of functionalized PAA-PVDF membranes. Initiator (KPS) concentration is fixed to 1 mol% in all experiments and Temperature of reaction is around 70~80$^{o}$C.

| **Batches (M, X)** | **Chemicals Used for Functionalization of Membranes** | |
|---|---|---|
| | **Monomer (M) (AA = Acrylic Acid)** | **Cross-Linker (X) (MBA=N, N′-Methylenebis (Acrylamide))** |
| A (10, 0.5) | 10 wt.% of solution | 0.5 mol% of AA |
| B (10, 1) | 10 wt.% of solution | 1 mol% of AA |
| C (10, 2) | 10 wt.% of solution | 2 mol% of AA |
| D (20, 0.5) | 20 wt.% of solution | 0.5 mol% of AA |
| E (20, 1) | 20 wt.% of solution | 1 mol% of AA |
| F (20, 2) | 20 wt.% of solution | 2 mol% of AA |

### 3.4 Pd-Fe Nanoparticle Immobilization in Functionalized Membranes

In situ immobilization of Fe and Pd NPs in the functionalized membrane pores was achieved by first doing ion exchange followed by reduction of Fe and subsequent Pd coating as reported in previous works [28, 39]. For cation exchange, PVDF-PAA membranes were soaked in NaCl (~68 mM) solution (pH ≥ 10). The ionized carboxyl groups chelated with $Na^+$ while releasing $H^+$ to cause a decrease in the pH of the solution. Therefore, to maintain the pH, NaOH was added in intervals. After 12~14 hrs, (solution pH > 8), the membranes were then washed with deoxygenated water to remove any excess NaCl/NaOH from the pores. For a second ion exchange, the membrane was put into a dead-end filtration cell. Then, 200 mL of $FeCl_2$ solution (~3.57 mM, pH = 5.0~5.5) was passed through under $N_2$ pressure (2~3 bar). This convective mode operation allows all $Na^+$ ions to be replaced by $Fe^{2+}$, thereby forming iron-carboxylate conjugates both in the surface and inside the pores. In the reduction step, $Fe^{2+}$ was immediately reduced to zerovalent iron NPs by passing 300 mL of $NaBH_4$ solution (~26 mM) under $N_2$ pressure (3~5 bar) through the membrane. Finally, the immobilization of Pd NPs on Fe surface was achieved by passing 200 mL (ethanol:water = 9:1 v/v) of $K_2PdCl_4$ solution (~153 μM, Pd as 1 wt.% of Fe) through the Fe-PAA-PVDF membrane under $N_2$ pressure (2~4 bar). This step was repeated until the $K_2PdCl_4$ solution turned colorless. This ensures all $Pd^{2+}$ were reduced by $Fe^o$, forming $Pd^o$ and $Fe^{2+}$. The prepared membranes were then washed and stored in pure ethanol in a cold room (4 $^oC$) for further use.

### 3.5 PCB 126 Dechlorination using Pd-Fe Nanoparticles

To assess the reactivity of immobilized Pd-Fe NPs in membranes, PCB 126 was taken as a model compound. Dechlorination experiments were conducted in both batch mode and convective flow mode. For batch experiments, 20 mL EPA glass vials were used. During the subsequent experiments the vials were placed on a shaker (250 rpm) to assure that all the PCB 126 can access the Pd-Fe NPs sites. Functionalized Pd-Fe-PAA-PVDF membranes (surface area of 17.3 $cm^2$ each) were then placed in vials (~15 μM PCB 126, $V_{ethanol}/V_{water}$ = 1/9, pH = 5.5~5.6). The experiment was terminated by removing 10 mL of organic solution from vials at different time intervals. To extract the organic compounds from both the solution and membrane phases, 10 mL of hexanes was poured into the

previously extracted 10 mL of organic solution ($V_{organic\ solution}/V_{hexanes}$ = 1/1). 10 µL of 1000 ppm naphthalene_d8 was then added as an internal standard. After 1~2 hours of shaking, the hexane phase was further analyzed using GC-MS. For conducting the convective flow study, a Pd-Fe-PAA-PVDF membrane was placed into a dead-end filtration cell. Here, the effective exposed membrane surface area is 13.2 $cm^2$. Then 30~50 mL of PCB 126 solution (~15 µM) was passed through the membrane under $N_2$ pressure. Permeate was collected after 8~10 minutes, when the reaction was observed to approach a steady state. Samples were collected at 10-minute intervals while varying the operating pressure (1.36 bar to 4.76 bar). The collected samples were then extracted in hexanes before being analyzed by the GC-MS following the same procedure mentioned earlier.

### 3.6 Nanoparticle Immobilized PAA-PVDF Membrane Characterization

To evaluate the successful polymerization of the PAA in the pores of the PVDF membranes, the functionalized membranes were characterized using TGA, ATR-FTIR, SEM, contact angle measurements, surface zeta potential measurement, and water permeability studies. Thermogravimetric analysis (TGA) was conducted to study the mass loss and thermal stability of pore-modified PAA-PVDF membrane using TGA Q50 analyzer (TA Instruments, USA). Sample sizes ranged from 4~12 mg. The scanning temperature range was from room temperature up to 750 $^oC$ with a heating rate of 10 $^oC$/min under $N_2$ atmosphere. The results were then analyzed using "TA Universal Analysis" software. Attenuated total reflectance Fourier transform infrared spectroscopy (ATR-FTIR, Varian 7000e) was used to examine the presence of functional groups in functionalized PVDF membranes. The samples were then placed on a diamond crystal, and the spectrum was evaluated between 500 and 4000 $cm^{-1}$, averaging 32 scans at a resolution of 4 $cm^{-1}$. Surface morphology of the functionalized membrane was studied using a scanning electron microscope (SEM, Hitachi S-4300). The membrane pore size and surface porosity (ratio of the pore area to the total membrane area) were analyzed using ImageJ software. The contact angles for both the bare and functionalized PVDF membranes were measured using a Krüss Drop Shape Analyzer instrument (DSA100). Zeta potential was analyzed using an Anton-Paar SurPASS electrokinetic analyzer to characterize the membrane surface charge. Water permeability of the bare and functionalized PVDF

membranes were performed using a laboratory-scale stainless steel pressure cell (Sepa ST, GE Osmonics, effective membrane area 13.2 $cm^2$) in dead-end mode [26].

The solution phase Pd-Fe nanoparticles were characterized by X-ray diffractometer (XRD) (Siemens D500) with Cu Kα (1.5418 Å) radiation (generator voltage of 40 keV, tube current of 30 mA). Inductively coupled plasma optical emission spectroscopy (ICP-OES, VARIAN VISTA-PRO) was used to quantify the concentration of Na and Fe ions in solution, after acidification with nitric acid (1 v/v %). The amount of absorbed Fe in the functionalized membranes during the ion exchange process was then determined by mass balance. The composition of the top layer of Pd-Fe-PAA-PVDF membrane was performed using X-ray photoelectron spectroscopy (XPS) (K-alpha, Thermo-Scientific) with aluminum anode. The measurement of NP size and distribution was conducted both on surface and inside the Pd-Fe-PAA-PVDF membrane pores after preparing a lamella using a FIB-SEM (FEI Helios Nanolab 660) instrument. A transmission electron microscopy (TEM, JEOL 2010F) coupled with energy dispersive x-ray spectroscopy (EDS) and an electron energy loss spectroscopy (EELS) were also used to observe the NP distribution inside Pd-Fe-PAA-PVDF membrane layer. Line scan and elemental mapping were conducted using a scanning transmission electron microscopy (STEM) mode.

Finally, while performing degradation studies using the Pd-Fe-PAA-PVDF membranes (both in batch and convective flow mode), the concentrations of produced biphenyl and the remaining PCB 126 were calculated using a coupled gas chromatography (Varian CP-3800)-mass spectrometry (Saturn 2200) instrument with helium as carrier gas.

### 3.7 Electrostatic Immobilization of Laccase in Functionalized Membranes

Laccase was immobilized into the pores of the PAA functionalized PVDF membrane by layer-by-layer assembly technique as demonstrated in **Figure 3.2**. PAA having a $pK_a$ value of ~5 remains negatively charged after treatment with DIUF (pH 6). In order to embed a positively charged electrolyte into the membrane pores, 100 mL of a 43µM solution of PAH (in DIUF) was permeated though the membranes at pH 3.9. The electrostatic interaction between the negatively charged carboxylic acid groups of PAA and the positively charged ammonium groups of PAH holds the PAH immobilized into the pores. After formation of the PAA-PAH layers, laccase was immobilized electrostatically

by permeating the membrane with 100 mL of a laccase solution (concentration varying from 50-150 ppm) in DIUF at pH 6. Laccase having a pI of ~3.5 is understood to attach electrostatically to the positively charged ammonium groups. As expected after immobilization of the PAH layers followed by the enzyme layers the flux of the membrane decreases significantly (by ~73%). The lower permeability with the laccase immobilization is desirable to achieve optimized residence time for effective degradation. The amount of laccase immobilized was determined by the difference in activity of the enzyme between the feed solution and the enzyme left in the permeate at the end of the immobilization. After the enzyme immobilization step, membranes were rigorously washed with DIUF water under convective flow mode in order to wash away any loosely bound enzymes. The washings were carried out with several 20 mL aliquots of DIUF water until the permeate is free of laccase enzyme. In general, the quantity of leached enzyme is negligibly low after the $3^{rd}$ or $4^{th}$ washing as quantified by Bradford assay shown in **Figure 3.3**. For cross verification purpose, aliquots from permeate were also tested for the presence of any enzyme by means of its reaction with ABTS. It should also be noted here that both these methodology for enzyme detection were accurate to use under these conditions; no color change of Bradford reagent or ABTS solution detected upon addition of either TCP or PAH only.

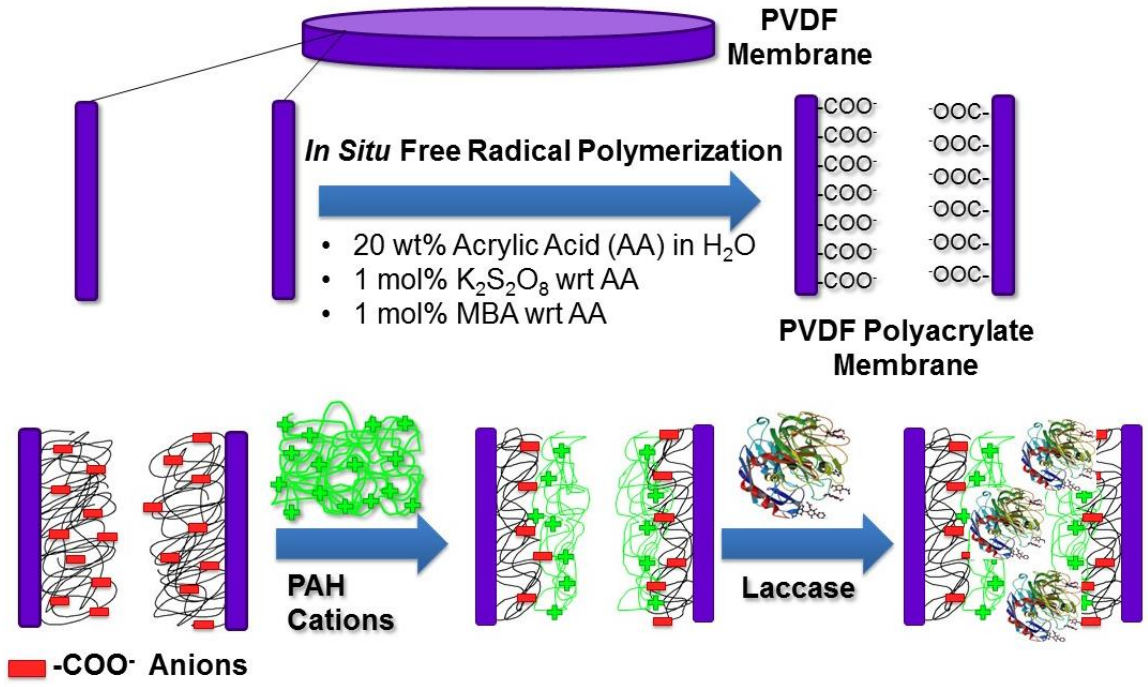


**Figure 3.2** Schematic of laccase immobilization in membrane platforms through layer-by layer approach: PVDF-PAA membrane with an electrostatically immobilized layer of PAH and subsequent laccase immobilization. (In the figure 'with respect to' is abbreviated as 'wrt').

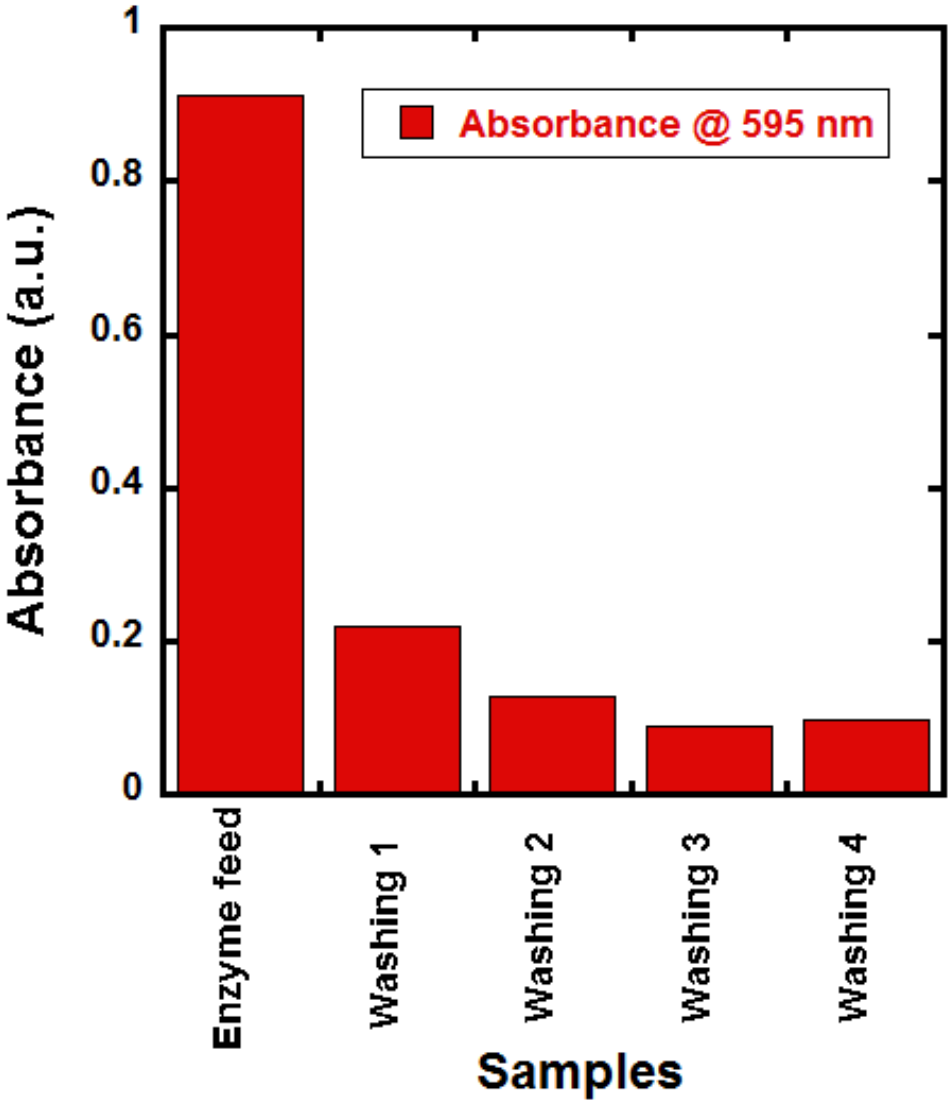


**Figure 3.3** Leaching of enzyme from immobilized membrane during washing as analyzed by Bradford assay.

### 3.8 Bradford Assay

The amount of the loosely bound enzyme leached out from the membrane with washing was quantified spectrophotometrically at 595 nm by means of its interaction with Bradford reagent. The protocol followed was as per the datasheet provided by VWR. The standard curve was obtained with BSA protein in the linear range of (0 µg/mL – 10 µg/mL). For each particular analysis 1 mL Bradford Reagent was added to each standard dilution (of protein/enzyme) with specific volume of 0.15 M NaCl solution and mixed it for 5 minutes before measuring the absorbance at 595 nm.

### 3.9 Assay of Laccase Activity

The activities of free and immobilized laccase was determined by monitoring the oxidation of 2,2´-azino-bis-(3-ethyl-benzthiazoline-6-sulfonic acid) (ABTS) spectrophotometrically at 420 nm ($\varepsilon_{max}$ = 36000 L $mol^{-1}$ $cm^{-1}$) with 0.2 mM ABTS as substrate in 0.25 M potassium phosphate buffer (pH 5.7) at 22 ºC. The kinetic parameters, $K_m$ and $k_{cat}$, were determined by measuring the initial rates of reaction between laccase and different concentrations of ABTS as the substrate (0.01-0.2 mM) in 0.25 M potassium phosphate buffer (pH 5.7) at 22 ºC. The kinetic parameters were estimated from the Michaelis–Menten equation.

### 3.10 Performance of the Laccase Immobilized Membranes towards Degradation of TCP

TCP degradation studies were performed under pressure driven flow using a laboratory-scale stainless steel pressure cell housing the functionalized membrane. In a typical degradation experiment 100 mL of 250 µM solution of TCP in DIUF (pH 5.6) was allowed to pass through the membrane and the flow rate was varied under positive pressure from an air gas tank. The collected permeate was then analyzed for the concentrations of TCP left using high-performance liquid chromatography (HPLC) with a Shimadzu instrument employing two pumps, an auto sampler, and a photodiode array detector. Standard solutions of TCP were prepared to obtain a standard curve with which to quantify TCP degraded upon passage through the membrane. The elution was performed by

pumping acetonitrile and water (55:45 v/v) at a flow rate of 0.6 mL/min. UV light absorption was measured over a wavelength window of 200-700 nm. The amount of TCP degraded by the laccase functionalized membrane was calculated using the following **equation 3.1**:

$$C_{deg} = C_{feed} - C_{per} \ldots\ldots\ldots\ldots\ldots\ldots \mathbf{EQ}\ (\mathbf{3.1})$$

where, $C_{deg}$ is the amount of TCP degraded by laccase; $C_{feed}$ is the initial concentration of TCP in the feed solution; $C_{per}$ is the amount of TCP in the permeate.

### 3.11 Multi-Enzymes Immobilization in Functionalized Membranes

Enzymes were immobilized into the pores of the PAA functionalized PVDF membrane by layer-by-layer assembly technique. PAA having a pKa value ~ 4.5 remains negatively charged after treatment with DIUF (pH 6). In order to embed a positively charged electrolyte into the membrane pores, 100 mL of a 45 µM solution of PAH (in DIUF) was permeated though the membranes at pH 3.9. The electrostatic interaction between the negatively charged carboxylic acid groups of PAA and the positively charged ammonium groups of PAH holds the PAH immobilized into the pores. After formation of the PAA-PAH layers, laccase was immobilized electrostatically by permeating the membrane with 100 mL of a 100 ppm (10 mg/100 mL) laccase solution in DIUF at pH 6. After embedding the laccase layer, solution of PAH (in DIUF) was permeated though the membranes at pH 3.9 one more time followed by permeating HRP solution (10 mg/100 mL) in DIUF at pH 6. This results in a membrane reactor with the pores filled up by entrapment of mixture of enzymes around the polymer nets. The process was then repeated to have the third enzyme (GO) immobilized as the final layer. The amount of enzyme immobilized was quantified spectrophotometrically by Bradford reagent determined by the difference in amount of the enzyme between the feed solution and the permeate. The membranes were rigorously washed with DIUF water after each immobilization step in order to wash away any loosely bound enzymes.

The enzyme immobilized membranes were stored at 4 $^{o}$C for weeks and the activities of these membranes towards degradation of the GGE were assessed to test their stability over a longer period.

### 3.12 Performance of the Multi-Enzyme Immobilized Membranes towards Degradation of Lignin Model Compound

GGE degradation studies were performed under pressure driven flow using a laboratory-scale stainless steel pressure cell housing the functionalized membrane. In a typical degradation experiment 100 mL of 3.1 mM solution of GGE in DIUF was allowed to pass through the membrane, and the flow rate was varied under positive pressure using an air gas tank. The collected permeate was then analyzed for the concentrations of GGE using high-performance liquid chromatography (HPLC) with a Shimadzu instrument employing two pumps, an auto sampler, and a photodiode array detector. Standard solutions of GGE were prepared to obtain a standard curve with which to quantify GGE degraded upon passage through the membrane. HPLC and LCMS was similarly used to assess oxidation products formed. The elution was performed by pumping acetonitrile and water (40:60 v/v) at a flow rate of 0.6 mL/min. The conversion of GGE degraded by the functionalized membrane is defined by **equation 3.2**:

$$Conversion\ of\ GGE = \frac{C_{feed} - C_{permeate}}{C_{feed}} \ldots\ldots\ldots\ldots\ldots\ldots \mathbf{EQ\ (3.2)}$$

### 3.13 Synthesis of Thiol Functionalized Membranes

Immobilization of thiol groups to the PAA-PVDF membrane was conducted by two methods. In the first method, an ion exchange process is proposed for immobilization of cysteamine (CysM) on the PAA-PVDF membrane using an alkaline solution (1 g/L of CysM adjusted with 0.1 N NaOH solution to pH ≈ 8.5; T = 22 °C), as depicted in **Figure 3.4**. This ion exchange process is partially derived from previous work by this group, using a dead-end cell (Sterlitech HP4750) to pass-through the CysM alkaline solution [26, 28, 39]. The ion exchange with CysM has advantage over Cys because of its higher affinity to be immobilized by ion exchange to the PAA-PVDF membrane at pH relevant to wastewater treatment. The Cysteine is a zwitterionic molecule with three pKa values, the carboxyl being the lowest (see **Table 3.2**) [148-151]. Cys is negatively charged at neutral pH (6-8) [152]. Meanwhile, CysM zwitterion has high two-pKa values. Compared to Cys, CysM can adsorb more strongly to a deprotonated PAA (which pKa is weakly acidic), because the CysM zwitterion is usually present in its cationic form (see **Table 3.2**) [19, 21, 153-154].

In the second method, EDC/NHS coupling is used to functionalize the membranes with Cys or CysM to generate Cys- and CysM-PAA-PVDF membranes (collectively referred to as thiol membranes) as depicted as a schematic in **Figure 3.5**. Amino compounds (Cys or CysM) can be covalently attached through activation of carboxyl groups with EDC. Since this reaction is performed in solution, the hydrolysis of the active EDC complex has to be avoided by the addition of NHS, forming a more stable intermediate that will react with the amino groups present in Cys and CysM [155-156]. Covalent attachment of Cys or CysM is achieved via bond formation between its primary amino group and the carboxylic acid groups of PAA.

A solution with a pH of 6.3 containing 5.0 mM EDC, 5.0 mM NHS, and 450 mM NaCl was passed through a PAA-PVDF membrane at a pressure of 6.9 ± 0.3 bar in convective flow mode using a dead-end filtration cell. The resulting NHS-PAA-PVDF membrane was rinsed with DI water at the same pressure. A 1.0 g/L of either Cys or CysM solution (pH 7.5) was subsequently passed through the NHS-PAA-PVDF membranes to incoporate thiol groups in the membrane. The resulting thiol membranes were rinsed with DI water. During this process the membranes were stored at 4~5 °C when not in use. The flux and volumes of feed, peremeate, and retentate were recorded throughout the functionalization processes, and the liquids were analyzed by TOC to calcuate the degree of thiol incorporation by carbon balance. Conversion of PAA-PVDF membranes to NHS-PAA-PVDF membranes during EDC/NHS functionalization and corresponding flux pattern is shown in **Figure 3.6**. Progressive attachment of thiol groups in NHS-PAA-PVDF membranes by CysM incorporation and flux pattern is shown in **Figure 3.7**.

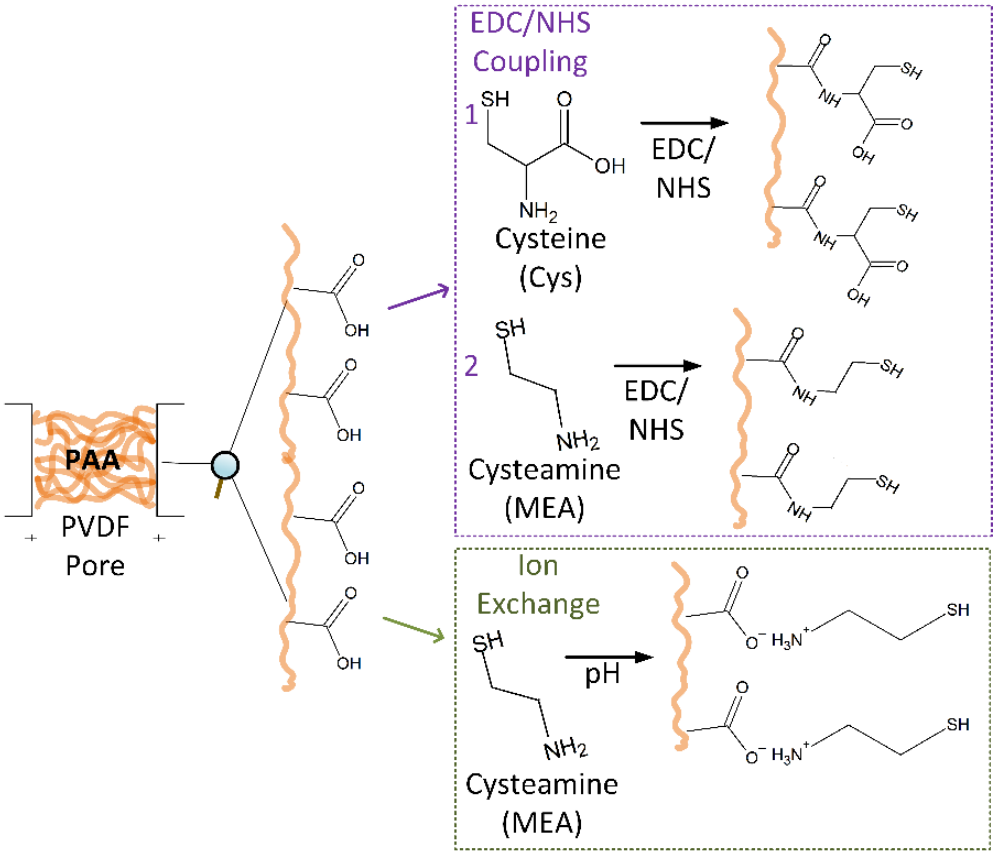


**Figure 3.4** General functionalization process of PAA-PVDF membranes with cysteine or cysteamine through two routes: EDC/NHS coupling with (1) Cysteine (Cys) or, (2) Cysteamine (CysM), and ion exchange with Cysteamine (CysM).

**Table 3.2** Dissociation constants of selected organic compounds in aqueous solution.

| Compounds | pKa | | | References |
|---|---|---|---|---|
| | Carboxyl | Thiol | Amine | |
| **Cysteine (Cys)** | 1.71<br>1.50 | 8.33<br>8.70 | 10.78<br>10.20 | [149]<br>[151] |
| **Cysteamine (CysM)** | -<br>-<br>- | 8.19<br>8.32<br>8.27 | 10.75<br>10.81<br>10.53 | [148]<br>[150]<br>[151] |
| **Acrylic acid (AA)** | 4.25 | - | - | [151] |
| **Poly (acrylic acid) (PAA)** | ≈ 4.5 – 4.7 | - | - | [19, 21, 153-154] |

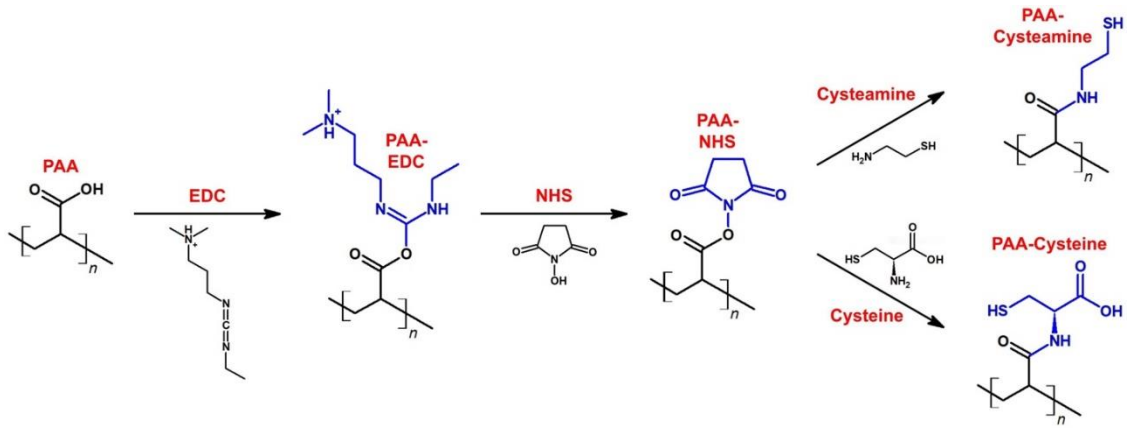


**Figure 3.5** Schematic of reaction steps to functionalize PAA-PVDF membrane with EDC/NHS solution followed by incorporation of thiol (-SH) groups by passing a thiol (-SH) precursor (Cys/CysM) solution.

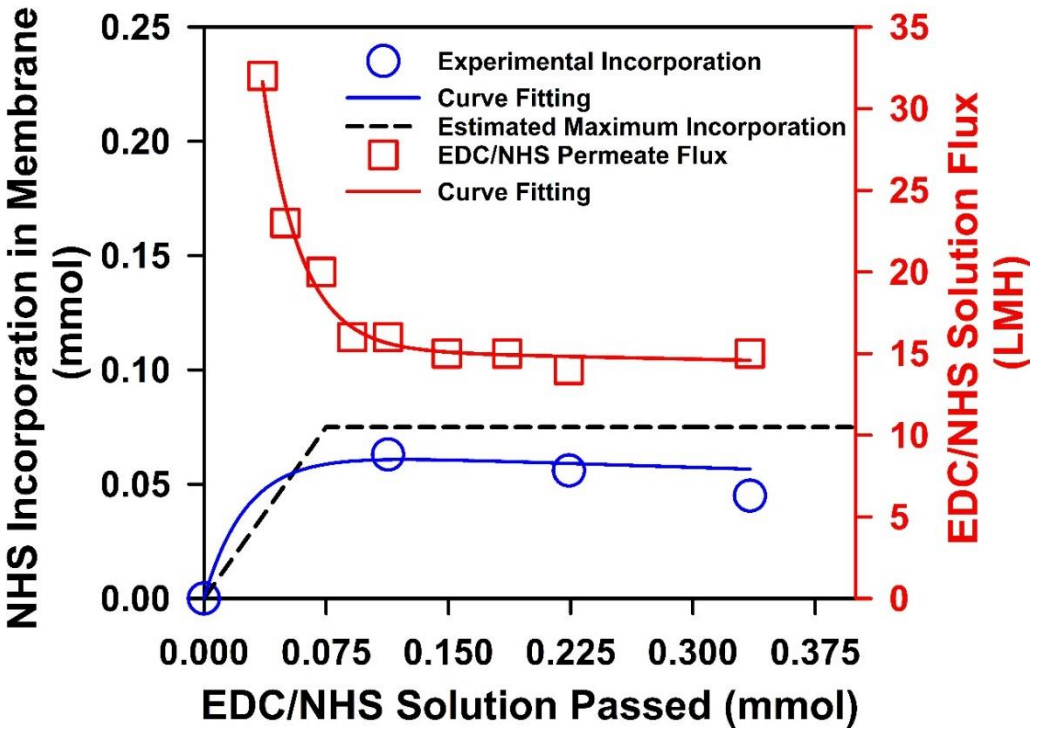


**Figure 3.6** The cumulative amount of NHS added to a PAA-PVDF membrane (surface area 13.2-cm$^2$) during passing a mixture of 5.0 mM NHS and 5.0 mM EDC solution (pH = 6.3) by convective flow through the membrane. The flux pattern during this EDC/NHS incorporation is shown on the right y-axis. The pressure during experiment was kept around 6.9 ± 0.3 bar. TOC analysis of feed and permeate samples was used to measure the incorporation. The estimated maximum capacity for incorporation was determined based on mass gained by the membrane during PAA functionalization.

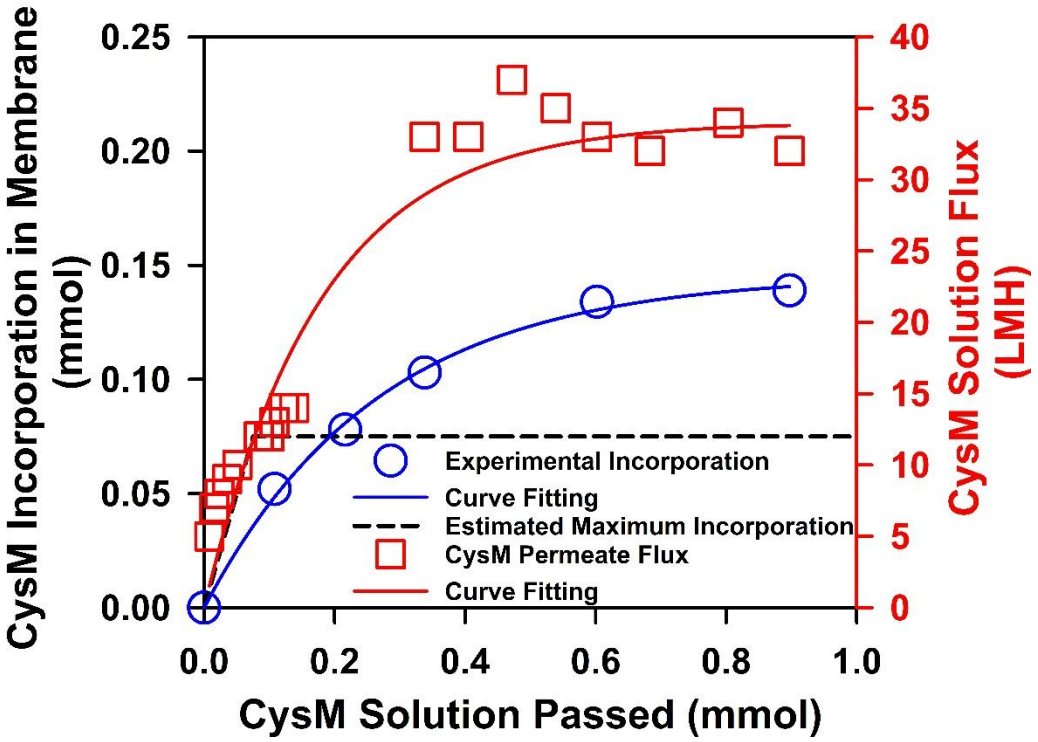


**Figure 3.7** CysM incorporation into an NHS-PAA-PVDF membrane (surface area 13.2-$cm^2$) during passing a 1.0-g/L, CysM solution (pH = 7.5) by convective flow through the membrane. The flux pattern during this CysM incorporation is shown on the right y-axis. The pressure during experiment was kept around 6.9 ± 0.3 bar. TOC analysis of samples of the feeds and permeates was used to determine the amount of CysM incorporation. The NHS-PAA-PVDF membrane used was obtained by the convective-flow of EDC/NHS solution through the membrane. The estimated maximum capacity for incorporation was determined using the mass gained by the membrane during PAA functionalization.

### 3.14 Characterization of Thiol Incorporated Membranes

Thiol membranes were characterized using Attenuated Total Reflectance Fourier Transformation Infra-Red (ATR-FTIR), X-ray photoelectron spectroscopy (XPS), Total-Organic Carbon (TOC), Scanning Electron Microscope (SEM), Focus Ion Beam SEM (FIB-SEM), Transmission Electron Microscopy EDS (TEM-EDS) contact angle measurements, and surface zeta potential measurement instruments. ATR-FTIR (Nicolet iS50 FT-IR Spectrometer, Thermo Scientific) was used to verify the membrane synthesis at various stages of functionalization of the PVDF membrane. XPS (Thermo Scientific K-alpha XPS System) was used to verify membrane synthesis and metal adsorption across the membrane cross-section.

TOC analysis was performed using a TOC-5000A (Shimadzu) instrument to verify membrane synthesis by calculating carbon balance during EDC/NHS functionalization and Cys or CysM incorporation. This TOC analyzer was calibrated using in-house prepared carbon standards. The experimental error during analysis was lower than 2%. Ultra-high purity oxygen was used as carrier gas (pressure of 6.0 bar and 150 mL/min) during TOC measurement. Surface morphology (membrane pore size and porosity) of the functionalized membrane was recorded by SEM (Hitachi S-4300). Membrane pore size and surface porosity (ratio of the pore area to the total membrane area) were determined using ImageJ software. Contact angles were measured using a Krüss Drop Shape Analyzer instrument (DSA100) to evaluate potential changes in hydrophobicity or hydrophilicity of the surface of the functionalized membranes. Zeta potential was analyzed using an Anton-Paar SurPASS electrokinetic analyzer to verify changes in surface charge due to incorporation of carboxyl and thiol functional groups in membranes. The distribution of heavy metals was measured both on surface and inside the pores of thiol membrane after preparing a lamella from the membrane using a FIB-SEM (FEI Helios Nanolab 660) instrument. TEM (JEOL 2010F) coupled with energy dispersive X-ray spectroscopy (EDS) and electron energy loss spectroscopy (EELS) were used to determine the captured heavy metal distribution across the cross-section of thiol membrane. Light scattering (Litesizer 500, Anton Paar) for particle analysis was used to determine the size distribution and particle diameter of HgS NPs. Further, the presence of thiol groups in functionalized membranes was also characterized by fluorescence-labelling, using Fluoraldehyde™ in the

presence of n-propylamine, using a confocal microscope (Zeiss LSM880 Multiphoton Microscope) shown in **Figure 3.8**. It is clear from **Figure 3.8** that the entire porous structure of the membrane was functionalized by thiol (C-SH) groups.

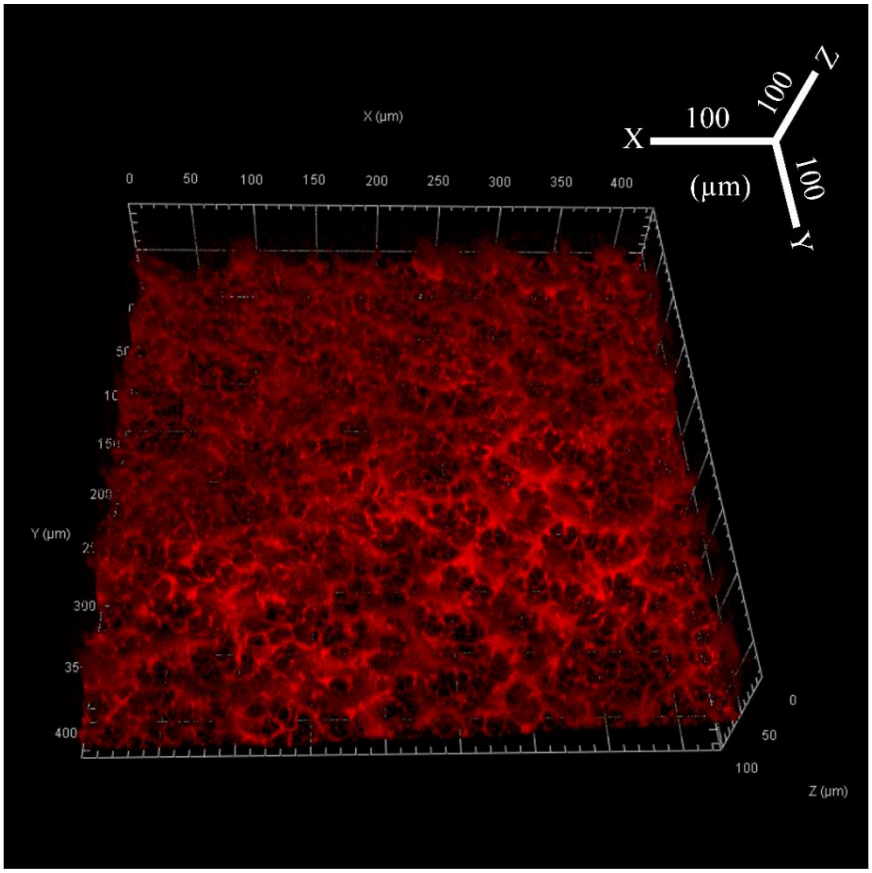


**Figure 3.8** Top surface of the CysM-PAA-PVDF with a red tag for the membrane structure (Fluoraldehyde™ Reagent Solution). Membrane used: PVDF (Nanostone PV700).

### 3.15 Permeability Measurements of Membranes and Its Impact on Functionalization

Changes in ionic stregnth of the solution permeating a carboxyl funcionalized PVDF membrane can cause charge-charge repulsion/attraction in polymer layers incorporated in membrane pores, resulting in swelling or shrinkage of pores and an associated change in permeability [6, 18]. Observation of the changes in transport properties, such as water permeability, after each functionalization step provides a qualitative assessment of the success of each functionalization step. Thus, the functionality of thiol membranes can be evaluated by measuring permeability of the unaltered PVDF membrane, the PAA-PVDF membrane, the PAA-PVDF membrane after transformation of carboxyl groups to NHS-esters by EDC/NHS chemistry, and finally the Cys- and CysM-PAA-PVDF membrane. Water permeability of the thiol membranes was measured with a laboratory-scale stainless steel pressure cell (Sepa ST, GE Osmonics, effective membrane area 13.2 $cm^2$) in dead-end mode. This approach allows convective flow of the permeate through a membrane. The permeability experiment was performed according to our protocol described elsewhere [39, 146]. The permeability of a PVDF membrane was measured after each step of the functionalization until the desired thiol membrane was formed.

### 3.16 Measurement of Adsorbed Cations in Functionalized Membranes

Synthetic water samples containing one cation per solution ($Ca^{2+}$, $Hg^{2+}$, $Ag^{+}$) and spiked wastewater samples containing multiple cations were passed through the thiol membranes by a convective flow process to **1)** understand the transport mechanisms, **2)** measure the cationic adsorption capacities, and **3)** measure the HgS NP removal effectiveness. Silver ($Ag^{+}$) containing synthetic water was used to quantify the metal adsorption capacity of the thiol membranes, based on the assumption that $Ag^{+}$ attaches to thiol groups in 1:1 molar ratio. Samples of feeds, permeates, and retentates were acidified with nitric acid (1 v/v%) and analyzed for $Ca^{2+}$, $Hg^{2+}$, and $Ag^{+}$ concentrations using inductively coupled plasma optical emission spectroscopy (ICP-OES, VARIAN VISTA-PRO). For $Ca^{2+}$ and $Hg^{2+}$ analysis the ICP-OES was calibrated from 0.5 to 100 ppm and from 0.5 to 1 ppm, respectively. For $Ag^{+}$ analysis the ICP-OES was calibrated in three different ranges as 0.1 to 1 ppm, 5 to 100 ppm and 10 to 100 ppm, depending on starting $Ag^{+}$ concentration in the solution. $Hg^{2+}$ concentrations were also measured by direct

injection in a Nippon Instruments Corporation (NIC) MA-3000 analyzer. The MA-3000 was calibrated from 1 to 100 ppb range. A material balance for the three cations enabled calculation of the removal and adsorption capacity of the thiol membranes.

### 3.17 Preparation of Fe and Pd-Fe Hollow Nanoparticles

To synthesize the hollow Fe nanoparticles modified one-pot hydrothermal method was followed [136-137]. Initially two solutions were prepared. The first solution contains 5~6 g of D-Glucose mixed in 20 mL of DIUF water. Second solution was prepared by putting 5M $(NH4)_2.Fe(SO_4)_2.6H_2O$ pre-cursor solution dissolved in 10 mL DIUF water. Both Solutions were mixed in a ratio of 5:1 and placed in Teflon autoclave. Then the autoclave was kept in the oven at 180$^o$C for 12 hours. After natural cooling prepared samples then filtered and washed first with DIUF water and then with ethanol for couple of times. After washing the prepared samples were dried at 60$^o$C for 5 hours in vacuum in an oven. After that samples were collected for XRD characterization. Finally, the samples were calcined at 550$^o$C for four hours with a heating rater of 4$^o$C/minute which allows to remove carbon cores resulting the hollow nanoparticles. The weight loss during this process is around 98%. The synthesized Fe hollow nanoparticles are well dispersed in ethanol as well as in water. For Pd-Fe hollow nanoparticles same procedure has been followed but potassium tetrachloropalladate (II) (99%) salt has been added in solution 1 as 4~6% of $(NH4)_2.Fe(SO_4)_2.6H_2O$ salt.

# CHAPTER 4. ROLE OF PVDF MEMBRANE PORE POLYMERIZATION CONDITIONS FOR pH RESPONSIVE BEHAVIOR AND CATALYTIC NANOPARTICLE LOADING

## 4.1 Overview

This chapter discusses the effects of changing monomer and cross-linker concentrations on the mass gain, water permeability, Pd-Fe nanoparticle (NP) loading, and the rate of degradation of 3,3',4,4',5-pentachlorobiphenyl (PCB 126) of pore functionalized polyvinylidene fluoride (PVDF) membranes. In this study, monomer (acrylic acid (AA)) and cross-linker (N, N′- methylene-bis (acrylamide)) concentrations were varied from 10 to 20 wt.% of polymer solution and 0.5 to 2 mol% of monomer concentration, respectively. Results showed that responsive behavior of membrane could be tuned in terms of water permeability over a range of 270 to 1 $L \cdot m^{-2} \cdot hr^{-1} \cdot bar^{-1}$, which is a function of water pH. The NP size on the membrane surface was found in the range of 16~23 nm. With increasing cross-linker density the percentage of smaller NPs (<10 nm) increases due to smaller mesh size formation of during in-situ polymerization of membrane. NP loading was found to vary from 0.21~0.94 mg per $cm^2$ of membrane area depending on the variation of available carboxyl groups in membrane pore domain. These PAA-PVDF membranes are characterized by TGA, contact angle measurement and surface zeta potential to reveal the details about the membrane surface and pores. Pd-Fe nanoparticles are quantified by analyzing the images collected using SEM and FIB techniques. Statistical analysis based on experimental results allows us to depict responsive behavior of functionalized membrane. Sections 4.2 to 4.7 are **published** in **Islam et al. (2018)**.

## 4.2 Mass Gain of Functionalized Membranes

The effective polymerization of PAA in the pores of PVDF membranes could be calculated by measuring the difference of weight change of membranes before and after functionalization. In **Figure 4.1**, the average mass gain for all the six batches (each with a different matrix of monomer (M) and cross-linker (X) concentrations) are represented in a bar chart. It is clear from **Figure 4.1** that when 10 wt.% of the monomer concentration was used during functionalization as in Batches A, B and C, the observed average mass gain was 4~5 % despite of using different concentrations of cross-linker (0.5 mol% to 2 mol%).

Whereas, when 20 wt.% of monomer concentration was used as in Batches D, E and F, these results have an average mass gain of around 15~16%. This mass gain data is consistent with our previous reported works [28, 34, 39].

To know the maximum mass gain, a bare PVDF membrane was soaked in DIUF water for 30 minutes. It was found a maximum mass gain of 21~23 wt.% (showed with a green dotted line in **Figure 4.1**). The maximum mass gain results reveal that values of mass gain of the different batches (A to F) of membrane are within the range. For a base porosity of 40%, functionalization of a PVDF membrane using a 10 wt.% polymer solution allows the membrane to retain porosity around 30 to 31 %, while when using a 20 wt.% of polymer solution, the membrane is only able to retain a porosity between 9 to 12% as shown in **Figure 4.1**. It is interesting to note that changing the concentration of the cross-linker does not affect the mass gain of the functionalized membrane, which is reasonable since X concentration is much lower compared to M concentration and it is used mainly to deter entanglement of polymer chains during the polymerization reaction. This is also confirmed by a factorial and response surface design analysis mentioned at the end of this document. One of the earliest researchers to report on the effect of cross-linking on the physical properties of polymers was Nielsen [157]. Later, Kjøniksen et al. and Zhao et al., reported the effect of cross-linking density on the rheology and its mechanical properties in different aspects [158-159]. However, none of them discussed the effect of cross-linkers on mass gain during polymerization reaction. It is also observable from **Figure 4.1** that mass gain increased three-fold when the monomer concentration was changed from 10 wt.% to 20 wt.%, despites of different cross-linker concentration.

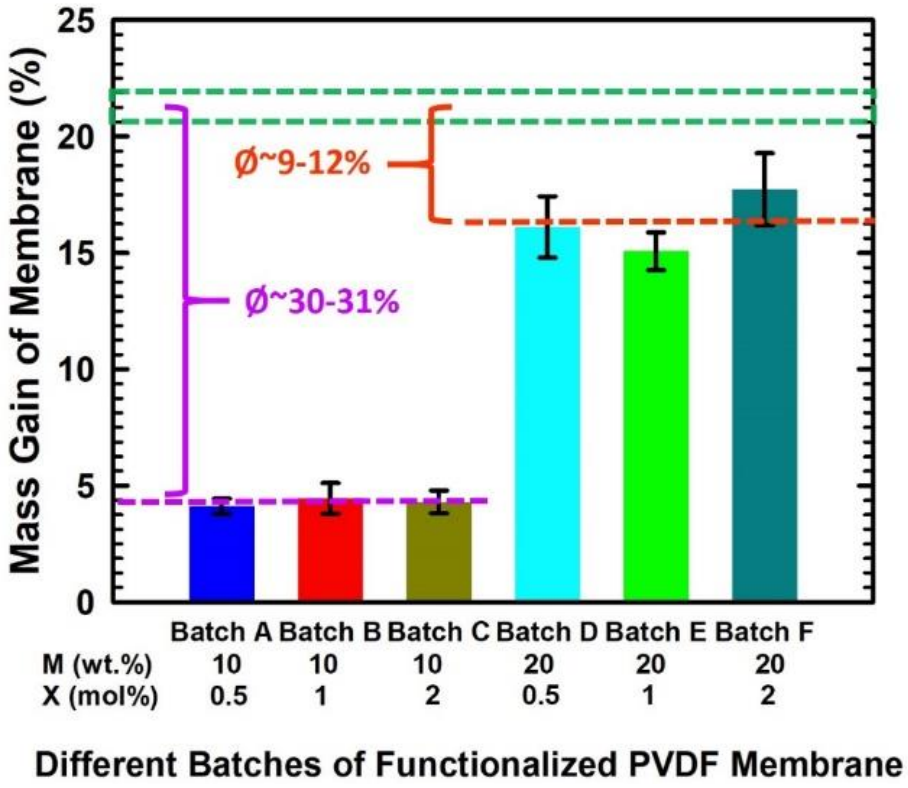


**Figure 4.1** Mass gain profile of different batches of functionalized PAA-PVDF membranes. The green dotted box is showing the maximum mass gain possible for PVDF membrane when all the pores are saturated with water with a base porosity (Ø) of 40%. For 10 wt.% of monomer concentration approximately 30~31% porosity (Ø) remains after functionalization (shown in purple lines). For 20 wt.% of monomer concentration almost 9~12% porosity (Ø) remains after functionalization (shown in orange lines) for permeation of water.

The mass gain profile of modified PAA-PVDF membrane was further investigated by the TG analysis. In **Figure 4.2** the TG analysis thermograms for bare PVDF membrane (blue line), 10 wt.% PAA-PVDF membrane (black big dashed line), 20 wt.% PAA-PVDF membrane (pink small dashed line) and PAA powder (red line) are shown. The TG analysis can provide information on PAA content, PAA decomposing temperature and membrane thermal stability by observing the minute weight change of the sample with temperature. The bare PVDF membrane shows only one-step sharp weight loss around 420~440 °C, which corresponds to the degradation of the $CF_2$ chain [160-161]. The PAA powder also shows one step wide weight loss in the temperature range 215~490 $^oC$. However, the PAA-PVDF membrane (-COOH form) exhibits a distinct three-step degradation process. The first slight weight loss is around temperature range of 215~310 °C due to the formation of anhydride [16, 162]. The second weight loss is observed at the temperature range from 310~485 °C, corresponding to further decomposition of polyacrylic anhydride [16, 162]. The final weight loss occurs at 485 °C, which is attributed to the decomposition of the PVDF side chains. From **Figure 4.2**, it is clear that with an increase of PAA content in PVDF membrane the thermograms are shifted towards the thermograms of PAA. This confirms difference in weight of the modified PAA-PVDF membrane due to difference in loading of PAA in bare PVDF membrane.

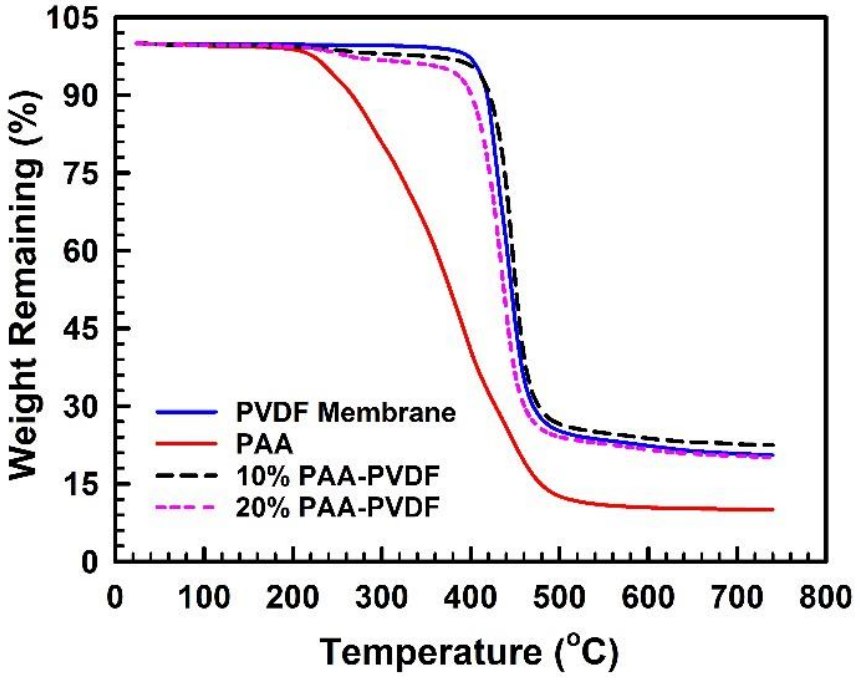


**Figure 4.2** TGA thermograms of bare PVDF membrane (blue line), 10 wt.% PAA-PVDF membrane (black line), 20 wt.% PAA-PVDF membrane (green line) and PAA (redline). With an increase in PAA percentage in PVDF membrane the TGA curves are shifted towards PAA curve.

## 4.3 ATR FT-IR Spectra and SEM Image Analysis of PAA-PVDF Membranes

The ATR FT-IR spectra of the bare and functionalized PVDF membranes shown in **Figure 4.3** confirm the resulting in situ polymerization inside membrane pores. The absorption peaks characteristic of fluorocarbon groups (−$CF_2$−) of the PVDF chains lie in the region of 950 - 1220 $cm^{-1}$, as expected are clearly visible in **Figure 4.3a** (blue line) [163]. The appearance of peaks around 1700 $cm^{-1}$ and 1550 $cm^{-1}$ in **Figure 4.3b** (green line) is due to carbonyl stretch and antisymmetric stretching of carboxyl groups (− COOH), respectively, of the polyacrylic acid polymer [164]. In addition, the broad peak in **Figure 4.3b** between 2700 and 3400 $cm^{-1}$ is demonstrating the presence of O−H group from the synthesized polymer [34]. Together, these results demonstrate the successful polymerization of PAA in PVDF membrane matrix.

Surface morphologies of the PVDF and PAA functionalized PVDF membranes were characterized by SEM as shown in **Figure 4.3**. The bare PVDF membrane (**Figure 4.3c**) shows a porous structure with an average pore size of 262 ± 60 nm. The polyester backing of the bare PVDF membrane is clearly visible in **Figure 4.3d**. The diameter and morphology of the membrane pores decreased substantially after the PAA polymerization reaction, becoming uniformly circular and smaller with an average pore size of 65 ± 7 nm (**Figure 4.3e**); which conform with our earlier reported works [39, 146]. The pores of the functionalized PVDF membrane reduced in size due to formation of PAA domain inside the pores.

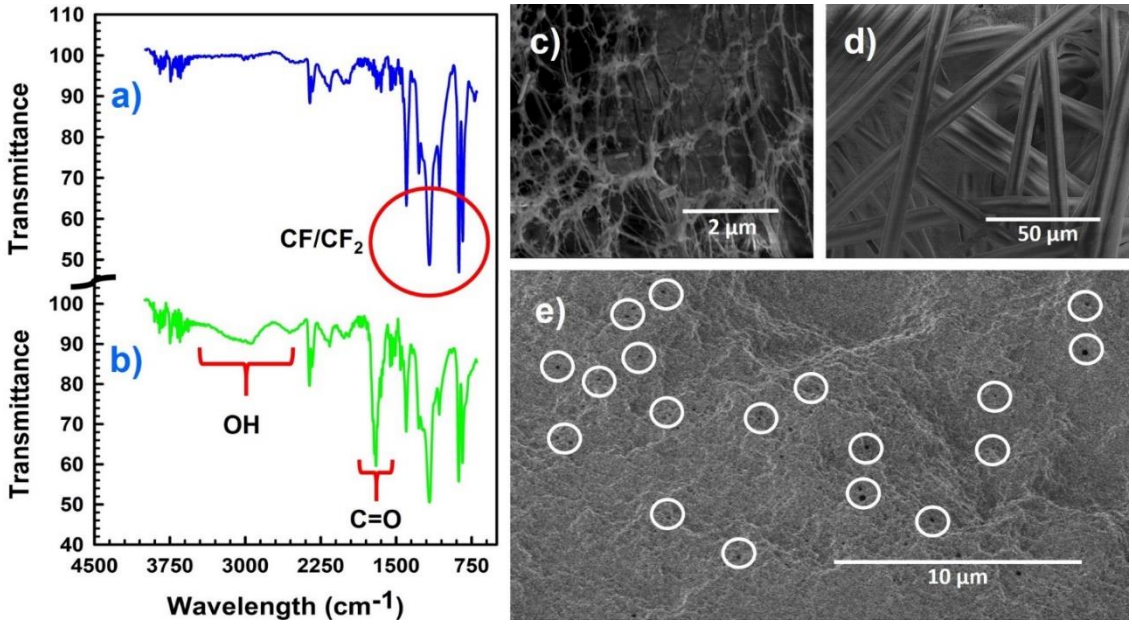


**Figure 4.3** ATR-FTIR spectra of **(a)** Blank PVDF membrane (blue line), **(b)** Functionalized PAA-PVDF membrane (green line); SEM images of **(c)** A bare PVDF Membrane (top surface) showing the open pore networks, **(d)** Back (polyester support materials) of the bare PVDF membrane, **(e)** Functionalized PAA-PVDF membrane. The white circles encircled some of the pores remaining after functionalization.

## 4.4 Contact Angle Measurement and Surface Zeta Potential Analysis

Contact angles (water, pH ~5.5) of the bare and functionalized PVDF membrane were measured to assess any change in the hydrophilicity of the modified layer. The contact angle decreased from 79.96$^{o}$ (±3.86$^{o}$) to 55.90$^{o}$ (± 0.06$^{o}$), indicating the membrane became more hydrophilic upon functionalization with PAA polymer. A sessile drop method was used to measure the contact angle of bare PVDF membrane. However, for hydrophilic surfaces it is difficult to measure the contact angle by sessile drop method due to: **i)** high surface free energy that causes water droplet to spread rapidly, and **ii)** fast absorption of water by PAA hydrogel [165]. To overcome those limitations, a captive bubble method was used for functionalized PAA-PVDF membrane [166-167].

The surface zeta potential of the bare PVDF and the functionalized PVDF membranes were compared to study the change in surface charge. **Figure 4.4** shows the comparison of the pH dependence of the zeta potential for blank PVDF membrane (green line) to that of functionalized PAA-PVDF membrane (red line). The blank PVDF membrane is showing overall negative change distribution on the surface. The blue line in the graph is representing the commercial hydrophilized PVDF membrane confirming the same trend of surface charge distribution as functionalized PAA-PVDF membrane. The PAA-functionalized membrane shows a phase transition (isoelectric point) near pH ~2.6, which is attributed to the pKa value of carboxyl groups present in PAA [146, 168-169]. A change in surface charge confirms the presence of PAA layer in functionalized PVDF membrane.

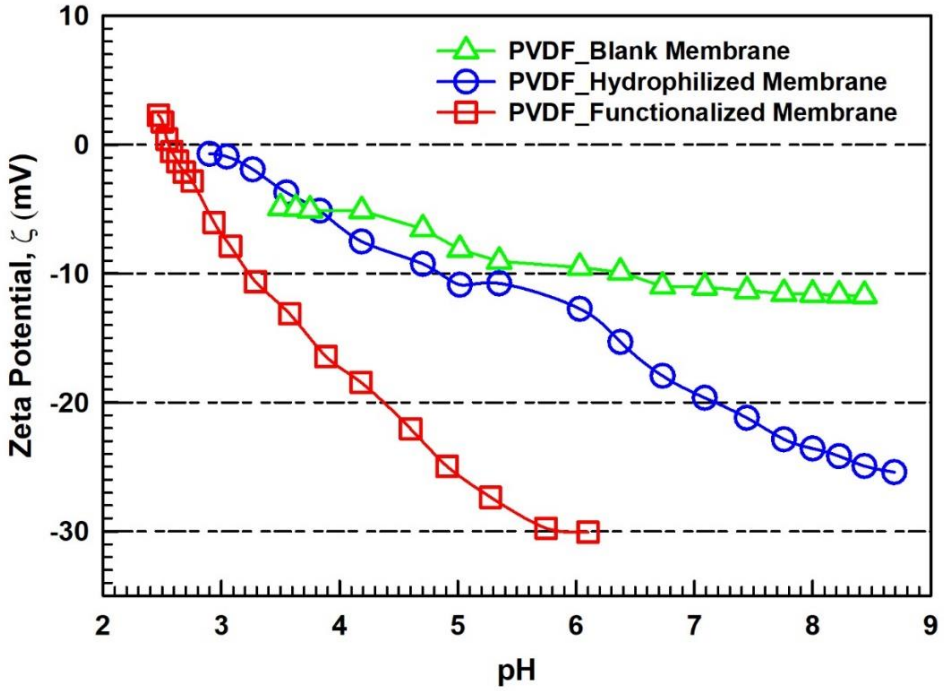


**Figure 4.4** Comparison of zeta potential as a function of pH for PVDF and PAA functionalized PVDF membranes.

## 4.5 Water Permeability Studies of pH Responsive Functionalized Membranes

To determine the pH response of the PAA functionalized membrane and the effects of monomer (M) and cross-linker (X) concentrations on its permeability, water flux tests were performed on six different batches (mentioned in **Table 3.1** in chapter 3) of membranes. The role of pH in the responsive behavior of the PAA functionalized membranes is thoroughly documented in literature [6, 18, 170]. The water permeability of the bare PVDF membrane was found around 6250 $L \cdot m^{-2} \cdot hr^{-1} \cdot bar^{-1}$ (LMH/bar) at pH 4. However, the permeability dropped substantially after functionalization making the membrane pH responsive. This responsive behavior of PAA-PVDF membrane allows the water permeability to be changed in response to different pH environments. In **Figure 4.5** the effects of pH on the water permeability of the PAA-PVDF functionalized membrane are shown. PAA hydrogel can swell or shrink by tuning its protonation state and the molar mass of the solution [170]. At high pH, PAA swells, resulting in a decrease in the effective pore size and water permeability. On the contrary, when the permeate pH is decreased, the polymer chain shrinks and the pores return to their original size, thereby increasing water permeability.

The permeability of the membranes shown in **Figure 4.5** decreased with increasing pH, confirming the successful PAA functionalization within the PVDF pores. This behavior of membrane water permeability is consistent with previous findings [18, 26, 146]. In **Figure 4.5a** the water permeability of batch C (M = 10 wt.%, X = 2 mol%) is provided. The water permeability with a different pH in **Figure 4.5a** can be fitted (continuous line in **Figure 4.5a**) with the **equation 4.1** to obtain the pKa value [18]. The resulting pKa value is 5.8 for batch C, where, $A_{,max}$ = 116 LMH/bar (low pH) and $A_{,min}$ = 59 LMH/bar (high pH). In **equation 4.1**, $A$ is the membrane water permeability in LMH/bar. Similarly, the water permeability data of batch F (M = 20 wt.%, X = 2 mol%) with different pH (as shown in **Figure 4.5b)** can also fitted (continuous line in **Figure 4.5b**) with **equation 4.1.** In this case the value of pKa is 6. Here, $A_{,max}$ = 2.75 LMH/bar (low pH) and $A_{,min}$ = 0.4 LMH/bar (high pH). It is worth mentioning that, while increasing the monomer concentration (M) from 10 to 20 wt.% while keeping the cross-linker concentration (X) constant at 2 mol%, the water permeability drops about 42 times at low pH (4) and around 147 times at high

pH (8.5). This change in water permeability pattern for varying M and X confirms the quantitative measurement of responsive behavior of PAA-PVDF membrane.

$$A = \left\{ {A_{max}}^{1/2} - \frac{[COO^-]}{[COOH] + [COO^-]} \left( {A_{max}}^{1/2} - {A_{min}}^{1/2} \right) \right\}^2 \quad \ldots\ldots\ldots\ldots\ldots\ldots \textbf{EQ } (\mathbf{4.1})$$

Where,

$$\frac{[COO^-]}{[COOH] + [COO^-]} = \frac{1}{1 + 10^{(pKa - pH)}}$$

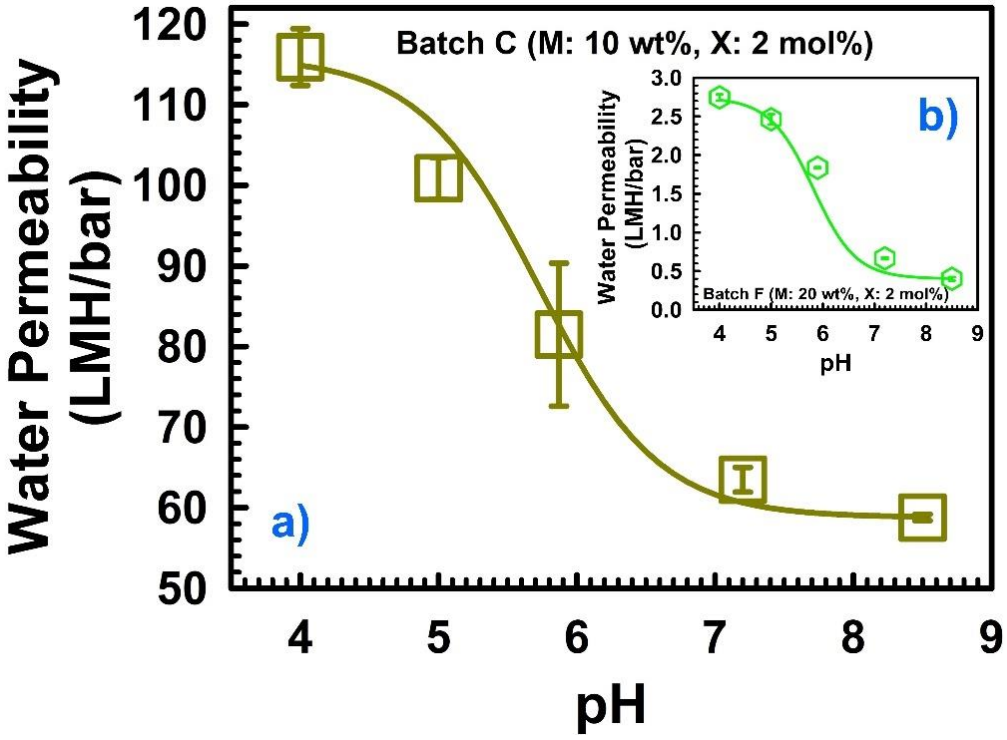


**Figure 4.5** Typical water permeability profile of two different batches of functionalized membranes **(a)** Batch C (10 wt.% monomer and 2 mol% cross-linker), **(b)** Batch F (20 wt.% monomer and 2 mol% cross-linker). PAA-PVDF membrane area = 13.2 $cm^2$. T = 22~23 °C.

Permeability data of six different batches of functionalized membranes at pH 4 and 8.5 are presented in **Figure 4.6**. It is observable that with an increasing M and X concentrations, the permeability of water through the membrane decreases. This allows a wide range of variation of responsive behavior of PAA functionalized membranes in quantified terms of water permeability that ranges from 270 to 1 LMH/bar, by altering M (10 wt.% to 20 wt.%) and X (0.5 mol% to 2 mol%) concentrations. Permeability data at two different pH (4 and 8.5) widely varies, while M is 10 wt.%. But it does not vary in the same range when the M is 20 wt.%. Another interesting finding is that with 20 wt.% monomer concentration, the flux remains constant for a pH 4 and a pH of 8.5 when the cross-linker concentration is increased from 1 to 2 mol% (Batch E and F in **Figure 4.6**). Further addition of a cross-linker will not affect swelling property of the functionalized membrane anymore, resulting in a fixed of permeability. This is due to high entanglement of polymeric chains inside the PAA-PVDF membrane pores resulting hindrance for charge neutral carboxyl groups for chain expansion and contraction. This explains why the swelling of the PAA resulted in a saturated pore domain with 1 mol% of cross-linker, sufficient to keep the monomer chains apart and reduce the entanglement of polymer chain in membrane pores. **Figure 4.6** confirms that the response behavior of PAA-PVDF membrane varies significantly in terms of difference in water permeability between low and high pH when monomer concentration is low (10 wt.%). However, it does not vary in the same extent when the monomer concentration is in the high end (20 wt.%).

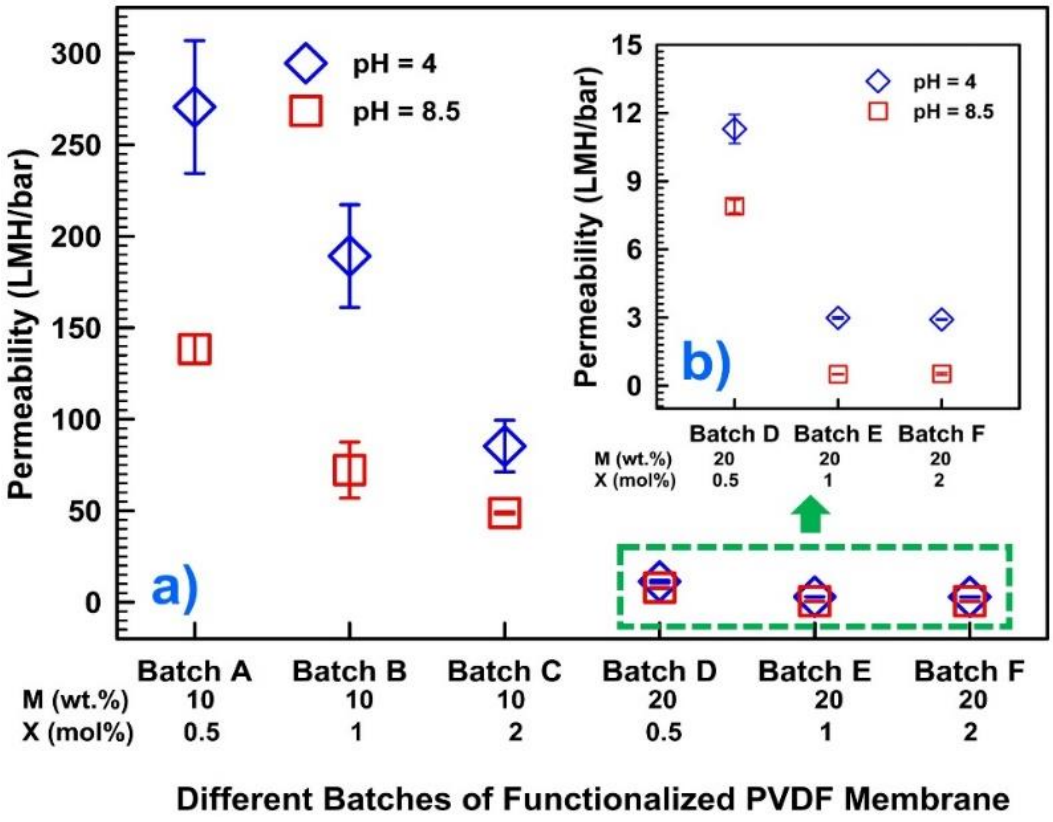


**Figure 4.6 (a)** Permeability data of six different batches of functionalized membranes at pH 4 and 8.5, **(b)** The green box in (a) are zoomed to show permeability data of three batches (D, E and F) with 20 wt.% monomer concentrations. PAA-PVDF membrane area = 13.2 $cm^2$. T = 22~23 °C.

### 4.6 Pd-Fe Nanoparticle Loading and Particle Size Distribution

To ensure that $Fe^{2+}$ is immobilized in the PAA network of the functionalized membrane and does not precipitate out of the membrane pores, we monitored the release of the cation displaced by $Fe^{2+}$ during ion exchange. For this reason and to prevent pH drop during $Fe^{2+}$ capture, PAA-PVDF membranes were first ion exchanged with $Na^{+}$ ($Na^{+}$-PAA-PVDF). There was no evidence of iron precipitation during immobilization, and no leaching of iron from the membrane was detected during the experiments. In **Figure 4.7**, it is demonstrated that the amount of Fe loading in mg/cm$^2$ surface area (0.225 cm$^3$ volume) of Fe-PAA-PVDF membrane is a function of different combinations of monomer (M) and cross-linker (X) concentrations. The amount of Fe loading varied from 2.83 to 12.4 mg per mentioned surface area which is equivalent of 0.21~0.94 mg/cm$^2$ of membrane surface area. The difference of loading is due to variation of available carboxyl groups in the membrane pore domain. The Loading was minimum when M and X concentrations were minimum (10 wt.% and 0.5 mol%, respectively), which proves the presence of less carboxyl groups during the functionalization of membrane. On average, the Fe loading was found to be in the range of 6.5 to 8 mg with the same specific volume for most of the combinations of monomer and cross-linker densities. This means that variation of M and X does not confirm variation of the available carboxyl group in the membrane domain to perform double ion exchanges for in-situ synthesize Fe NPs in the membrane.

However, Fe loading is maximized to a value of 12.4 mg in the same surface volume, when M and X densities are 20 wt.% and 1 mol% respectively. This suggests that a specific combination of M and X reveal a maximum amount of deprotonated carboxyl groups in the PAA chains in PVDF membrane in order to capture $Fe^{2+}$ during ion exchange. In contrast, a slight increase in cross-linker concentration as in batch F (M:20 wt.% & X:2%) resulted in a lower loading (6.49 mg) of Fe (see **Figure 4.7**). This is due to the fact that a higher concentration of cross-linker results in an increase in the entanglement of the PAA chains in membrane domain, hindering the ability of the carboxyl groups to be involved in ion exchange. Such higher concentration also cause some of the swollen gel to come out of pores and lose the stability of the PAA gel [26]. The permeability data during the $Fe^{2+}$ ion exchange experiments are shown on the right y-axis of **Figure 4.7**. Interestingly during $Fe^{+2}$ ion exchange the water permeability of membrane increases slightly compare

to that of PAA-PVDF membrane due to overall charge positivity of membrane, especially when the monomer concentration is 10 wt.%. However, this observation is not so prominent when monomer concentration is 20 wt.%, indicating that at higher concentration of monomer and cross-linker the PAA-PVDF membrane is losing its responsive nature in course of $Fe^{2+}$ loading. The most interesting aspect of responsive nature of PAA-PVDF membrane is, it is always possible to restore responsive nature by dislodging the NPs if there is any significant loss of reactivity performance of NPs. This attribute makes it suitable for long time usage. After the Fe NPs are synthesized by reduction with $NaBH_4$, solution of $K_2PdCl_4$ solution (Pd as 1 wt.% of Fe) was passed through Fe-PAA-PVDF membrane reducing $Pd^{2+}$ to $Pd^{o}$ for all the batches of membrane.

In order to understand the impact of variation of monomer and cross-linker concentrations on the metallic NP size distribution during ion exchange process, the size distribution of NPs was measured on the surface and inside the membrane pores after the immobilization of the Pd-Fe NPs. PAA acted as a stabilizer of the Fe precursor in the NP synthesis. It also able to control the particle size depending on the available proximity distance between polymer chains. Both the rates of nucleation and particle growth could be retarded in presence of PAA in functionalized membrane pores [17, 171]. In **Figure 4.8** we have shown the variation of the Pd-Fe particle size distribution for different batches of Pd-Fe-PAA-PVDF membranes in a bar chart. At the top of all blue bars in **Figure 4.8**, we put the average value of particle size with their standard error of the mean. The average particle size varies from 16 to 23 nm, which agrees with available reported data [172]. However, around 68~87% of NPs fall in the range of 10~25 nm for different combinations of M and X. In **Figure 4.8**, it is also shown that when the X concentration increases while the M concentration is kept the same, the percentage of smaller particles (green bars) has increased and vice versa (red bars). This implies that by tuning the cross-linker concentration during the polymerization reaction it is possible to get much smaller particles by in-situ synthesis.

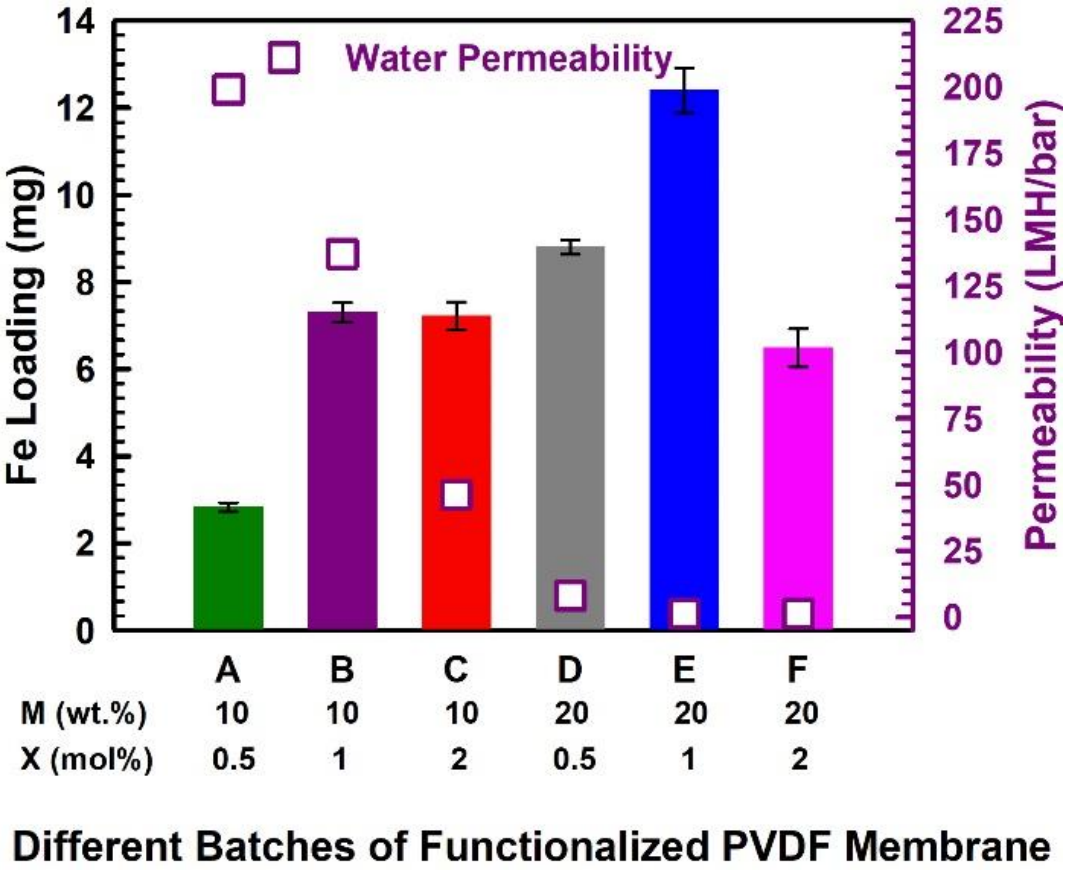


**Figure 4.7** Bar charts for the amount (mg) of Fe loading for different batches of functionalized membranes (membrane surface area = 13.2 $cm^2$, membrane volume = 0.225 $cm^3$), water permeability data during $Fe^{2+}$ ion exchange are shown in right hand side y-axis, pH = 5.0~5.5, T = 22~24ºC.

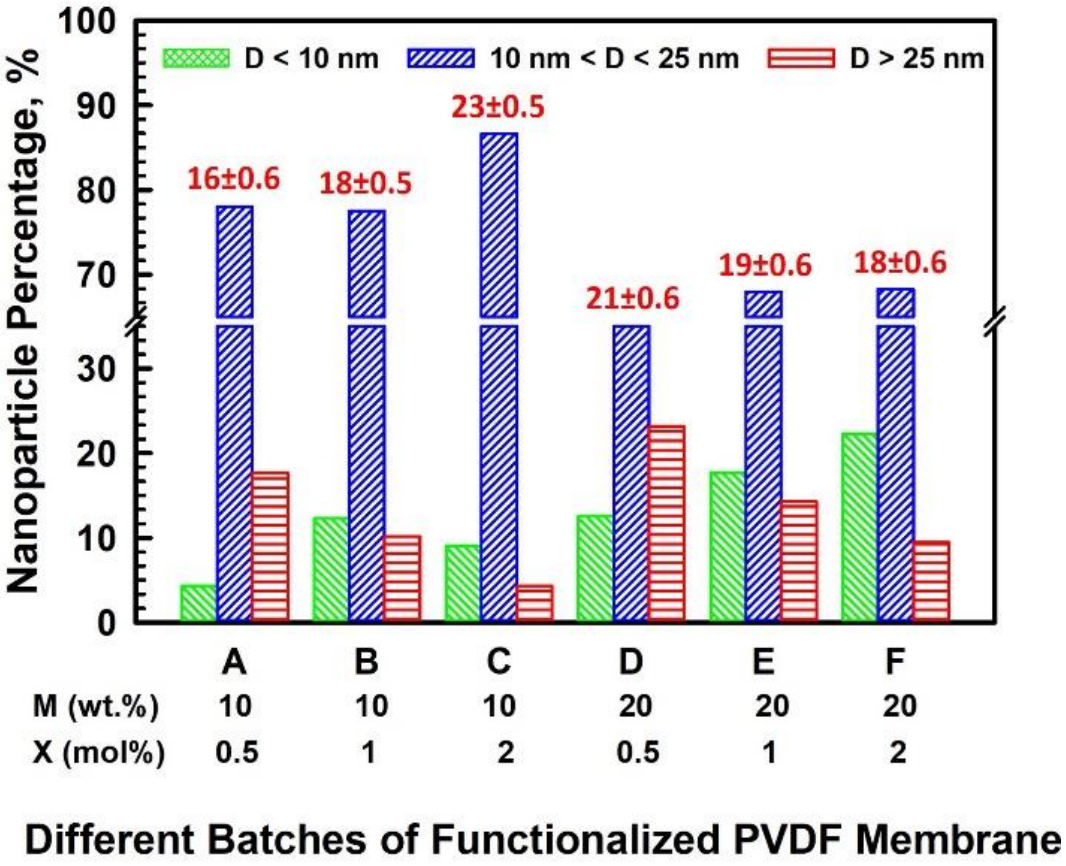


**Figure 4.8** Particle size distribution and average particle size of different batches of functionalized membranes (total count is in the range of 300~400 NPs).

## 4.7 Statistical Analysis between Input (Monomer and Cross-Linker) and Response Variables

A two-way factorial design with repetitions was performed in order to determine whether the M and X concentrations significantly affected the response variables. To perform statistical analysis, it has been considered M has three levels (0, 10 and 20 wt. %) and X has four levels (0, 0.5, 1.0 and 2.0 mol %). Although numerous responses resulting from these combinations of M and X can be analyzed, such as the NP size or the rate of reaction; however, these responses are affected mainly by two main responses: **i)** the amount of PAA present within the functionalized membranes (mass gain) and **ii)** the permeability (A). Permeability was considered because it is a dynamic response on the actual separation/reaction process on PAA-PVDF membrane platform, unlike the static mass gain. As the permeability changes with pH, the response analyzed is the ratio between permeability values at high pH and at low pH ($A_{min}/A_{max}$). The change in responsiveness factor ($A_{min}/A_{max}$) could affect ion exchange process, hence affecting Fe loading, NP size and, dechlorination performance. The present analysis was performed with 95% confidence in all cases.

A response surface design was selected to better understand the response results. This methodology was used to refine the models after determination of the factorial design analysis (discussed in detail in **section 4.7.1)** and helps to detect curvatures in the response surfaces. The Interaction effects and main effects (individual effects) of the concentrations of M and X on mass gain (%) and responsive factor ($A_{min}/A_{max}$) are shown in **Figure 4.9** and **Figure. 4.10**. In **Figure 4.11** the raw response surfaces (in color scale) and the fitted values (contours) are shown as a function of M and X. The effects of M and X concentrations are increasing for mass gain but decreasing for the responsiveness ($A_{min}/A_{max}$). The regression equations for each response surface are:

$$\textbf{Mass Gain (\%)} = -1.04\times10^{-16} - 0.46\cdot M + 1.84\times10^{-16}\cdot X + 0.031\cdot M^2 - 6.58\times10^{-17}\cdot X^2 + 0.54\cdot MX \quad \ldots\ldots\ldots\ldots\ldots\ldots \text{EQ } (4.2)$$

$$\textbf{A}_{min}/\textbf{A}_{max} = 1.14 - 0.037\cdot M - 0.57\cdot X + 0.0015\cdot M^2 + 0.28\cdot X^2 - 0.02051\cdot MX \quad \ldots\ldots\ldots\ldots\ldots\ldots \text{EQ } (4.3)$$

As mentioned in the factorial design analysis (**section 4.7.1**), the effect of X is not significant above 1.0 mol % for almost all mass gain values. The value of mass gain increases only where X is higher than about 1.8 mol % and M is higher than 15 wt. %. As expected, mass gain increases with an increase in M for all cases as depicted in **Figure 4.11a**. However, the responsiveness ($A_{min}/A_{max}$) decreases with an increase of M (**Figure 4.11b**). Since more PAA is in the membranes at higher M, the swelling is larger at higher pH. However, when $X \leq 0.5$, $A_{min}/A_{max}$ does not change significantly due to fewer polymer entanglements, decreasing the swelling capacity of the cross-linked PAA. It is worth mentioning that these statistical analyses between input variables (M and X) to response variables only work for the type of membrane selected for these experiments and any changes in the membrane support (pore size, thickness, etc.) will affect the responses. However, the discussed procedure related to the parameters of the examined membrane can be extended to other membrane types as well.

### *4.7.1 Factorial Design Analysis*

According to the results obtained from the factorial design analysis, it is concluded that M and X have significant effects on mass gain and responsiveness ratio ($A_{min}/A_{max}$), shown in **Figure 4.9** (interaction effects) and **Figure 4.10** (main/individual effects). The effect of different levels of M depends on what level of X is present. The interaction between M and X is synergistic in nature for most of the responses. This means that the effect of M and X is greater than the sum of their individual effects. M and X levels reinforce each other's effects. For mass gain, X has almost no effect due to their low concentration (almost parallel lines), only affecting when its concentration is the highest (2.0 mol%). The regression also confirms this with the coefficients for X to the order of magnitude of $10^{-16}$, (see **equation 4.2)**. The responsiveness ($A_{min}/A_{max}$) is negative as expected, at higher monomer concentrations, due to the PAA's swelling blocks the membrane pores. This is also true in the synergistic interaction (**Figure 4.9b**), where the biggest effect on the decreasing responsive factor ($A_{min}/A_{max}$) is when X is at the highest value (2.0 mol %). For the main/individual effects (**Figure 4.10**), one can see that M has steep and positive effects in mass gain but not in responsiveness ($A_{min}/A_{max}$).

### *4.7.2 Response Surface Design Analysis*

A statistically significant interaction between M and X exists. M contributes the most in the responses, as shown in **Figure 4.9** and **Figure 4.10**, and larger contributions from X are at high M values. This is important because there is a non-synergistic interaction when X is 2.0 mol %, which is related to less mobility of the PAA chains; that could impede complete ion exchange of Fe ions into the membrane matrix, hence the results in low Fe loading.

From an analysis of variance (ANOVA) and a Normal Probability test of the residuals, it can be concluded that the residuals are adjusted to a normal distribution. It was evident that the residuals did not have a recognizable behavior or pattern with respect to the analyzed variable or to the order of the experiments, thus the assumption of randomness was verified. This behavior was not seen in the normal probability plot of the residuals for permeability. This is due to the lack of squared terms in the response model from the factorial design, which can be added into a subsequent response surface design. With respect to the response in permeability discussed previously, the quadratic effect of the X is statistically significant, along with the other effects surpassing the significance limit. This quadratic effect (once included, the effect is redistributed) contributes significantly to the response in permeability.

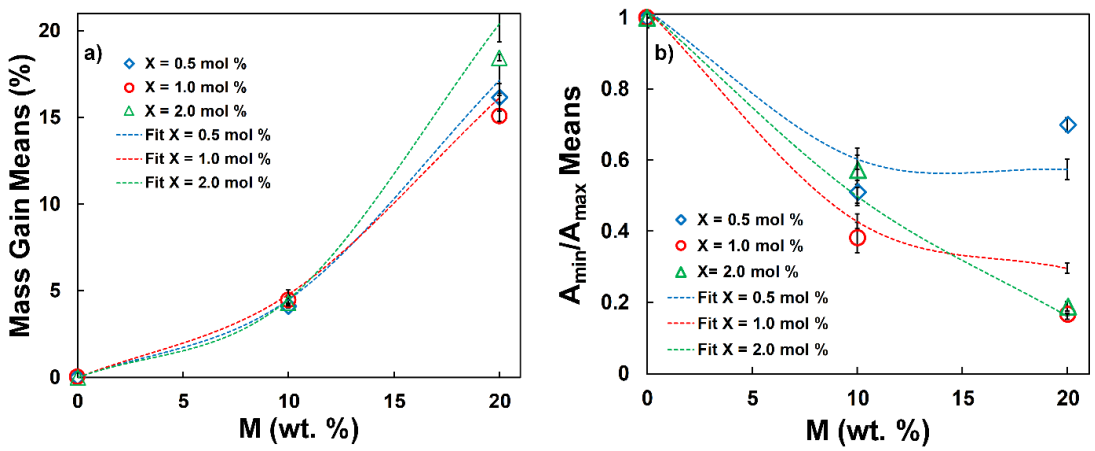


**Figure 4.9** Interaction effects of the concentrations of monomer, M (wt.%) and cross-linker, X (mol%) on **(a)** Mass Gain (%), **(b)** Responsiveness Factor ($A_{min}/A_{max}$).

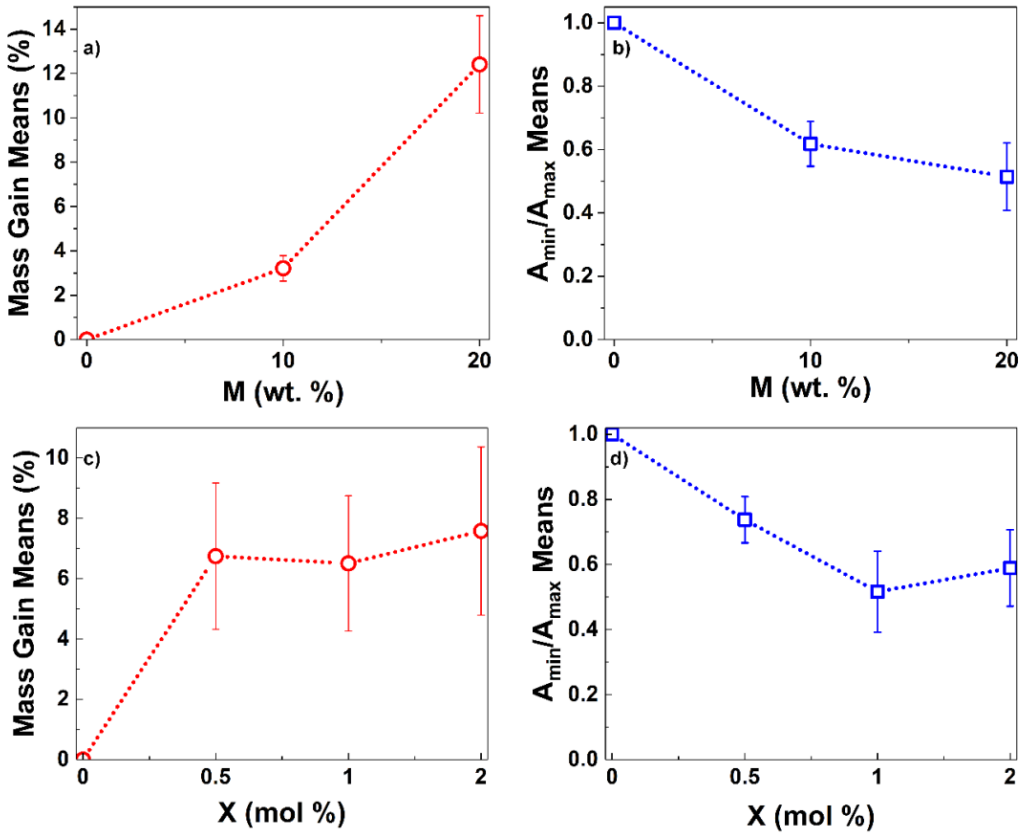


**Figure 4.10** Main effects (Individual effects) of the concentrations of monomer, M (wt.%) and cross-linker, X (mol%) on Mass Gain (%) and Responsiveness Factor ($A_{min}/A_{max}$). **(a)** Mass Gain (%) to M (wt.%), **(b)** Responsiveness Factor ($A_{min}/A_{max}$) to M (wt.%), (c) Mass Gain (%) to X (mol %), (d) Responsiveness Factor ($A_{min}/A_{max}$) to X (mol %).

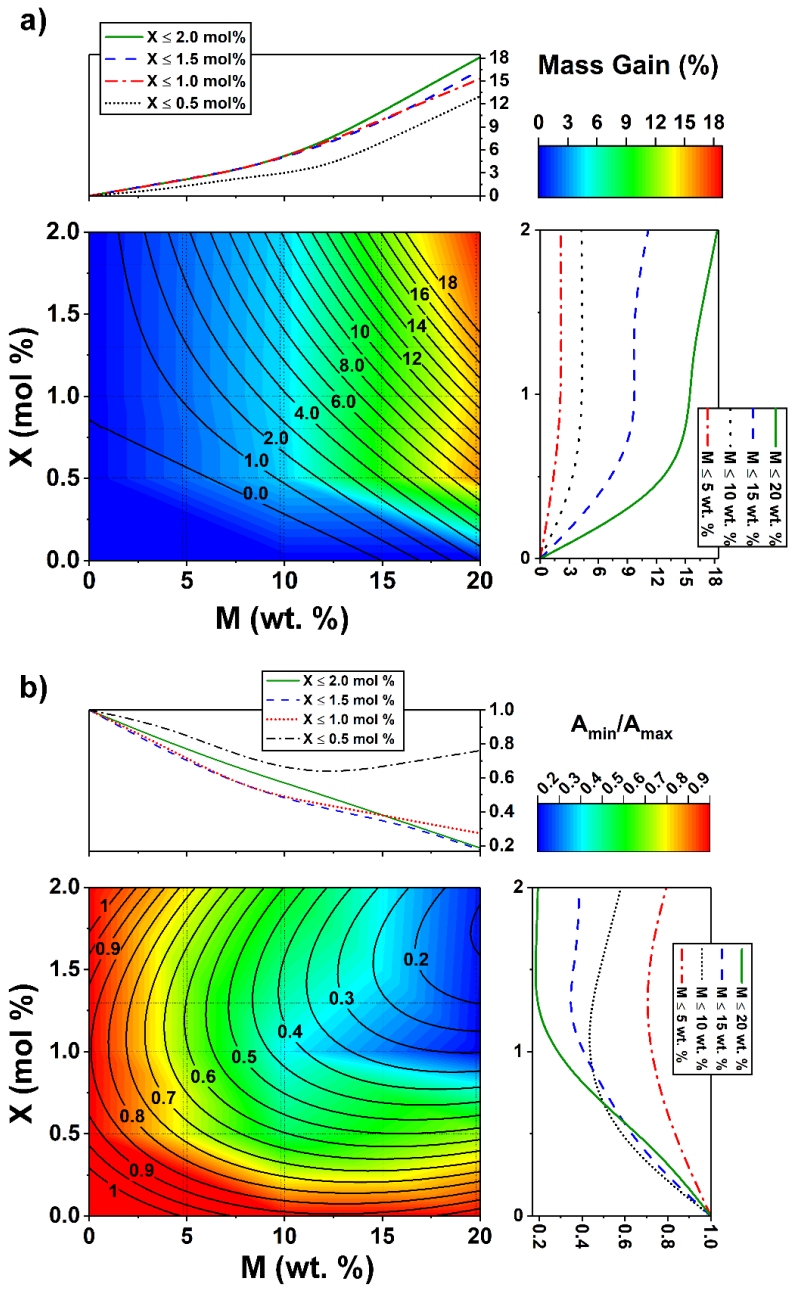


**Figure 4.11** Response surfaces and depth profiles based on the concentrations of monomer, M (wt. %) in x-axis and cross-linker, X (mol%) in y-axis. Experimental response surface is in color scale and fitted response is in contour. On the right and upper sides for X and M, respectively, a depth profile is shown maintaining the other factor constant at different intervals. **(a)** Mass Gain (%), **(b)** Permeability ratio, $A_{min}/A_{max}$.

# CHAPTER 5. CHARACTERIZATION OF BIMETALLIC NANOPARTICLE AND EFFECT OF NANOPARTICLE LOADING ON PAA-PVDF MEMBRANES FOR PCB DEGRADATION

## 5.1 Overview

This chapter discusses the characterization of bimetallic nanoparticles in solution phase as well as in membrane. These Pd-Fe nanoparticles and Pd-Fe-PAA-PVDF membranes are characterized by TEM, EDS, XRD, XPS, SEM, and FIB to reveal the details about the nanoparticles size, shape and size-distribution in solution phase as well as in membrane surface and pores. It also covers how the different nanoparticle loading effects the rate of degradation of 3,3',4,4',5-pentachlorobiphenyl (PCB 126) of pore functionalized polyvinylidene fluoride (PVDF) membranes. From Chapter 4, NP loading was found to vary from 0.21~0.94 mg per $cm^2$ of membrane area depending on the variation of available carboxyl groups in membrane pore domain. The NPs functionalized membranes were then tested for use as a platform for the degradation of PCB 126. The observed batch reaction rate ($K_{obs}$) for PCB 126 degradation for per mg of catalyst loading was found 0.08~0.1 $hr^{-1}$. Degradation study in convective flow mode shows 98.6% PCB 126 is degraded at a residence time of 46.2 seconds. The corresponding surface area normalized reaction rate ($K_{sa}$) is found about two times higher than $K_{sa}$ of batch degradation; suggesting elimination of the effect of diffusion resistance for degradation of PCB 126 in convective flow mode operation. Sections 5.2 to 5.5 are **published** in **Islam et al. (2018)**.

## 5.2 Preparation and Characterization of Solution Phase Zero Valent Iron and Pd-Fe Nanoparticles

Before immobilization of nZVI in the pore matrix of the functionalized PAA-PVDF membrane, iron NPs in solution phase were prepared by dissolving $FeCl_2$ salt in deoxygenated water (pH 5.5~5.7). Afterwards, the addition of $NaBH_4$ in the solution was used to reduce the $Fe^{2+}$ to $Fe^{o}$. From TEM images of **Figure 5.1a, b, c** we can see all the NPs diameters are in the range of 5 ~33 nm. In addition, HRTEM images in **Figure 5.1d** confirms formation of amorphous Fe structures together with iron oxides on the edges which is consistent with the literature [27, 173-175]. Further, peaks from the EDS spectrum in

**Figure 5.2** confirm the formation of Fe NPs in the solution phase. The Pd-Fe NPs are prepared in solution phase are analyzed by XRD. The crystalline structure of Pd, and Fe were analyzed and confirmed through comparison with XRD patterns published in the literature [39]. In **Figure 5.3** the XRD pattern of crystalline phases of bimetallic Pd-Fe nanoparticles were demonstrated. Based on the dominant peak and using Scherrer formula the particle size could be measured [176]. In this case the metallic $Fe_{[110]}$ is the dominant peak and corresponding particle size was calculated is around 16 nm, which falls in the limit of nanoparticle size we have mentioned earlier based on corresponding TEM data.

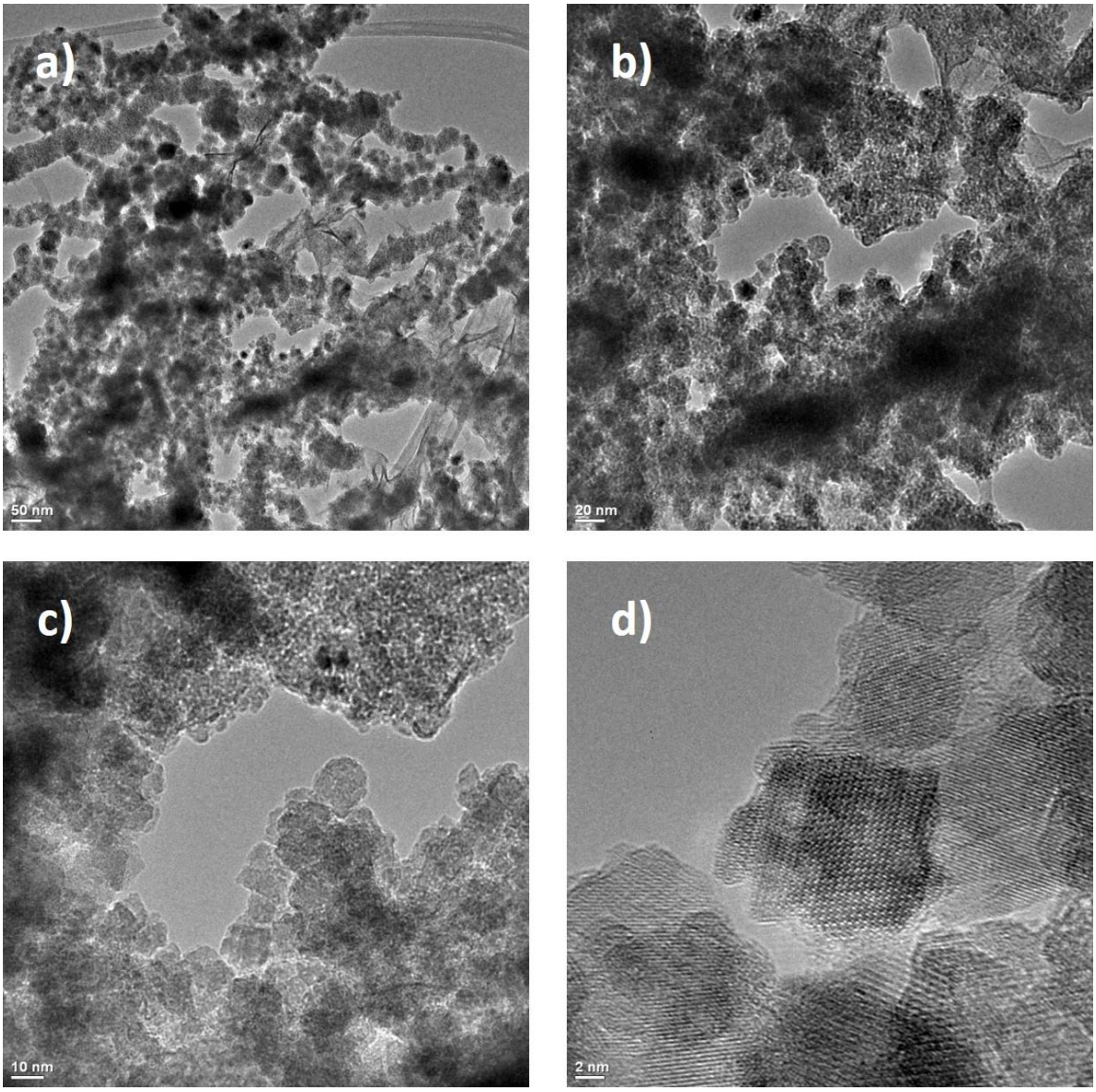


**Figure 5.1** TEM images of Fe nanoparticle formed in solution phase. The sample was placed over copper grid during imaging. **(a)** magnification 20 K, **(b)** magnification 50 K, **(c)** magnification 120 K, **(d)** magnification 500 K.

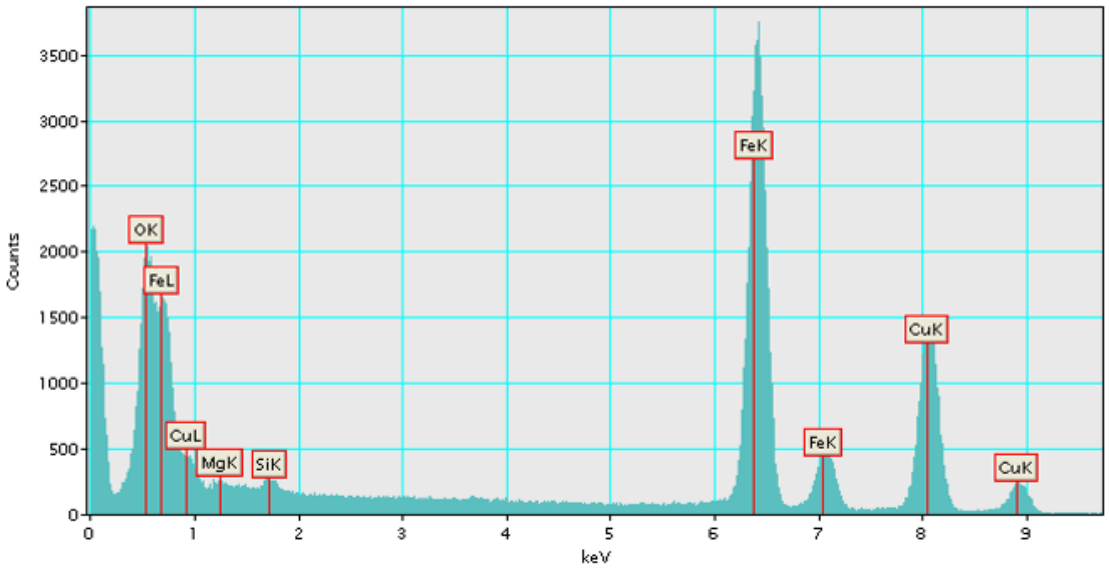


**Figure 5.2** EDS spectrum showing elemental peaks of Fe nanoparticle formed in solution phase at 500 K magnification. Copper signal is due to the sample holder.

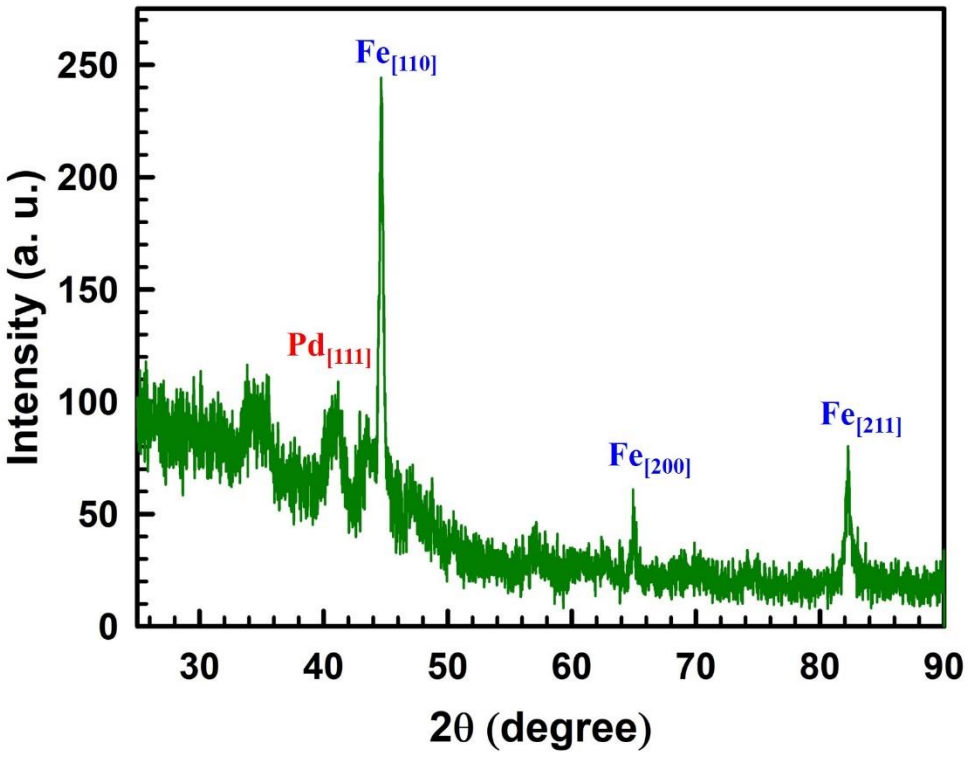


**Figure 5.3** XRD pattern of Pd-Fe nanoparticles showing characteristics peaks for elemental Pd and Fe. The nanoparticles are prepared in solution phase and dried under vacuum before characterizing by XRD.

## 5.3 Surface Analysis of Pd-Fe-PAA-PVDF Membrane by XPS Analysis

The Fe and Pd NPs are immobilized in the PAA-PVDF membrane pore domain following the method discussed earlier. **Figure 5.4** shows a typical FIB-SEM image which confirms a homogeneous immobilization of NPs in Pd-Fe-PAA-PVDF membrane surface. The XPS analysis results shown in **Figure 5.5** was performed to study the surface composition of Pd-Fe-PAA-PVDF membrane. The XPS survey scan (**Figure 5.5a**) shows the presence of $Pd^{o}$ and $Fe^{o}$ over the top surface of the membrane. In addition of Pd and Fe peaks, the other observed peaks are for the elements C, N, O, F and Na. The C 1s peak at binding energy of 289 eV is due to the presence of carbon in PVDF, AA and cross-linker MBA. The N 1s peak at binding energy of 402 eV is for N as amide ($-NH_2$) in cross-linker MBA. The O 1s peak at binding energy of 534 eV is due to the presence of O in carboxyl groups (-COOH). The F 1s peak at binding energy of 691eV is for F which is present in fluorocarbon groups ($-CF_2-$) of PVDF. A small peak of Na 1s was observed around binding energy of 1074 eV due to presence of some Na while reducing $Fe^{2+}$ to $Fe^{o}$ and $Pd^{2+}$ to $Pd^{o}$ using sodium borohydride. The distinct doublet peaks for Fe 2p which are observed at binding energies of 713 and 727 eV are assigned for Fe $2p_{3/2}$ and Fe $2p_{1/2}$ are due to presence of $Fe^{o}$ which is clearly shown in **Figure 5.5b** [177]. Apart from that Fe 3p and Fe 3s peaks are observed at the binding energies of 60 and 98 eV respectively depicted in survey scan in **Figure 5.5a**. Two doublet peaks at binding energies of 338 and 343 eV are attributed to Pd $3d_{5/2}$ and Pd $3d_{3/2}$, associated with $Pd^{o}$ that was deposited on top of Fe NPs shown in **Figure 5.5c** [177].

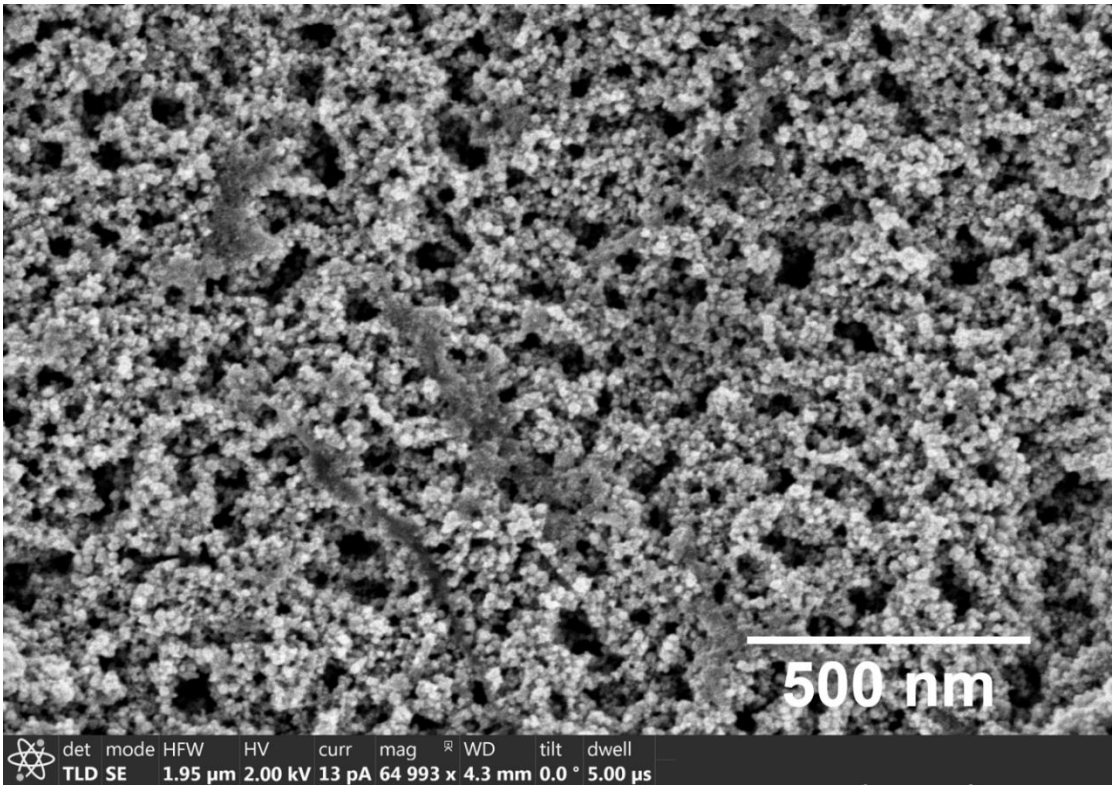


**Figure 5.4** FIB-SEM image of the surface of the Pd-Fe-PAA-PVDF membrane (10 wt.% of monomer, 1 mol% of cross-linker, 7.3 mg of Fe, 1 wt.% of Pd).

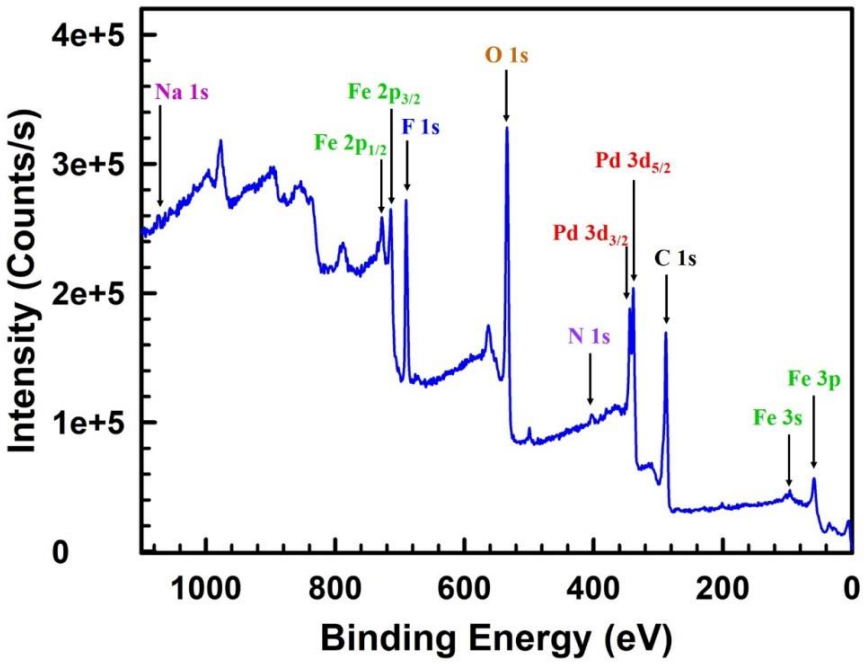


**(a)**

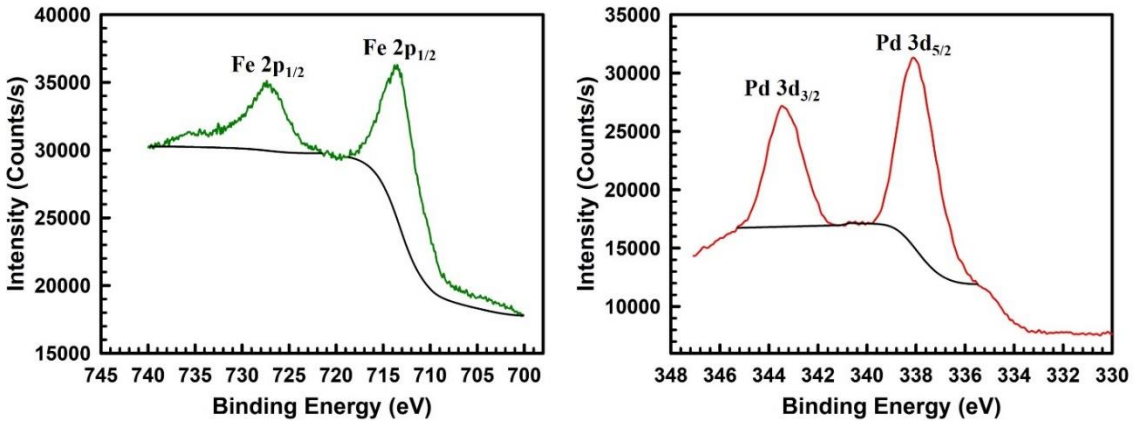


**(b)** **(c)**

**Figure 5.5** XPS spectrum of Pd-Fe-PAA-PVDF membrane. **(a)** Survey scan on the top surface of the membrane showing presence of the elements Pd, Fe, C, N, O, F and Na, **(b)** The doublet peaks for Fe 2p are assigned for Fe $2p_{3/2}$ and Fe $2p_{1/2}$ are due to presence of $Fe^{o}$, **(c)** Two doublet peaks are attributed to Pd $3d_{5/2}$ and Pd $3d_{3/2}$, associated with $Pd^{o}$ which is deposited on top of $Fe^{o}$.

## 5.4 Pd-Fe-PAA-PVDF Membranes Pore Characterization by FIB-SEM and TEM

Immobilization, size and morphology of the Pd-Fe NPs inside the pores at various depths were measured using FIB-SEM as shown in **Figure 5.6**. Some aggregations of Pd-Fe NPs were observed in surface (**Figure 5.4**) but fewer aggregates and more homogeneity of the Pd-Fe NPs were observed inside the pores as shown in **Figure 5.6**. At a depth of 3.196 µm from the top surface we can see (**Figure 5.6a**) all Pd-Fe NPs are well immobilized on the wall of the pores. For another membrane with different combinations of M and X, we also observe (**Figure 5.6b**) the even distribution of Pd-Fe NPs inside the pore. However, due to a smaller distance (500 nm) from the top surface, few aggregations of NPs were detected. This explains why with the increase of the distance from the top surface the Pd-Fe NPs are uniformly immobilized. In **Figure 5.6c** a zoomed image of the square box in **Figure 5.6a** is shown, which confirms that most of the Pd-Fe NPs are circular in nature. It is very interesting to find out that particle size inside the pores are smaller (9~14 nm) in size than those on the surface (16~23 nm) as well as more uniformly dispersed in pore wall. To explain this phenomenon during immobilization of Pd-Fe NPs, PAA-PVDF membrane has been exposed to a constant pressure gradient throughout convective flow mode ion exchange process. This overcomes the mass transfer limitation during immobilization process resulting less agglomeration of NPs, well dispersion of NPs inside pore domain ultimately creating smaller NPs inside [178]. However, on the surface the initial immobilized NPs are exposed continuously exposed in order to make more clusters of Pd-Fe NPs resulting relatively bigger NPs.

Finally, the inner surface of the membrane was characterized by TEM, high resolution TEM and selected area electron diffraction (SAED) as shown in **Figure 5.7**. A typical TEM image of the inside surface of Pd-Fe-PAA-PVDF membrane is shown in **Figure 5.7a**, where one can distinctly see the dispersion of Pd and Fe NPs. The light grey areas are Fe NPs and the darker ones are Pd NPs, further confirmed by a single point scanning transmission electron microscopy (STEM) and point EDS shown in **Figure 5.8**. It is also clear from **Figure 5.7a** that, most of the Pd NPs are deposited on the surface of the Fe NPs, and not over the carbon polymer layer. The EDS spectrum taken in the same area shown in **Figure 5.7b**, demonstrates the presence of Pd and Fe peaks. In **Figure 5.7c** SAED pattern displays a diffraction halo (representing core carbon of the polymer) and

multiple diffraction rings, representing different phases of Pd and Fe elements which agrees with literature [27, 47]. All these characterizations by TEM were conducted by removing a thin lamella of membrane from the inside of the membrane with the help of FIB depicted in **Figure 5.7d**. Lastly, line scanning of the inner surface performed in STEM mode (**Figure 5.7e**) further reveals a uniform distribution of Pd and Fe elements (**Figure 5.7f**) inside the Pd-Fe-PAA-PVDF membrane. In addition of detail characterization of the Pd-Fe-PAA-PVDF membrane with TEM, the elemental mapping inside of the functionalized membrane was performed using FIB. **Figure 5.9** demonstrates the elemental mapping of the Pd-Fe-PAA-PVDF membrane. The Pd and Fe are well incorporated inside the pore domain of PAA-PVDF membrane which is clear from **Figure 5.9**. The corresponding EDS analysis in the same area of the lamella shows the atomic distribution of Pd and Fe elements inside functionalized Pd-Fe-PAA-PVDF membrane shown in **Figure 5.10**.

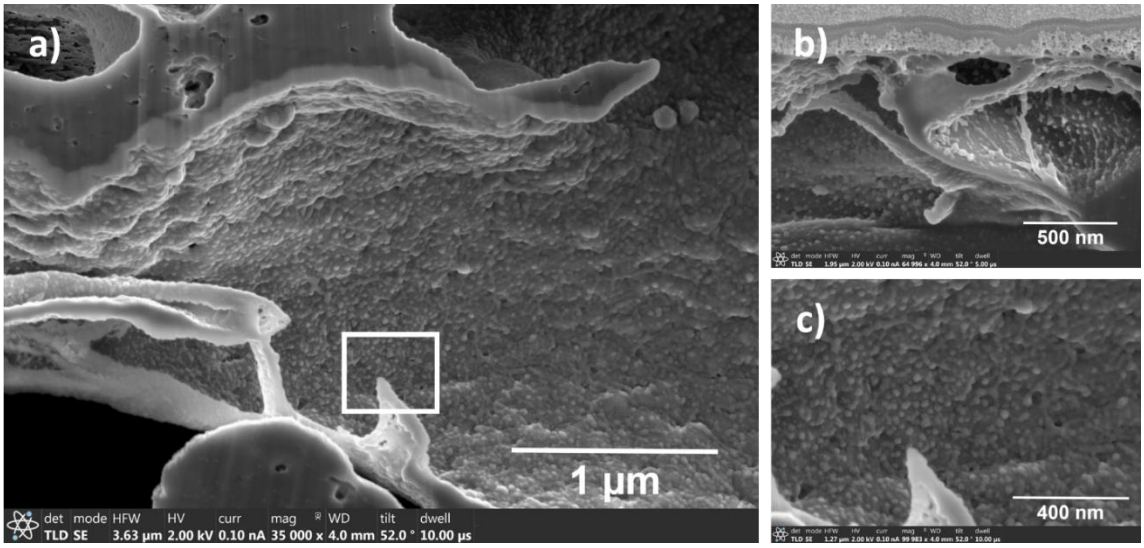


**Figure 5.6** FIB-SEM images of Pd-Fe-PAA-PVDF membrane inner pores showing presence of Pd-Fe nanoparticles inside the pores. **(a)** Distance from the top surface in 3.196 µm (10 wt.% of monomer, 1 mol% of cross-linker, 2.83 mg of Fe and 1 wt.% of Pd), **(b)** Distance from the top surface is 500 nm (10 wt.% of Monomer, 2 mol% C. L., 7.22 mg of Fe and 1 wt.% of Pd), **(c)** Zoomed image of the white squared box area of image (a) showing almost uniform Pd-Fe NPs are attached to pore wall evenly.

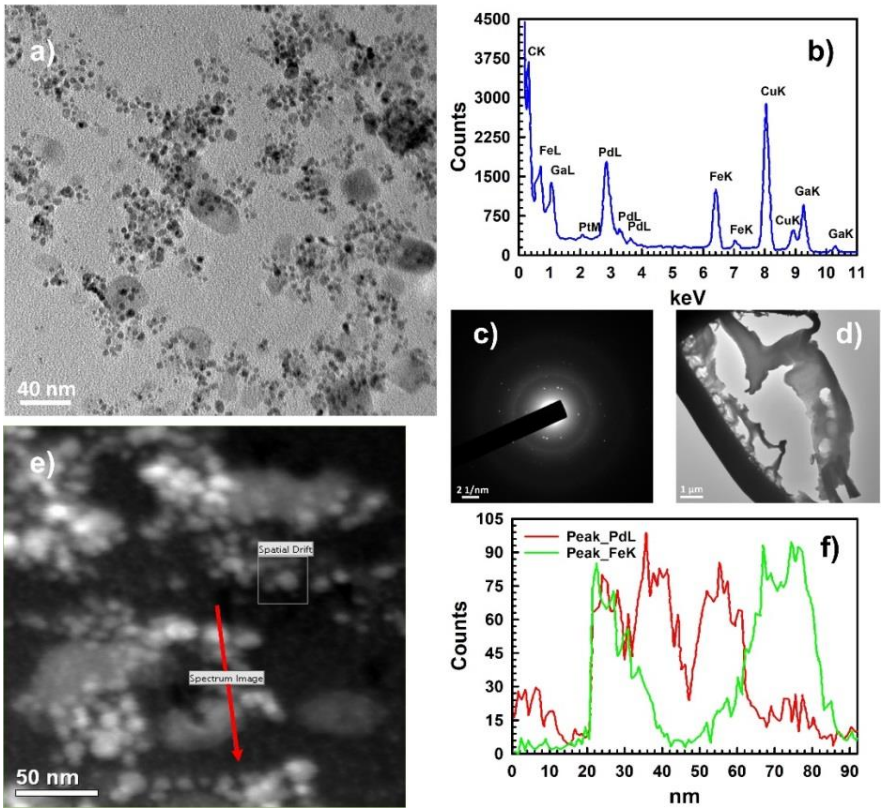


**Figure 5.7** Inner surface (a thin lamella was prepared and lifted out from the inside with the help of FIB) of the Pd-Fe-PAA-PVDF membrane (20 wt.% monomer and 1 mol% cross-linker) characterized by TEM, HRTEM and selected area electron diffraction (SAED). **(a)** A typical TEM image of the inner surface showing Pd/Fe nanoparticles (50 K magnification), **(b)** Reproduced EDS spectrum showing peaks of Fe and Pd elements (100 K magnification). During preparation of lamella, Gallium was used, and signal confirms that. The copper signal is due to the sample holder made of copper, **(c)** The SAED pattern shows a diffraction halo (representing core carbon of the polymer) and multiple diffraction rings representing different phases of Pd and Fe elements (100 K magnification), **(d)** The lamella of the inner surface where HRTEM and SAED were conducted (2K magnification), **(e)** Survey image of inner surface conducted STEM mode (200 K magnification), **(f)** Reproduced EDS signal profile for elemental mapping of the survey image (e) showing presence of Pd and Fe elements distribution in the high-lighted red arrowed line (200 K magnification).

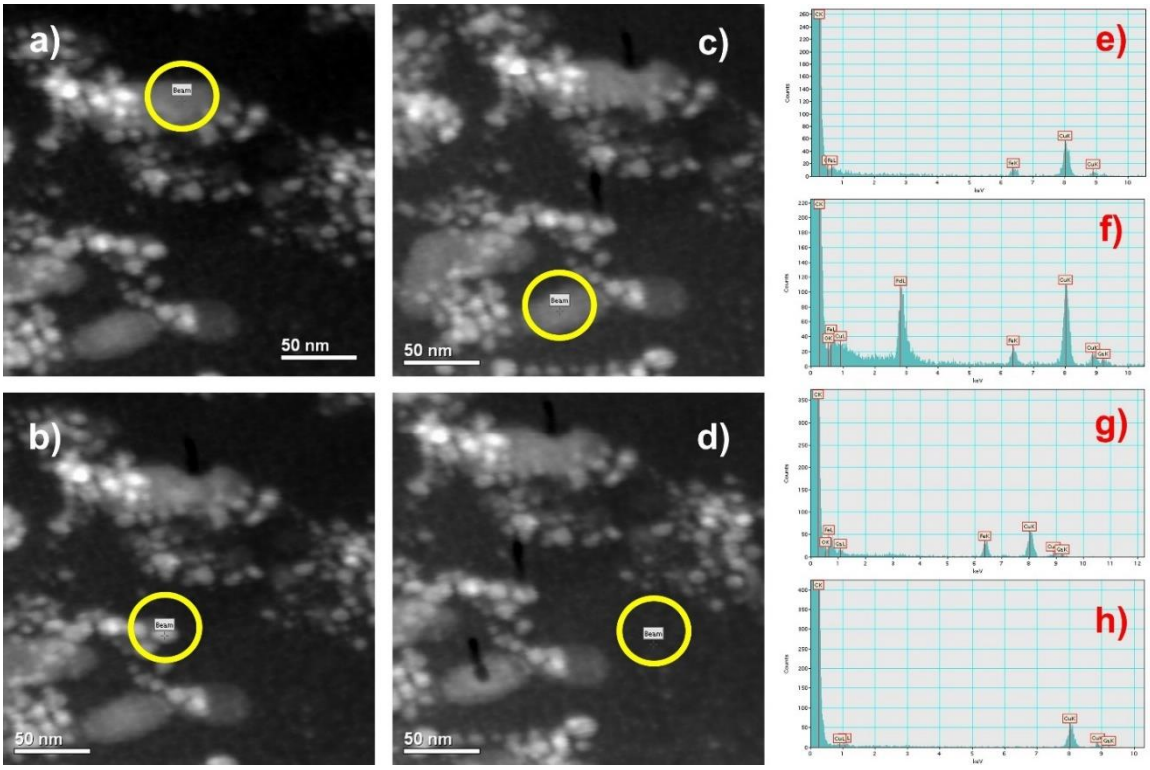


**Figure 5.8** STEM images and EDS spectrum of Pd/Fe nanoparticles inside the membrane (cross-section of the membrane layer). All images are taken at 200 K magnification. **(a)** The encircled grey area representing Fe nanoparticles, **(b)** The encircled bright white area demonstrating presence of Pd nanoparticles on the top of Fe nanoparticles, **(c)** Another encircled grey area confirms the presence of Fe nanoparticles, **(d)** The encircled black area is showing the background of polymer layer which is mostly carbon, **(e)** EDS spectrum of image (a) showing Fe peak, **(f)** EDS spectrum of image (b) showing both Pd and Fe peaks, **(g)** EDS spectrum of image (c) showing Fe peak, **(h)** EDS spectrum of image (c) showing only C peak. Copper signal in (e), (f), (g) and (h) is due to the sample holder.

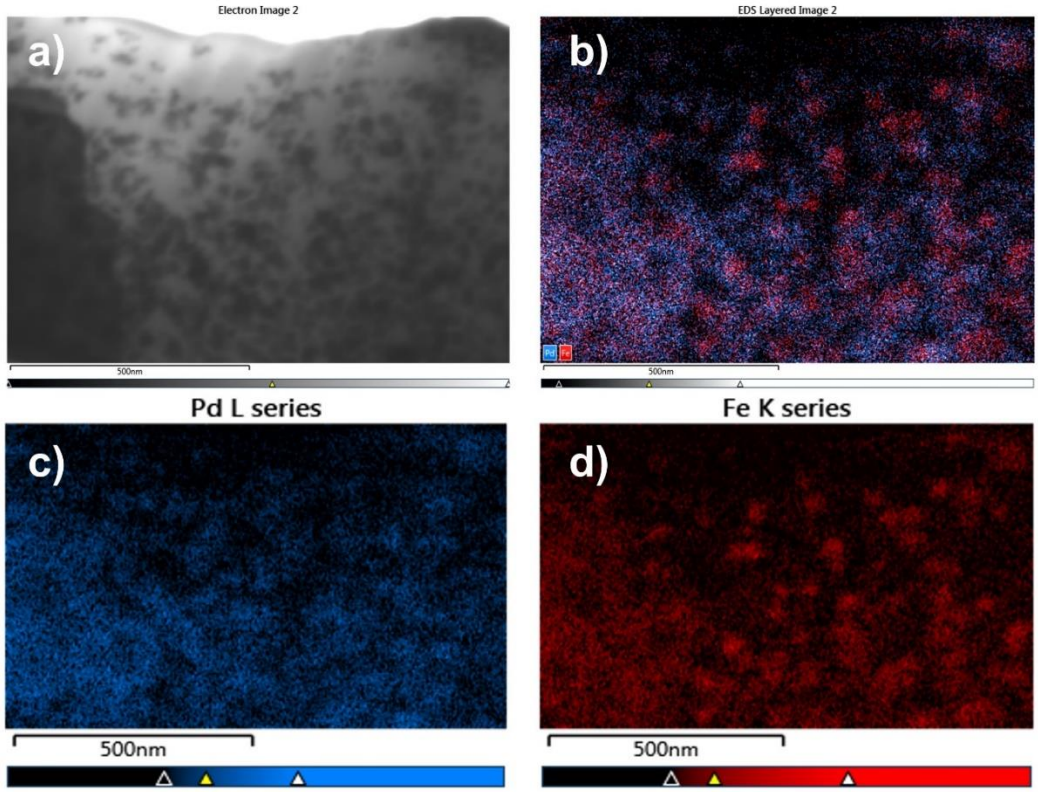


**Figure 5.9** Elemental mapping inside the Pd-Fe-PAA-PVDF membrane conducted by FIB. **(a)** The part of the lamella where elemental mapping was conducted, **(b)** Distribution of Pd and Fe elements in the lamella, **(c)** Distribution of Pd (blue dots) in the selected area, **(d)** Distribution of Fe (red dots) in the selected area.

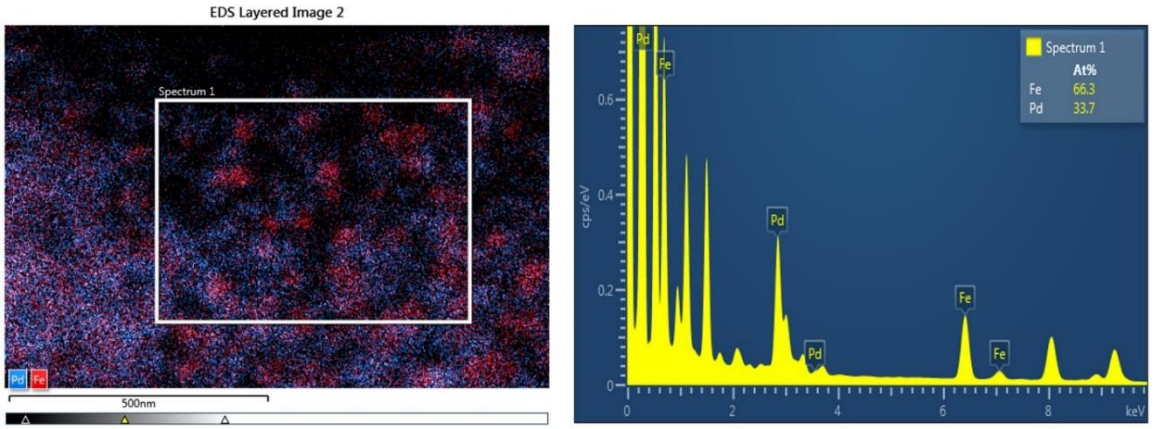


**(a)** **(b)**

**Figure 5.10** EDS analysis conducted on the lamella taken from the inside of the Pd-Fe-PAA-PVDF membrane. **(a)** The area of the lamella where EDS was conducted. Blue dots representing presence of Pd and red dots showing presence of Fe elements, **(b)** EDS spectrum showing elemental peaks of Pd and Fe inside the membrane.

## 5.5 Dechlorination Study of PCB 126 Using Pd-Fe-PAA-PVDF Membranes

Immobilized Pd-Fe NPs on polymer domain of functionalized PAA-PVDF membrane offers an opportunity to study the dechlorination of PCB 126. Bimetallic Pd-Fe NPs have been extensively used for degradation of chlorinated organics for their superior catalytic activity [15, 43-44, 53, 179]. However, mass transfer during dechlorination in Pd-Fe-PAA-PVDF membrane platform could be critical due to its dependence on membrane pore size, porosity, Pd-Fe NPs loading, available reaction surface area, channeling and finally, fluid mixing during reaction. To address most of these issues, PCB 126 degradation in batch and convective flow modes were studied. Initially, solution phase dechlorination experiment was conducted. In this case, almost all the PCB 126 was converted to biphenyl within 4 hours, as shown in **Figure 5.11**.

### *5.5.1 Degradation Study Using Pd-Fe-PAA-PVDF Membranes in Batch Mode*

The dechlorination results from batch studies are shown in **Figure 5.12**. A control experiment was performed to address the evaporation of the reactant. The rate of PCB 126 degradation varies with the different amount of Fe loading for different batches of membrane. From **Figure 5.12** we see PCB 126 concentration reduces to 40%, while the Fe loading is 2.83 mg; whereas, it reduces to almost zero when the Fe loading is 12.4 mg, in a same time scale of 4.5 hrs. This suggests, it is possible to tune the dechlorination of PCB in same membrane surface domain, by manipulating the Fe loading. To explain this phenomenon, it is well documented that in presence of water Fe acts as electron source in corrosion mechanism [53]. It continuously converting from $Fe^{o}$ to $Fe^{2+}$ making $H_2$ gas and $OH^-$ radical. In presence of Pd, $H_2$ is quickly converted to H·radical, which ultimately enhance the dechlorination reaction. The degree of surface Pd loading is proportional to the initial amount of Pd [53, 180]. However, more Fe loading offers more Pd to do ion exchange and attach onto the Fe shell during ion exchange process. This ultimately creates more reactive Pd-Fe NPs surfaces available for dechlorination reaction in the membrane pore domain, proportional to the initial Fe loading. The maximum yield of biphenyl in the experiment was found around 63%, which defers from theoretical estimation. This deviation of mass balance is also reported in available literature [39, 181]. Formation of PCB intermediates, adsorption of some biphenyl in hydrophilic membrane, and further degradation of biphenyl might account for this deviation [39]. However, investigations have

shown that catalytic hydro-dechlorination by Pd usually leads to the formation of a small amount of chlorinated intermediates, likely to be attributed to complete dissociation of carbon-chlorine bonds at the Pd surface [53].

PCB 126 dechlorination by Pd-Fe NPs follows a pseudo-first order rate law during batch study experiments following **equation 5.1** [53]:

$$r = -\frac{dC}{dt} = -\mathrm{K_{obs}}C = -K_{sa}\rho_m a_s C \quad \ldots\ldots\ldots\ldots\ldots\ldots \mathbf{EQ\ (5.1)}$$

where, $r$ is the reaction rate (mol·L$^{-1}$·hr$^{-1}$), $C$ is concentration of PCB 126 (mol·L$^{-1}$) at reaction time, $t$ (hr), $\mathrm{K_{obs}}$ is the observed rate constant (hr$^{-1}$), $K_{sa}$ is surface-area normalized rate constant (L·m$^{-2}$·hr$^{-1}$), $\rho_m$ is the nanoparticle loading density (g·L$^{-1}$), and $a_s$ is the specific surface area of Pd-Fe NPs immobilized in membrane (m$^2$·g$^{-1}$). In **Figure 5.13** we have shown the variation of observed reaction rate $\mathrm{K_{obs}}$ (hr$^{-1}$) with loading (mg) of Fe in membrane domain. The observed reaction rate, $\mathrm{K_{obs}}$ (hr$^{-1}$) varies linearly from the value of 0.22 to 1.35 (hr$^{-1}$) with the amount of Fe loading from 2.83 to 12.4 mg for different batches of membrane. This means for per mg of catalyst loading in Pd-Fe-PAA-PVDF membrane the observed batch reaction rate ($\mathrm{K_{obs}}$) for PCB 126 degradation is 0.08~0.1 hr$^{-1}$. On the right y-axis of **Figure 5.13** data for surface normalized reaction rate, $K_{sa}$ (L·m$^{-2}$·hr$^{-1}$) is given, which varies from 0.033 to 0.054 (L·m$^{-2}$·hr$^{-1}$). Dechlorination of PCB 126 is a surface mediated reaction, which usually involves several steps in the overall reaction including the diffusion of reactant PCB 126 to the surface, a chemical reaction on the surface, and the diffusion of a product biphenyl back into the solution [53]. For the variation of Fe loading from 2.83 mg to 12.4 mg in membrane pores, the loading densities ($\rho_m$) varied from 0.145 to 0.62 (g L$^{-1}$). The specific surface area ($a_s$), also a function of Pd-Fe NPs diameter varied from 33 to 48 (m$^2$ g$^{-1}$) when the NPs diameters varied from 16 to 23 nm. As $K_{sa}$ is a function of nanoparticle loading density ($\rho_m$) and specific surface area ($a_s$), it did not vary that much due to small variation of average Pd-Fe NPs diameter. However, the magnitude of variation results due to the difference in iron loading that is for loading density ($\rho_m$). **Figure 5.13** shows that when the Fe loading is increased during the ion exchange experiment, the available Pd-Fe core shell structures also increase proportionately creating more surface area for degradation reaction.

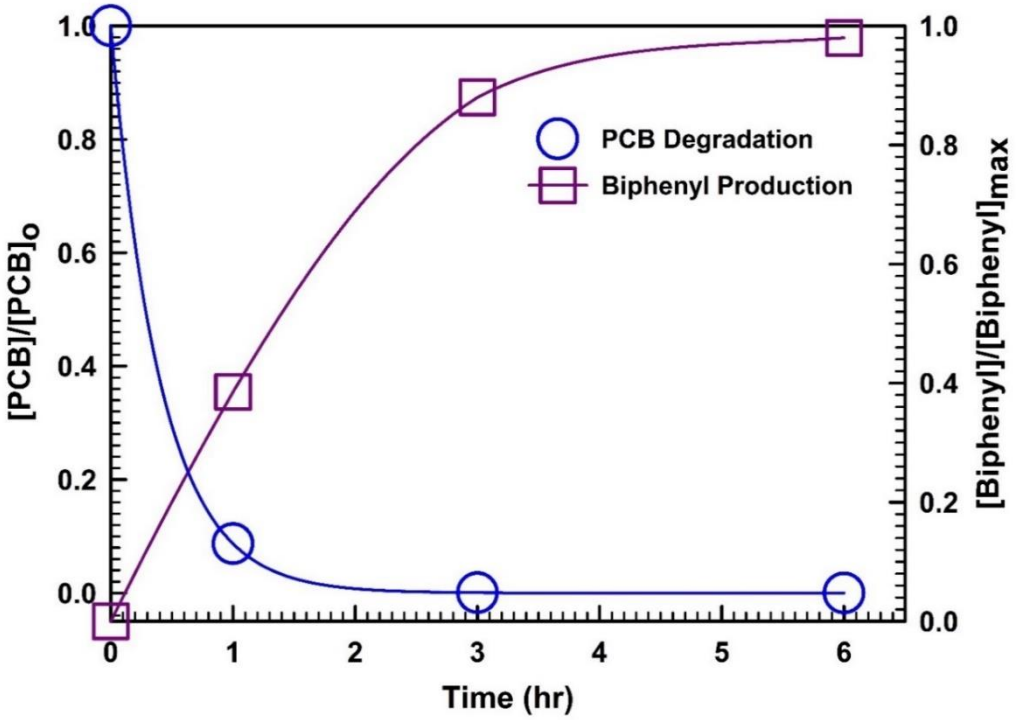


**Figure 5.11** Solution phase study of PCB 126 degradation and biphenyl formation by Pd-Fe nanoparticles. $[PCB\ 126]_o$ = 15 µM, [Fe] = 0.2 g/L, [Pd] = 1 wt.% of as Fe, pH = 5.6, T = 23°C.

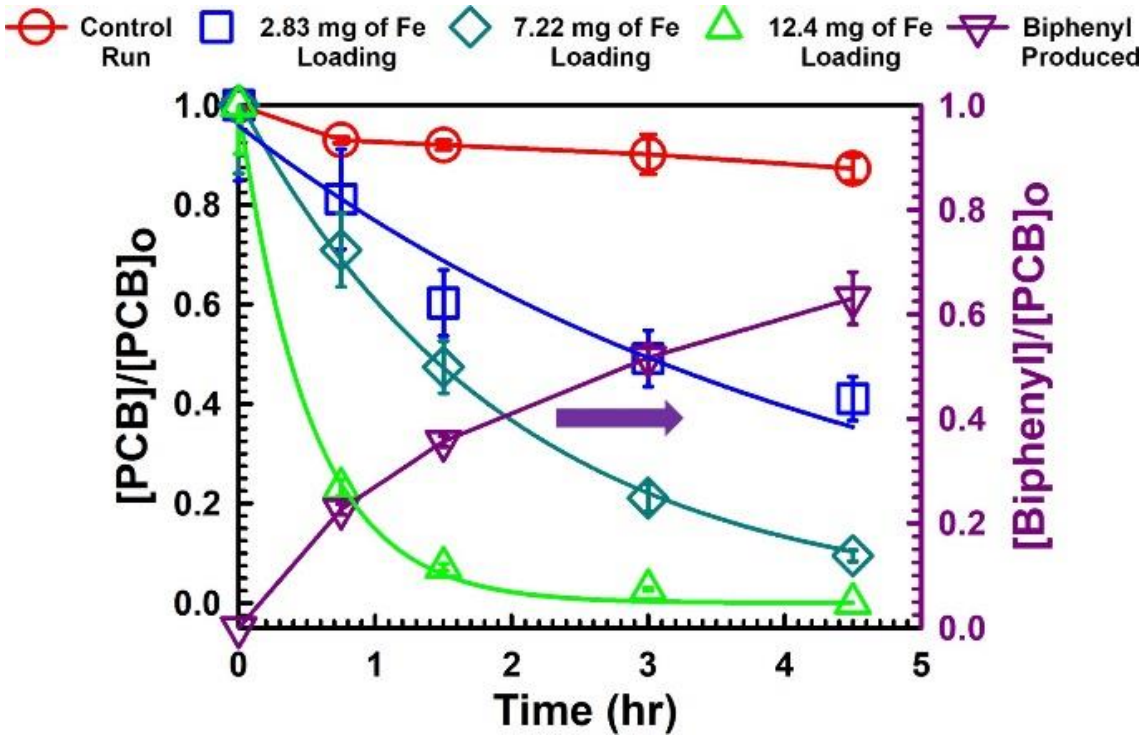


**Figure 5.12** Batch study of PCB 126 degradation by three different batches of Pd-Fe-PAA-PVDF membranes with different loading of Fe NPs. $[PCB\ 126]_o$ ~15 µM, [Fe] = 0.71 g/L in Solution, [Pd] ~ 1 wt.% of Fe, pH = 5.6~5.7, T = 22~24$^oC$.

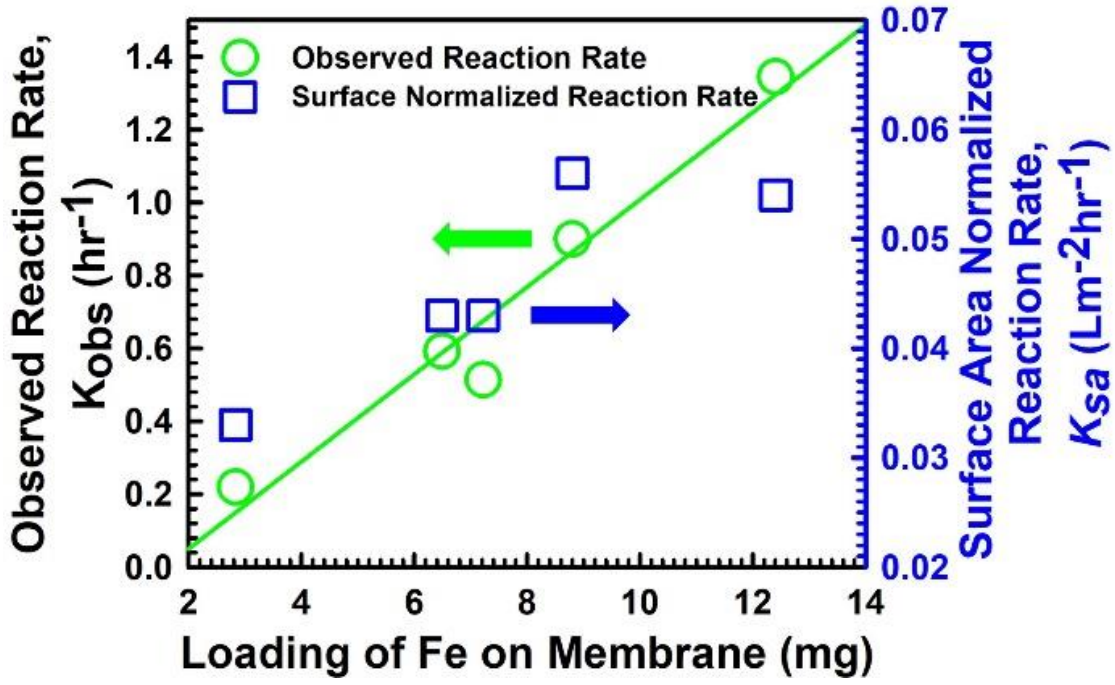


**Figure 5.13** Profile of observed reaction rate, $K_{obs}$ (left y-axis) and surface area normalized reaction rate, $K_{sa}$ (right y-axis) along with Fe loading on membrane effective surface area of 13.2 $cm^2$.

### *5.5.2 Convective Flow Mode Degradation and Kinetics Study Using Pd-Fe-PAA-PVDF Membranes*

To understand the kinetics of PCB dechlorination in a convective flow mode, Pd-Fe particles are regarded to be uniformly distributed in the assumed cylindrical pores inside the membrane. A laminar flow reactor (LFR) model could be perceived in this cylindrical pore due to the small Reynolds number (Re << 1) [182-183]. For laminar flow in each cylindrical pore, the flow profile is described by **equation 5.2** [182]:

$$u(r) = 2u_0\left(1 - \frac{r}{R}\right)^2 \ldots\ldots\ldots\ldots\ldots\ldots \mathbf{EQ\ (5.2)}$$

Where, $R$ is the pore size of the functionalized membrane. $u_0$ and $u(r)$ are the velocities at center and radius r, respectively.

Due to the large Peclet number ($10^2$~$10^3$) in this study, the mass diffusion term can be neglected from the general convection-diffusion equation. In addition, $u(r)$ is only related to pore radius. The convective-diffusion equation (at steady state) can be simplified and integrated as a function of pore axial distance shown in **equation 5.3**:

$$C(r,z) = C(r,0)\exp\left[-\frac{\mathrm{K_{obs}}z}{u(r)}\right] \ldots\ldots\ldots\ldots\ldots\ldots \mathbf{EQ\ (5.3)}$$

A cross-section averaging method was used to integrate the concentration over the radial dimension to obtain the mean concentration $\bar{C}$ at certain axial distance z [182-183]. The mean outlet concentration $\bar{C}_{final}$ (z = membrane thickness) can be calculated using **equation 5.4** [182]:

$$\bar{C}_{final} = \frac{\int_0^r C(r,z)u(r)2\pi r dr}{\int_0^r u(r)2\pi r dr} \ldots\ldots\ldots\ldots\ldots\ldots \mathbf{EQ\ (5.4)}$$

This equation can be used to fit $\mathrm{K_{obs}}$ values from experimental reaction data ($\tau, \bar{C}_{initial}, \bar{C}_{final}$). Matlab was used to find the most fitted $\mathrm{K_{obs}}$. The Pd-Fe-PAA-PVDF membrane used in convective flow dechlorination was with maximum amount of Fe loading (12.4 mg/13.2 $cm^2$ membrane surface area). The permeability during degradation study for this membrane was found around 1.33 LMH/bar. The residence time ($\tau$) was varied by changing applied cell pressure from 8.16~11.56 bar. For residence times of 5.15

s, 11.2 s, 27.17 s and 46.2 s, the corresponding dechlorination percentages of PCB 126 were found to be 84%, 93%, 98% and 98.6%, respectively as shown in **Figure 5.14**. In this experiment, we also ran a PCB 126 solution through a Fe-PAA-PVDF membrane as a control so as to detect any possible interference of nZVI. The fitted $K_{obs}$ value was found to be 0.452 $s^{-1}$. If the membrane is considered a plug flow reactor (PFR) the corresponding $K_{obs}$ is found to be 0.09 $s^{-1}$. However, if the membrane is assumed to be a continuous stirred-tank reactor (CSTR) the $K_{obs}$ is obtained to be 1.38 $s^{-1}$. The calculated $K_{sa}$ ($L \cdot m^{-2} \cdot hr^{-1}$) for convective flow mode degradation in membrane platform was calculated from $K_{obs}$ (0.452 $s^{-1}$) data. The value of $K_{sa}$ is 0.113 $L \cdot m^{-2} \cdot hr^{-1}$ which is 2.1 times higher than $K_{sa}$ of batch degradation results, suggesting degradation of PCB 126 in a convective flow mode eliminates the effect of diffusion resistance. Here comparing the $K_{sa}$ values for both batch and convective flow mode degradation is just to confirm membrane-based platform for degradation of chloro-organics is much suitable, fast and less energy intensive. The experimental condition for both cases is different. In batch study, a fixed volume of PCB-126 is exposed to chopped off membrane pieces. Continuous shaking is required to diffuse the PCB-126 through the membrane as most of the NPs are in the pores. While, in convection flow mode, PCB-126 passes through the membrane very fast due to applied pressure. It only allows very small amount of PCB-126 to pass through the membrane. This volume is equivalent of the void volume of the membrane. So, in large the experimental conditions are different. In this regard, surface-area normalized rate constant, $K_{sa}$ brings a unique platform to compare the degradation results of batch and convective flow mode study.

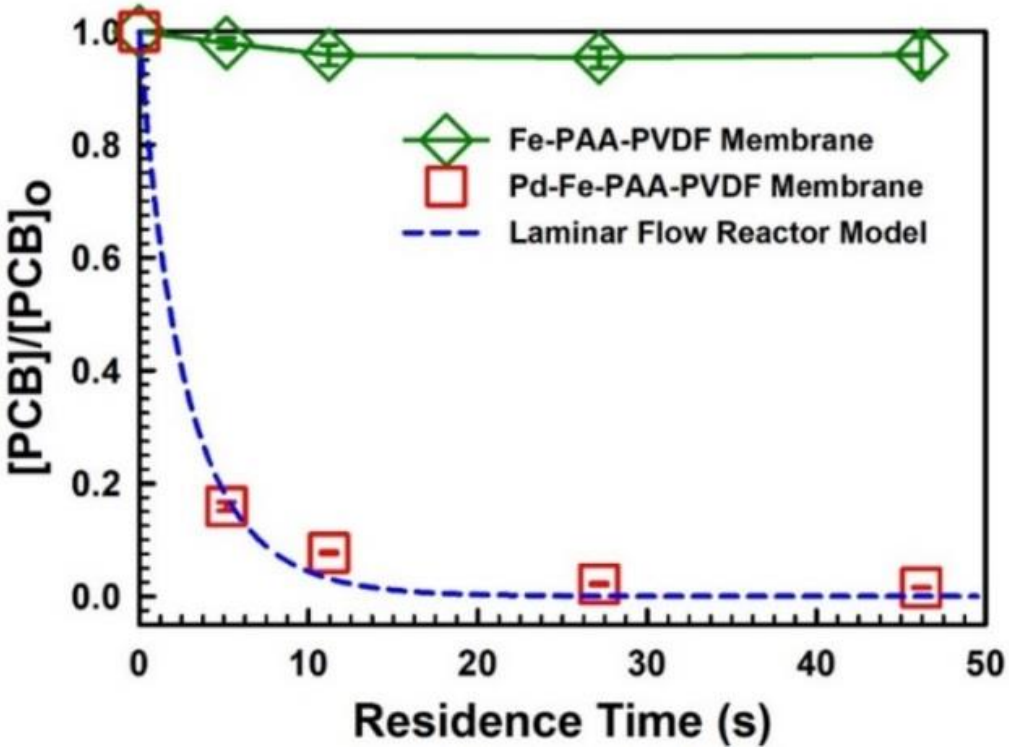


**Figure 5.14** Convective flow study of PCB 126 degradation by Pd-Fe-PAA-PVDF membranes. Fe-PAA-PVDF membrane served as blank control. Laminar flow reactor model was used for experimental data fitting (dashed blue line). Here, M = 20 wt.%, X = 1 mol%, $[PCB]_o$ ~15 μM, Fe Loading = 12.4 mg/13.2 $cm^2$ of membrane surface area, [Pd] ~1 wt.% of Fe, pH = 5.6~5.7, T = 22~24°C.

# CHAPTER 6. LAYER-BY-LAYER ASSEMBLED LACCASE ENZYME OF STIMULI-RESPONSIVE PVDF MEMBRANES FOR CHLORO-ORGANICS DEGRADATION

## 6.1 Overview

This chapter discusses the versality of PVDF functionalized membranes as a platform for incorporation of bio-catalysts and nanostructured materials for efficient and benign environmental remediation. The existing techniques for remediating chloro-organics in water consist of both physical and chemical means mostly using metal oxide-based catalysts, despite associated environmental concerns. To offer bioinspired remediation as an alternative, we herein demonstrate a layer-by-layer approach to immobilize laccase enzyme into pH-responsive functionalized membranes for degradation of chloro-organics from water. Efficacy of these bioinspired membranes towards dechlorination of 2,4,6-trichlorophenol (TCP) is demonstrated under pressure driven continuous flow mode (convective flow) for the first time to the best of our knowledge. Over 80% of the initial TCP was degraded at optimum flow rate under an applied air pressure of about 0.7 bar or lower. This corresponds to degrading a substantial amount of the initial substrate in only 36 seconds residence time, which in a batch reaction take hours. This, in fact, demonstrates an energy efficient flow through system with potential large-scale applications. Comparison of the stability of the enzyme in solution phase vs. immobilized on membrane phase showed a loss of some 65% of enzyme activity in the solution phase after 22 days, whereas the membrane-bound enzyme lost only a negligible percentage of activity in comparable time span. Finally, the membrane was exposed to rigorous cycles of TCP degradation trials to study its reusability. The primary results reveal a loss of only 14% of the initial activity after four cycles of use in a period of 25 days, demonstrating its potential to reuse. Regeneration of the functionalized membrane was also validated by dislodging the immobilized enzyme followed by immobilization of fresh enzyme on to the membrane. Sections 6.2 to 6.5 are **published** in **Sarma, Islam et al. (2017)**.

## 6.2 Characterization of Laccase Immobilized Membrane

The laccase functionalized membranes were characterized by ATR FT-IR, SEM, contact angle measurement, surface zeta potential measurement and XPS analysis to assess the successful incorporation of enzyme in PAA-PVDF membrane.

### *6.2.1 ATR FT-IR Spectral Analysis*

ATR FT-IR spectra of PVDF and functionalized PVDF membranes attest to successful fabrication of the membranes. **Figure 6.1** compares a PVDF membrane as supplied, a PAA-PAH functionalized PVDF membrane, and a laccase-functionalized PVDF membrane. The absorption peaks characteristic of fluorocarbon groups ($-CF_2-$)of the PVDF chains lie in the region of 1050 – 1280 $cm^{-1}$, as expected, for all the membranes (the PVDF, the PAA-PAH functionalized PVDF and, the laccase-functionalized PVDF) [163]. Successful polymerization of PAA in the membrane matrix is revealed by the appearance of new peaks at 1717 $cm^{-1}$ and 1544 $cm^{-1}$ (**Figure 6.1**, black line) corresponding to the carbonyl stretch and antisymmetric stretching of carboxyl groups (− COOH), respectively, of the polyacrylic acid polymer.[164] The FT-IR spectrum of free laccase is known to include two absorption bands, near 1645 $cm^{-1}$ and 1540 $cm^{-1}$ corresponding to the peptide backbone amide I and amide II modes, respectively [184].Recorded spectra for laccase-functionalized PVDF membranes showed similar peaks (**Figure 6.1**, blue line). The peak at 1642 $cm^{-1}$ was due to the stretching vibration of the C=O amide bond and the 1545 $cm^{-1}$ peak was assigned to the combination of bending vibration of the N-H bond and stretching vibration of the C-N bond of the peptide backbone, signifying immobilization of laccase on the membrane support [72]. Moreover, the presence of more peaks (convolution of protein (-NH's), protein (-OH's) and water) features in the range 3500-3300 $cm^{-1}$ suggests the presence of the amine groups belonging to the protein.

### *6.2.2 SEM Imaging of Laccase Functionalized Membranes*

The morphologies of the PVDF and PAA functionalized PVDF membranes were characterized by Scanning Electron Microscopy (SEM) as shown in **Figure 6.2**. The bare PVDF membrane (**Figure 6.2a**) shows a fairly porous structure with an average pore size of 192 ± 50 nm. The diameter and morphology of the membrane pores changed substantially after the PAA polymerization reaction, becoming uniformly circular and

smaller with an average pore size of 112 ± 5 nm (**Figure 6.2b**). These direct observations of pore diameter shrinkage demonstrate that PAA has polymerized into the pores. On successive modification of the membrane by immobilizing PAH and the enzyme the average pore diameter further reduced to 70 ± 12 nm as can be seen in the **Figure 6.2c**.

### *6.2.3 Contact Angle Measurement*

To quantify any change in the hydrophilicity of the membranes, we compared the contact angle of water on functionalized membranes to that on bare PVDF membrane. The contact angle decreased from 80$^{o}$ to 56$^{o}$ indicating that membrane became more hydrophilic upon functionalization with the PAA polymer. This is consistent with the other spectroscopic characterizations of the membranes in indicating successful functionalization. As expected, the contact angles did not change significantly (**Table 6.1**) upon further modification of the membranes by putting in PAH and laccase into the pores.

### *6.2.4 Surface Zeta Potential Analysis*

After polymerization of PAA, the next step in preparing the membranes was to add PAH and laccase. The success of these steps was assessed via comparison of the membrane zeta potentials, as the zeta potential measures the surface charge on the membrane. **Figure 6.3** shows the comparison of pH dependence of the zeta potential for PVDF membranes to that of functionalized PVDF membranes. The PAA-functionalized membrane shows an obvious phase transition near pH 3, which is attributable to the pKa of carboxyl groups in PAA. The surface charge for the PAH immobilized membranes were positive, as expected, due to the presence of the ammonium ions. The isoelectric point of the membranes shifted to ~3.5 after laccase immobilization (redline in **Figure 6.3**). These data are consistent with the literature value of ≈ 3.5 for the pI value of laccase from *Trametes versicolor* [185] suggesting successful immobilization of laccase onto the PAA functionalized PVDF membranes.

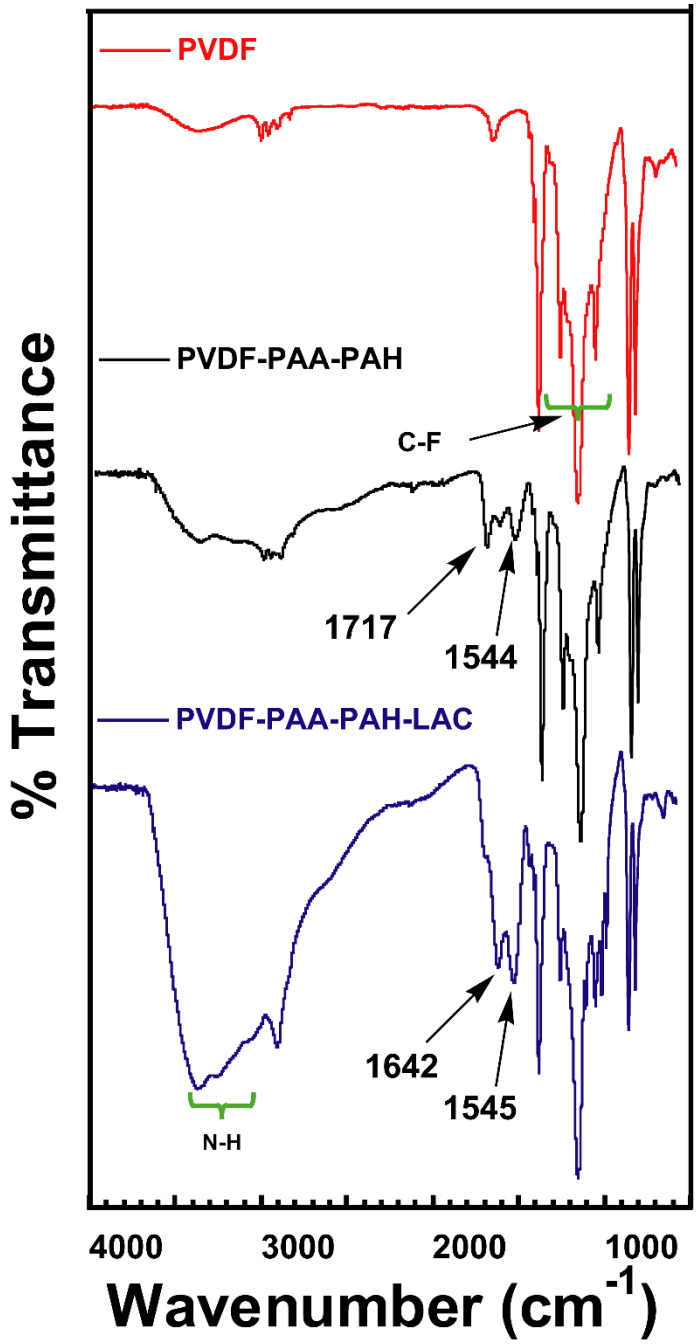


**Figure 6.1** ATR FT-IR spectra of PVDF and laccase-functionalized PVDF-membranes.

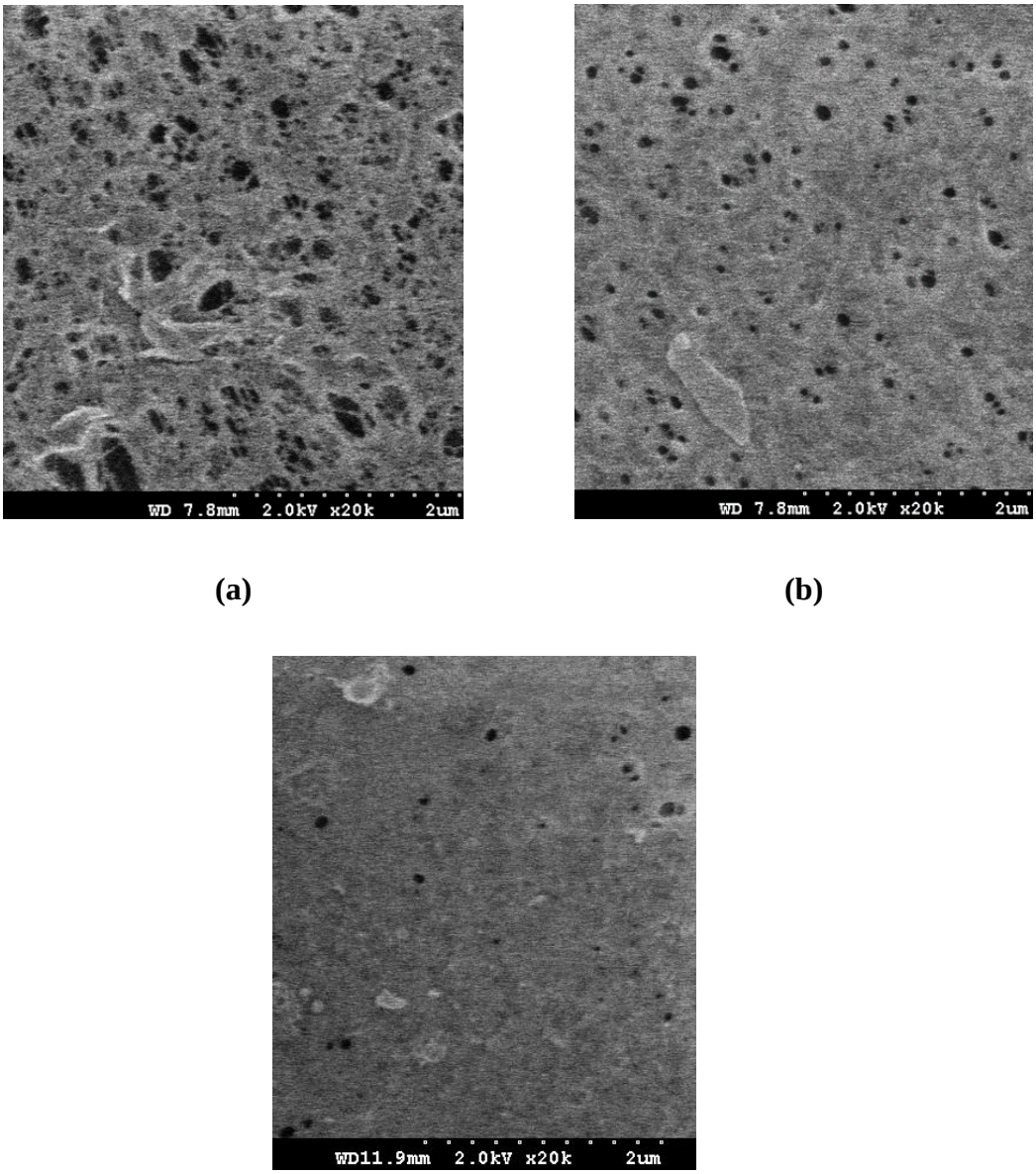


**(a)** **(b)**

**(c)**

**Figure 6.2** Scanning Electron Microscopy (SEM) images of **(a)** bare PVDF membrane, **(b)** PAA functionalized PVDF membrane and **(c)** Laccase Immobilized PVDF membrane.

**Table 6.1** Contact angle measurements for the membranes after each stage of fabrication.

| **Stages of Functionalization of Membrane** | **Contact Angle (º)** |
|---|---|
| Bare PVDF Membrane | 79.96 (±3.86) |
| Functionalized with PAA | 55.90 (±0.06) |
| Functionalized with PAA and PAH | 56.69 (±2.24) |
| After Enzyme Immobilization | 56.10 (±1.08) |

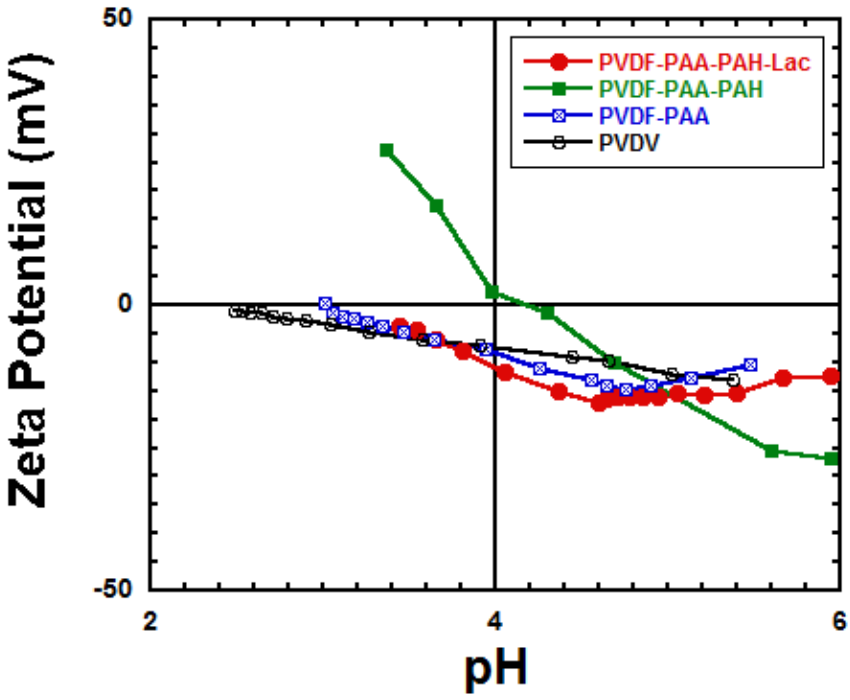


**Figure 6.3** Comparison of the zeta potential as a function of pH for PVDF, PVDF-PAA, PVDF-PAA-PAH and PVDF-PAA-PAH-laccase functionalized membranes.

### *6.2.5 XPS Analysis of Laccase Functionalized Membranes*

The surface compositions of bare PVDF membranes, PAA-functionalized PVDF membranes and laccase immobilized PVDF-PAA membranes were explored by X-ray photoelectron spectroscopy (**Figure 6.4**). Survey spectra of these membranes show that the functionalized PVDF membrane (**Figure 6.4b**) contains significant N and considerably higher C content than the bare PVDF membrane (**Figure 6.4a**). The N content of the functionalized membrane is explained by the cross linker, *N*, *N*'- methylenebisacrylamide (MBA) used during polymerization. Deconvolution of the C1s peak near 290 eV for the functionalized membrane yielded three peaks corresponding to carbon in C-C (285 eV), C-O (287 eV), and the C=O (289 eV) functionalities (**Figure 6.4c**), in addition to a signature of C-F attributed to the PVDF support. Curve-fitting analysis of the XPS spectra for the laccase immobilized PVDF-PAA membranes fit well with the expected bond chemistry found in the enzyme (**Figure 6.4d**). The peak at the largest binding energy at 285 eV can be attributed to the abundant C–C bonds while the shoulder near 286 eV arises due to C–N bonding in the peptide backbone. The peak near 289 eV is a broad peak and can be attributed to both peptide (N-C=O) and the carboxylate (O-C=O) bonds. The signature of C-F bond due to the PVDF support is still visible near 292 eV. These results further substantiate the successful installation of polymerized PAA and laccase into the PVDF membranes [26].

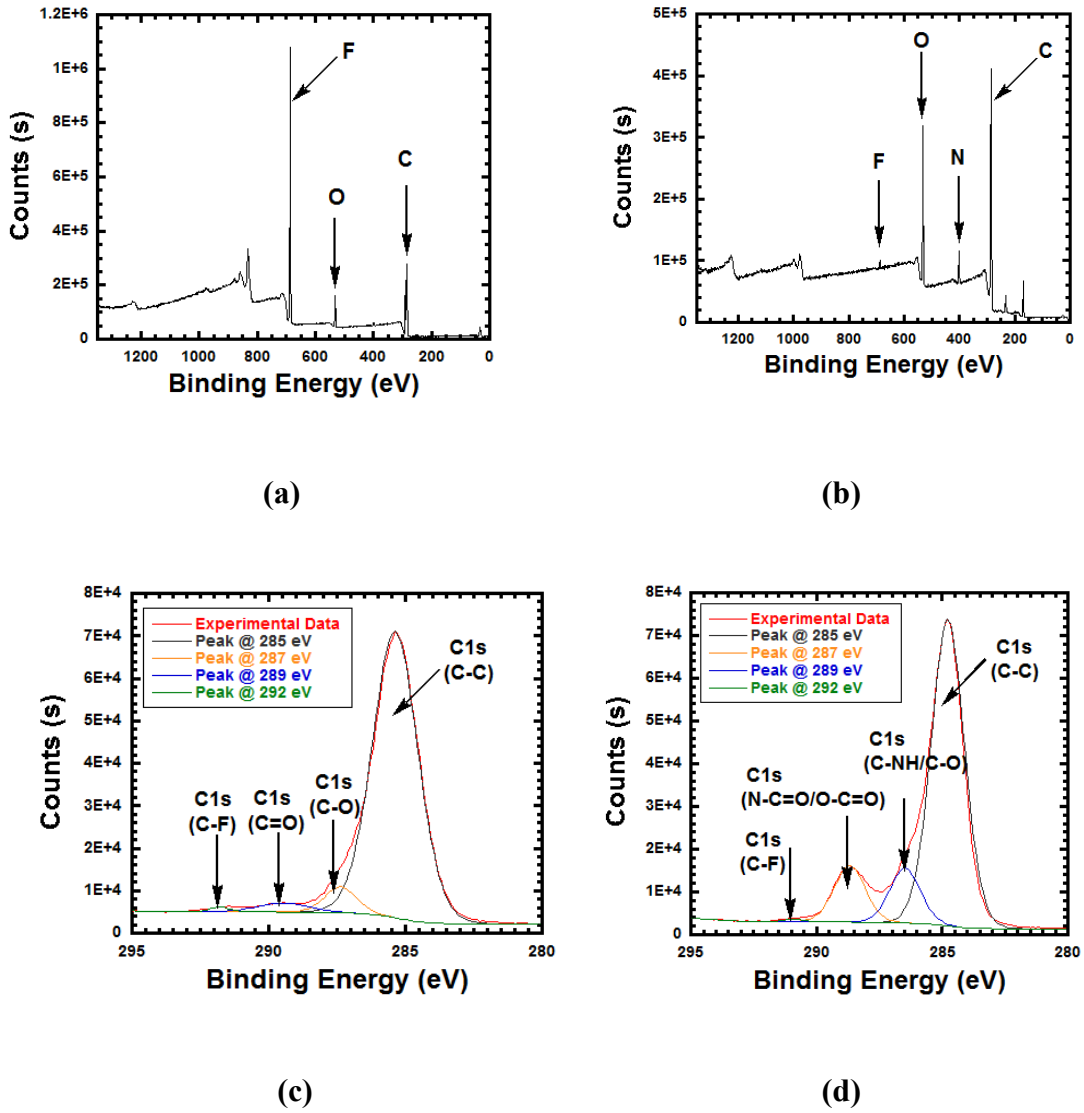


**Figure 6.4** XPS survey spectra of **(a)** bare PVDF membrane, **(b)** PAA functionalized PVDF membrane, XPS C1s core-level spectra of **(c)** PAA functionalized PVDF membrane and, **(d)** laccase immobilized PVDF-PAA membrane.

## 6.3 Catalytic Activity of Free and Immobilized Laccases

The kinetic parameters of enzymatic catalysis $K_M$ (the Michaelis constant) and $k_{cat}$ (the turnover number) for both free and immobilized laccase were determined using ABTS as the model substrate. The $k_{cat}$ reflects the rate of the catalytic steps whereas the $K_M$ signifies the substrate binding efficiency of the enzyme. The **Table 6.2** data demonstrate that the apparent $k_{cat}$ value of immobilized enzyme is comparable to that of the free laccase, indicating that immobilization via the LBL strategy does not impair the catalytic active site. The apparent Michaelis constant, $K_M$, for the immobilized membrane, however, increased nearly six times than the free enzyme. This higher $K_M$ of immobilized laccase than that of free laccase is consistent with restriction of substrate access to the active sites of the immobilized enzymes by slowed diffusion through the polymer matrices combined with repulsion by the polyelectrolytes. Similar observation of elevated $K_M$ values for immobilized systems compared to the free enzyme are reported in the literature, while the $k_{cat}$ values for immobilized systems lies anywhere between comparable to lower depending on the methodology and the success of the immobilization method [186]. This higher $K_M$ for immobilized laccase compared to free laccase, decreased the catalytic efficiency ($k_{cat}/ K_M$) of the enzyme in the functionalized membrane.

**Table 6.2** Michaelis-Menten kinetic parameters $K_M$ and $k_{cat}$ of free and immobilized Laccase.

| **Laccase** | $K_M$ **(μM)** | $k_{cat}$ **($s^{-1}$)** | $k_{cat}/K_M$ **($s^{-1}mM^{-1}$)** |
|---|---|---|---|
| Free | 13.8±1.9 | 21.1±0.7 | 1528.9±217.5 |
| Immobilized | 88±5.3 | 22.7±0.7 | 257.9±17.6 |

## 6.4 Stability of Free and Immobilized Laccases

For industrial application of biocatalysts better storage stability is an essential criteria. Thus, the stabilities of solution phase laccase and membrane-immobilized laccase were examined, both stored at 4 $^{o}$C, and the results are shown in **Figure 6.5**. The laccase immobilized membranes were stored immersed in DIUF water (pH 5.9). Solution phase laccase lost 30% of its initial activity after 3 days and 65% after 22 days of storage. However negligible loss of activity was detected for the membrane-immobilized laccase. These results are consistent with earlier reports on stability of immobilized laccase [185]. Enzymes are subject to damage mainly by other enzymes, chemicals, and extremes of pH and temperature. Unlike in the solution state, immobilization imparts extra stability to the enzyme as it prohibits the individual enzyme molecules from interacting with each other. In another words, the unfolding movements of the enzymes are restricted thereby inhibiting subsequent aggregation processes under these conditions [187]. Furthermore, as the immobilized membranes were stored immersed in DIUF water there is little chance of contamination with other chemicals. One more interesting advantage of the immobilization in membrane is that, the immobilized enzymes are inaccessible to bacteria due to the small size of the pores and hence to other enzymes that those bacteria might produce. Lastly, the storing pH is near neutral, so there are no concerns over the denaturation of the protein during storage. These factors combined to contribute towards the higher stability of the membrane immobilized enzyme compared to the solution phase.

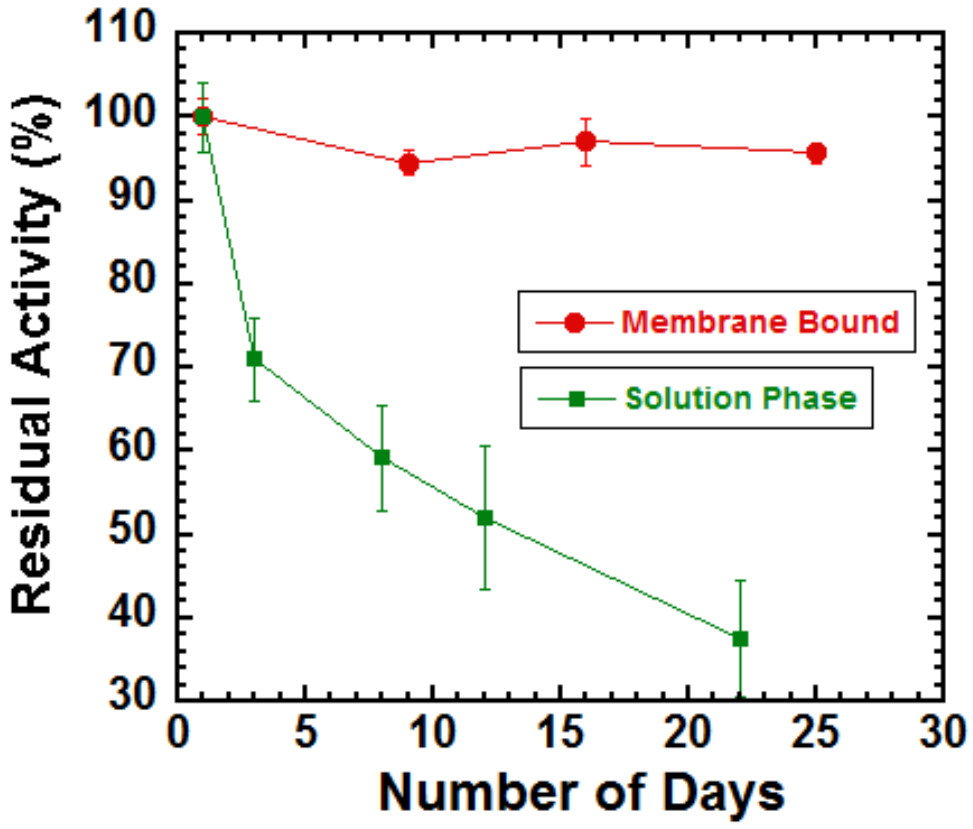


**Figure 6.5** Comparison of storage stability of solution phase and membrane-immobilized laccase stored at 4 °C (DIUF water, pH 5.9).

## 6.5 Degradation and Removal of TCP by Laccase Immobilized Membranes

In order to demonstrate the applicability of the laccase-functionalized membrane towards remediation of contaminated water, an aqueous solution of TCP was passed through the membrane under positive pressure of air from a gas tank. It should be noted here that laccase uses oxygen as the electron accepting secondary substrate during the oxidation of the primary substrate. Thus, the air flow from the air gas tank serves dual purpose; **(i)** ensures continuous oxygen atmosphere and **(ii)** maintains necessary positive pressure for controlling the flow rate. Initially the permeate was analyzed by UV-Visible spectroscopy to check the changes in the absorption behavior of TCP to confirm its conversion to metabolic products. TCP absorbed in a wide range from 280-300 nm (absorption maxima at ~295 nm) with two soldiers around 230 nm and 310 nm (**Figure 6.6**). The permeate (light pink in color), however, absorbed at significantly different wavelength with a peak maxima at 277 nm, presumably attributable to the formation of dichloro-1,4-benzoquinone [188],which clearly demonstrates the metabolism of the TCP molecules. A closure look at the spectra in the visible region displayed another broad peak near 525 nm which can be attributed to the formation of 2,6-dichloro-3-hydroxy-1,4-benzoquinone [188]. HPLC analysis along with the UV-vis spectra of the permeate solutions revealed diminution of the TCP content and new presence of various oxidation products of TCP (**Figure 6.7**). Similar observations were made by Hu et al. in their study of degradation of TCP with the formation of various oxidation products along with a pink coloration[188]. LC-MS analysis demonstrated that the peak recorded at about 8 minutes corresponds to dichloro-1,4-benzoquinone, the major degraded product of TCP (**Figure 6.8**).That the reaction corresponds to dechlorination was further confirmed by detection of approximately 1 mol chloride/mol TCP degraded, as determined using a chloride sensing electrode (**Figure 6.9**). Control experiments were performed to check the presence of enzyme leached with the permeate during the degradation of TCP. We neither saw significant amount of enzyme by Bradford assay (**Figure 6.10**) nor saw significant enzyme activity towards ABTS (0.2 mM, pH 5.8) in the aliquots from the permeate. It should be noted that had the enzyme been leached out from the membrane (and the degradation of TCP had been due to the released laccase in the permeate), there would have been a gradual change in the concentration of the TCP in the collected permeate samples over time.

However, the amount of TCP and the chloride concentration in the permeate collected did not change with time (within ~24 hours) confirming no significant leaching of enzyme with the permeate.

Under HPLC conditions, TCP had a retention time of 11 minutes (**Figure 6.7**) and this peak was used to quantify the amount of TCP degraded as a function of different flow rates (**Figure 6.11**). The data indicated that more than 80% of the TCP could be degraded at flow rate of 2 LMH under applied pressure of 0.7 bar or lower. This data showing remarkable degradation at a considerably low applied pressure, suggests an encouraging energy efficient flow through system with potential implementation beyond lab scale. The inset in **Figure 6.11** shows the extent of TCP degradation as a function of residence time. It should be noted here that residence time is the average length of time during which a substrate is travelling through the pores and is different than a clock time. Residence time was calculated based on the permeability of the membranes. A high residence time indicates a lower flow rate which corresponds to lower applied pressure. The data in **Figure 6.11** demonstrate the advantage of flow through system over a batch reaction, degrading as high as 83% of the initial substrate in only 36 seconds residence time, which in a batch reaction takes hours. **Table 6.3** summarizes several recent reports on both solution phase and immobilized laccase with applications mainly towards degradation of organic pollutants in waste water [189-197].These reports, including this current study, agree on moderately good activity of the immobilized laccase to support its potential application in the wastewater management system. Despite the substantial amount of research on laccase immobilized systems the practical applicability of this versatile enzyme is still limited mainly due to stability issues and resistance towards harsh pH and chemicals. Use of membrane as the support material might be an answer to such issues as undesired chemicals can be restricted from coming into contact with the enzyme and secondly any destructive by product formed during the degradation can be washed away instantly.

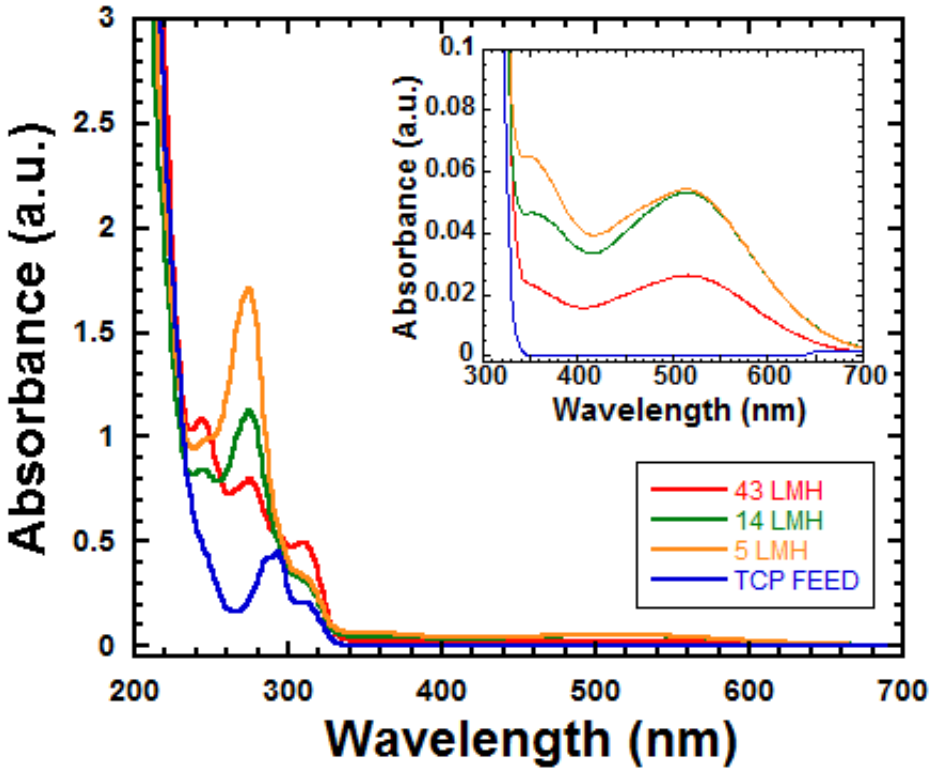


**Figure 6.6** Degradation of TCP with of PVDF-PAA-PAH-Laccase in a flow through experiment as studied by UV-Vis Spectroscopy. Inset showed the formation of visible color band. Experiments were performed at a temperature of 22 °C and a pH of 5.6 (In the legend 'LMH' refers to the unit of flux L/m$^2$-hr and is used to designate samples collected at different flux).

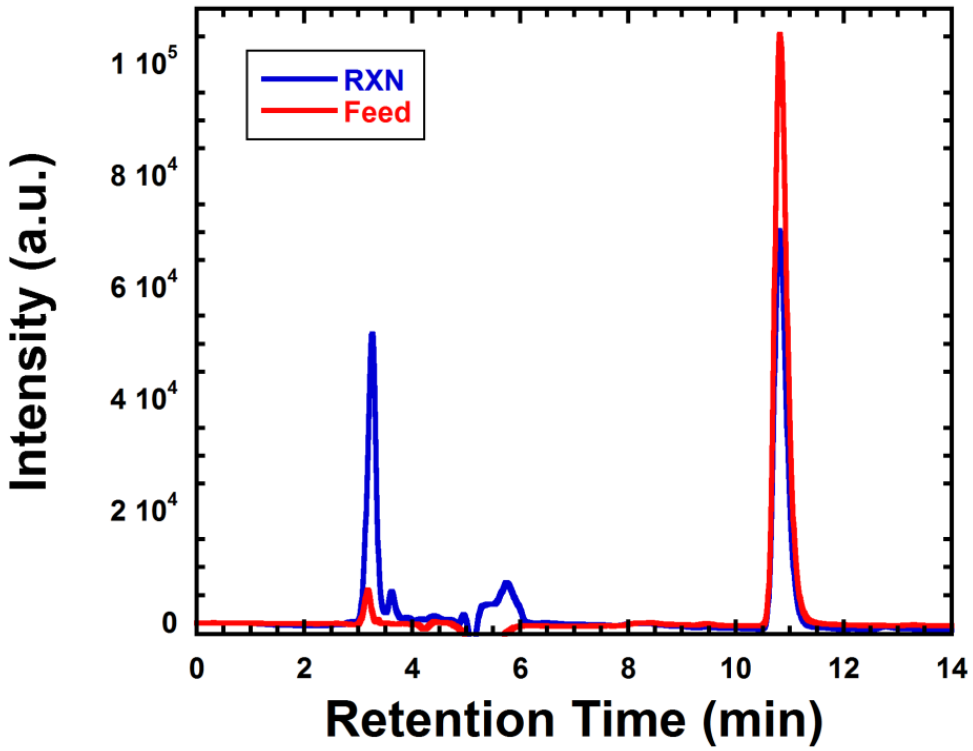


**Figure 6.7** Degradation of TCP (initial TCP Concentration 0.25 mM) with PVDF-PAA-PAH-Laccase membrane in a flow through experiment as studied by HPLC (In the legend the samples from reaction is abbreviated as 'RXN').

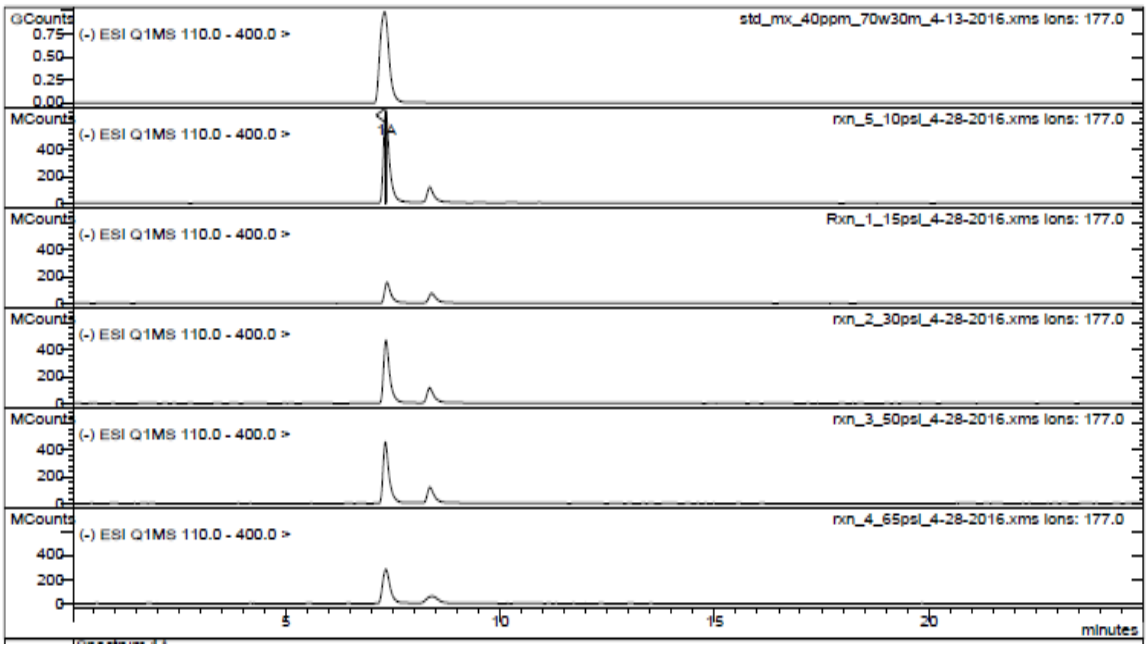


**Figure 6.8** Chromatogram from LC-MS to show formation of dichloro-1,4-benzoquinone (M+H = 177) from degradation of TCP.

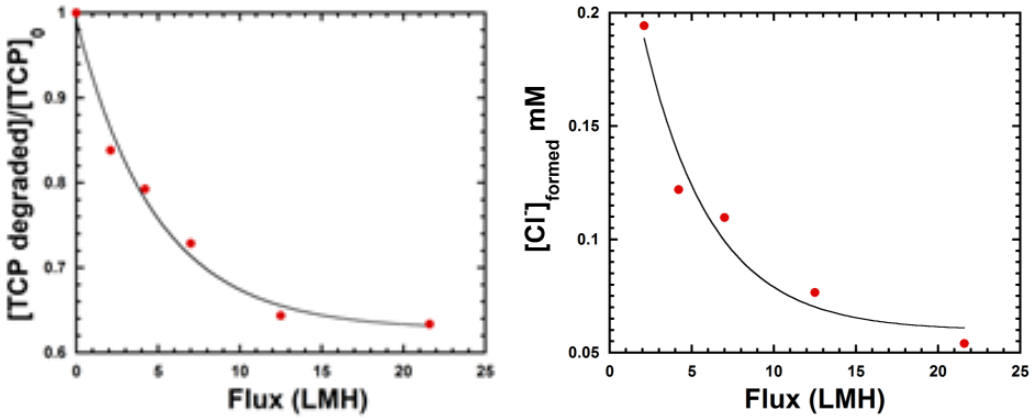


**(a)** **(b)**

**Figure 6.9 (a)** Degradation of TCP (initial TCP Concentration 0.25 mM), **(b)** chloride ions formed from degradation of TCP as a function of varied flow rate in a flow through experiment. Experiments were performed at a temperature of 22 °C and a pH of 5.6.

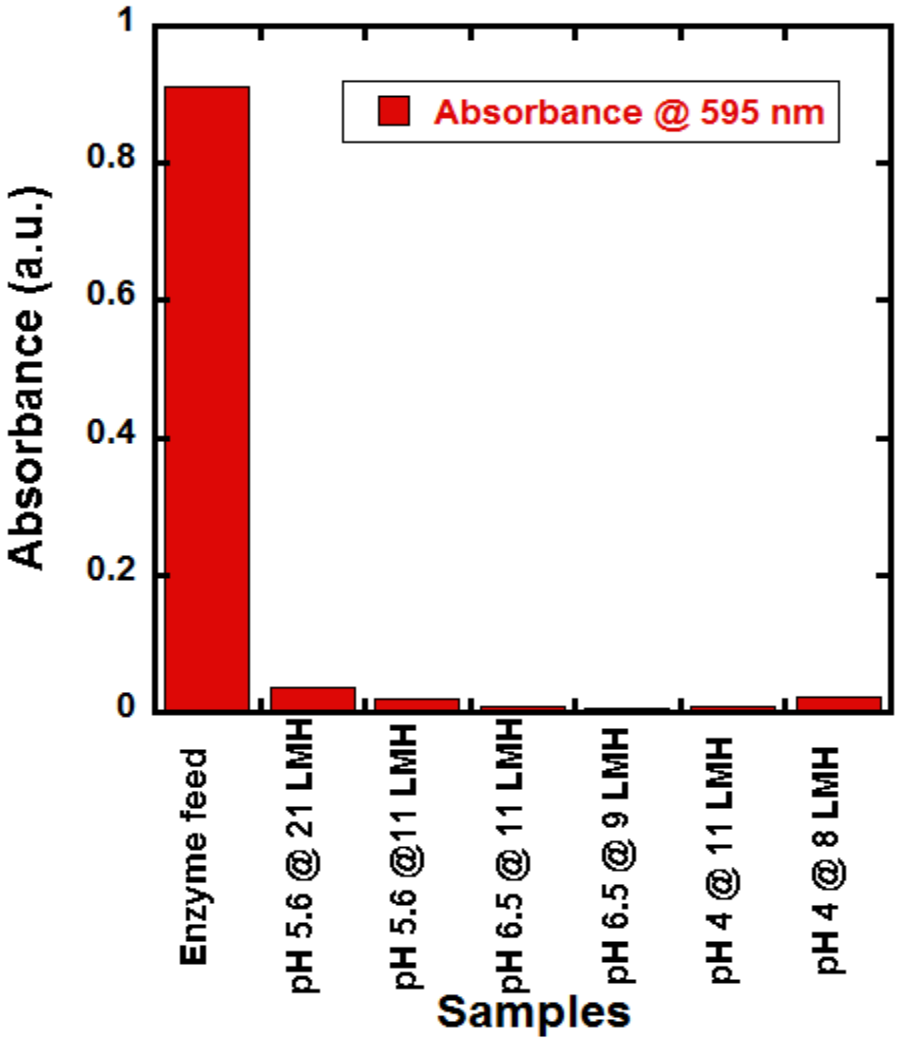


**Figure 6.10** Leaching of enzyme from immobilized membrane during TCP degradation studies at three different pH, as analyzed by Bradford assay.

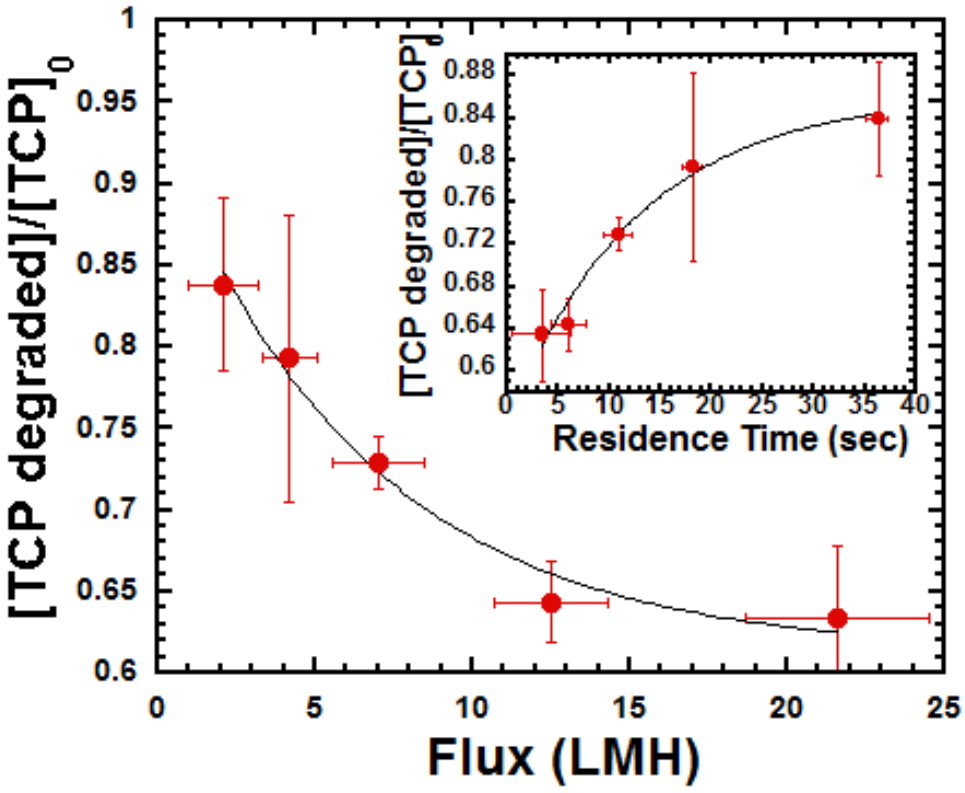


**Figure 6.11** Degradation of TCP by laccase-functionalized membrane as a function of flow rate 3.2 mg enzyme.

**Table 6.3** Several recent reports on laccase immobilization and their performance.

| Support | Application | pH | Degradation Performance (%) | Reference |
|---|---|---|---|---|
| Solution phase | Chlorophenol degradation | 6 | 82.1 | Reference [189] |
| Solution phase | Chlorophenol degradation | 5.6 | 83 | This work |
| Wheat grains | Chlorophenol degradation | 4.5 | 52.1 | Reference [190] |
| Silica | Chlorophenol degradation | 5 | 86.9 | Reference [191] |
| Polyacrylonitrile Nanofibrous Membrane | Chlorophenol degradation | 4.5 | 87 | Reference [72] |
| Oxidized Bacterial cellulose – $TiO_2$ | Dye degradation | 5-6 | 80 | Reference [193] |
| MWCNTs modified LCEFMs | Bisphenol A | 4-7 | 80 | Reference [192] |
| Chitosan/$CeO_2$ micros pheres | Dye degradation | 5.4 | 83.3-92.6 | Reference [194] |
| Mesoporous silica-modified electrospun | Dye degradation | - | 88 | Reference[196] |
| Carbon-based mesoporous magnetic composites | Phenol and chlorophenol degradation | 6 | 78-84 | Reference [195] |
| Magnetic $Cu^{2+}$-chelated silica support | Chlorophenol degradation | 5 | 82.9 | Reference [197] |
| PVDF Membrane | Chlorophenol degradation | 5.6 | 60-83 | This study |

### *6.5.1 Effect of Different Amount of Laccase Enzyme Loading*

In order to demonstrate the degradation activity of the membranes with variable loading of enzyme, a series of membranes with three different enzyme loading, viz. 3.2, 3.8, and 9.7 mg, were tested for its ability to degrade TCP. Normally as enzyme loading is tripled, one expects the conversion to go up by about 1.5 times if all the active sites can be accessed. **Figure 6.12** shows the conversion did increase substantially (about 1.45 times) as the enzyme loading is tripled for a fixed residence time of 12 s. **Figure 6.13** demonstrates degradation of TCP as a function of time as different enzyme concentration. **Figure 6.14** shows the overall effect of the enzyme loading on TCP conversion. This does indicate the impact of active sites crowding in the LBL membrane domain with high enzyme loading.

### *6.5.2 Reusability of Laccase Incorporated Membranes*

The reusability of the enzyme-functionalized membrane as assessed as retention of capacity to catalyze degradation of TCP under convective flow mode is shown in **Figure 6.15**. As evident from the figure, after 4 cycles of operation our enzyme-functionalized membrane displayed a loss of only 14%, of its initial activity, despite the duration of use of 25 days. As noted earlier, degradation of TCP leads to the formation of various oxidation products, some of which gets absorbed into the polymer matrix over time even after rigorous washing of the membranes. This limits the accessibility of the substrate TCP to the enzyme active site portraying a lower activity of the membrane during subsequent uses. As we do not see leaching of enzyme during the degradation studies some deactivation of the immobilized enzyme by the oxidized products seems to be a possible explanation of the loss of activity after repetitive use. We have also checked the reusability of the laccase functionalized membranes by regenerating the membranes by detaching the used laccase followed by immobilizing fresh laccase enzyme. The dislodging was achieved by permeating a 0.5 M NaCl solution (pH 7) through the membrane under pressure driven flow and then the fresh laccase was immobilized as mentioned before. ABTS activity assay of the dislodged membrane showed lowering of activity signifying detachment of approximately 85% of the immobilized laccase. The regenerated membrane after re-immobilization of fresh laccase enzyme showed comparable activity to freshly prepared membrane as confirmed by the ABTS activity study. The detachment - reimmobilization steps were repeated to obtain consistent results. This study demonstrates the reusability of

the PAA-PAH functionalized membrane domain for laccase enzyme immobilization through LBL approach, which is significantly advantageous over covalent modification technique.

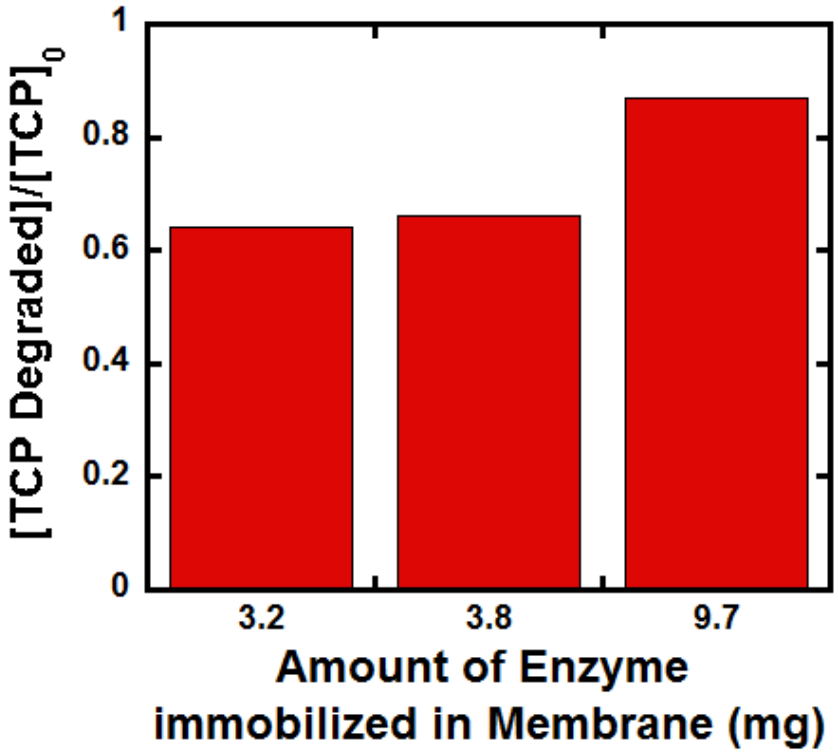


**Figure 6.12** Degradation of TCP as a function of enzyme loading onto the laccase-functionalized membranes for a residence time of 12 s.

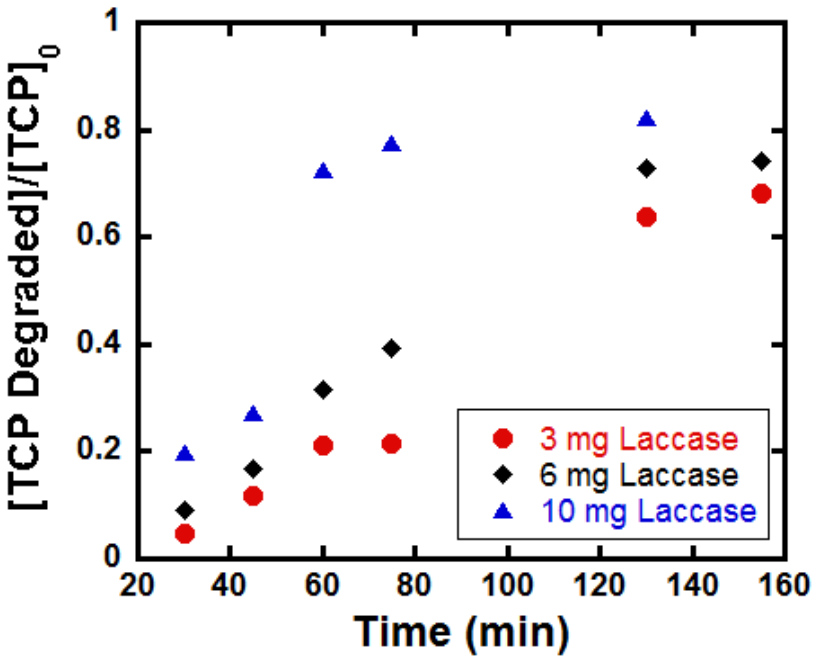


**Figure 6.13** Degradation of TCP (initial TCP Concentration 0.25 mM) as a function of time at different enzyme concentration. Experiments were performed at a temperature of 22 °C and a pH of 5.6.

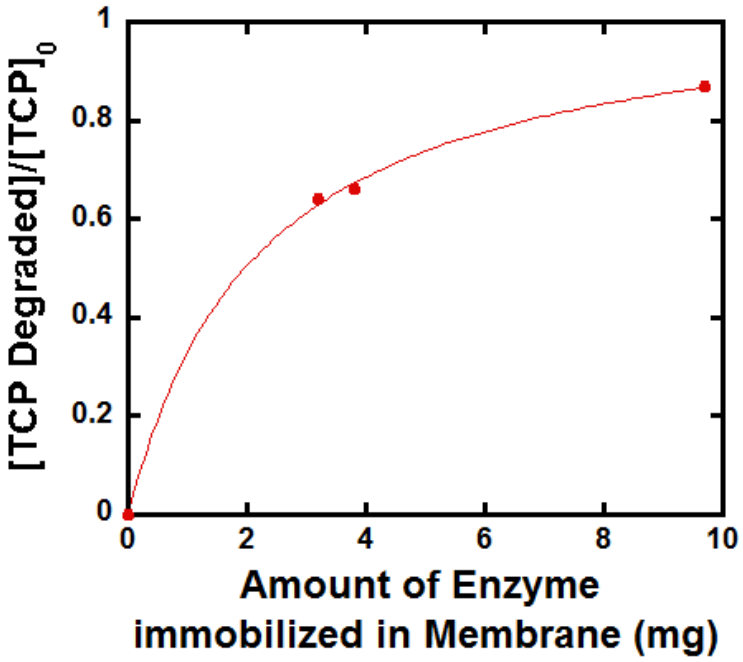


**Figure 6.14** Degradation of TCP (initial TCP Concentration 0.25 mM) as a function of different enzyme loading. Experiments were performed at a temperature of 22 °C and a pH of 5.6.

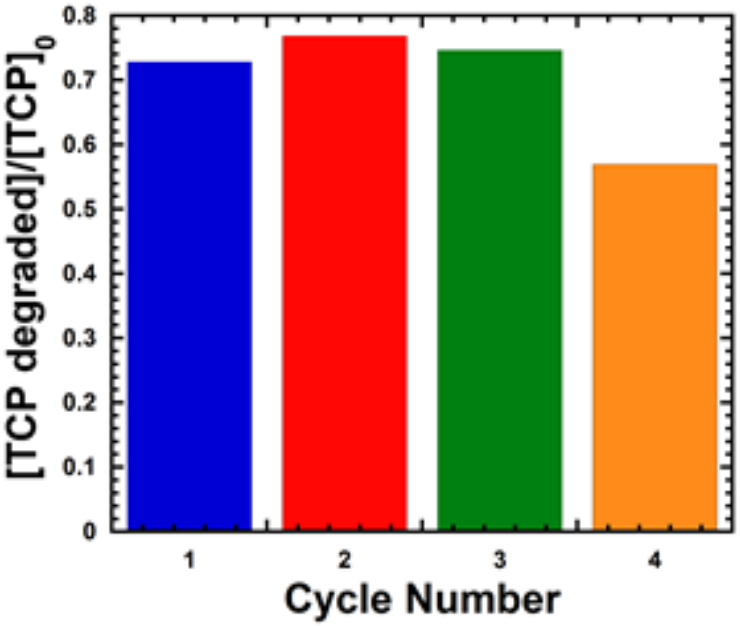


**Figure 6.15** Reusability of the laccase-functionalized membrane for residence time of 12 s. Experiments were performed at a temperature of 22 °C and a pH of 5.6. The initial substrate concentration was 250 µM.

# CHAPTER 7. MULTIENZYME IMMOBILIZED PVDF MEMBRANE REACTOR FOR THE TRANSFORMATION OF A LIGNIN MODEL COMPOUND

## 7.1 Overview

This chapter covers the development a multienzyme functionalized membrane reactor for bioconversion of lignin model compound involving enzymatic catalysis. Layer-by-layer approach was used to immobilize three different enzymes (glucose oxidase, peroxidase and laccase) into pH-responsive membranes. This novel membrane reactor couples the in-situ generation of hydrogen peroxide (by glucose oxidase) to oxidative conversion of a lignin model compound, guaiacylglycerol-B-guaiacylether (GGE). Preliminary investigation of the efficacy of these functional membranes towards GGE degradation is demonstrated under convective flow mode. Over 90% of the initial feed could be degraded with the multienzyme immobilized membranes at a residence time of approximately 22 seconds. GGE conversion product analysis revealed formation of oligomeric oxidation products with peroxidase, which might be potential hazard to membrane bioreactors. These oxidation products could be further degraded by laccase enzymes in the multienzymatic membranes explaining the potential of multienzyme membrane reactors. The multienzyme incorporated membrane reactors were active for about a month time of storage at 4 $^{o}$C, and retention of activity was demonstrated after repetitive use. Sections 7.2 to 7.5 are **published** in **Sarma, Islam et al. (2018)**.

## 7.2 Solution Phase Activity Measurement of the Enzymes

The initial activity of the laccase and HRP enzymes were measured in the solution state prior to immobilization with the conventional colorimetric assay in the presence of 2,2´-azinobis(3-ethylbenzothiazoline-6-sulfonic acid)-diammonium salt (ABTS). **Figure 7.1** shows solution phase activity of laccase and HRP enzymes used for immobilization It should be noted here that presence of multiple enzyme in the membrane makes it difficult to measure the activity assay of the immobilized enzymes. However, the loading of the enzyme into the membrane matrix was confirmed by the Bradford protein assay of the enzyme feed and the permeate during enzyme immobilization. In general, 35-60% of each enzyme could be loaded on the membranes.

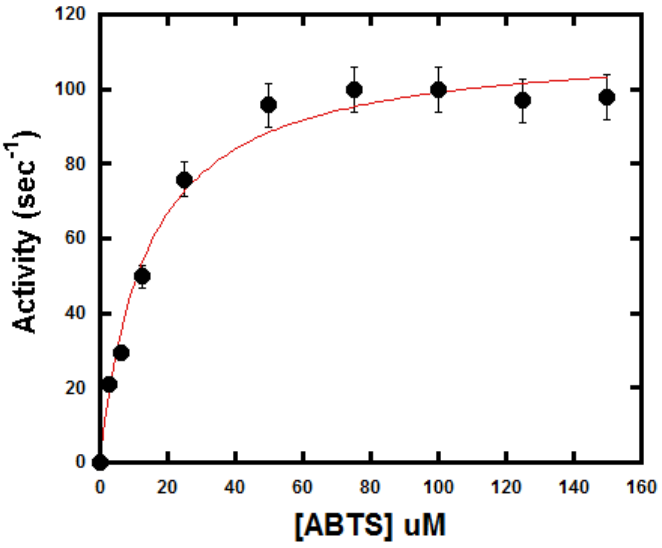


**(a)**

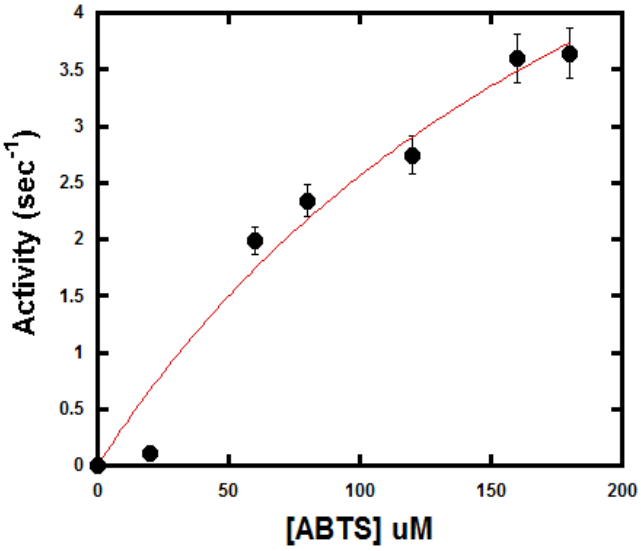


**(b)**

**Figure 7.1** Solution phase activity of **(a)** laccase and, **(b)** HRP used for immobilization.

## 7.3 Reactivity of the Membrane Bioreactors Towards GGE Degradation

The applicability of the enzyme-functionalized membrane towards degradation of lignin model compound was demonstrated by passing an aqueous solution of GGE through the membrane in a dead-end cell. The multienzyme immobilized membranes had three enzymes on it (Lac, HRP and GO) to be able to work as bioreactor. It should be noted here that laccase uses oxygen whereas the enzyme HRP uses hydrogen peroxide as the electron accepting secondary substrate during the oxidation of the primary substrate. A continuous oxygen atmosphere for the laccase enzyme was maintained by air flow from the air gas tank, which also maintains necessary positive pressure for controlling the flow rate. During the experiments the necessary concentration of hydrogen peroxide was maintained by adding glucose into the feed which on reaction with GO produces hydrogen peroxide in situ. HPLC and LC-MS analysis of the permeate solutions was used to monitor diminution of the GGE content and to detect presence of various oxidation products of GGE as shown in **Figure 7.2**. The **Figure 7.3** portrays the degradation of GGE by enzymatic membranes as function of different flow rates. The data in **Figure 7.3** are from Lac-HRP-GO membrane (Feed 3.1 mM GGE) in the presence (blue diamonds) or absence (red circles) of glucose (3 mM) in the feed. The approximate amount of enzymes on the membrane used in this experiment were laccase 5.6 mg, peroxidase 5.3 mg and glucose oxidase 3.9 mg. The data indicated that with glucose in the feed close to 95 % of the GGE could be degraded at a flow rate of 15 liter$\cdot m^{-2} \cdot hr^{-1}$ (LMH) under applied pressure of around 4 bars. At such a slow flow rate (high residence time, 22 sec, **Figure 7.4**) comparable degradation could be achieved without glucose in solution (~85 %, 17 sec residence time). Comparison at a higher flow rate (lower residence time) reveals that the membrane works much better when all the three enzymes work simultaneously. A degradation as high as 90 % was achieved at 64 LMH (5 sec residence time, **Figure 7.4**) with glucose in the feed. In contrast, in the absence of glucose in the feed, the membrane could degrade only 65% of the initial GGE under similar flow rate. The data in **Figure 7.5** is a GGE degradation profile from an independent laccase immobilized membrane. These data closely resemble the data from the multienzyme membrane reactor without glucose in the feed (**Figure 7.3**, red circle) to prove that in the absence of the necessary substrate, hydrogen peroxide, the multienzyme membrane reactor could act as a single enzyme membrane reactor. This demonstrates the

efficacy of the multienzyme membrane towards the degradation of lignin model compounds.

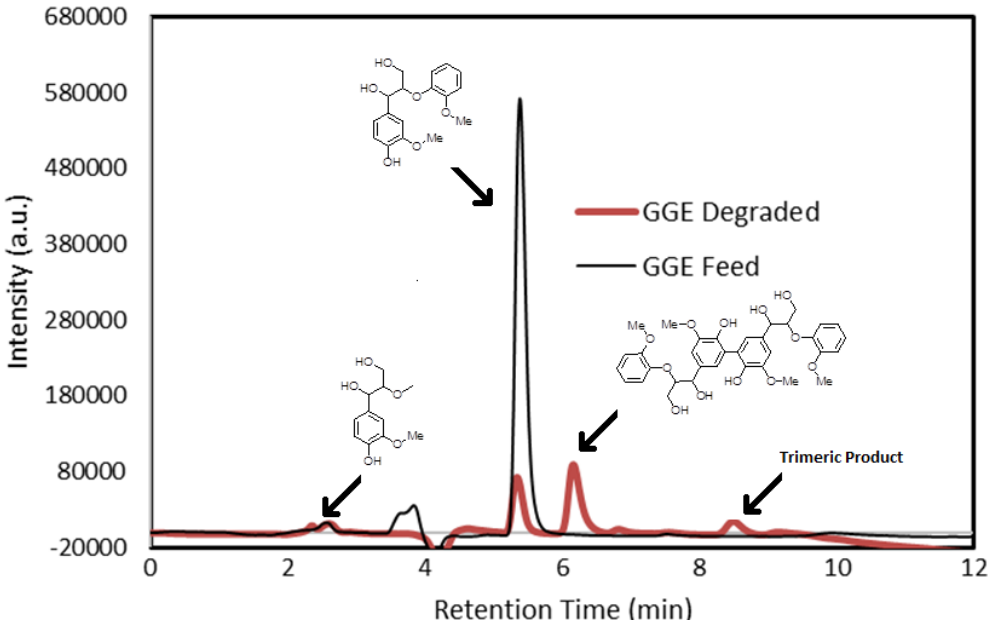


**Figure 7.2** Degradation of GGE (initial GGE Concentration 3.1 mM) with PVDF-PAA-PAH-ENZ membrane in a flow through experiment as studied by HPLC.

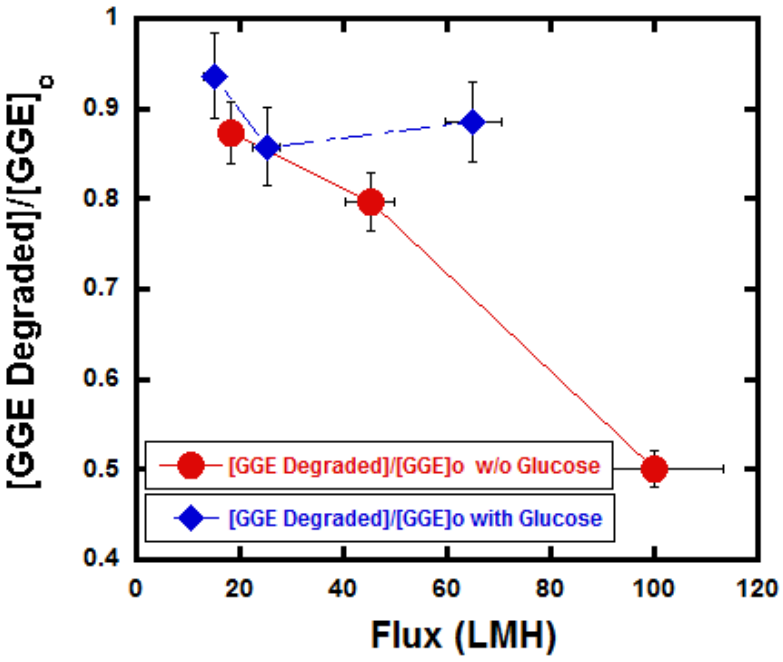


**Figure 7.3** Degradation of GGE by multienzyme-functionalized membrane. Experiments were performed at a temperature of 22 °C and a pH of 5.6. The initial substrate concentration was 3.1 mM GGE in water.

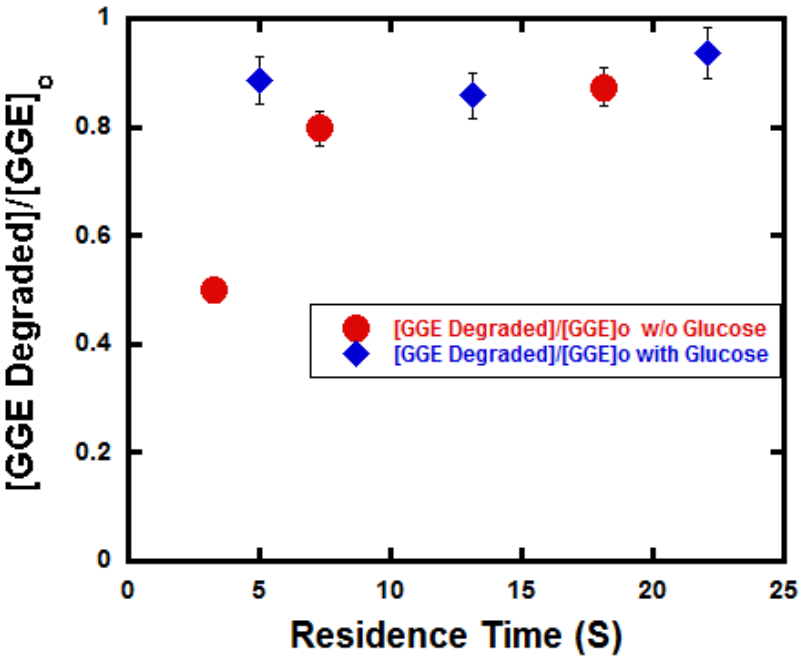


**Figure 7.4** Degradation of GGE as a function of residence time. Experiments were performed at a temperature of 22 °C and a pH of 5.6. The initial substrate concentration was 3.1 mM GGE in water.

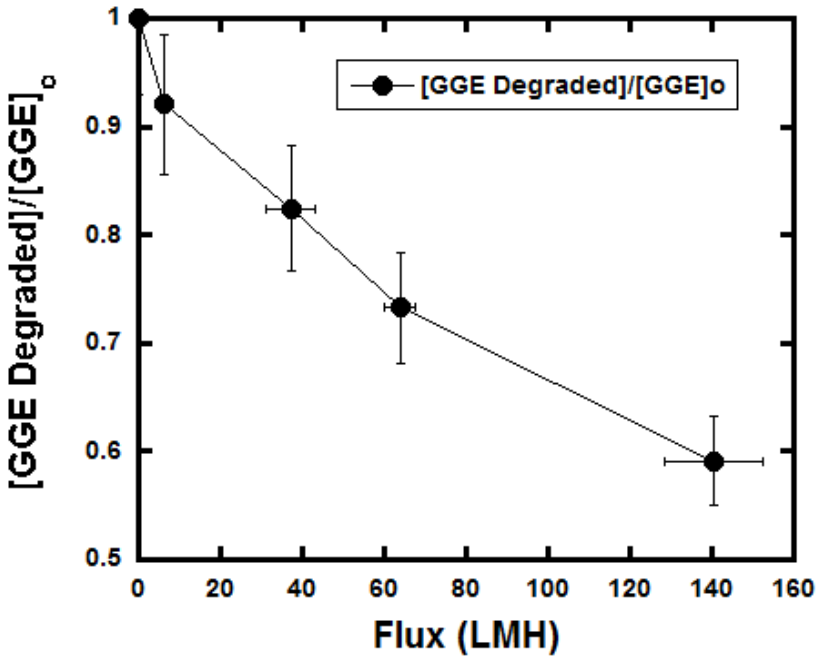


**Figure 7.5** Degradation of GGE by the laccase-functionalized membrane as a function of flow rate and. Experiments were performed at a temperature of 22 °C and a pH of 5.6. The initial substrate concentration was 3.1 mM GGE in water.

## 7.4 Reusability of Multienzyme Functionalized Membrane

The reusability (3 repeat cycles) of the multienzyme-functionalized membrane as assessed by retention of its capacity to catalyze conversion of GGE under convective flow mode shown in **Figure 7.6**. In this case a membrane with laccase (3.3 mg) peroxidase (2.4 mg) was used and stoichiometric amount of hydrogen peroxide was added into the feed (3.1 mM of GGE in water). As evident from the **Figure 7.6**, the enzyme-functionalized membrane displayed encouraging retention of activity, after multiple cycles of operation. This is consistent with our earlier observation [146] where we have discussed similar stability of enzyme immobilized membrane matrix.

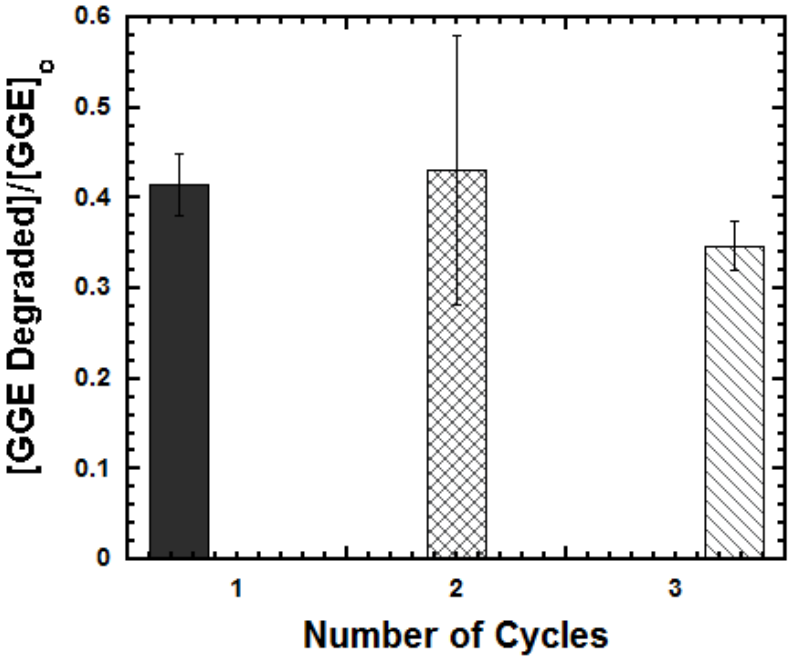


**Figure 7.6** Activity of multienzyme functionalized membrane towards GGE degradation after multiple cycles. Experiments were performed at a temperature of 22 °C and a pH of 5.6. The initial substrate concentration was 3.1 mM GGE in water.

## 7.5 Product Analysis of Conversion of GGE to Different Oxidation Products

Effort was made to characterize the degraded products from the enzymatic reactions. LC-MS analysis of the reaction products of GGE conversion yielded multiple oxidized products with m/z ranging from 251 $[M + Na]^+$ up to 979 $[M + Na]^+$. Enzymatic conversion of GGE (MW 320) to multiple polymeric oxidized product with higher molecular weight is reported by other researchers as well [198]. It is noteworthy to point out that generation of such oligomeric products is enzyme dependent. Our findings on this is that horseradish peroxidase usually generates the high molecular weight dimeric (m/z 661, **B**) and trimeric (m/z 979, **C**) products to a greater extent than the low molecular weight (m/z 251, **A**). However, laccase produces a higher amount of (m/z 251) than (m/z 661) and none of the higher ones were seen. To be specific, laccase produces 99% of **A** and only 0.8% of **B** of the total GGE conversion product. In contrast, with HRP only 43% of the total GGE conversion product was **A**. Formation of **B**, in this case, was ten times more than in case of laccase reaction. Moreover about 2% of the trimeric adduct **C** was formed with HRP, which was not seen in the laccase reaction. All the data are tabulated in **Table 7.1**. The effect was also seen in case of the multienzyme membrane with formation of 62% of the degraded product **A** compared to only 0.7 and 0.4 % of the oligomeric products. Based on GGE degradation patterns it can be concluded that reactions performed by HRP resulted in oxidative oligomerization, probably formed through C−C coupling of the phenolic units [199]. Laccase, on the other hand, degrades the GGE and the oligomeric products from the HRP reactions through an alkyl-phenyl ether bond cleavage reactions.[96] The fact that laccase was able to break down such oligomers to monomeric units justify the unification of multiple enzymes to the membrane reactor to protect its activity. Various such multienzymatic systems are studied from time to time [81-83, 97, 200]. While immobilized enzymes generally have better stability over solution phase, the shortening of diffusion time of the substrate or transformed substrate from one enzyme to another enzyme in multienzymatic systems makes them more potent with higher observed catalytic activity. Jia et al. recently discussed a comparison of efficiency of substrate conversion by such multienzymatic system to free enzyme and in a few cases decrease in performance was also observed [82].

**Table 7.1** Conversion of GGE to different oxidation products.

| **Reactors** | **Of the Total GGE Conversion Product** | | | **Total GGE Conversion** |
|---|---|---|---|---|
| | **A** (m/z 251) | **B** (m/z 661) | **C** (m/z 979) | |
| Laccase | 99% | 0.8% | - | 73% |
| HRP | 43% | 9.9% | 2.4% | 57% |
| Multienzyme | 62% | 0.7% | 0.4% | 95% |

# CHAPTER 8. THIOL-FUNCTIONALIZED MICROFILTRATION MEMBRANE FOR HEAVY METAL REMOVAL FROM WATER

## 8.1 Overview

This chapter discusses the characterization and effectiveness of thiol functionalized membranes for heavy metal sorption under convective flow conditions. Specifically, this study explores the sorption capacity of ionic mercury in a polyacrylic acid functionalized polyvinylidene fluoride (PAA-PVDF) membrane immobilized with cysteamine (CysM). Here, CysM is used as a precursor of thiol groups. Thiol functionalized membrane was characterized by ATR-FTIR, zeta potential and contact angle measurement. Later, permeance results of membranes during various stages of thiol functionalization has been reported. Two methods of CysM immobilization to the PAA-PVDF membrane have been assessed. The **i)** ion exchange (IE) and, **ii)** carbodiimide crosslinker chemistry using 1-(3-Dimethylaminopropyl)-3-ethyl carbodiimide hydrochloride (EDC) and N-hydroxysuccinimide (NHS), known as EDC/NHS coupling. The ion exchange method demonstrates that cysteamine (CysM) can be immobilized effectively on PAA-PVDF membranes without covalent attachment. The effectiveness of the CysM immobilized membranes to remove ionic mercury from the water was evaluated by passing a dissolved mercury (II) nitrate solution through the membranes. The sorption capacity of mercury for CysM immobilized membrane prepared by the IE method is 1015 mg/g PAA. On the other hand, the sorption capacity of mercury for CysM immobilized membrane prepared by EDC/NHS chemistry is 2446 mg/g PAA, indicates membrane functionalization by EDC/NHS coupling enhanced mercury sorption 2.4 times compared to IE method. The efficiencies of Hg removal are 94.1±1.1 and 99.1±0.1% respectively, for the CysM immobilized membranes prepared by IE and EDC/NHS coupling methods. Finally, adsorption capacity of thiol functionalized membrane is compared with other commercial and reported materials. Sections 8.2 to 8.3 are **submitted** as manuscript as **Islam et al.** and section 8.4 are **published** in **Hernández, Islam et al. (2020)**.

## 8.2 Characterization of Thiol Functionalized Membranes

Functionalization of PVDF membranes to thiol membranes using EDC/NHS chemistry consists of multiples steps, with PAA-PVDF and NHS-PAA-PVDF functionalized membranes as intermediates. The different functionalization steps (PAA-PVDF, NHS-PAA-PVDF, and Cys/CysM-PAA-PVDF) can be tracked by observing changes in ATR-FTIR spectra, surface charge (zeta potential) and interaction of the boundary layer of the functionalized membrane with water (surface water contact angle), which are discussed in detail in the following sub-sections

### *8.2.1 ATR-FTIR Spectra Analysis of Thiol Functionalized Membranes*

Analyzing the absorption peaks of fluorocarbons, carboxyl, amine and thiol groups will ascertain the functionality of each step. The ATR-FTIR spectrum during measurement was set between 400 and 4000 $cm^{-1}$. The built-in OMNIC software was used with the instrument to set and record the parameters of measurement. The resolution was set to a value of 4 $cm^{-1}$, the number of scans was 64 respectively during FTIR measurement. The samples were placed on a diamond crystal while recording the signal. The ATR-FTIR spectra of different stages of membrane functionalization is shown in **Figure 8.1**. All the characteristic peaks are identified by comparing to the published data [100-101, 146, 163-164, 201]. The characteristic peaks such as C-F bonds (~1170 $cm^{-1}$), C-$F_2$ bonds (~1200 $cm^{-1}$), and vibration of $CH_2$ bending (~1400 $cm^{-1}$) of the blank PVDF membrane for are shown by the blue line in **Figure 8.1** [100, 163]. The appearance of peaks around 1700 $cm^{-1}$ and 1550 $cm^{-1}$ in **Figure 8.1** (red line) is due to carbonyl stretch and antisymmetric stretching of carboxyl groups (-COOH), respectively, of the polyacrylic acid polymer [146, 164, 201]. In addition, the broad peak in **Figure 8.1** (red line) between 2700 and 3400 $cm^{-1}$ is demonstrating the presence of O-H group from the synthesized polymer [164]. Introduction of EDC/NHS chemistry on PAA-PVDF membrane leads to incorporate amine groups on PAA-PVDF functionalized membrane. The ATR-FTIR spectra of NHS-PAA-PVDF membrane is demonstrated in **Figure 8.1** (green line). The appearance of a deformation peak centered at 1650 $cm^{-1}$ wavelength could be attributed to amide II bending [101]. The sharp peak around 3300 to 3500 $cm^{-1}$ is due to primary amine stretching. Primary amine produces two N-H stretching while secondary amides yields only one. The absorbance spectra of CysM-PAA-PVDF membrane is depicted in **Figure 8.1** (pink line). The small amide I band is visible

around wavelength 1650 $cm^{-1}$, however it is smaller compare to the same peak for NHS-PAA-PVDF membrane, due to incorporation of thiol (-SH) groups in the membrane [101]. In addition, a broad peak in the wavelength range of 2450 $cm^{-1}$ to 3500 $cm^{-1}$ is clearly visible (pink line), which is sharply different than the broad peak of PAA-PVDF membrane (red line). This broad peak is due to overlap of amide II stretching peak and mercaptan (S-H stretching) peak, suggesting covalent attachment of thiol (-SH) groups on PAA-PVDF membrane.

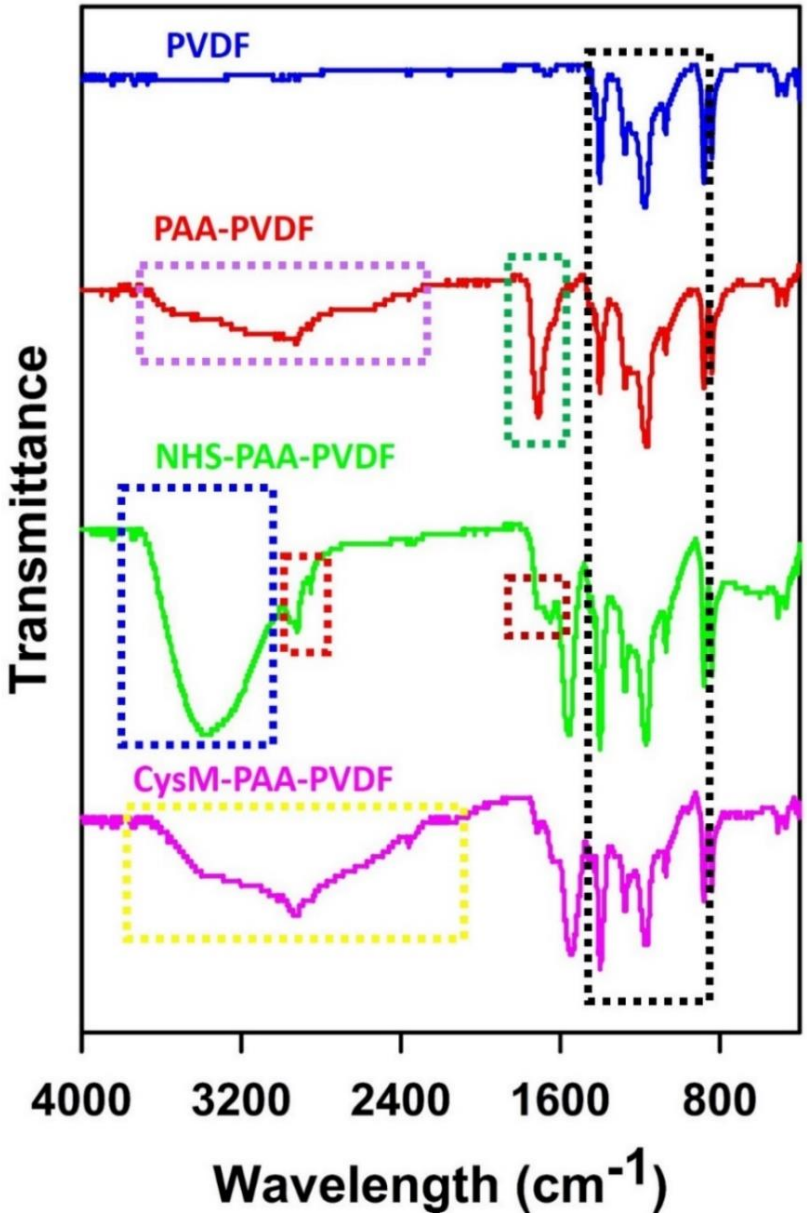


**Figure 8.1** The ATR-FTIR spectra of different stages of functionalization. The blank PVDF membrane is represented by the blue line, The PAA-PVDF membrane (red line) after functionalization of PVDF membrane with acrylic acid to introduce carboxylic groups (-COOH), The NHS-PAA-PVDF membrane (green line) while introducing EDC/NHS chemistry on PAA-PVDF membrane and, finally the CysM-PAA-PVDF membrane (pink line) after incorporation of thiol (-SH) groups in PAA-PVDF membrane.

### *8.2.2 Surface Zeta Potential of NHS-PAA-PVDF Membrane*

The surface charge (represented by zeta potential (ξ), also known as electrokinetic potential) of solid materials in contact with an aqueous solution gives an idea of charge distribution at the interface of a solid surface and the surrounding liquid to evaluate surface chemistry [202]. The surface zeta potential (ξ) of NHS-PAA-PVDF membrane is depicted in **Figure 8.2**. The NHS-PAA-PVDF membrane was selected for zeta potential (ξ), measurements because it is expected to contain both carboxylic and amine groups. The zeta potential (ξ) as a function of pH titrations between 3 and 9, depicted in **Figure 8.2**, indicates two distinct changes in surface charge between pH 3 and 3.5 and between pH 8 and 9.5, indicating the presence of carboxyl groups and amine groups, respectively. The sharp changes of the surface charge for those pH ranges is due to the buffering effect of the corresponding carboxyl (pH 3~3.5 ($\Delta\xi$ = 16 mV)) and amine (pH 8~9 ($\Delta\xi$ = 7 mV)) groups [151, 203], suggesting for this membrane $pK_a$ values around 3 and 8.5. For both carboxyl groups and amine groups, the $pK_a$ value shifts by 0.5 unit due to presence of charge repulsion groups and the for base PVDF layer present in the samples.

### *8.2.3 Contact Angle Measurement at Various Stages of Functionalization*

The measured surface contact angle during each functionalization step are shown in **Figure 8.3**. PVDF membranes are hydrophobic in nature, resulting in a water contact angle of approximately 80°, which was measured by a sessile drop method. The PAA functionalized membranes evaluated in this study have more hydrophilic characteristics due to **i)** high surface free energy that causes water droplet to spread rapidly, and **ii)** fast absorption of water by PAA hydrogel, resulting in a lower water contact angle, which was measured by a captive-bubble method [166-167]. The contact angle of PAA-PVDF membranes was approximately 57° due to changes in the surface properties from hydrophobic to hydrophilic [100]. The EDC/NHS coupling resulting in the formation of NHS-PAA-PVDF membranes increased hydrophobicity, indicated by a water contact angle of 72 °. This increase in hydrophobicity is caused by the coupling of an NHS functional group to the hydroxyl group on the carboxyl functional group, impacting the hydrophilic nature of the carboxyl group. The subsequent amine exchange to form CysM-PAA-PVDF membranes did not significantly impact the water contact angle, suggesting that this step did not change the hydrophobicity of the membranes. The adsorption of $Ag^+$, used as a model compound

for heavy metals, on CysM-PAA-PVDF membrane also did not change the contact angle significantly, implying that the transformation of thiol groups to Ag-thiol bond has little impact on water to solid surface interaction of the thiol membranes.

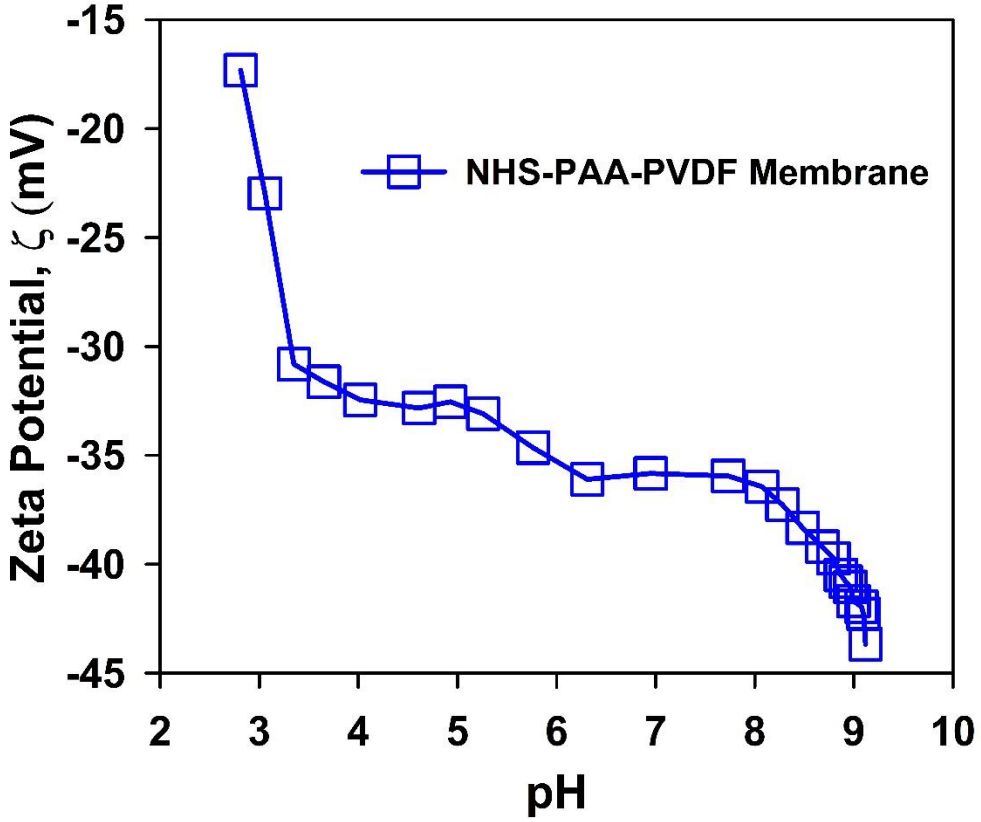


**Figure 8.2** Surface zeta potential (ξ) of a NHS-PAA-PVDF membrane (Mass gain ~ 5 %). An electrolyte solution of 0.01 M KCl was used as background solution for pH titration. The measurement of ξ was conducted four times by flowing the electrolyte solution twice in forward and twice in reverse direction. 0.05 M HCl and 0.05 M of NaOH solutions were used for automated pH titration. Measurements of ξ for pH ranging between 2 and10 are shown. Strong declines in ξ between pH of 3 and 3.5 and between pH 8 and 9.5 is consistent with the presence of carboxyl groups and amine groups, respectively.

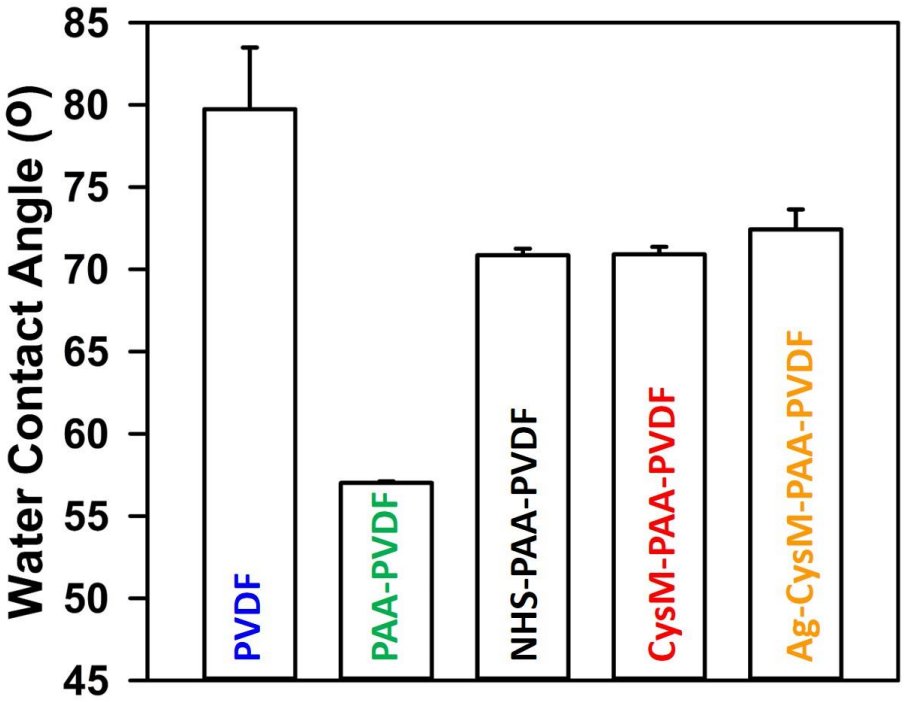


**Figure 8.3** Surface water contact angle of the top surface of PVDF, PAA-PVDF, NHS-PAA-PVDF, CysM-PAA-PVDF and Ag-CysM-PAA-PVDF (after attaching Ag) membranes. The water pH was adjusted to 6.6-6.7. A sessile drop method was used for unmodified membranes (pH ~ 5.5). For other membranes air bubbles were used for captive bubble contact angle measurements at multiple locations of the samples. A 1~2 μL of DI water/air droplet was placed on the top of the membrane surface to measure the contact angle. A minimum of three measurements were collected at separate locations on each membrane surface. Average values and standard deviations are presented.

## 8.3 Permeance Study of Membranes at Various Stages of Thiol Functionalization

EDC/NHS coupling is well known for incorporation of amine groups by reaction with carboxyl groups through covalent bonds to form an NHS ester. The resulting O-NHS group becomes a good leaving group that can be substituted by an amine containing thiol functional groups to form a stable conjugate thiol amide [102]. However, there is no reported data on permeation results when this EDC/NHS chemistry is applied on solid substrate to incorporate thiol functionality. The permeance behaviour during each step of functionalization was evaluated. The results are shown in **Figure 8.4**. The water permeability of PAA-PVDF membranes was measured as approximately 133 LMH/bar, consistent with previous observations by this group [100]. The permeability changed significantly as a result of EDC/NHS coupling, implying a relationship to reaction mechanisms during the substitution of functional groups. EDC/NHS coupling reduced the permeability from 133 LMH/bar to approximately 6 LMH/bar, presumably due to the effect of the amine functional groups (*pKa* 8~9) [151]. The addition of amine groups to the carboxyl groups of PAA-PVDF membranes increases the overall *pKa* value from 3~4 for just the carboxyl groups to 8~9 for amine group causes changes in the negative charge density inside the membrane pore domain, resulting in reduced permeability of NHS-PAA-PVDF membranes. An increase in chain length of the functional groups on the membrane as a result of EDC/NHS coupling might have contributed to this strong reduction in permeability. The substitution of the NHS-O leaving group with thiol containing amine groups with *pKa* values similar to NHS groups increased the permeability of CysM-PAA-PVDF membrane approximately three-fold to ~17 LMH/bar. This is likely caused by a decrease in the negative charge density in membrane pores. Adsorption of $Ag^{+}$ and $Hg^{2+}$ cations on thiol membranes increased the permeability of the membrane to 66 LMH/bar and 51 LMH/bar, respectively. This increase of permeability is presumably caused by charge neutralization in membrane pores through the adsorption of heavy metals. The theoretical capacity of the membranes to remove $Hg^{2+}$ is approximately half of the capacity for the removal of $Ag^{+}$ because the majority of $Hg^{2+}$ ions are expected to attach to two thiol groups. The expected initial permeability during heavy metal adsorption should be close to the permeability of PAA-PVDF membrane. The adsorption of metals could cross-link with thiol groups resulting in reduced permeability.

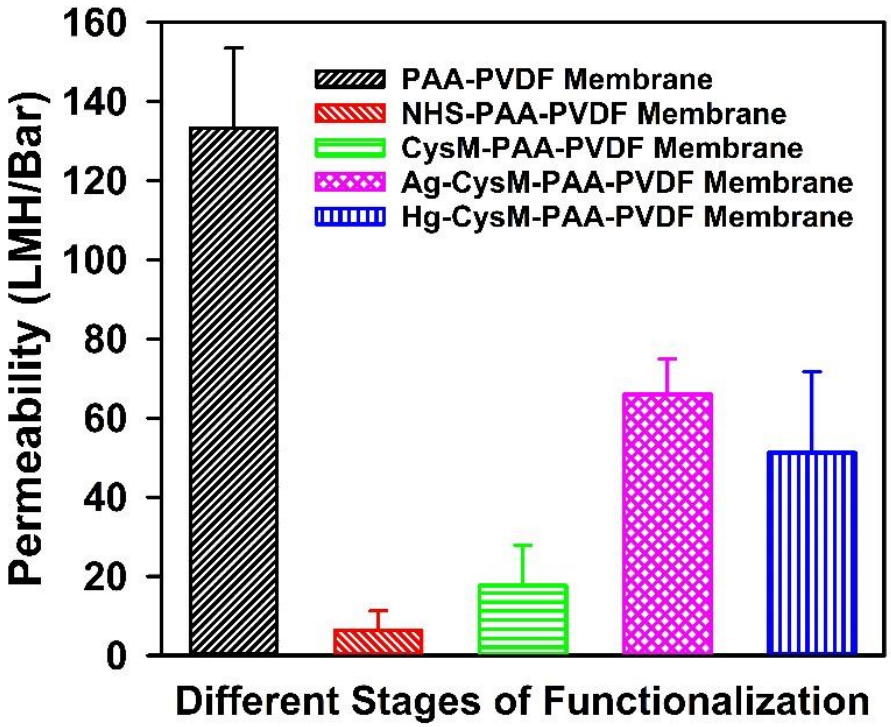


**Figure 8.4** Permeability of PVDF membranes during various stages of functionalization. Average values and standard deviations are presented for different batches of membrane. The average mass gain of the membranes used is around 5~7%. The pH of the solution is adjusted in the range of 5.2~7.

## 8.4 Mercury Sorption Analysis on Thiol Functionalized Membranes

Mercury capture in membranes functionalized with CysM through ion exchange (IE) is significantly affected by pH. The breakthrough of Hg through the membrane is observed at <50 $L/m^2$ of treating a 162 ppb $Hg(NO_3)_2$ solution at pH 4.5. At pH 6.3, no significant breakthrough was observed during the 400 $L/m^2$ experiment. The removal of mercury was 6.9 and 20.2% with respect to the feed solution at the end of the pH 4.5 and 6.3 runs, respectively. The breakthrough curve in of the experiments are shown in **Figure 8.5**. The poor breakthrough performance of the membrane functionalized with CysM through ion exchange at low pH may be caused by multiple mechanisms. The permeance increased during each experiment due to the decreasing pH within each experiment. This increase in permeance results less residence time in pore domain, ultimately causes less mercury sorption by thiol groups immobilized at the end of PAA chain. The high mercury capacity of the membrane functionalized with CysM through ion exchange (IE) was not achieved, possibly due to the low pH. A decrease in pH from 6.3 to 4.5 results 50% less CysM incorporation in PAA-PVDF membrane due to protonation of carboxylic groups present in the PAA. The concentration of $Hg^{2+}$ in permeate fluctuated significantly due to pH responsiveness of PAA at pH 6.3 as demonstrated in **Figure 8.5**. Once pH of the membrane permeance was stabilized, the $Hg^{2+}$ concentration did not increase with time as volume treated, as in the beginning.

Mercury capture with membrane functionalized with CysM through EDC/NHS coupling achieved higher $Hg^{2+}$ sorption than membranes functionalized by ion exchange (IE) route at lower pHs. Membrane functionalized by the EDC/NHS coupling, concentration of $Hg^{2+}$ in permeate is also constant compared to the membrane prepared by ion exchange (IE), due to complete substitution to thiol groups of CysM from carboxylic acid group of PAA chain. This allowed a constant $Hg^{2+}$ capture of 98.6% of the feed solution and prevents the dislodge of CysM due to variations in pH, which may occur with ion-exchange (IE) membranes and affect their sorption efficiencies. The variability of the $Hg^{2+}$ capture by CysM immobilized by EDC/NHS coupling shown in **Figure 8.5**, could be due to a small pH responsiveness from the free carboxylic groups present.

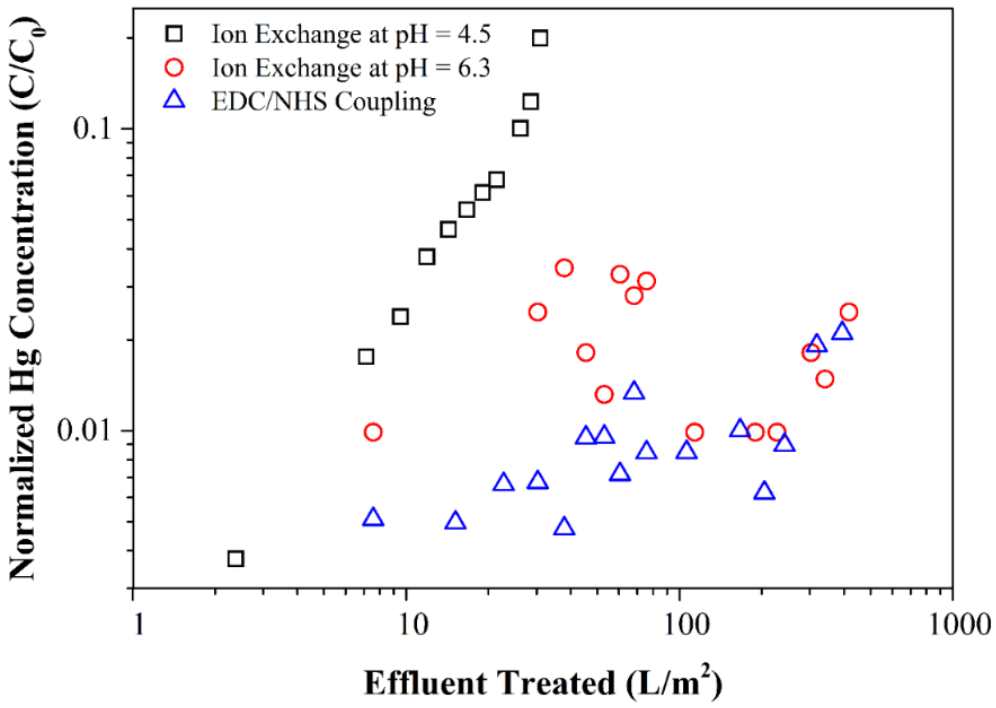


**Figure 8.5** Sorption of $Hg^{2+}$ (solution volume per area of the membrane) by CysM-PAA-PVDF membranes functionalized by ion exchange (IE) and EDC/NHS coupling. Operating pressure = 2.1 bar, Initial Hg concentration ~ 160 ppb.

### *8.4.1 Efficiency of Mercury Sorption on Thiol Functionalized Membranes*

The efficiency of $Hg^{2+}$ sorption under mild conditions for all thiol functionalized membranes tested is shown in **Figure 8.6**. The diagonal line indicates the theoretical complete sorption of all $Hg^{2+}$ passed through the membranes. The efficiencies of Hg capture by CysM functionalized membranes are 94.1±1.1 and 99.1±0.1% for ion exchange (IE) and by EDC/NHS coupling, respectively. The idea of pore functionalization is to functionalize the whole pore domain not only the pore wall. This leads to pass the fluid through the functionalized hydrogel when an external pressure is applied. This allows the permeate (in this case Hg water) to pass through the thiol functionalized polymer domain resulting high encounters with thiol groups to allow adsorption of heavy metals. This ultimately results high metal capture leading to high adsorption efficiency. However, sometimes pore channels results due to poor functionalization during fabrication of membrane. The sorption capacity of the EDC/NHS functionalized membrane is more stable than for the ion exchange (IE) functionalized membrane due to the covalent grafting of CysM that make the sorption sites more stable and reduce the probability of losing CysM due to changes in permeate pH.

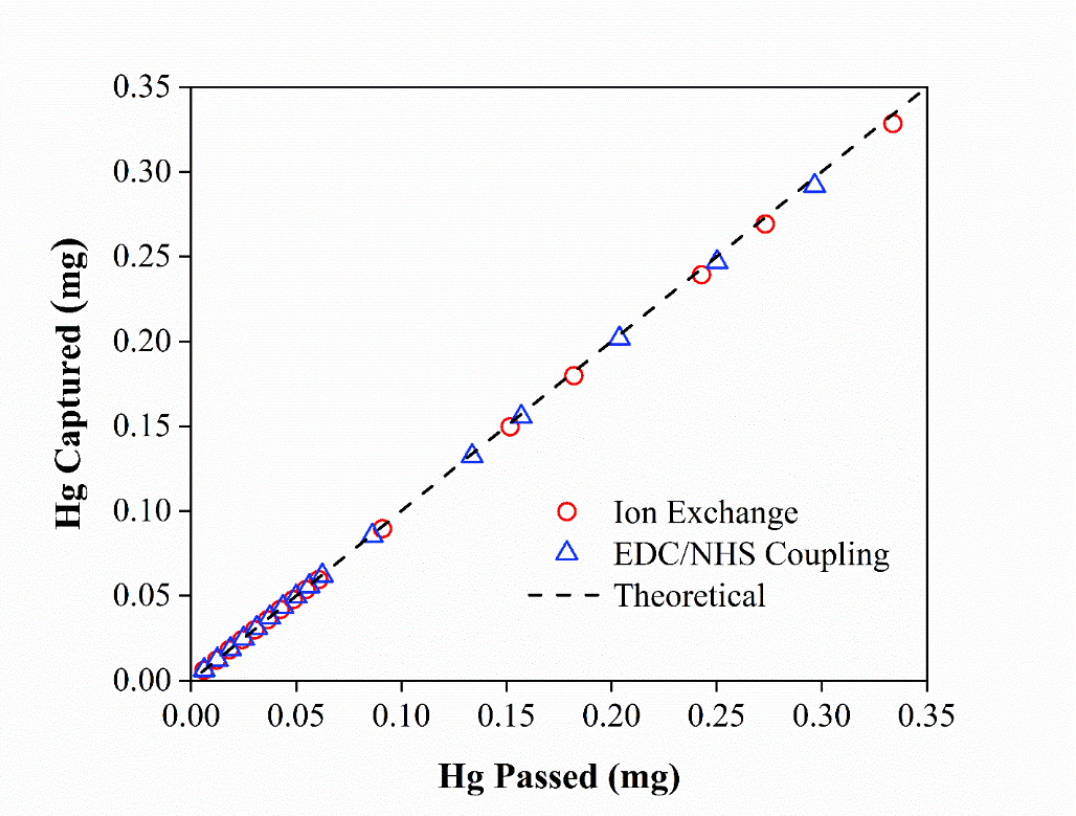


**Figure 8.6** Relationship between Hg passed through the membrane and Hg captured, in CysM-PAA-PVDF membranes functionalized by ion exchange (IE) and EDC/NHS coupling. Operating pressure = 2.1 bar.

### *8.4.2 Capacity Analysis for Mercury Sorption on Thiol Functionalized Membranes*

The measured $Hg^{2+}$ sorption capacity is 1015 mg/g PAA for CysM immobilized PAA-PVDF membrane prepared by ion exchange (IE). On the other hand, the measured $Hg^{2+}$ sorption capacity 2446 mg/g PAA for CysM immobilized PAA-PVDF membrane prepared by EDC/NHS chemistry. Based on this result, capacity of a membrane module has been assessed to treat wastewater. An 8040-commercial membrane module was used as a basis with a total surface area of 31.6 $m^2$ (340 $ft^2$) per module. Further considering an operating pressure of 2.0 bar, the calculation reveals, with a $Hg^{2+}$ concentration of 1.0 mg/L in water, the potential volume of water could be treated are 212 and 512 $m^3$/module by thiol functionalized membrane prepared by ion exchange and EDC/NHS chemistry. In **Table 8.1** comparison of the adsorption capacity of thiol functionalized membrane with other commercial and reported materials is shown. However, the adsorption capacity of CysM immobilized PAA-PVDF membrane could be increased by incorporating more thiol groups in the membrane. This could be done by increasing the concentration of PAA and cross-linker (MBA) during initial in-situ polymerization of PVDF membrane but might result in a flux drop instead [100].

**Table 8.1** Comparison of adsorption capacity of thiol functionalized membrane with other commercial and reported materials.

| Sl. No. | Types of Materials | Functional Groups | Capacity | Reference |
|---|---|---|---|---|
| **1** | CysM-PAA-PVDF Membrane (By Ion-Exchange) (with a functional layer thickness of 70 µm) | Thiol | 96 g/L memb§<br>1015 mg/g PAA<br>55 mg/g memb | This Work |
| **2** | CysM-PAA-PVDF Membrane (By EDC/NHS Chemistry) (with a functional layer thickness of 70 µm) | Thiol | 232 g/L memb§<br>2446 mg/g PAA<br>133 mg/g memb | This Work |
| **3** | Commercial AMBERSEP™ GT74 Chelating Resin | Thiol | ≥1.4 eq/L /<br>358 mg/g* | Reference [204] |
| **4** | Magnetic Porous Organic Polymers (MOP-SH) | Thiol | 703 mg/g | Reference [124] |
| **5** | Azo-linked Magnetic Porous Organic Polymers (AzoMOP-SH) | Thiol | 910 mg/g | Reference [124] |
| **6** | Thiol-/Thioether-Functionalized Porous Organic Polymers (POP-SH/SMe) | Thiol | 180 mg/g | Reference [125] |
| **7** | Layered Double Hydroxide Intercalated with the $MoS_4^{2-}$ Ion ($MoS_4$-LDH) | $(MoS_4)^{2-}$ | 500 mg/g | Reference [127] |
| **8** | Functionalized Porous Organic Polymer (POP-SH) | Thiol | 1216 mg/g | Reference [128] |
| **9** | Molybdenum Disulphide ($MoS_2$) | Sulfide | 2506 mg/g | Reference [121] |
| **10** | Single Walled Carbon Nanotube (SWCNT-SH) | Thiol | 131 mg/g | Reference [129] |
| **11** | Sulfur/Reduced GO nanohybrid (SRGO) | Sulfur | 908 mg/g | Reference [126] |
| **12** | Luminescent Metal-Organic frameworks (LMOF-263) | Thiol | 380 mg/g | Reference [130] |

**§** memb = Membrane

* This value was calculated based on the bulk density (784 g/L) of the product given in product data sheet

# CHAPTER 9. STUDY OF THE CYSTEAMINE FUNCTIONALIZED MEMBRANE TO REMOVE HEAVY METALS FROM INDUSTRIAL WASTEWATER, EFFECT OF PRESENCE OF OTHER CATIONS AND MATHEMATICAL MODELING OF THE MEMBRANE

## 9.1 Overview

This study demonstrates a sustainable three-step process consisting of primary pre-filtration followed by ultrafiltration (UF) and adsorption with thiol functionalized microfiltration membranes (thiol membranes) to effectively remove mercury sulphide nanoparticles (HgS NP) and dissolved mercury ($Hg^{2+}$) from wastewater. Thiol membranes were synthesized by incorporating either cysteine (Cys) or cysteamine (CysM) precursors onto polyacrylic acid (PAA) functionalized polyvinylidene fluoride (PVDF) membranes. Carbodiimide chemistry was used to crosslink thiol (-SH) groups on membranes for metal adsorption. The thiol membranes and intermediates of the synthesis were tested for permeability and long-term mercury removal using synthetic waters and industrial wastewater spiked with HgS NPs and a $Hg^{2+}$ salt. Results show that treatment of the spiked wastewater with a UF membrane removed HgS NPs to below the method detection level (MDL) (<2 ppb) for up to 12.5 hours of operation. Flux reductions that occurred during the experiment were reversable by washing with water, suggesting negligible permanent fouling. Dissolved $Hg^{2+}$ species were removed to non-detect levels by passing the UF treated wastewater through a CysM thiol membrane. The adsorption efficiency in this long-term study (>20 hours) was approximately 97%. Addition of $Ca^{2+}$ cations reduced the adsorption efficiencies to 82% for the CysM membrane and to 40% for Cys membrane. The inferior performance of Cys membranes may be explained by the presence of a carboxyl (-COOH) functional group in Cys, which may interfere in the adsorption process in the presence of multiple cations because of multi cation absorption. CysM membranes may therefore be more effective for treatment of wastewater than Cys membranes. Focus Ion Beam (FIB) characterization of a CysM membrane cross-section demonstrates that the adsorption of heavy metals is not limited to the membrane surface but takes place across the entire pore length. Experimental results for adsorptions of selected heavy metals on thiol membranes over a wide range of operating conditions finally predicted by developing a mathematical model. Sections 9.2 to 9.10 are **submitted** as manuscript as **Islam et al**.

## 9.2 Process Description and Primary Filtration of Industrial Wastewater

Mercury removal from wastewater may be very different than removal from synthetic waters (i.e., aqueous solutions generated in the laboratory by adding chemicals to tap, deionized, or distilled water), in part because of the presence of dissolved mercury species and other dissolved salts or gases, HgS NPs and other solids, or dissolved or free phase organic materials, which can significantly impact the adsorption performance of the treatment process [131]. The wastewater composition may depend on the source of the water, e.g., sediment, surface water, ground water, or industrial wastewater, which could also alter the adsorption performance.

Long term operation for heavy metal adsorption can also affect the overall performance of the treatment process. The effectiveness of a water treatment process in general, or heavy metal removal from wastewater in particular, is usually determined by a site-specific treatability study. The industrial wastewater used for this study, which was collected from a US industrial site based in California described in **Table 9.1**, contained particulate Hg (HgS NPs), other particulate matter, dissolved $Hg^{2+}$, and a variety of dissolved salts. However, the HgS and $Hg^{2+}$ quantities varied from stream to stream and with time. The wastewater was spiked with an additional 200 ppb of HgS (average hydrodynamic diameter 20~30 nm by DLS) and 110 ppb $Hg^{2+}$ (added as $Hg(NO_3)_2 \cdot xH_2O$ ($x = 1-2$)) for adsorption experiments using thiol functionalized membranes, which was needed to allow for quantitative measurements of removal efficiencies. The resulting total HgS NP and dissolved $Hg^{2+}$ was approximately 200 ppb and 110 ppb, respectively. The suspension of HgS nanoparticls (NPs) (1 ppm) was received on January 25, 2018 from Dr. Gregory V. Lowry (Carnegie Mellon University, Pittsburgh, PA).

A process that effectively removes both HgS NP and dissolved mercury species from wastewater and is robust enough for long-term treatment requires multiple processing steps. Based on the quality of the industrial wastewater we propose a three steps treatment process, consisting of pre-filtration followed by ultrafiltration and membrane adsorption. The proposed treatment process is depicted in **Figure 9.1**. The first step consists of pre-filtration with a PVDF 700 microfiltration (MF) membrane to remove large particulates that could potentially foul or damage membranes in the second and third steps. The second step consistst of ultrafiltration (UF) to remove HgS NPs through size exclusion. Any

carryover of HgS NPs will adversely affect the removal of $Hg^{2+}$ and membrane flux in the third step. The third step uses a thiol membrane to adsorb dissolved $Hg^{2+}$ species. The three steps are needed because carry through of particulates can cause significant flux reductions by fouling of membrane surfaces, and clogging of membrane pores. The initial flux and changes in flux over time for the primary filtration step were measured using De-Ionized Ultra-Filtered (DIUF) water and industrial wastewater.

The flux data as well as images of the membrane and wastewater before and after the primary filtration step are provided in **Figure 9.2** to show changes in membrane and wastewater condition. The flux was consistent at a value around 600 LMH ($L \cdot m^{-2} \cdot hr^{-1}$) at atmospheric pressure and membrane condition after initial treatement shows removal of most of the particulates.

**Table 9.1** Constituents of industrial wastewater as tested.

| Name of the Compound | Amount (ppm) | Method Used |
|---|---|---|
| As HgS | 80% HgS NPs ≤ 20 ~ 30 nm | DLS |
| As $Hg^{2+}$ | 0.001 to 0.050 | Mercury Analyzer and ICP-OES |
| As Na | ~357 | ICP-OES |
| As Mg | 25 ~ 26 | ICP-OES |
| As Ca | 52 | ICP-OES |
| As K | ~ 17 | ICP-OES |
| TOC | 0 ~ 4 | TOC Analyzer |
| TDS | < 2000 | TDS Meter |
| pH | ~ 7 | pH Meter |

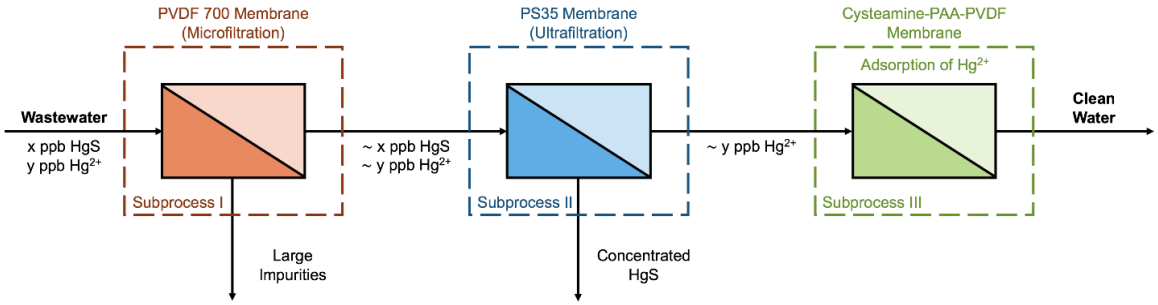


**Figure 9.1** Proposed treatment process for removal of mercury (HgS Nanoparticles, dissolved $Hg^{2+}$) from wastewater. The values of the concentration of HgS and $Hg^{2+}$ in this graphic is just to represent arbitrary concentration. Depending on the source of wastewater x and y can vary.

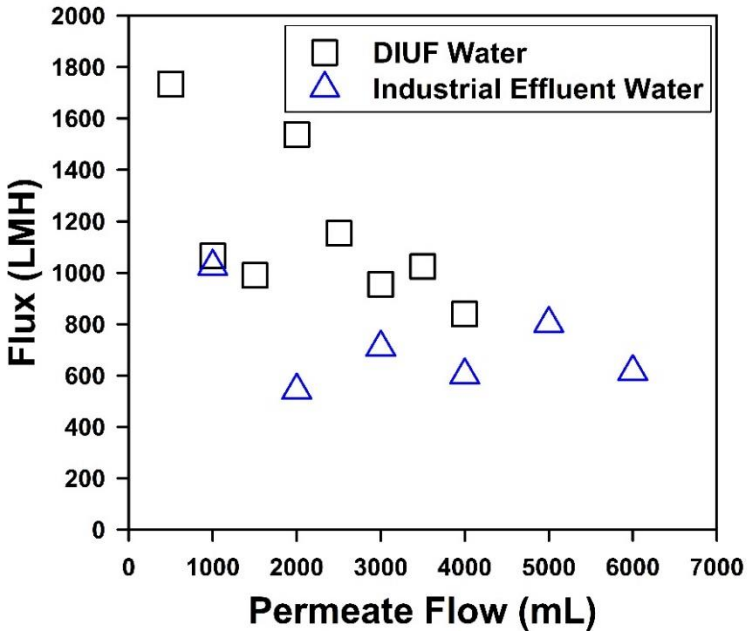


**(a)**

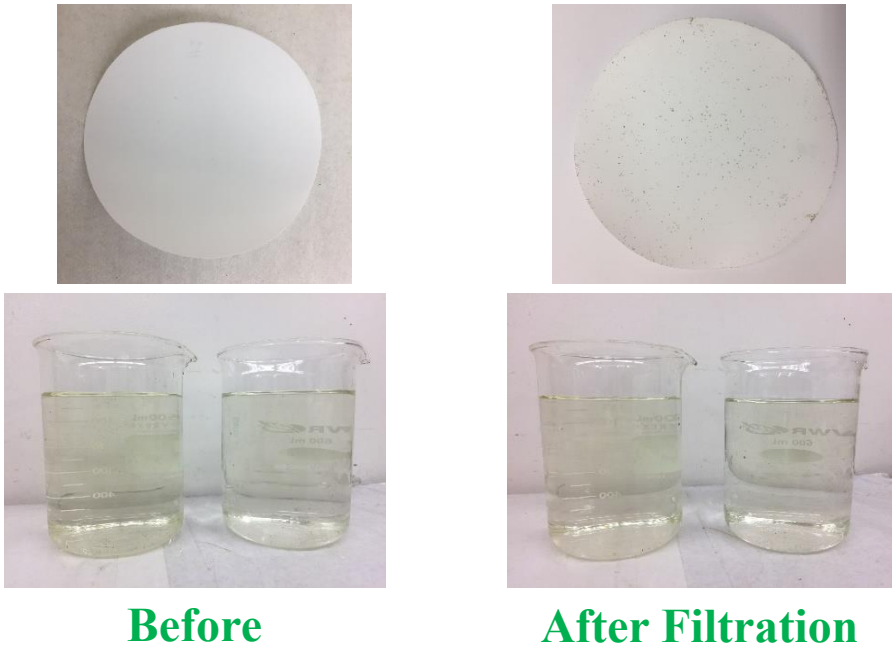


**(b)**

**Figure 9.2 (a)** Flux profile for DIUF and wastewater using PVDF membrane for initial filtration to remove particulates. Effective membrane surface area is 65.03 $cm^2$. **(b)** Images of membrane used and wastewater condition before and after initial filtration.

## 9.3 Removal of HgS Nanoparticles by Ultrafiltration (UF) Membrane

The feed water quality can significantly affect the separation of HgS NPs in the presence of different cations (such as $Na^+$, $Ca^{2+}$, or $Mg^{2+}$) and organic matter [131]. The high removal of HgS can be adversely affected due to changes in the electrostatic repulsion between particles caused by the presence of other cations which will have impact on overall ionic strength of feed water [205-207]. In addition, the presence of dissolved organic matter could affect the colloidal properties of HgS NPs [208]. This will eventually cause fouling of the membrane and affect the overall performance of the treatment process. Thus, in order to separate HgS NPs, a size exclusion process should be considered based on the size of NPs that will have zero permeation of the HgS NPs, is less susceptible to fouling and high processing capacity in a single pass and is durable for long term operation. Based on these attributes, a commercially available polysulfone ultrafiltration (UF) membrane (PS35) was selected to separate HgS NPs from wastewater. The specification of the UF membrane is summarized in **Table 9.2**. After primary filtration, the spiked wastewater containing both HgS and $Hg^{2+}$ was passed through the PS35 UF membrane at 2.72 bar in dead-end mode in order separate HgS particles. The overall performance of this filtration step in terms of DIUF water flux, spiked wastewater flux, removal of HgS NPs, fouling, and recovery of flux is demonstrated in **Figure 9.3**. The flux for DIUF water shown in **Figure 9.3a** indicates that the initial flux was approximately 1400 LMH at 2.72 bar and declined steadily to approximately 600 LMH after 55 minutes of operation, during which 1000 mL of DIUF was passed through the filter.

The long-term flux behaviour of wastewater was measured by passing 10 individual batches of 100 ml spiked wastewater to a total of 1000 ml, which took approximately 750 minutes (12.5 hours). The flux data are depicted in **Figure 9.3b**. The initial flux of approximately 350 LMH at 2.72 bar declined rapidly to approximately 100 LMH during the first three batches of wastewater, after which the decline was relatively minor to a final flux around 35 LMH at the end of the experiment. Flux recovery was observed at the beginning of each new batch of spiked wastewater added to dead-end cell, indicated by peaks in **Figure 9.3b**. The accumulation of the HgS NPs and other particulates on top of the membrane surface are primarily responsible for the observed flux drop. The observed flux recovery after each batch of spiked wastewater may be caused by a small amount of

back flow caused by changes in pressure differentials between changeouts of the batches, resulting in (partial) removal of particulates from the membrane pores. Subsequent washing of the surface of the membrane with DIUF water resulted in full flux recovery (blue line in **Figure 9.3b**), suggesting that membrane fouling under these conditions can be reversed. The distribution profile of the HgS NPs in feed and permeate is depicted in Error! Reference source not found.**9.3c**, showing no detectable particles in the permeate by D ynamic Light Scattering (DLS). Atomic adsorption measurements confirm removal of 200 ppb HgS NP based on the difference between total mercury concentrations of the MF and UF permeates. This observation also suggests that no significant amount of dissolved mercury species, including organic complexes, were removed by either MF or UF membranes. The membrane was not significantly fouled as evident from flux recovery data. The visual inspection of UF membrane before and after washing with DIUF water, depicted in **Figure 9.3d**, supports the observation that passing wastewater through the UF membrane did not result in permanent fouling during this experiment. The calculated removal rate for 200 ppb HgS NPs using a PS35 UF membrane for this experiment is approximately 12 $mg \cdot m^{-2} \cdot hr^{-1}$.

**Table 9.2** Detail data of Ultrafiltration membrane used for HgS nanoparticle separation.

| | |
|---|---|
| Manufacturer | Nanostone |
| Types of membrane | Ultrafiltration |
| Membrane reference | PS35 |
| MWCO | 20 kDa |
| pH process limits | 2 - 10 |
| Membrane area | 13.2 $cm^2$ |

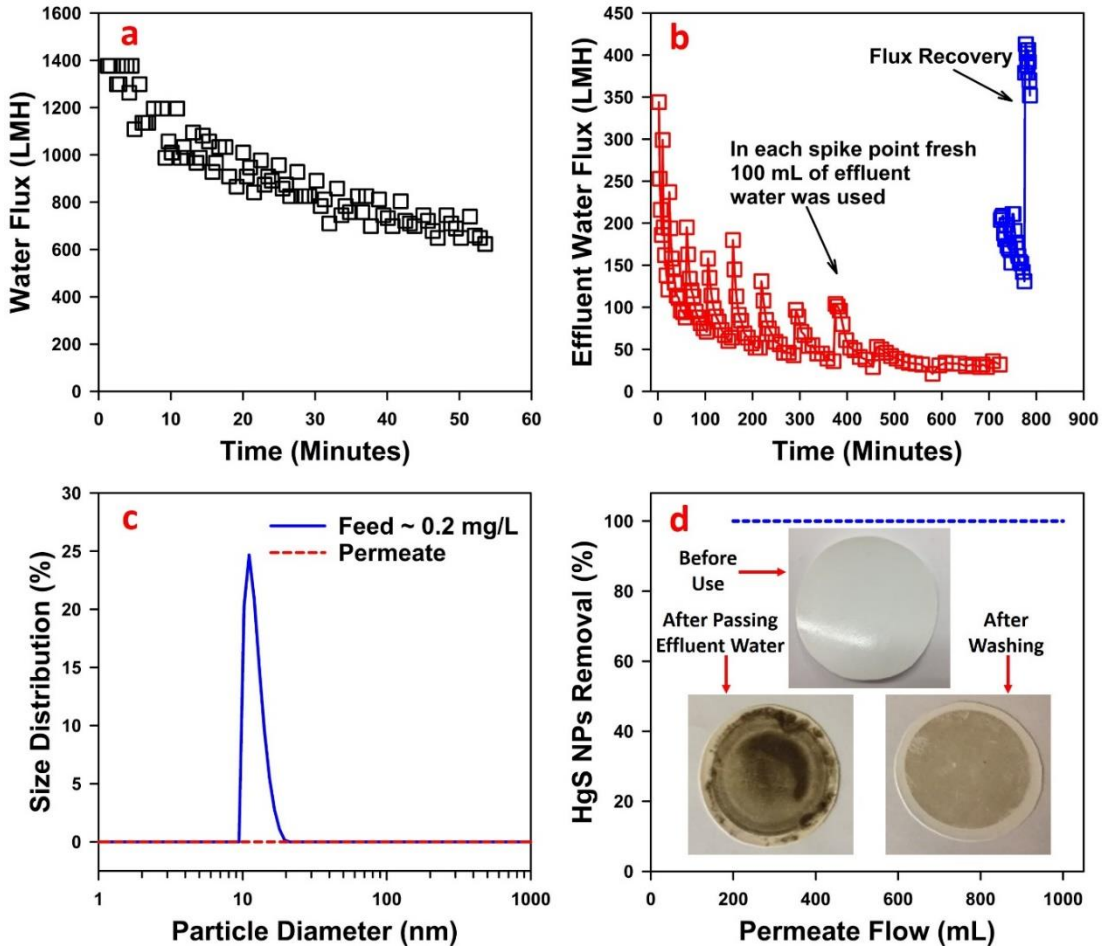


**Figure 9.3** Flux profile for a PS35 ultrafiltration (UF) membrane by dead end mode operation measured at 2.72 bar using **(a)** DIUF water and, **(b)** wastewater (pH ~7) spiked with HgS NPs and $Hg^{2+}$ and pre-treated by MF. Total ~1000 mL of DIUF and wastewater was passed through a membrane in convective flow mode. Effective membrane surface area utilized is 13.2 $cm^2$. **(c)** Particle size distribution of HgS NPs in feed and permeate measured by DLS, **(d)** Images of UF membrane fouling by visual observation of PS35 UF membranes, showing the color of the membrane before use, after passing spiked wastewater, and after cleaning with DIUF water. Initial concentration of HgS NPs in wastewater is approximately 200 ppb.

## 9.4 Removal of Dissolved $Hg^{2+}$ by CysM-PAA-PVDF Membrane and Long-Term Performance Study

A thiol membrane was used to adsorb dissolved $Hg^{2+}$ after removal of HgS NPs and other particles from wastewater by a UF membrane. The efficacy of thiol membranes to adsorb heavy metals from synthetic water has been established in previous study by this group [101]. The source of wastewater, concentration of dissolved $Hg^{2+}$, and water quality parameters (e.g., pH, types of other cations present) can have a strong impact on the membrane adsorption efficiency [131]. The hydrolysis or complexation of $Hg^{2+}$ cations could also affect the adsorption process, as $Hg^{2+}$ hydrolyzes readily in a wide range of pH to form a variety of complexes with organic and inorganic ligands [209-210]. Long-term operation for removing $Hg^{2+}$ by CysM-PAA-PVDF membranes will also affect the adsorption efficiency. The long-term adsorption performance of a CysM-PAA-PVDF membrane to remove $Hg^{2+}$ from UF filtered wastewater is depicted in **Figure 9.4**. The flux pattern during sorption of $Hg^{2+}$ by a thiol membrane is also shown in **Figure 9.4**. Approximately 1700 mL of wastewater was processed by the membrane for a period of 1250 minutes (20.8 hrs) at 2.72 bar. The wastewater flux reduced eight-fold to approximately 25 LMH during the course of the experiment. Several factors may have caused or contributed to this flux reduction. Adsorption of $Hg^{2+}$ cations may have led to a reduction in the accessibility of free thiol groups in the membrane pore domain. $Hg^{2+}$ cations attached to surface thiol groups may also have cross-linked with existing functionalized polymer, resulting in a reduction of pore channel sizes or complete blockage of pores. In addition, the presence of other cations such as $Na^{+}$, $Ca^{2+}$, $Mg^{2+}$, which are present at concentrations orders of magnitude higher than $Hg^{2+}$ but that have a lower affinity to thiols, may have participated in the adsorption, leading to a drop in effluent flux over time. No visible fouling of the CysM-PAA-PVDF membrane occurred during treatment of the UF filtered wastewater. However, washing of the membrane with DIUF after the completion of the experiment helped to recover the flux to a value of 50 LMH at 2.72 bar, shown in red squares in **Figure 9.4**. The remaining dissolved $Hg^{2+}$ cations concentration in permeate is shown on the secondary (right) y-axis in **Figure 9.4**. The remaining dissolved $Hg^{2+}$ cation concentration in wastewater is in the range of 3~4 ppb which is close to the EPA guideline for mercury in drinking water [211]. Adding a second CysM-PAA-PVDF membrane in series may remove

additional $Hg^{2+}$ cations from permeate, potentially to significantly below EPA drinking water specifications. The adsorption efficiency in this long-term study is around 97%, as depicted in **Figure 9.5,** confirming the effectiveness of CysM-PAA-PVDF membranes for removal of $Hg^{2+}$ cations from wastewater.

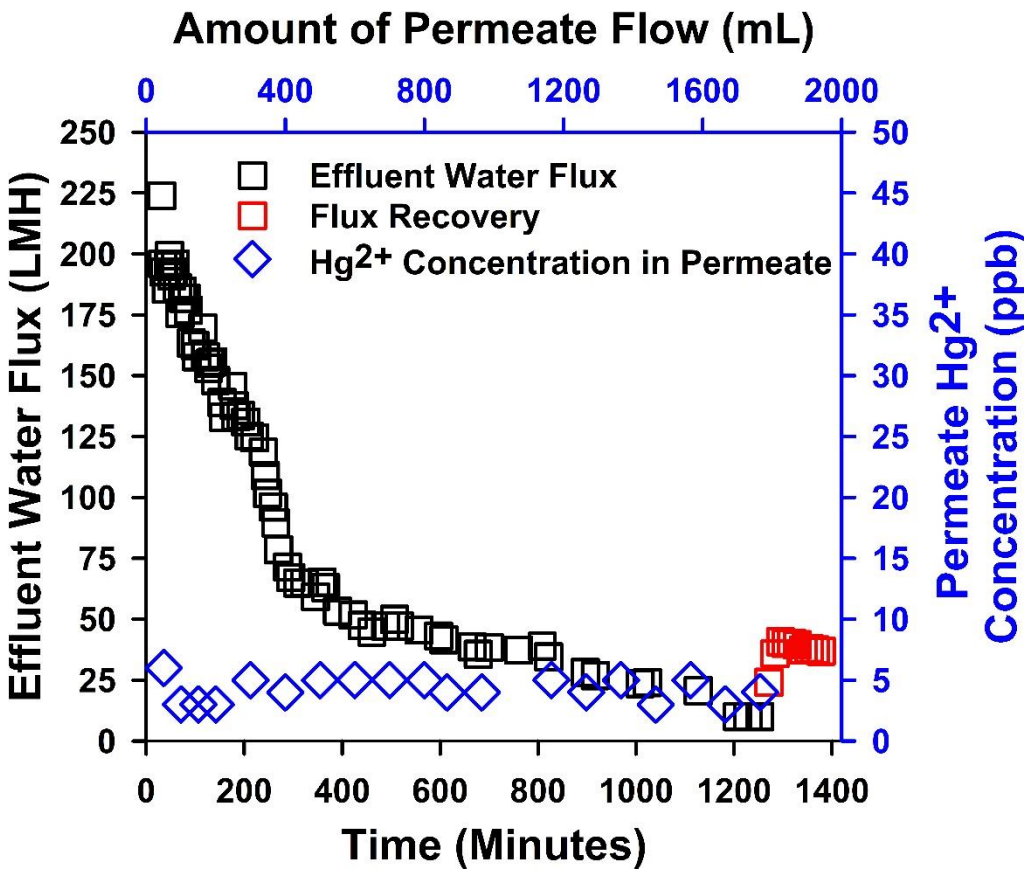


**Figure 9.4** Long term $Hg^{2+}$ adsorption study on CysM-PAA-PVDF membrane. A total of ~1700 mL spiked wastewater was passed through the membrane in convective flow mode at 2.72 bar. Initial concentration of $Hg^{2+}$ was approximately 110 ppb. Membrane Surface area was 13.2 $cm^2$. The test pressure is 2.72 bar. Flux pattern of spiked wastewater and flux recovery after adsorption study are shown on the primary (left) y-axis and the remaining dissolved $Hg^{2+}$ concentration in permeate is shown on the secondary (right) y-axis during 1300 minutes of operation.

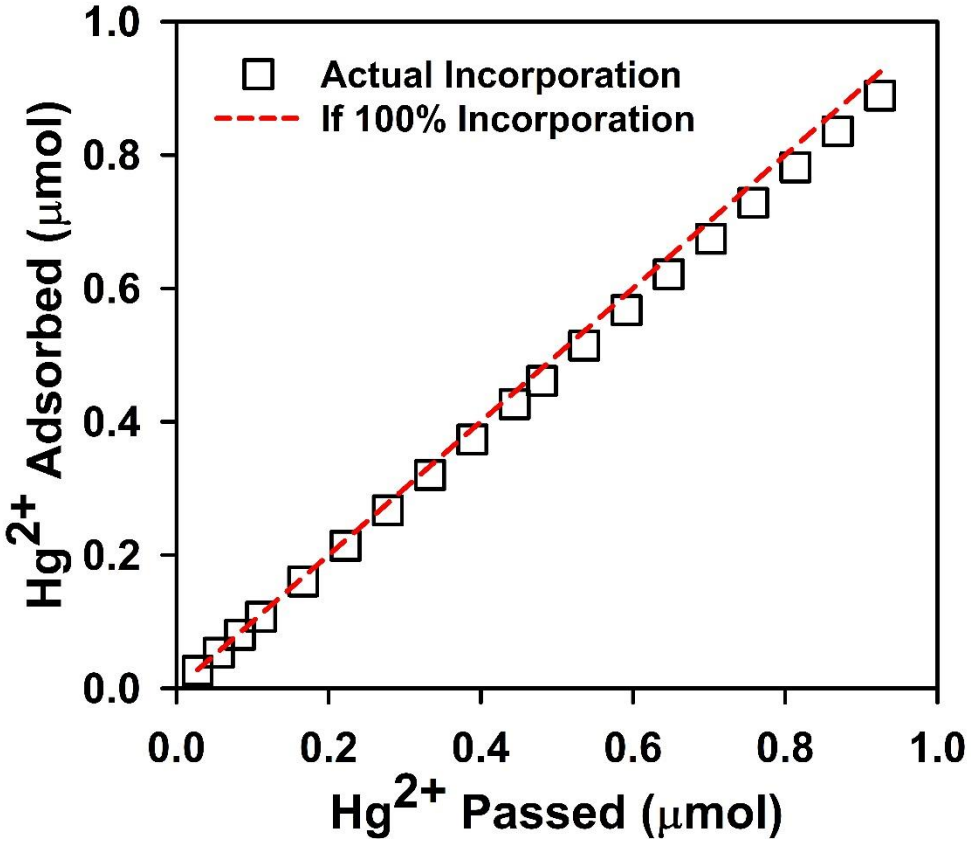


**Figure 9.5** Long term $Hg^{2+}$ adsorption performance (efficiency) of the CysM-PAA-PVDF membrane. A total of ~1700 mL spiked wastewater was passed through the membrane in convective flow mode at 2.72 bar. Initial concentration of $Hg^{2+}$ was approximately 110 ppb. Membrane Surface area was 13.2 $cm^2$. The test pressure is 2.72 bar.

## 9.5 Adsorption-Desorption Study of $Ag^{+}$ and $Hg^{2+}$ Cations on PAA-PVDF Membrane

Adsorption-desorption of heavy metals ($Ag^{+}$ and $Hg^{2+}$) on a PAA-PVDF membrane is also studied. The PAA-PVDF membrane could adsorb heavy metal ions ($Ag^{+}$ and $Hg^{2+}$) from water as it has carboxylic groups (-COOH) at the end of the polymer chain. The heavy metal ions ($Ag^{+}$ and $Hg^{2+}$) can hydrolyze in wide range of pH and enable to attach with carboxylic groups (-COOH) by replacing $H^{+}$ in a suitable pH [209]. However, this attachment is not permanent and by passing a low pH solution through the membrane it could be easily desorbed from the PAA chain of PAA-PVDF membrane. The adsorption-desorption profile is shown for silver (**Figure 9.6**) and mercury (**Figure 9.7**). The results confirm it is possible to attach and dislodge heavy metals in PAA chain of PAA-PVDF membrane. However, this PAA-PVDF membrane is not suitable for industrial application as if pH changes the heavy metals can easily detached from the PAA chain. It is worth to mention that, not all the $Ag^{+}$ and $Hg^{2+}$ cations attached in the PAA chain is not desorbed and a small fraction is permanently remain in the polymeric chain. These results support the hypothesis that the metal adsorption mechanism by thiol membranes involves covalent bonds, which limits desorption from the functionalized membrane [101].

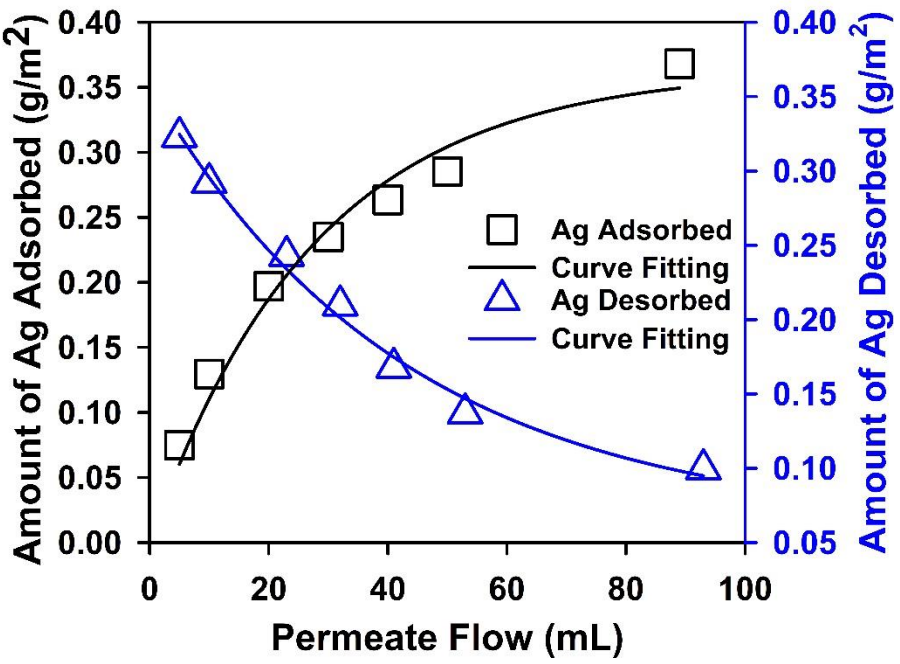


**Figure 9.6** The adsorption and desorption profile of $Ag^+$ cations on PAA-PVDF membrane. Membrane mass gain is 3.99%, water flux = 38.38 LMH at 2.04 bar, water pH = 5.2, flux during $Ag^+$ cations adsorption is 37.92 LMH at 2.04 bar. $Ag^+$ solution pH = 4.75. The initial concentration of $Ag^+$ solution is around 20 ppm. The flux during $Ag^+$ cations desorption is 45.6 LMH at 2.04 bar. Desorption solution pH =3.1. The effective membrane surface area is 13.2 $cm^2$. The cation solution is passed in convective flow mode across the membrane. Silver nitrate ($AgNO_3$) salt was used to prepare the cationic solution.

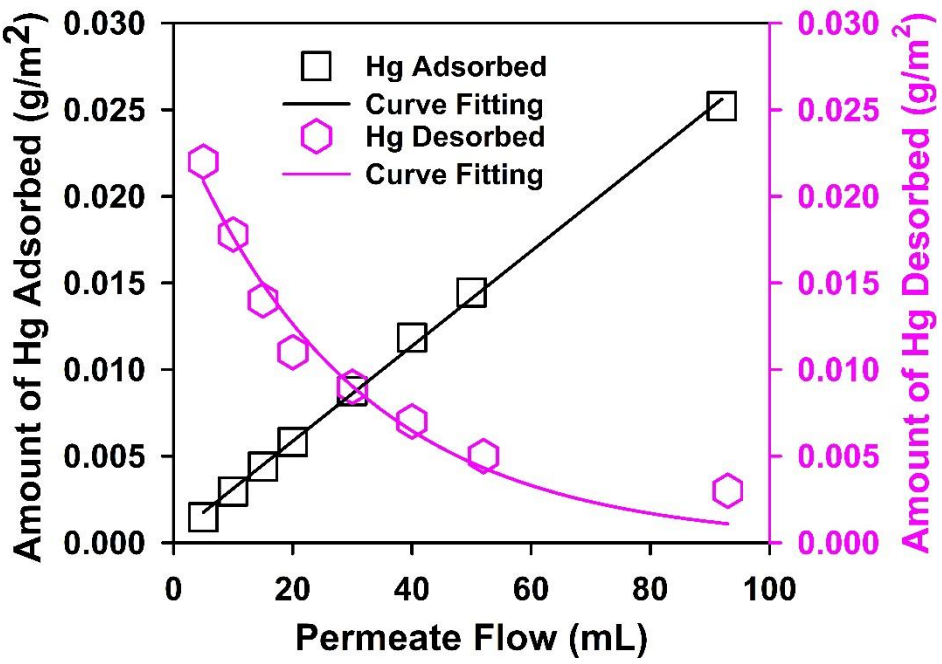


**Figure 9.7** The adsorption and desorption profile of $Hg^{2+}$ cations PAA-PVDF membrane. Membrane mass gain is 3.16%, water flux = 18.18 LMH at 2.72 bar, water pH = 5.1, flux during $Hg^{2+}$ cations adsorption is 12.86 LMH at 2.72 bar. $Hg^{2+}$ solution pH = 4.7. The initial concentration of $Hg^{2+}$ solution is around 400 ppb. The flux during $Hg^{2+}$ cations desorption is 21.6 LMH at 2.04 bar. Desorption solution pH =2.9. The effective membrane surface area is 13.2 $cm^2$. The cation solution is passed in convective flow mode across the membrane. Mercury (II) nitrate hydrate ($Hg(NO_3)_2 \cdot xH_2O$, x= 1-2) salts were used to prepare the cationic solution.

## 9.6 Adsorption Efficiency of Heavy Metals on Thiol Membrane

The adsorption efficiency of heavy metals on thiol membrane is further studied in detail. Here, adsorption efficiency is defined by number of thiol (-SH) groups are attached during convective flow of the permeate. In a simpler way it is the cations remain in the permeate divided by the cations in the feed times hundred. Once the PAA-PVDF membrane is functionalized with thiol (-SH) groups it can adsorb heavy metals from water. However, not all the thiol groups attached to the membrane will be exposed to adsorb heavy metals from water. The complex geometry of the membrane pores, small channeling to by-pass the attached thiol groups, inherited defects of the membrane pore structure, residence time and fouling with time are the key factors to hinder all the attached thiol groups to capture heavy metals from the solution. In order to study the adsorption efficiency of the heavy metals on thiol functionalized membranes, a CysM-PAA-PVDF membrane is exposed to capture heavy metals from water. Here, $Ag^+$ cations are used as a model compound and $Ag^+$ molar attachment to thiol groups is always 1 to 1. The synthetic water is used to avoid interference of adsorption of other cations and fouling. The result of the adsorption efficiency is shown in **Figure 9.8**.

The study was conducted for 820 minutes (approximately13.5 hours) by passing around 650 mL $Ag^+$ cation solution to make the experiment more pragmatic. During the whole experiment the solution permeability is kept constant to a value around 8 LMH/bar. The permeability is kept low to allow more residence time for adsorption of $Ag^+$ cations. In the first cycle, the calculated adsorption efficiency is around 77% while passing only 190 mL $Ag^+$ cation solution for 235 minutes (3.9 hours). However, the adsorption efficiency dropped to 48% during second cycle when another 190 mL $Ag^+$ cation solution passed for 310 minutes (5.16 Hours). For the next two cycles (third and fourth) the adsorption efficiency is almost constant to around 35% on average. The third cycle runs for for 231 minutes (3.85 hours) while passing 136 mL of $Ag^+$ cation solution and fourth cycle runs for 241.5 minutes (4 hours) passing 138 mL of solution. Though, it is expected the adsorption efficiency should be 100%, however, the factors mentioned earlier of this discussion play a pivotal role to reduce the heavy metal capture efficiency, deviating from the model membrane performance. It is worth to mention here that at initial stage, pore channeling plays a significant role on adsorption efficiency, but in later stage, less

accessibility to thiol (-SH) groups on pore vicinity and fouling eventually dominates the adsorption efficiency. This study confirms that removal of all dissolved heavy metal cations is not a realistic expectation for any industrial application. Pore channeling, reduced accessibility to thiol groups on pore vicinity, and fouling from wastewater constituents eventually limits the adsorption efficiency.

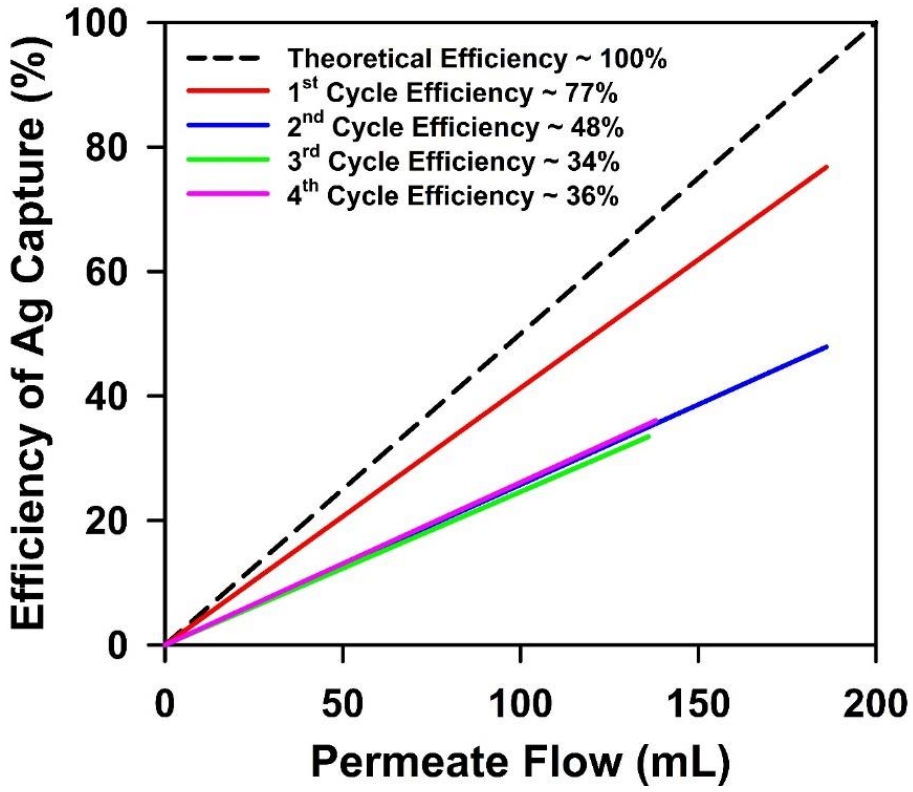


**Figure 9.8** The adsorption efficiency trend to capture $Ag^+$ cations on CysM-PAA-PVDF membrane. The membrane mass gain was 9.79%. Effective membrane surface area is 13.2 $cm^2$.The ICP-OES analysis of feed, permeate and retentate samples were used to do mass balance in order to calculate $Ag^+$ cations capture. Total experiment time was 820 minutes. Silver nitrate ($AgNO_3$) salt is used to prepare the cationic solution. The $Ag^+$ cation solution pH ~ 5.8 to 6.8. For, first cycle (red line), solution passed = 186 mL, time of operation = 235 minutes, $Ag^+$ cation concentration in feed = 10 ppm, for second cycle (blue line), solution passed = 186 mL, time of operation = 310 minutes, $Ag^+$ cation concentration in feed = 30 ppm, for third cycle (green line), solution passed = 136 mL, time of operation = 231 minutes, $Ag^+$ cation concentration in feed = 30 ppm,, for fourth cycle (pink line), solution passed = 138 mL, time of operation = 241.5 minutes $Ag^+$ cation concentration in feed = 20 ppm.

## 9.7 Effect of Presence $Ca^{2+}$ Cations in Wastewater on $Hg^{2+}$ Adsorption by Thiol Functionalized Membranes

Due to preferential cation adsorption, the presence of relatively high concentrations of common cations such as $Na^{+}$, $Ca^{2+}$, $Mg^{2+}$ in wastewater could reduce the sorption efficiency for soft Lewis acids with a strong affinity to thiols, specifically $Ag^{+}$ and $Hg^{2+}$ [131, 209]. The presence of dissolved salts in wastewater results in a specific in ionic strength, which causes multi cationic adsorption [131]. The impact of $Ca^{2+}$ cations on the adsorption of $Hg^{2+}$ efficiency of Cys and CysM thiol membranes was evaluated using synthetic water containing $Ca^{2+}$ and $Hg^{2+}$ salts and with wastewater spiked with $Ca^{2+}$ and $Hg^{2+}$. Results are depicted in **Figure 9.9**.

In this study, $Ca^{2+}$ was chosen due to its presecne in sample wastewater (see **Table 9.1**) and its location in activity series compare to $Ag^{+}$ and $Hg^{2+}$ cations [209]. Initially, an adsorption-desorption study of $Ca^{2+}$ cations on Cys-PAA-PVDF and CysM-PAA-PVDF membranes was conducted. The results of adsorption-desorption of $Ca^{2+}$ cations using thiol membranes (Cys/CysM-PAA-PVDF) are shown in **Figure 9.9a**. A 30 ppm of $Ca^{2+}$ solution was prepared using $CaCl_2$ salt with DIUF water (synthetic water). The resulting pH was approximately 5.8. This solution was passed through a membrane by convective flow at 1 bar, followed by a low pH (~ 2.5) solution to desorb the $Ca^{2+}$ cations. The results, depicted in **Figure 9.9a**, confirm that the majority of $Ca^{2+}$ was leached out of both membranes during the desorption study. The same sets of membranes were subsequently used to treat wastewater containing approximately 50 ppb $Hg^{2+}$ and 70 ppm $Ca^{2+}$ cations. The $Ca^{2+}$ adsorption profile for these wastewater sample is shown in **Figure 9.9b**, indicating that the CysM membranes adsorbed approximately 8% more $Ca^{2+}$ than the Cys membrane. **Figure 9.9c** depicts the adsorption profile of $Hg^{2+}$ from synthetic water that contained 150 ppb of $Hg^{2+}$ (prepared by dissolving $Hg(NO_3)_2 \cdot xH_2O$ (x= 1-2) salt in DIUF water). The adsorption efficiency is similar (~98%) for both Cys-PAA-PVDF and CysM-PAA-PVDF membranes. In contrast to the result of **Figure 9.9c**, the adsorption of $Hg^{2+}$ cations has significant affect with the presence of $Ca^{2+}$ cations in wastewater shown in **Figure 9.9d**. For CysM functionalized membranes the presence of $Ca^{2+}$ reduces $Hg^{2+}$ adsorption from 97.64% to 82% because both cations were adsorbed to the membrane. In comparison, for Cys functionalized membranes the adsorption dropped from 98% to 40%. This is due to all thiol

groups attached using Cys on membrane pore domain has an additional carboxyl group in functional chain. The $Ca^{2+}$ cations have a high affinity in the charge domain of membrane pores to carboxy group and hinder the covalent association of $Hg^{2+}$ cations to thiol groups, as demonstrated in **Figure 9.9d**. In literature the use of Cys and its derivatives to adsorb $Hg^{2+}$ shows a very common trend to use due to most of the adsorption results demonstrated based on synthetic water application [25, 107, 116]. The presence of other cations could result in reduced adsorption of heavy metals such as $Ag^{+}$ and $Hg^{2+}$ wastewater. In this context, CysM might be the preferred alternative for heavy metal adsorption due to its high adsorption in the presence of other cations.

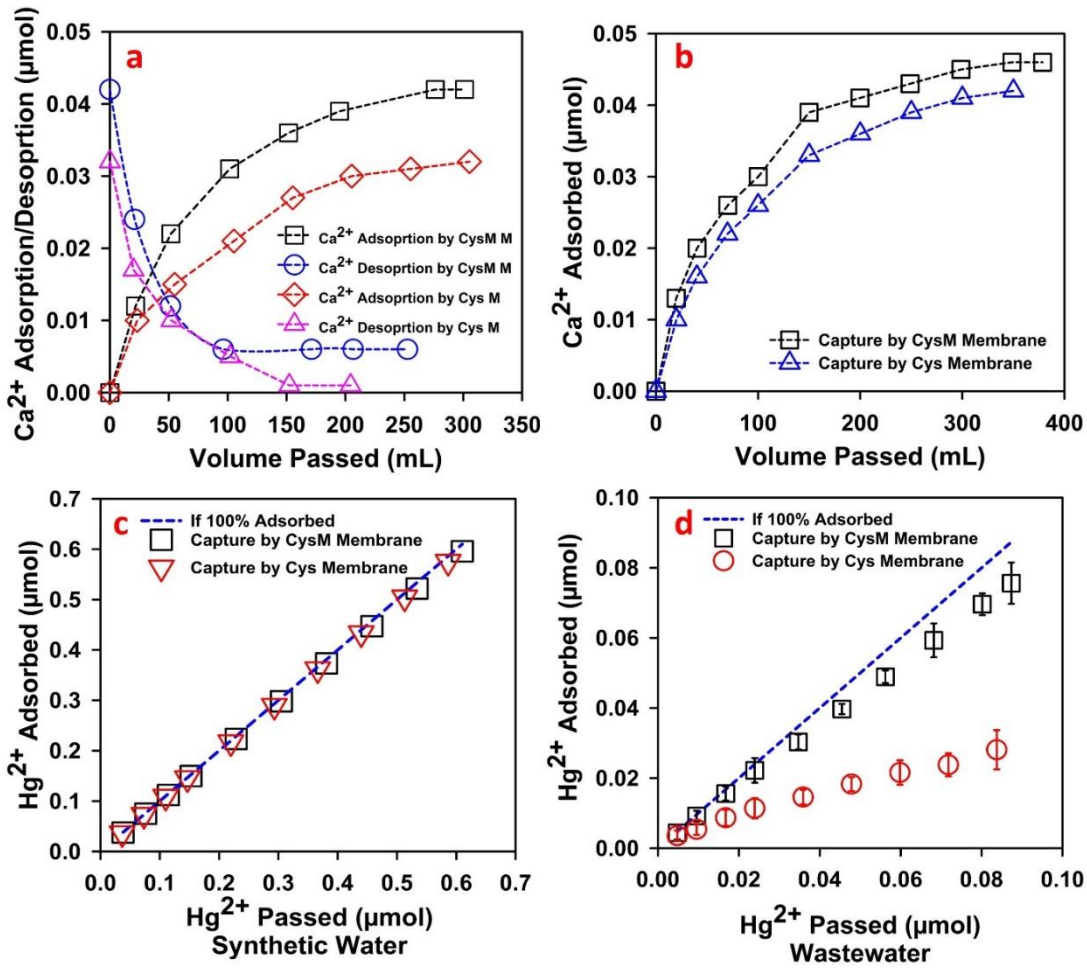


**Figure 9.9** Effect of the presence of $Ca^{2+}$ cations in synthetic and wastewater on $Hg^{2+}$ adsorption by thiol membranes (Cys/CysM-PAA-PVDF). **(a)** Adsorption and desoprtion profile of $Ca^{2+}$ in thiol membranes from synthetic water with an initial $Ca^{2+}$ concentration around 30 ppm, **(b)** Adsorption profile of $Ca^{2+}$ from the wastewater with the addition of $Hg^{2+}$, and $Ca^{2+}$ ions are to make a total feed concentration of approximately 50 ppb $Hg^{2+}$ and 70 ppm $Ca^{2+}$ , **(c)** Adsorption of $Hg^{2+}$ by thiol membranes from synthetic water with an initial $Hg^{2+}$ concentration of ~ 150 ppb, **(d)** Adsorption profile of $Hg^{2+}$ from spiked wastewater in presene of $Ca^{2+}$ cations for both thiol membranes. Initial concenteration of $Hg^{2+}$ ~ 50 ppb. The spiked wastewater pH was around 6.5 ~ 7. The mass gain of all the membranes used for this study was in the range of 5 ~ 8%.

## 9.8 Mercury Adsorption Analysis on CysM-PAA-PVDF Membrane by XPS

The analysis of the XPS spectrum back-up the adsorption of heavy metals ($Ag^{+}$/$Hg^{2+}$) on thiol (-SH) functionalized PAA-PVDF membrane. Both survey scan and high-resolution scan were conducted for XPS analysis. The Beta angles (degrees from vertical) of the XPS instrument was as following: monochromator (crystal) $60^{o}$, ion gun $58^{o}$, flood gun $58^{o}$ and height adjust microscope $45^{o}$, respectively. No tilt was used. The step size was 1 eV and 0.1 eV for survey and high-resolution scan. The pass energy was 200 eV and 50 eV for survey and high-resolution scan. XPS spectra were calibrated (charge correction) to a C1s peak value of 284.8 eV. The XPS survey scan after adsorption of $Hg^{2+}$ on CysM-PAA-PVDF membrane is demonstrated in **Figure 9.10a** showing the presence of Hg and S peaks over the top surface of the membrane. In addition of Hg and S peaks, the other observed peaks are for the elements C, N, O and F. The characteristic peaks of all the elements (Hg, S, C, N, O and F) are identified by comparing to the available literature data [100-101, 124, 212-213]. The leftmost peak identified in **Figure 9.10** around 100 eV is representing the Hg4f. The appearance of this peak is due to the binding of Hg with S of thiol (-SH) group yielding HgS. This is basically doublet peaks at binding energies of 101 and 106 eV which could be attributed to Hg 4f7/2 and Hg 4f5/2, shown separately in **Figure 9.10b** [101, 124, 212]. The next peak around binding energy of 164 eV could be assigned to R-SH binding or to presence of sulfur (S2p) from thiol (-SH) groups [124, 212]. Further observed peak around binding energy of 225 eV could be assigned to S2s peak as in this region the expected peak is for Molybdenum (Mo3d). However, in the examined sample there is no scope of presence of Molybdenum. However, it is worth to mention that S2s region strongly overlaps with Mo3d, when sulfur is present as sulfate. The next peak around binding energy of 286 eV is attributed to C1s peak [100, 213]. This is due to the presence of carbon in PVDF membrane, as well as, for the functionalization with AA and cross-linker MBA during incorporation of carboxylic (-COOH) groups in membrane. The N1s peak at binding energy of 400 eV is for N as amide (-NH2) in cross-linker MBA[100, 213]. The O1s peak at binding energy of 532 eV is due to the presence of O in carboxyl groups (-COOH) [100, 213]. The final identified peak at binding energy of 689 eV is for F1s [100]. This peak represents organic F which is present in fluorocarbon groups (-CF2-) of PVDF membrane.

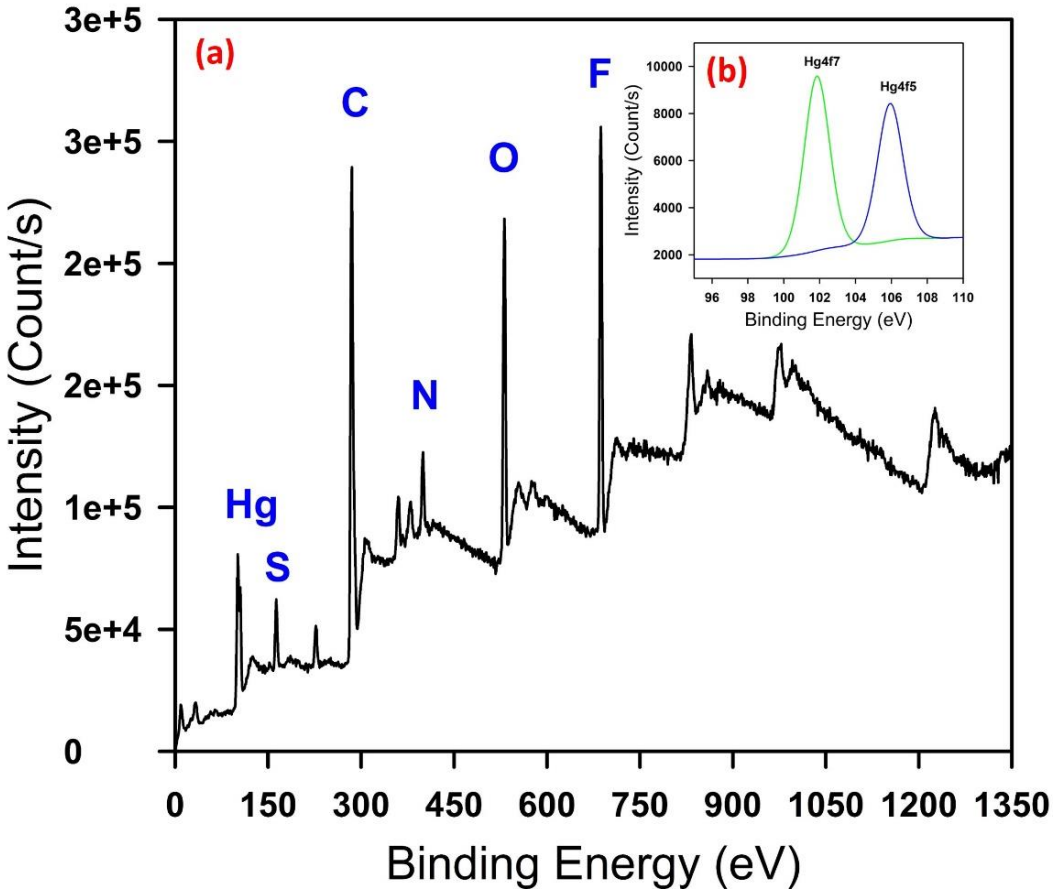


**Figure 9.10** The XPS spectrum of CysM-PAA-PVDF membrane after sorption of $Hg^{2+}$ from industrial effluent water. **(a)** The survey scan is showing the presence of elements Hg, S, C, N, O and F (from left to right), **(b)** The high-resolution scan shows elemental Hg confirmed by doublet peaks (Hg4f7 and Hg4f5).

## 9.9 Characterization of Depth Profile of Thiol Functionalized Membrane After Heavy Metal Capture

In order to confirm that the adsorption of $Ag^{+}$ and $Hg^{2+}$ on CysM-PAA-PVDF membrane occurs across the pore depth and not only on surface of the membrane, the cross-section of the membrane was characterized by FIB, depicted in **Figure 9.11**. The cross-section of the membrane was milled using the FIB instrument using the technique mentioned elsewhere [35]. This method of characterization allows for precise slices with smooth surfaces for characterization inside the membrane pores. Only adsorption of $Ag^{+}$ on CysM-PAA-PVDF membrane was characterized to avoid contamination of the FIB sample chamber by $Hg^{2+}$ adsorbed membranes. In **Figure 9.11a,** the whole cross-section of the sample membrane is visible, which is milled along with r- and z-direction. In **Figure 9.11b**, the atomic ratio of Ag to F at different depths in z-direction of the membrane demonstrates a relatively even adsorption of $Ag^{+}$ cations across the entire cross-section (i. e. the whole pore) of the membrane. The distribution of atomic C, F, S and Ag in the milled area is shown in **Figure 9.11c**. This observation is consistent with literature describing membranes for other applications [180, 214]. The coexistence of Ag and S in the same location of the membrane cross-section, shown in **Figure 9.11c,** suggests reaction of thiol groups to Ag in a 1 to 1 molar ratio (shown Ag in red and S in green). Another distinct observation is that S and Ag are concentrated on the circumferences of pore mouths. This suggests that the pores are not blocked due to thiol functionalization using CysM, but that thiol functionalization take place across the pore walls of PAA-PVDF membrane. The line scan data of F and Ag atomic percentage in r-direction at a distance of 53 µm from the membrane top surface, as shown in **Figure 9.11d,** suggests a homogenous distribution ratio of F and Ag. The EDX scanning results for the top surface of CysM-PAA-PVDF membrane after adsorption of $Ag^{+}$ cations from synthetic water is depicted in **Figure 9.12** and summarized in **Table 9.3**. This detail characterization of cross-section of CysM-PAA-PVDF membrane by FIB demonstrates that the adsorption of heavy metals is not only a surface phenomenon but occurred across the entire length of the membrane pores.

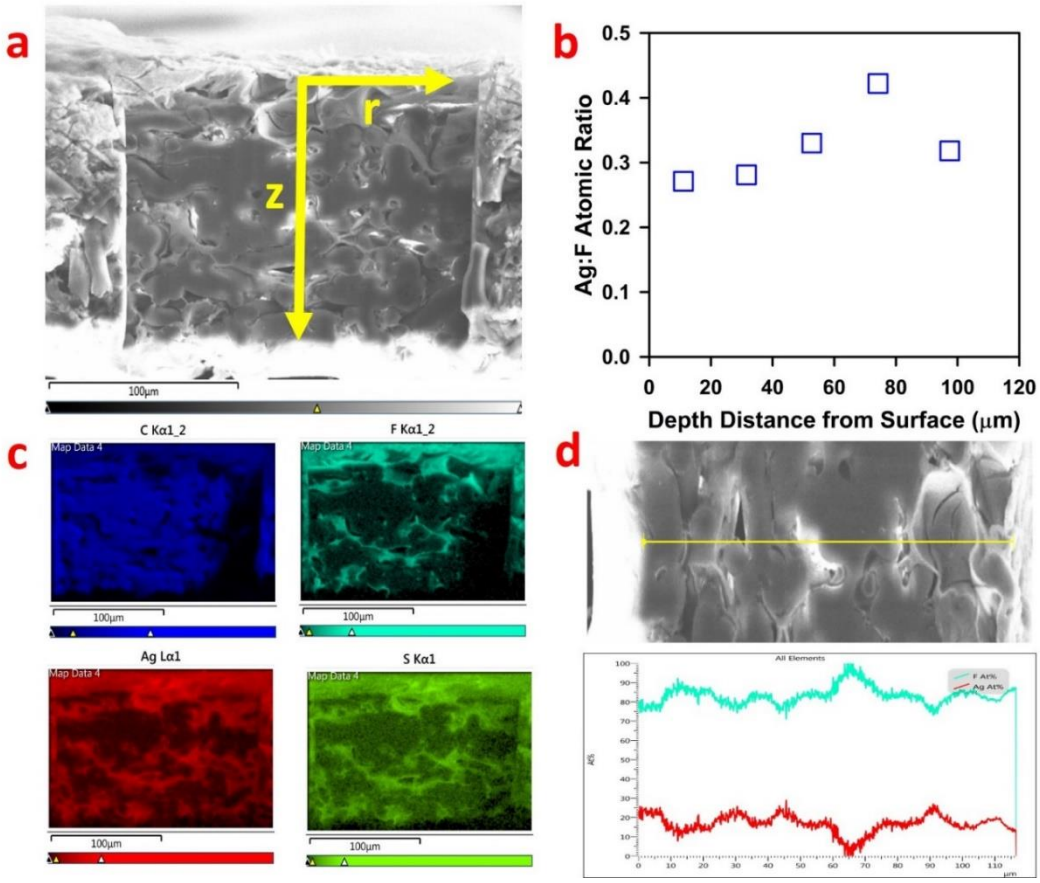


**Figure 9.11** Characterization of the cross-section of CysM-PAA-PVDF membrane by FIB instrument to assess the elemental composition after adsorption of Ag as a model compound. The FIB was used to prepare the entire cross-section (~120 µm) with an ion beam (2.5~6 nm) ensuring minimum damage of the sample. **(a)** The sample of whole membrane cross-section, the smooth area in the center was removed by FIB, the elemental composition is assessed in both z- and r-direction, **(b)** The Ag to F atomic ratio in different depth of the membrane confirming almost even adsorption of $Ag^+$ cations across the whole cross-section (i. e. the whole pore) of the membrane. The F is used as a standard as it is homogeneously distributed in PVDF membrane, **(c)** The distribution profile of atomic C, F, Ag and S in a depth of around 53 µm from the top surface is demonstrated. The Ag (red) and S (green) are almost evenly distributed confirming all the thiol (-SH) sites are utilized, **(d)**The line scan data of F and Ag atomic percentage in r-direction at a distance of 53 µm from the top surface.

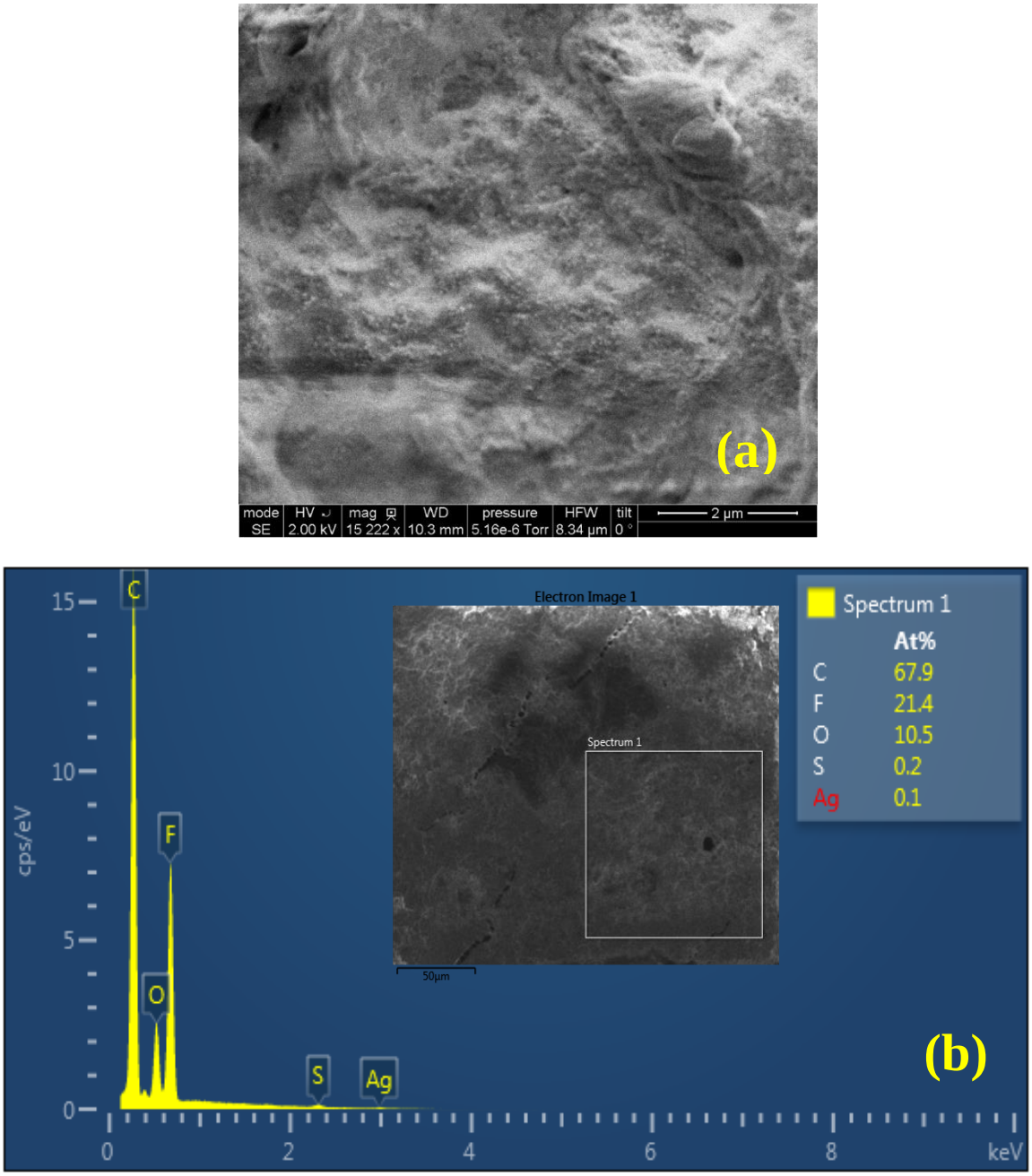


**Figure 9.12 (a)** The SEM image of CysM-PAA-PVDF membrane after adsorption of $Ag^{+}$ cations from the solution by convective flow mode, **(b)** the EDX analysis shows the presence of Ag on the surface of CysM-PAA-PVDF membrane along with C, F, O and S. The inset picture is also showing the atomic percentage of C, F, O, S and Ag. The membrane mass gain was 4.49%. The feed concentration was around 90 ppm.

**Table 9.3** Summary of the EDX scanning results for the top surface of CysM-PAA-PVDF membrane after adsorption of $Ag^+$ cations from the water. The membrane mass gain was 4.49%. The feed concentration of $Ag^+$ cation solution was around 90 ppm was passed through the membrane in convective flow mode. The solution pH was around 4.8-5.3. The solution was prepared by using $AgNO_3$ salt. The atomic composition of Carbon (C), fluorine (F), oxygen (O), sulfur (S), and silver (Ag) were measured in different locations of the membrane sample during EDX analysis.

| Location | C (At%) | F (At%) | O (At%) | S (At%) | Ag (At%) |
|---|---|---|---|---|---|
| **1** | 67.87 | 21.42 | 10.49 | 0.15 | 0.07 |
| **2** | 66.53 | 22.63 | 10.56 | 0.19 | 0.10 |
| **3** | 66.54 | 19.89 | 13.20 | 0.24 | 0.13 |
| **Average** | 66.98 | 21.31 | 11.42 | 0.19 | 0.10 |
| **Standard Deviation** | 0.77 | 1.37 | 1.54 | 0.05 | 0.03 |

## 9.10 Mathematical Model to Predict Break-through Profile for Adsorption of Heavy metals on Thiol Functionalized Membrane

For industrial application, a membrane model with similar attributes of thiol membrane used for experimental study can be used to predict heavy metal adsorption breakthrough profiles to evaluate the life span of the operation. A well-defined model can assist with optimizing the wastewater flux, adjust concentration profile, calculate life span of membrane, and predict performance efficiency of adsorption. In this regard, a thiol membrane was modeled to predict the adsorption profile of heavy metal cations in the membrane. From the experimental study the adsorption is linear with time, and the membrane model can be considered a one-dimensional unsteady state problem where the adsorption is taking place only in the direction of pore length [24, 215]. In order to obtain a realistic model of the adsorption to match the experimental results, an $Ag^+$ cation adsorption study was conducted because it attaches with thiols groups in 1:1 molar ratio. The membrane model can be described in terms of three different phases: **i)** inert polymer phase ($\boldsymbol{\emptyset_{PVDF}}$), **ii)** thiol functionalized phase ($\boldsymbol{\emptyset_{SH\text{-}PAA}}$), and **iii)** aqueous $Ag^+$ cation solution phase occupying part of the free volume fraction of the membrane ($\boldsymbol{\emptyset_{free\ space}}$). The schematic of the model membrane is shown in **Figure 9.13** as a combination of the three phases.

The following terminology is used for the model:

$\emptyset_{pore}$= Pore volume fraction;

$\emptyset_{PVDF}$ = PVDF volume fraction;

$\emptyset_{pore} = \emptyset_{free\ space} + \emptyset_{SH\text{-}PAA}$ … … … … **EQ (9.1)**

Here, $\emptyset_{pore} + \emptyset_{PVDF} = 1$ … … … … **EQ (9.2)**

$C'$ = Concentration of $Ag^+$ in liquid phase (moles of $Ag^+/m^3$ of liquid);

$q'$ = concentration of silver in SH-PAA layer (moles of $Ag^+/m^3$ of SH-PAA layer);

$q_{eq}$ =maximum concentration of silver in PAA-SH layer for $C'$ (moles of $Ag^+/m^3$ of SH-PAA layer);

$J_W$ =membrane water flux (m/s);

$t'$= time (s);

$z'$ = distance down the membrane thickness (m).

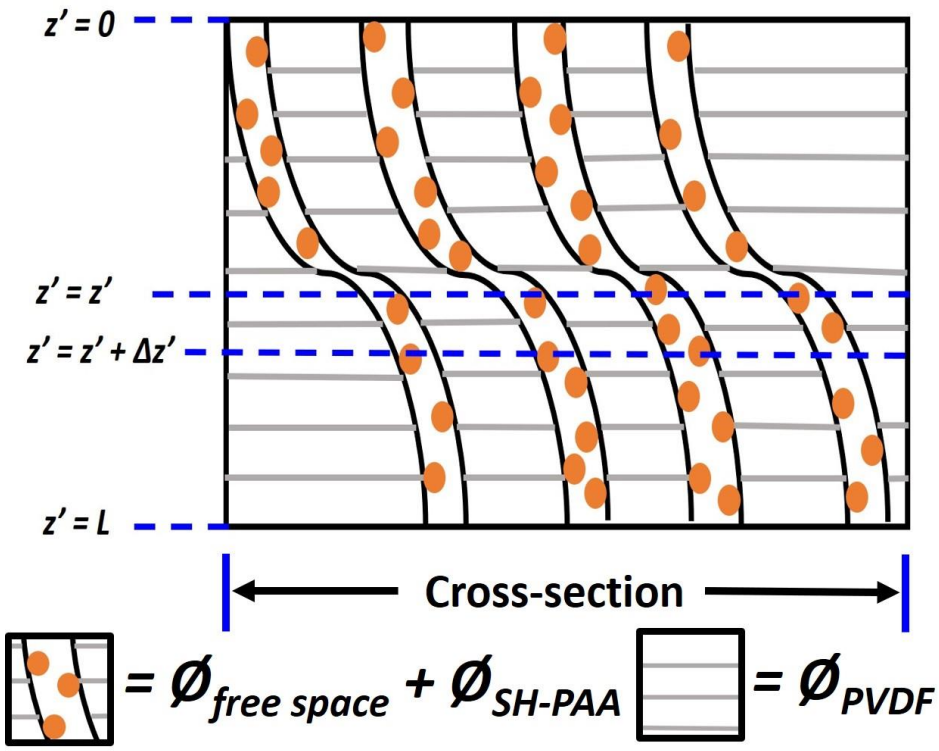


**Figure 9.13** Schematic representation of the cross-section of the CysM-PAA-PVDF membrane for mathematical modelling.

All quantities used in model are initially expressed in SI units. The quantities are subsequently converted to suitable units for comparison and discussion of the experimental and predicted results. The partial differential equations (PDE) governing linear adsorption are described by **equation 9.3** and **equation 9.4** [215]. **Equation 9.3** is a mass balance of $Ag^+$ on the liquid phase and **equation 9.4** is the mass balance of $Ag^+$ on stationary phase (SH-PAA). This is a modification of our previously published model for mixed matrix membrane containing thiol functionalized silica particles [24].

A mass balance of $Ag^+$ in the liquid phase over an element shown in **Figure 9.13** yields

$$\emptyset_{free\ space}\frac{\partial C\prime}{\partial t\prime}+J_W\frac{\partial C\prime}{\partial z\prime}+\left(1-\emptyset_{PVDF}-\emptyset_{free\ space}\right)\frac{\partial q'}{\partial t'}=0 \ldots\ldots\ldots\ldots \textbf{EQ (9.3)}$$

A mass balance of $Ag^+$ in the stationary phase (SH-PAA) will consequently derive

$$\frac{\partial q'}{\partial t'}=K(q_{eq}-q') \ldots\ldots\ldots\ldots \textbf{EQ (9.4)}$$

Where, $K$ is the mass transfer coefficient of $Ag^+$ into the stationary phase (SH-PAA). The initial boundary conditions are:

$$C'(0, t') = C_0, \qquad q'(z', 0) = 0, \qquad C'(z', 0) = 0$$

For this system the axial diffusion can be neglected as compared to axial convection. To solve **equation (9.3)** and **(9.4)** the following linear relationship between $q_{eq}$ and $C'$ is assumed:

$$q'_{eq}=\gamma C' \ldots\ldots\ldots\ldots \textbf{EQ (9.5)}$$

Here, γ = silver-thiol affinity constant. In this model, γ is a function of pore density of thiol groups [24]. Substituting **equation (9.5)** into **equation (9.4)** generates:

$$\frac{\partial q'}{\partial t'}=K(\gamma C'-q') \ldots\ldots\ldots\ldots \textbf{EQ (9.6)}$$

The above equation can be made dimensionless by defining the following variables as:

$$C=\frac{C\prime}{C_0} \qquad q=\frac{q\prime}{q_\infty} \qquad z=\frac{z\prime}{L} \qquad t=\frac{t\prime}{T_S} \qquad \text{Where,}$$

$C_0$ = inlet feed concentration of $Ag^+$ (mol of $Ag^+/m^3$);

$q_\infty$ = maximum $Ag^+$ capture (mol of $Ag/m^3$ of SH-PAA);

$L$ = membrane thickness (m);

$T_S$ = time at which break-through of $Ag^+$ adsorption was observed, and experiment was terminated (s).

The break-through for $Ag^+$ adsorption can vary depending on the thickness of the thiol functionalized layer on membrane, the concentration of the heavy metal solution, and the residence time.

The final dimensionless system of initial PDE (**Equations 9.3** and **9.4**) consists of two unsteady state partial differential equations:

$$\frac{\emptyset_{free\ space}\, L}{J_w T_s}\frac{\partial C}{\partial t} + \frac{\partial C}{\partial z} + \left(1 - \emptyset_{PVDF} - \emptyset_{free\ space}\right)\frac{KL}{J_w}\left(\gamma C - q\frac{q_\infty}{C_0}\right) = 0 \ldots\ldots\ldots\ldots \textbf{EQ (7)}$$

and

$$\frac{\partial q}{\partial t} = \frac{KT_s C_0}{q_\infty}\left(\gamma C - q\frac{q_\infty}{C_0}\right) \ldots\ldots\ldots\ldots \textbf{EQ (8)}$$

COMSOL Multiphysics 5.4 software platform was used to solve **equations 9.7** and **9.8**. Multiphysics convection-diffusion transient state analysis was applied to the one-dimensional domain [215]. The model parameters are mostly obtained from the experimental study and are as follows:

$C_0$ = feed of $Ag^+$ cation concentration = 0.85 mol/$m^3$ (~90 ppm);

$L$ = $120\times10^{-6}$ m (120 µm) (membrane thickness along with backing material measured by FIB instrument);

$J_W$ = $6.93\times10^{-5}$ m/s (~250 LMH);

$\emptyset_{pore}$ = 0.52 (based on membrane data sheet);

$\emptyset_{PAA\text{-}SH}$ = 0.35 and γ = 5021.

Both $\emptyset_{SH\text{-}PAA}$ and γ are calculated based on a previous study [24, 100]. In **equation 9.7** an artificial diffusion term is added to get a stable numerical solution. A diffusivity value of $1.80\times10^{-9}$ $m^2/s$ for $AgNO_3$ was used for calculations based on the reported literature data [216]. The only unknown parameter remaining was the volumetric mass transfer coefficient ($K$), which was used as an adjustable parameter to match the predicted data with experimental data. Mass transfer coefficients for packed columns (gas-liquid) typically range between 0.005 and 0.02 $s^{-1}$ [217]. A $K$ value of 0.0058 $s^{-1}$ is therefore well-fitted in the range [24]. The predicted and experimental breakthrough curves are shown in **Figure 9.14**. The breakthrough of $Ag^+$ cation adsorption on membranes appears around the same elapsed time (~38 minutes) of operation for both predicted and experimental studies. However, for our experimental study, pore channeling, lower accessibility to thiol groups on pore

vicinity, and fouling limits the adsorption efficiency to ~80%. The rational agreement between predicted and experimental data in this study anticipates that the membrane model is helpful to predict experimental results over a wide range of operating conditions and parameters like thiol loading in terms of membrane mass gain, wastewater flux, heavy metal adsorption capacity, wastewater metal concentration and membrane thickness. More broadly, this model may be used to model other membrane adsorption processes.

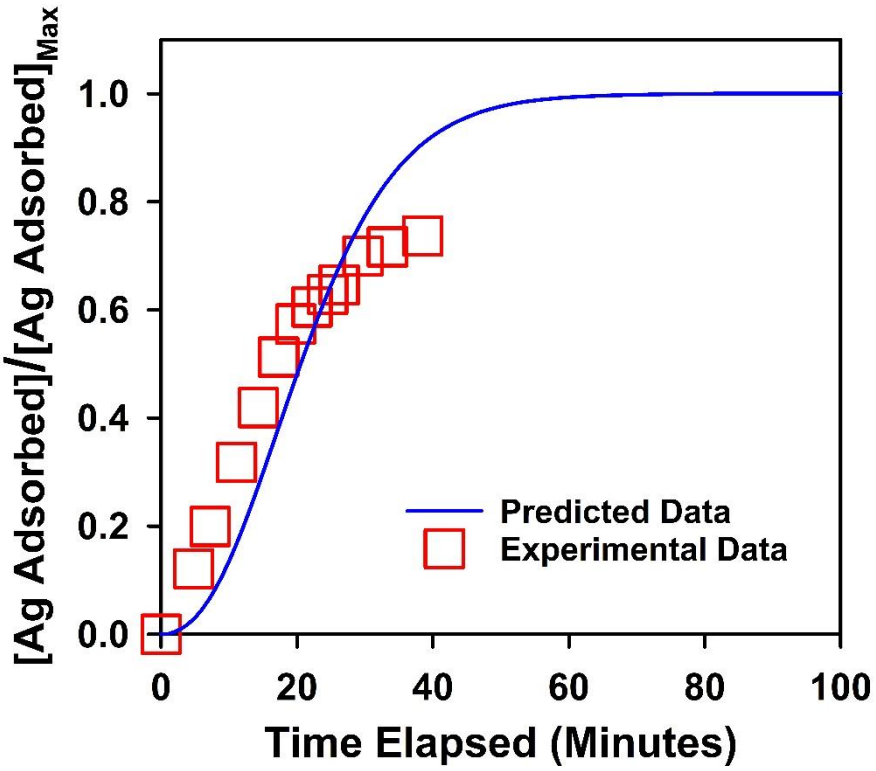


**Figure 9.14** Comparison of experimental and predicted data for breakthrough profile for $Ag^{+}$ cations adsorption on thiol membrane. Here Ag used as a model compound.

# CHAPTER 10. HOLLOW (FE AND PD-FE) NANOPARTICLES CHARACTERIZATION AND APPLICATION TOWARDS DEGRADATION OF CHLORINATED ORGANIC COMPOUNDS

## 10.1 Overview

This chapter discusses the detail characterization and preliminary application towards degradation of chlorinated compounds using in-house synthesized hollow nanoparticles (NPs). Hollow NPs are a unique class in the functional materials and get attention due to their thin shell, inner void space and, doubled surface area [218-219]. These hollow and porous NPs have potential applications is the area of drug delivery, controlled release of drugs, catalysis, artificial cells, chemical storage, lightweight fillers, adsorptive materials, and chemical sensors [220-222]. Two types of hollow NPs were prepared. Fe and Pd-Fe. Details characterization of the prepared samples were conducted by XRD, BET, DLS, TEM, SEM and FIB. Initial study reveals this fabricate Fe hollow spheres have 2.6 times higher surface area and 4.28 times pore volume compare to commercial Fe catalyst. The average size of the Fe hollow NPs is in the size range of 100 to 1200 µm. However, the DLS measurement reveals 30% of the hollow NPs are in 100 nm size. However, some bigger hollow spheres are also formed in the range of 500 nm to 1.2 µm, which helped to characterize the particles with TEM, SEM and FIB by cutting the cross-section of the spheres. The shell thickness is in the range of 20 to 40 nm. Finally, these prepared Fe, Pd-Fe hollow NPs are used towards degradation of chlorinated organic compounds. Initial investigation reveals that these prepared hollow NPs can completed degrade polychlorinated biphenyl (PCB-1) with an 74% recovery of biphenyl within 20 minutes anticipating future potential for water remediation application.

## 10.2 Characterization of Hollow Fe Nanoparticles

All the prepared hollow NPs are characterized by XRD, BET, DLS, TEM, SEM and FIB instrument to understand the morphology, structure, size, shape and formation of the nanoparticles.

### *10.2.1 XRD, BET Surface Analysis and DLS Measurements for Hollow Nanoparticles*

The XRD pattern of Fe hollow spheres before (red color) and after calcination (blue color) is shown in **Figure 10.1.** The patter indicates high crystalline form of iron oxide NPs

due to the iron precursor used and due to calcination. Sharp, strong, and well-resolved diffraction peaks reveal the phase purity and crystalline structure of as-prepared nanomaterial which are consistent with reported literatures [137, 223-224]. Existing peaks become more intense after calcination at 550°C for 4 hours. Additional $Fe_2O_3$ [104] peak pops up after calcination.

Brunauer-Emmett-Teller (BET) surface area, Barrett-Joyner-Halenda (BJH) average pore diameter, and pore size distribution were measured using nitrogen adsorption at -196°C with a Micromeritics TriStar 300 instrument. Particles were degassed at 140°C for three hours with flowing ultra-high purity (UHP) Nitrogen gas prior to analysis. Nitrogen adsorption isotherms as measured are shown in **Figure 10.2**. The calcined hollow Fe NPs, commercial Fe catalyst and uncalcined hollow Fe NPs are depicted blue, green and red color as shown in **Figure 10.2**. For all, type III isotherms are observed. High hysteresis loop in hollow Fe NPs suggests nonuniform size of hollow spaces. This is due to different sizes of hollow NPs formation during calcination stage. For uncalcined hollow Fe NPs there is no nitrogen adsorption-desorption observed. **Figure 10.3** shows pore distribution of calcined hollow Fe NPs depicted in blue color. Here, calcined hollow Fe demonstrates bimodal peak. The first peak around 3 nm is probably due to the intraparticle distances and the second broad peak around 20 nm is the hollow passage throw the core shell of the spherical wall. For commercial catalyst a single peak around 2 nm is observed which is for intraparticle distances as shown in green color in **Figure 10.3**. No pore was observed before calcination of hollow Fe NPs as shown in red color in **Figure 10.3**. The measured BET surface area and BJH pore volume for calcined hollow Fe NPs, commercial Fe catalyst and uncalcined hollow Fe are tabulated in **Table 10.1**. Hollow Fe NPs has BET surface area of 79.4 $m^2/g$, which is 2.5 times higher than commercial Fe catalyst with a BET surface area of 31.1 $m^2/g$. Calcination of Fe NPs increases the surface area 58.8 times BJH pore volume for hollow Fe NPs and commercial Fe catalyst is 0.403 and 0.094 $cm^3/g$, which is 4.28 times higher, suggesting huge hollow area inside the core shell wall of Fe NPs.

**Figure 10.4** shows the size distribution of Fe NPs dissolved in methanol. The prepared Fe NPs are well dispersed in methanol, ethanol and water. The distribution in **Figure 10.4** is 20 times dilution of original samples revealing 30% of the hollow Fe NPs

are in 100 nm size. The measurement was conducted with in half, 10 times and 20 times dilution. Both in 10- and 20-times dilution the average particle diameter was observed around 100 nm.

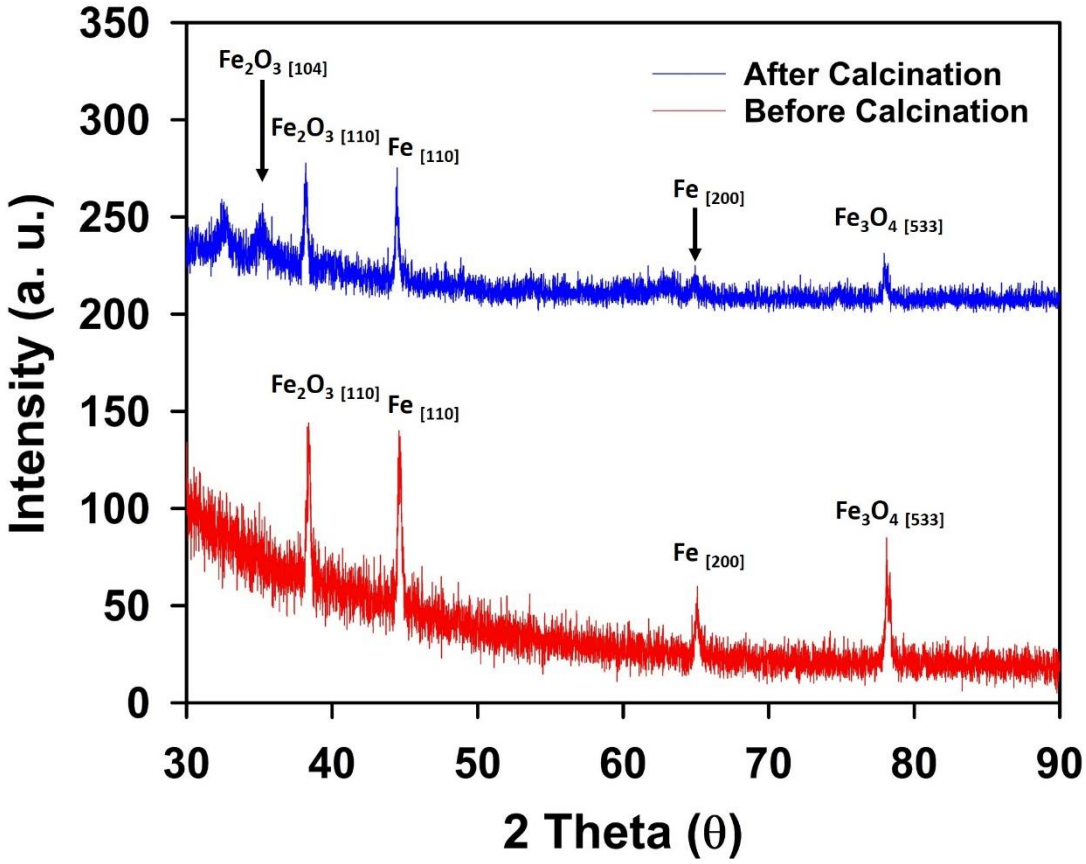


**Figure 10.1** XRD pattern of hollow iron oxide nanoparticles before (red) and after calcination (blue). Existing peaks become more intense after calcination. Additional $Fe_2O_3$ [104] peak pops up after calcination.

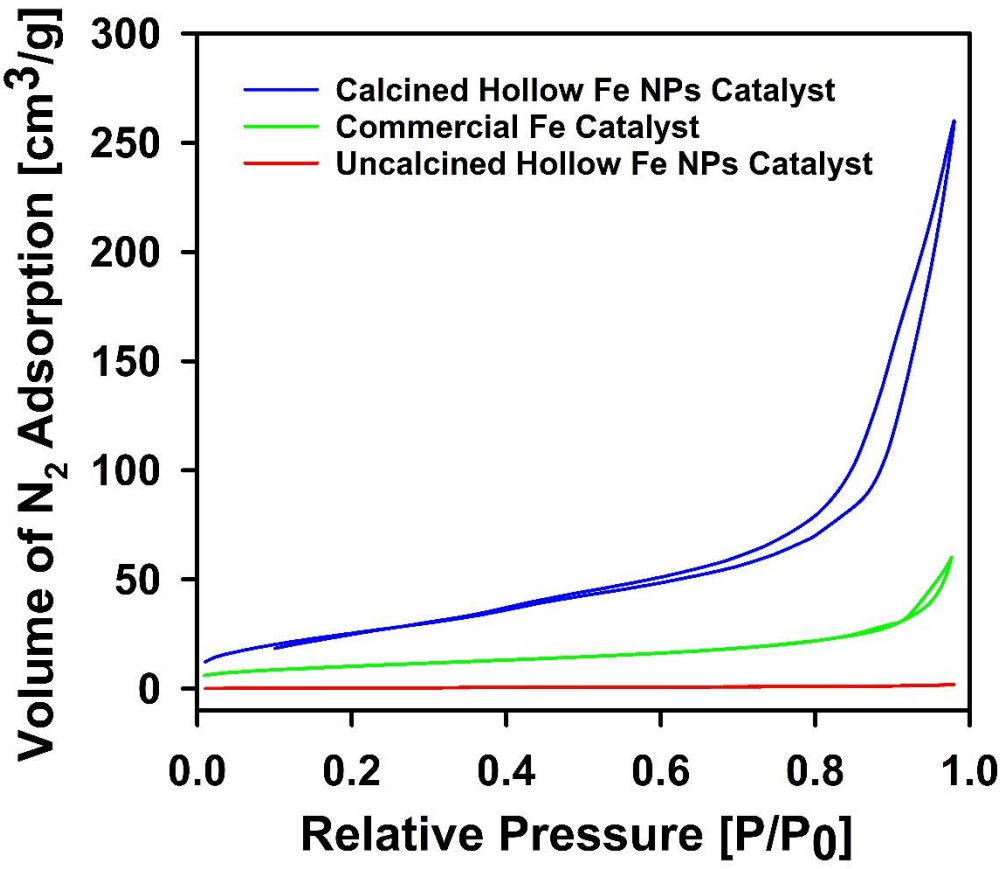


**Figure 10.2** Nitrogen adsorption-desorption isotherms of calcined hollow Fe NPs (blue), commercial Fe catalyst (green) and uncalcined hollow Fe NPs (red) measured by BET surface analyzer.

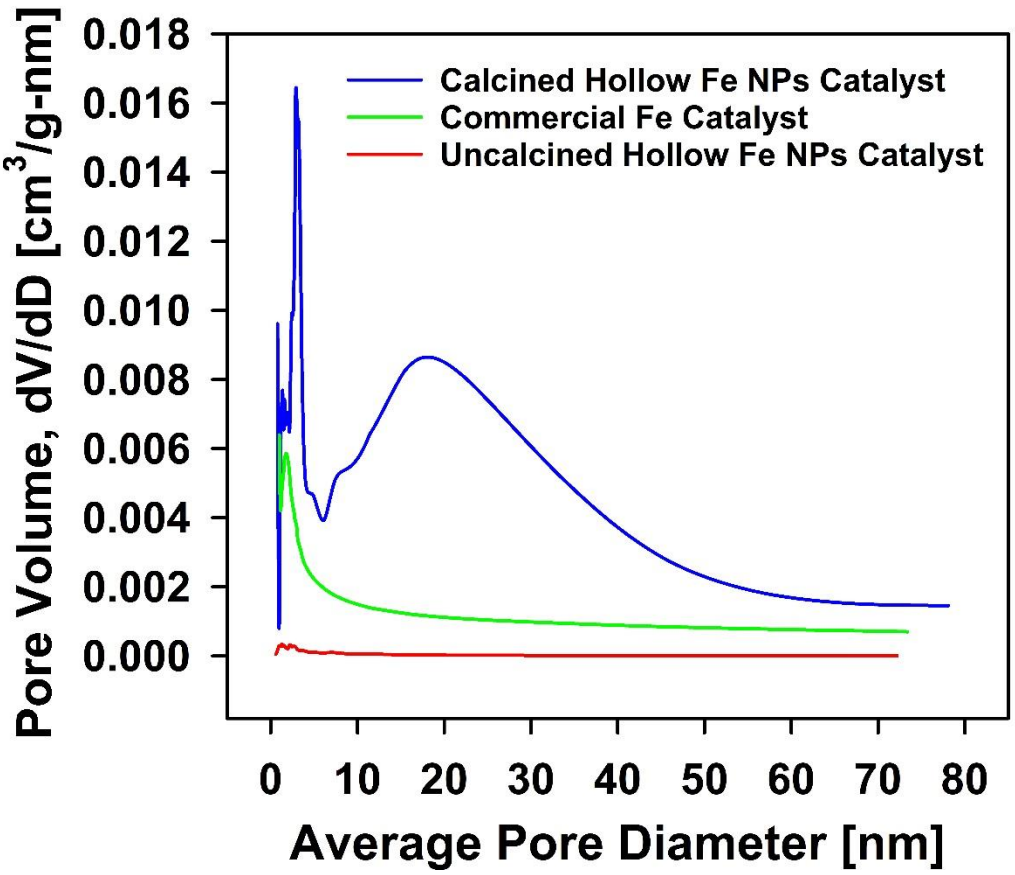


**Figure 10.3** Pore distribution of calcined hollow Fe NPs (blue), commercial Fe catalyst (green) and uncalcined hollow Fe NPs (red) measured by BET surface analyzer.

**Table 10.1** Comparison of BET surface area, pore volume and pore diameter of hollow and commercial Fe Catalysts.

| Sample | BET Surface Area ($m^2/g$) | BJH Pore Volume ($cm^3/g$) | Average Pore Diameter (nm) |
|---|---|---|---|
| **Calcined Hollow Fe** | 79.4 | 0.403 | 20 |
| **Uncalcined Fe** | 1.35 | 0.003 | - |
| **Commercial Fe Catalyst** | 31.1 | 0.094 | - |

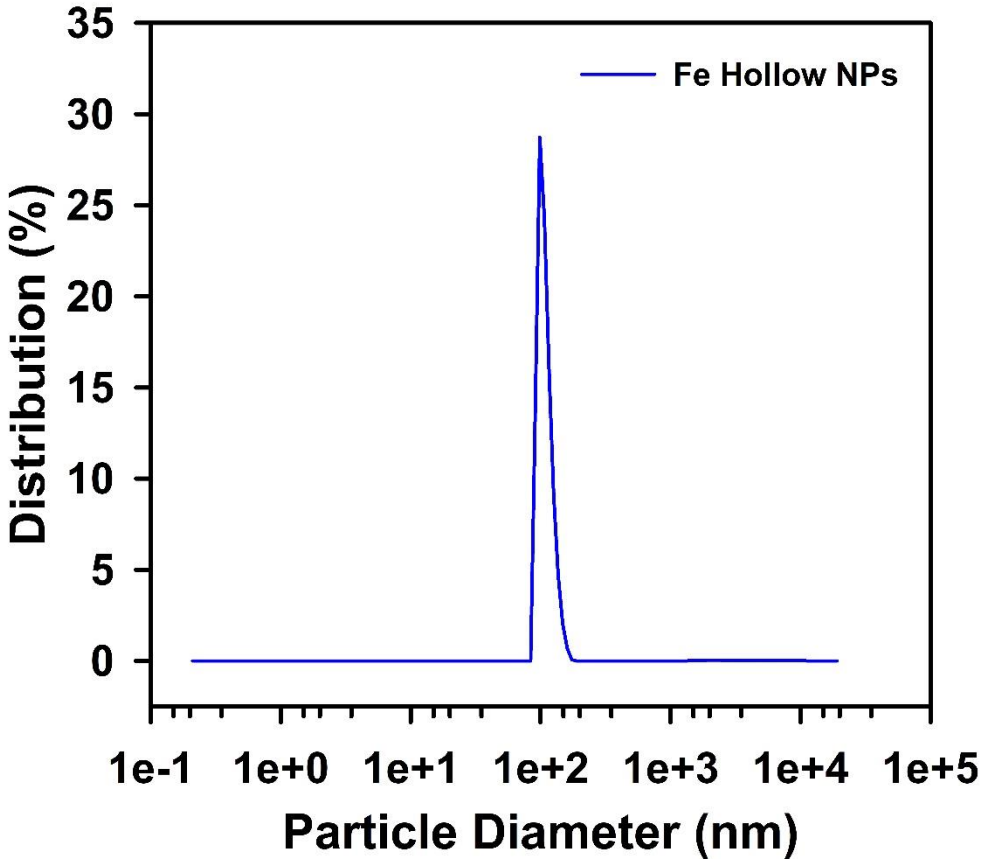


**Figure 10.4** Nanoparticles size was measured by dissolving hollow Fe NPs in methanol by DLS instrument. The solution was 20 times.

*10.2.2 TEM, SEM and FIB Analysis for Hollow Nanoparticles*

Hollow spherical structure of Fe NPs is confirmed by TEM characterization. **Figure 10.5** shows the TEM and HR-TEM images of the synthesized hollow Fe NPs structures as typical representatives from two different locations of copper grid. The low-resolution TEM image **Figure 10.5 (a, b, e, f)** further suggest homogeneous sized spherical nature of the synthesized Fe NPs. The difference in the contrast in the corresponding magnified TEM images shown in **Figure 10.5 (a, b, e, f)** confirmed the formation of hollow spherical nanostructures with a shell thickness of 20 to 40 nm. A representative high-resolution transmission electron microscopy (HR-TEM) images of the Fe NPs nanostructures are shown **Figure 10.5 d, h**. These images suggest the sheets to be very thin and composed of 3 to 4 stacked iron oxide layers. These results also match with the reported literatures where different metals were used to prepare hollow structured materials [133, 137, 139, 144]. **Figure 10.6 a, b** shows EDS analysis in two different locations confirming formation of Fe-oxide NPs. The SAED diffraction pattern in location 1 (**Figure 10.6a**) of Fe hollow NPs is shown in **Figure 10.6c**. Multiple diffraction rings representing phases of oxides of hollow Fe NPs. EDS line scanning profile across the thin shell of hollow Fe NPs is shown in **Figure 10.7a**. The red arrow is showing the direction of line scanning. EDS profile across the path of line scanning in STEM mode is shown in **Figure 10.7b.** The corresponding presence of Fe and O in relative ratio across the line of scanning in STEM mode is shown in **Figure 10.7c**.

**Figure 10.8** shows the corresponding SEM images of the synthesized Fe NPs obtained by FIB instrument. The SEM images of the as Fe NPs indicates the formation of spheres with a size range of 500 nm to 1.3 mm as well as with rough surfaces. From **Figure 10.8a** the pores are clearly visible on the surface of the sphere shell. In the broken part of the synthesized spheres, the presence of solid material in the inner part confirmed that the synthesized spheres were solid, and the thickness of outer coat was observed to be 20 to 40 nm. The empty interior in some of the partially broken spheres, which are clearly noticeable in **Figure 10.8b**, confirmed the hollow nature of the calcined Fe spheres. **Figure 10.9** shows the FIB images of a single Fe hollow nanoparticle. The particle is being sputter coated with platinum before cutting from front and back as clear from images. The images are representing the progress of cutting with time. After completion of cutting from both

sides the ring shape of thin shell of Fe NP is clearly visible confirming the structural stability of synthesized Fe NPs.

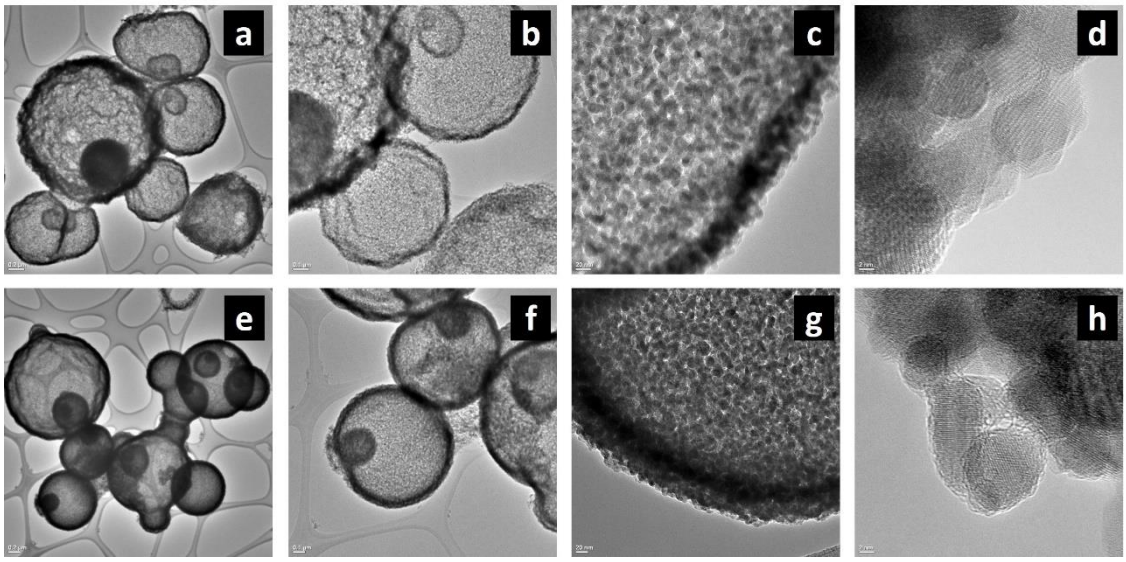


**Figure 10.5** TEM and HR-TEM images of hollow Fe NPs in two different locations. Location 1 (top row), location 2 (bottom row). **(a)** 5K magnification, scale 0.2 µm, **(b)** 10K magnification, scale 0.1 µm, **(c)** 50K magnification, scale 20 nm, **(d)** 500K magnification, scale 2 nm, **(e)** 4K magnification, scale 0.2 µm, **(f)** 8K magnification, scale 0.1 µm, **(g)** 40K magnification, scale 20 nm, **(h)** 500K magnification, scale 2 nm.

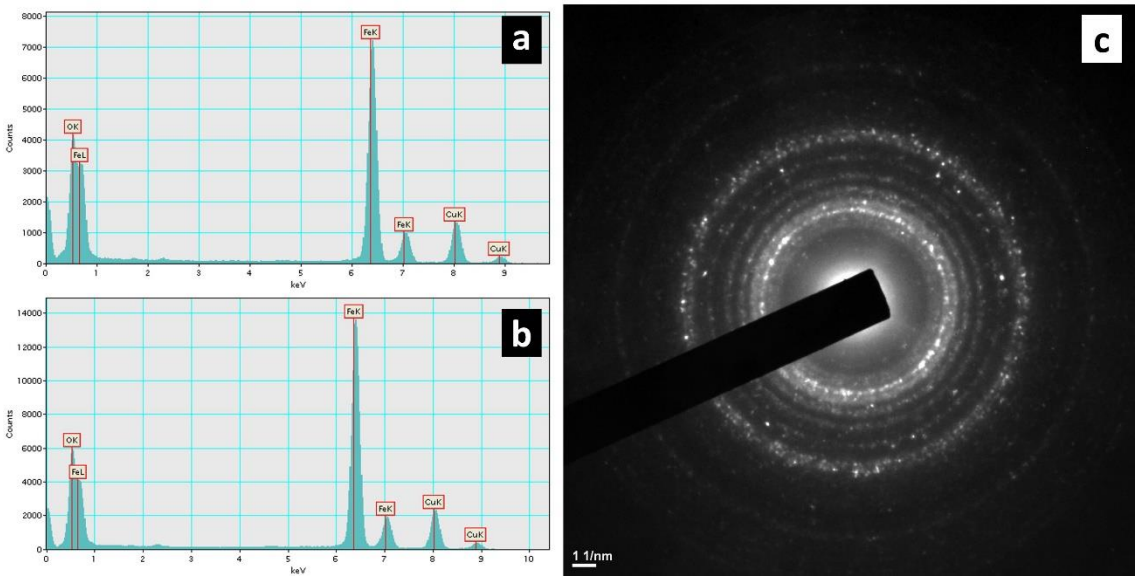


**Figure 10.6** EDS analysis and the SAED diffraction pattern of Fe hollow NPs. **(a)** EDS analysis in location 1 (Figure 10.5d), **(b)** EDS analysis in location 1(Figure 10.5h), **(c)** SAED diffraction pattern of Fe hollow NPs in location 1 (Figure 10.5d). Multiple diffraction rings representing phases of oxides of hollow Fe NPs. All images are at 500K magnification.

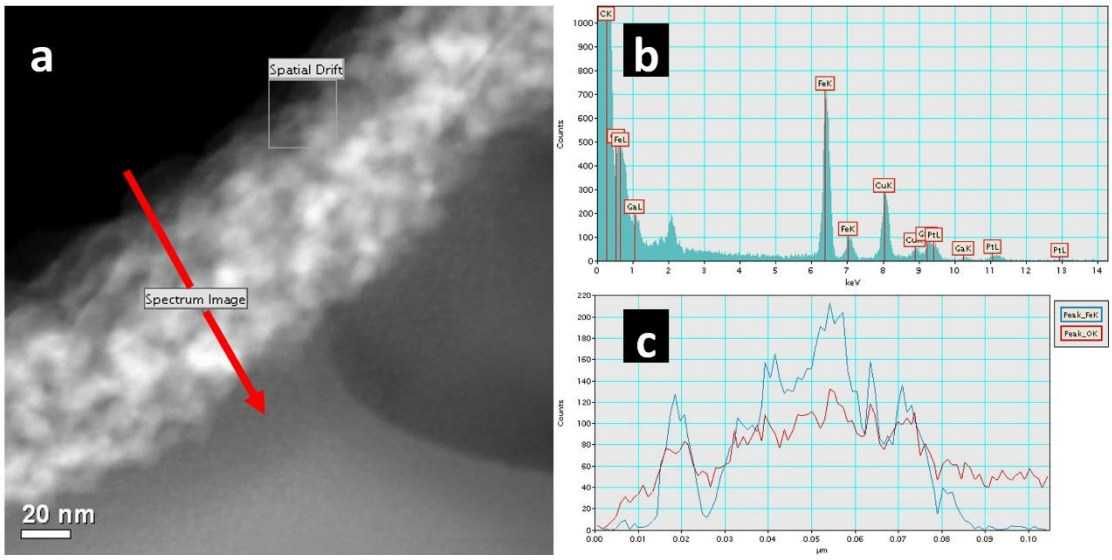


**Figure 10.7 (a)** EDS line scanning profile across the thin shell of hollow Fe NPs. The red arrow is showing the direction of line scanning. The image is taken at 400K magnification and the scale is 20 nm, **(b)** EDS profile across the path of line scanning in STEM mode, **(c)** The presence of Fe and O in relative ratio across the line of scanning in STEM mode.

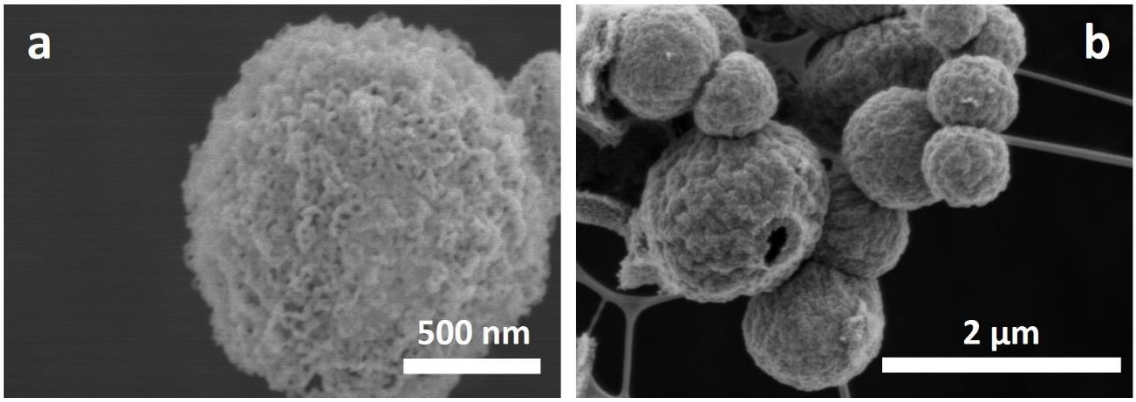


**Figure 10.8** SEM images of hollow Fe nanoparticles. **(a)** single hollow NP, **(b)** clustered hollow NPs attached to copper grid. SEM images are taken using FIB instrument.

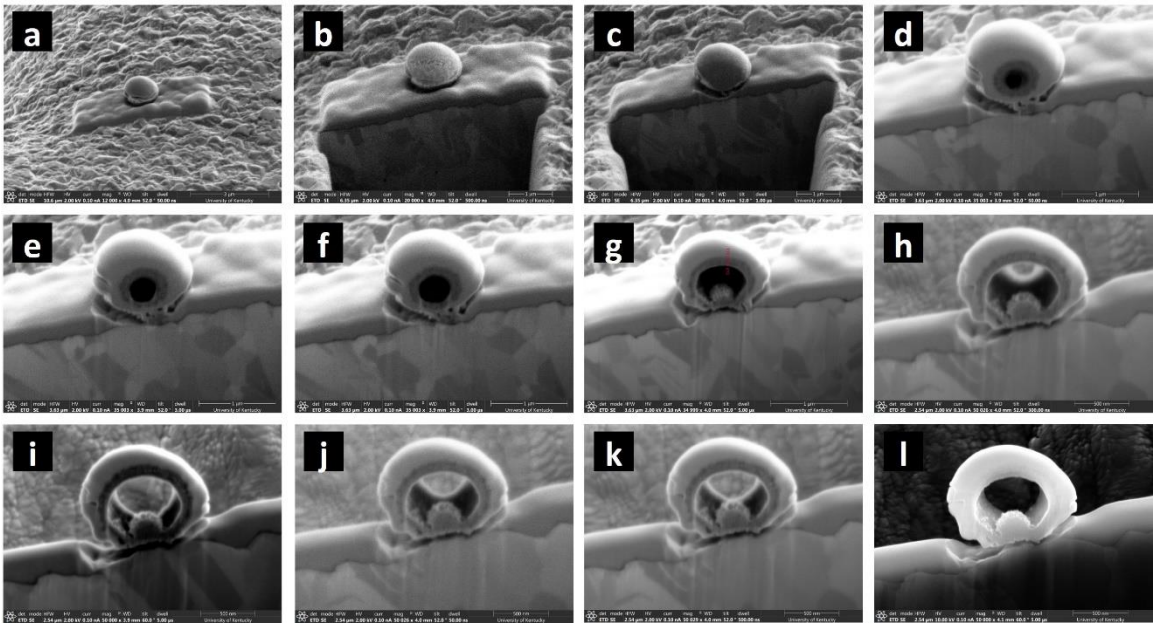


**Figure 10.9** FIB images of a single Fe hollow nanoparticle. The particle is being sputter coated with platinum. Then the nanoparticle is chopped from front and back as clear from images. Here, images in a, b, c, d, e, f, g, h, i, j, k and l are representing the progress of cutting with time. After completion of cutting from both sides the ring shape of thin shell of Fe NP is clearly visible.

## 10.3 Degradation of PCB-1 using Hollow Nanoparticles

The synthesized Fe and Pd-Fe hollow NPs are then investigated for the application of degradation of chlorinated organic compounds using the same protocol used earlier by our research group [35, 39, 100]. Prior to that we have investigated the role of individual NPs (Fe, Pd), combined NPs (Pd-Fe) and PAA hydrogel towards the degradation of chlorinated organic compounds discussed in the following section. For degradation study polychlorinated biphenyl (PCB-1) used as a model compound.

### *10.3.1 Effect of Fe, Pd, Pd-Fe and Hydrogel towards Degradation of PCB-1*

PCB-1 degradation study results using Fe, Pd, Pd-Fe nanoparticles and PAA hydrogel is shown in **Figure 10.10**. The objective of this study is to verify the effect of individual and synergistic effect of Fe and Pd NPs. PAA hydrogel is also included as it is the backbone of PVDF membrane functionalization before incorporating nanoparticles. The results verify there is no catalytic effect to degrade PCB-1 by lone Fe, Pd NPs. However, all most 90% of PCB-1 degraded to biphenyl with a recovery of 66% of the yield. Interestingly, the PAA hydrogel adsorbed PCB-1 with the course of time span. Primary results revealed around 2 ppm of [PCB-1]/[gm of PAA hydrogel] was adsorbed in 120 minutes resulting 50% reduction of the initial concentration of PCB-1.

### *10.3.2 Application of Hollow Nanoparticles towards PCB-1 Degradation*

Initial investigation reveals both Fe and Pd-Fe hollow NPs have potential for the application towards degradation of chlorinated organic compounds. However, for Fe NPs Pd NPs are incorporated for degradation study. **Figure 10.11** shows primary results of PDB-1 degradation study by Pd-Fe hollow NPs. Complete degradation of PCB-1 within 20 minutes of reaction time with 74% of yield of biphenyl. High surface area enables faster degradation of the chlorinated compounds. Further study requires to calculate the rate of degradation and estimate surface area normalized reaction rate. In addition, these hollow NPs could have other potential application such as adsorption of dyes and other cations form wastewater which needs further investigation.

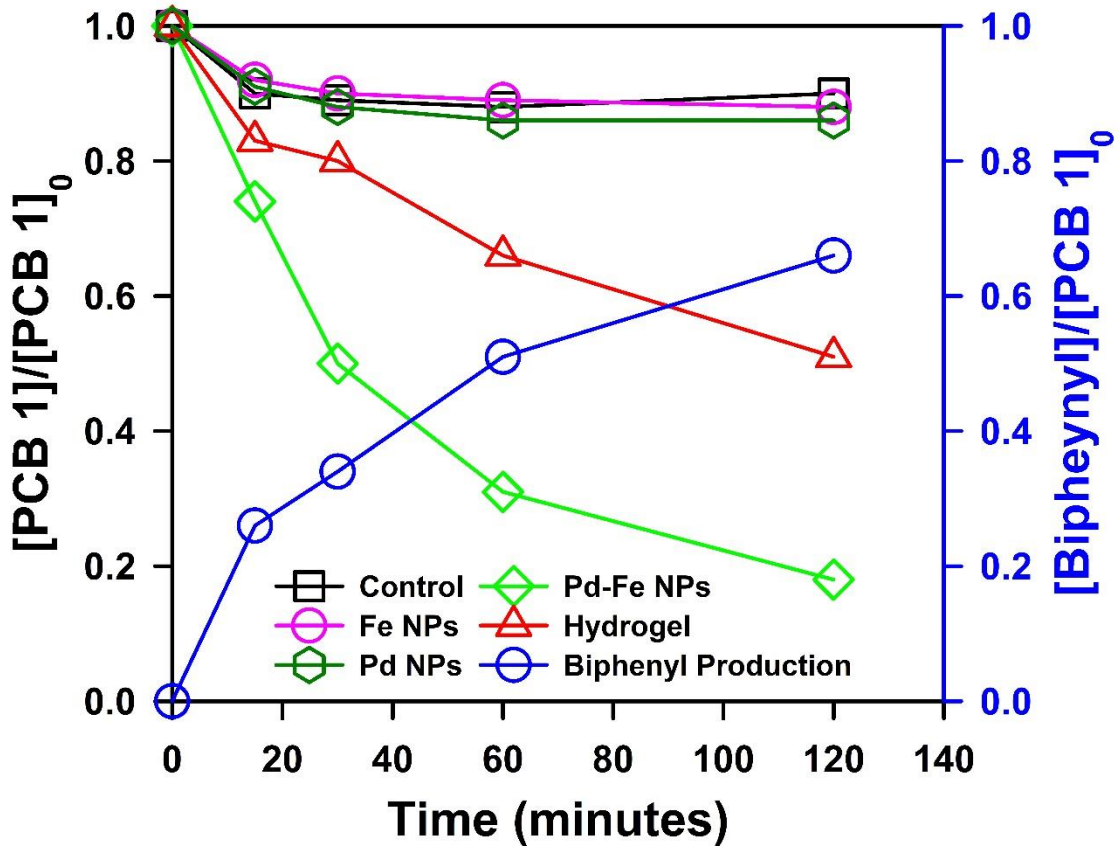


**Figure 10.10** Time dependent PCB-1 degradation studies for Fe, Pd, Pd-Fe nanoparticles and PAA hydrogel. Fe NPs concentration ~ 1000 ppm, Pd NPs concentration ~ 150 ppm, Biphenyl produced only from Pd-Fe NPs batch studies. For PAA hydrogel around 2 g of hydrogel was taken for each vial.

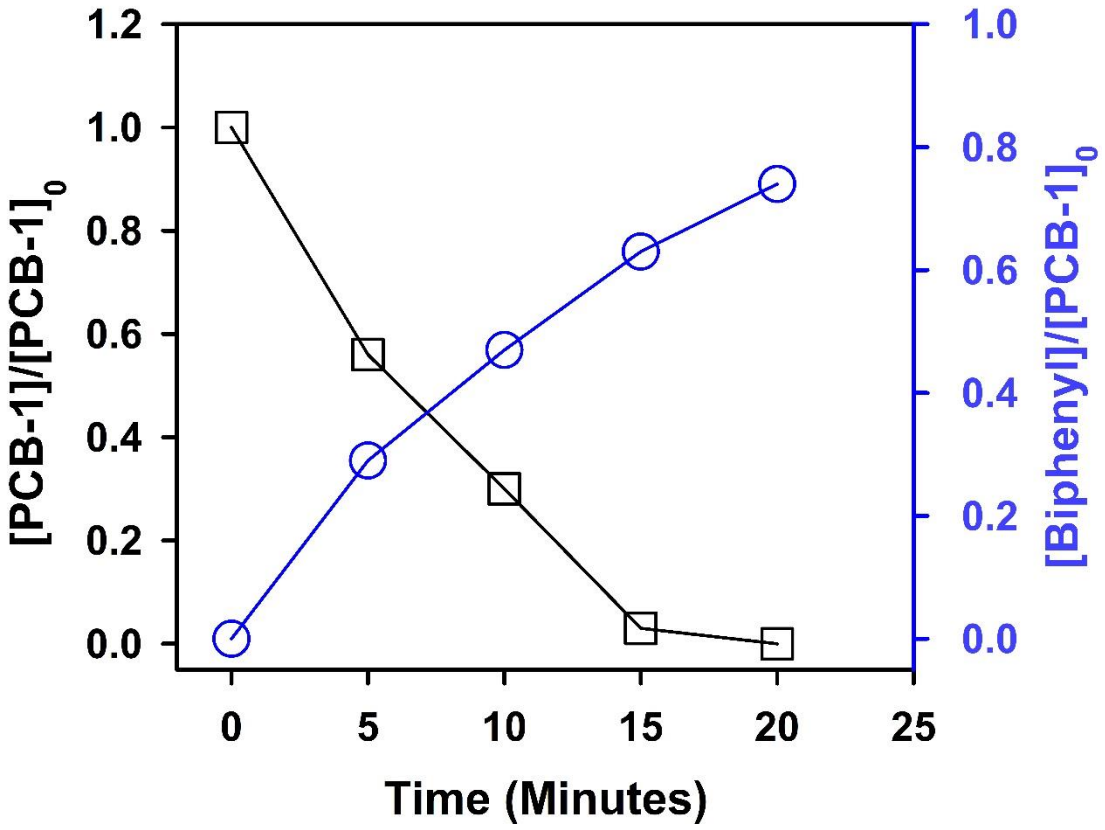


**Figure 10.11** Batch phase PCB-1 degradation study using hollow bimetallic Pd-Fe Nanoparticles. Initial concentration of PCB-1 ~ 8 ppm, Pd Content = 3~5% of Fe, Reaction time = 20 minutes, Temperature = 22~23ºC.

# CHAPTER 11. CONCLUSION

## 11.1 Overview

In this dissertation, three different pore functionalization approaches of microfiltration membranes for the application of chloro-organic remediation to heavy metal sorption was evaluated. PVDF microfiltration membrane was initially functionalized with polyacrylic acid (PAA) polymer to incorporate carboxylic acid (-COOH) group in membrane pores. This PAA functionalized PVDF membrane was then investigated for three different pore functionalization approaches for water treatment application. Primarily, **i)** as a catalytic reactor bed by incorporation of bimetallic (Pd-Fe) nanoparticles for the remediation of chlorinated organic compounds (COCs); then, **ii)** as a bio reactor by incorporation of enzymes by layer-by-layer (LBL) assembly towards degradation of polychloro-organics; and, **iii)** as adsorption bed by incorporation of thiol (-SH) functionalized group in PVDF membranes for heavy metal sorption from water. Finally, a new kind of hollow (Fe and Pd-Fe) nanoparticles are synthesized for the application towards degradation of chlorinated organic compounds (COC) specifically PCB-1 was assessed.

## 11.2 Specific Accomplishments

Nanoparticle incorporated PAA-PVDF membrane as a catalytic reactor bed (Chapter 4 and Chapter 5):

- Demonstrated the effect of monomer and cross-linker concentration during the functionalization of pH responsive membrane on mass gain, water permeability, Pd-Fe NPs loading, and the degradation of PCB 126 quantitatively.
- The results obtained during this study confirm quantitative tuning of the responsive behavior of membrane in terms of water permeability, NPs size, metal loading and rate of PCB 126 degradation by varying monomer and cross-linker concentration.
- Statistical analysis of interaction between inputs (monomer, cross-linker) and response variables (mass gain, permeability ratio) show that statistically significant interaction exists between monomer and cross-linker concentration.

- Details of Pd-Fe-PAA-PVDF membranes surface and pores as well as size, shape and size-distribution of Pd-Fe nanoparticles have been established by using different characterization tools such as TGA, contact angle measurement, surface zeta potential, XRD, SEM, XPS, FIB, TEM and other methodologies.
- Degradation study in convective flow mode through Pd-Fe-PAA-PVDF membrane platform shows 98.6% PCB 126 is degraded at a residence time of 46.2 seconds. Based on surface normalized reaction rate data for PCB 126 dechlorination, a convective flow through mode reveals a much faster degradation due to overcoming the mass transfer limitation, suggesting practical application for water remediation application.

Enzyme Immobilized PAA-PVDF membrane as a bio reactor (Chapter 6 and Chapter 7):

- Fabrication of PVDF microfiltration membranes as platforms for laccase immobilization is demonstrated. Laccase was successfully immobilized on the membrane using the established layer-by-layer assembly method. Although layer-by-layer assembly technique is known and used in various studies of enzyme immobilization, to our best of knowledge, this is the first ever study of laccase immobilized membrane showing application under convective flow mode.
- The membrane-bound laccase displayed comparable activity to that of free solution phase laccase, as indicated by the Michaelis-Menten parameters. This is mainly because there is no physical bond formation or breaking involved other than short range /non-covalent interactions or ionic interactions. In this respect we anticipate the $k_{cat}$ of the immobilized laccase to be comparable to that of free laccase. The higher apparent Michaelis constant, $K_M$, for the immobilized membrane can be accounted for by restricted access of substrate to the active sites of the immobilized enzymes by slowed diffusion. However, slight conformational changes of the enzyme during immobilization and possibility of hindrance offered by the polyelectrolytes to the substrate can't be ruled out.
- The laccase immobilized membrane was used to remove 2,4,6-trichlorophenol (TCP), resulting in more than 80% degradation at a favorable flow rate of 2 LMH under a lower applied pressure of only 0.7 bar. This data suggests that unlike batch

mode reaction, convective flow method can lead to degradation of ~80% of TCP in a residence time of only 36 $s^{-1}$. Combination of HPLC, LC-MS and UV-Visible spectroscopic analysis demonstrated dichloro-1,4-benzoquinone to be the major degraded product of TCP.

- The impressive performance of the laccase functionalized membrane along with the improved storage stability and the reusability for the oxidation of chloroorganics, indicate its potential for industrial applications in the field of wastewater bioremediation.
- Fabrication of multi-enzyme immobilized PVDF microfiltration membranes is demonstrated. The functionalized membranes were used for oxidative degradation of the lignin model compound GGE.
- Multi-enzyme immobilized membranes, engineered through layer-by-layer assembly method, were capable of breaking main chain linkage in lignin type molecules. Preliminary investigation revealed over 90% of initial GGE degradation with the multienzyme immobilized membranes under optimum flow rate. A combination of HPLC, LC-MS analysis on GGE conversion product confirmed formation of oligomeric oxidation products with peroxidase which acts as substrate for the laccase enzyme. The oligomeric units were further degraded by laccase, explaining the potential of multienzyme membrane reactors. This study opens perspectives for further evolution of multienzyme membrane reactor systems and indicate its potential for industrial applications in the field of biodegradation of renewables.

<u>Thiol incorporated PAA-PVDF membrane as heavy metal adsorption bed (Chapter 8 and Chapter 9):</u>

- Demonstrated the incorporation of thiol groups (using both cysteamine, CysM, and cysteine, Cys) in PAA functionalized PVDF microfiltration membrane by ion-exchange and EDC/NHS coupling route.
- This thiol functionalized PAA-PVDF membrane has high adsorption capacity to remove mercury from water. The mercury adsorption capacity of CysM immobilized PAA-PVDF membrane is of 1015 mg/g PAA and 2446 mg/g PAA

respectively, for the membranes prepared by the IE and the EDC/NHS coupling methods.

- With the mentioned capacity, a commercial membrane module with a surface area of 31.6 $m^2$ could theoretically treat approximately 512 $m^3$ of industrial wastewater with a 1 mg/L of dissolved mercury.
- The efficiencies of Hg removal are 94.1±1.1 and 99.1±0.1% respectively, for the CysM immobilized membranes prepared by the IE and the EDC/NHS coupling methods.
- Demonstrated treatment of industrial wastewater containing mercury with commercially available ultrafiltration (UF) membrane in combination with in-house fabricated thiol membranes can remove HgS NPs and adsorb dissolved $Hg^{2+}$ from wastewaters.
- Over 12 hours of continuous operation shows consistent removal of ~200 ppb HgS NPs from wastewater by UF membrane filtration. While membrane fouling occurred, it was demonstrated that a water wash could recovery the flux. Dissolved $Hg^{2+}$ from UF filtered wastewater was effectively removed by a CysM-PAA-PVDF membrane.
- Long-term (1250 minutes) treatment of wastewater with an adsorption efficiency of 97% suggesting in-house functionalized membrane is well suited for sustainable mercury removal applications.
- The presence $Ca^{2+}$ cations reduced the adsorption efficiency to 82% for CysM-PAA-PVDF membrane and to 40% for Cys-PAA-PVDF membranes, suggesting that CysM thiol membranes will be superior for removal of mercury from wastewater compared to Cys thiol membranes.
- Characterization of cross-section of CysM-PAA-PVDF membrane by FIB confirmed that the adsorption takes place across the entire pore length and is not limited to the membrane surface.
- Finally, mathematical modeling of heavy metal adsorption on thiol membranes was effective in predicting experimental results over a wide range of operating conditions, suggesting a high potential for commercialization.

Synthesis of hollow nanoparticles for the application towards degradation of chlorinated organic compounds (Chapter 10)

- Synthesis, characterization and preliminary application towards degradation of chlorinated compounds using in-house synthesized hollow nanoparticles (NPs) was demonstrated by preparing two types (Fe and Pd-Fe) of hollow NPs were prepared.
- Details characterization of the prepared samples were conducted by XRD, BET, DLS, TEM, SEM and FIB. Initial study reveals this fabricate Fe hollow spheres have 2.6 times higher surface area and 4.28 times pore volume compare to commercial Fe catalyst. The average size of the Fe hollow NPs is in the size range of 100 to 1200 µm. However, the DLS measurement reveals 30% of the hollow NPs are in 100 nm size. However, some bigger hollow spheres are also formed in the range of 500 nm to 1.2 µm, which helped to characterize the particles with TEM, SEM and FIB by cutting the cross-section of the spheres. The shell thickness is in the range of 20 to 40 nm.
- Finally, these prepared Fe, Pd-Fe hollow NPs are used towards degradation of chlorinated organic compounds. Initial investigation reveals that these prepared hollow NPs can completely degrade polychlorinated biphenyl (PCB-1) with an 74% recovery of biphenyl within 20 minutes anticipating future potential for water remediation application.

### 11.3 Key Advances in Science and Engineering

- Different pore functionalization approaches for microfiltration membranes (in-situ synthesis of catalytic nanoparticle, enzyme immobilization and incorporation of amine and thiol groups) for chloro-organic remediation to metal sorption was demonstrated.
- Role of pore polymerization condition for polyacrylic acid functionalized microfiltration membranes to tune pH responsive behavior and to control size of in-situ catalytic metal nanoparticle synthesis was quantified.
- Synthesis of solid, hollow and membrane bound Pd-Fe nanoparticles was demonstrated for the application towards degradation of PCB.

- Immobilization of enzymes by layer-by-layer assembly in functionalized microfiltration membranes revealed faster degradation of chloro-organics and lignin model compound in convective flow mode.
- Demonstrated long-term heavy metal sorption from industrial wastewater by thiol functionalized microfiltration membrane.
- Effect of the presence of interfering cations during removal of heavy metals from industrial wastewater was demonstrated.

## NOMENCLATURE

### Chapter 1

| | |
|---|---|
| MWCO | Molecular weight cut-off |
| MF | Microfiltration |
| UF | Ultrafiltration |
| NF | Nanofiltration |
| RO | Reverse Osmosis |
| Q | Flux |
| D | Diffusivity |
| S | Sorption coefficient |
| M | Molecular mass |
| μ | viscosity |
| CMS | Carbon molecular sieves |
| CNT | Carbon nano tubes |
| AAO | Anodized aluminum oxide |
| GO | Graphene oxide |
| MOF | Metal organic framework |
| CNM | Carbon nanomembrane |
| NATM | Nanoporous atomically thin membrane |
| PVDF | Polyvinylidiene fluoride |
| PAA | Poly acrylic acid |
| PAH | Poly(allylamine-hydrochloride) |
| PLL | Poly (L-lysine hydrochloride) |
| PSU | Polysulfone |
| PES | Polyether Sulfone |
| PAN | Polyacrylonitrile |

| | |
|---|---|
| PE | Polyethylene |
| PP | Polypropylene |
| PVC | Polyvinyl Chloride |
| CA | Cellulose Acetate |
| PA | Polyamide |
| PMAA | Poly(methacrylic acid) |
| COCs | Chlorinated organic compounds |
| nZVI | Nano scale zero valent iron |
| NPs | Nanoparticles |
| TCP | 2,4,6-trichlorophenol |
| LBL | layer-by-layer |
| HRP | Horseradish peroxidase |
| GO | Glucose oxidase |
| GGE | Guaiacylglycerol-β-guaiacylether |
| IE | Ion-exchange |
| EDC | Ethyl(dimethylaminopropyl) carbodiimide |
| NHS | N-Hydroxysuccinimide |
| Cys | Cysteine ($C_3H_7NO_2S$) |
| CysM | Cysteamine or β-Mercaptoethylamine ($C_2H_7NS$) |

**Chapter 2**

| | |
|---|---|
| M | Monomer |
| X | Cross-linker |
| PCB 126 | 3,3',4,4',5-pentachlorobiphenyl |
| MBA | N, N′- methylenebis (acrylamide) |
| PCB-1 | 2-Chlorobiphenyl |

**Chapter 3**

| | |
|---|---|
| KPS | Potassium persulfate |
| DIUF | Deionized ultrafiltered |
| A | Permeability |
| ABTS | 2,2´-Azinobis(3-ethylbenzothiazoline-6-sulfonic acid)-diammonium salt |
| GO | Glucose oxidase |
| $\varepsilon_{max}$ | Extinction coefficients |
| $K_M$ | Michaelis constant |
| $k_{cat}$ | Turnover number |

**Chapter 4**

| | |
|---|---|
| Ø | Porosity |
| $A_{min}$ | Permeability at pH 4 |
| $A_{max}$ | Permeability at pH 8.5 |
| $A_{min}/A_{max}$ | Responsiveness factor/ Permeability ratio |
| ANOVA | Analysis of variance |

**Chapter 5**

| | |
|---|---|
| $K_{obs}$ | Observed batch reaction rate |
| $K_{sa}$ | Surface area normalized reaction rate |
| $R$ | Reaction rate ($mol \cdot L^{-1} \cdot hr^{-1}$) |
| $t$ | Reaction time, (hr) |
| $C$ | Concentration of PCB 126 ($mol \cdot L^{-1}$) at reaction time, $t$ (hr) |
| $\rho_m$ | Nanoparticle loading density ($g \cdot L^{-1}$) |
| $a_s$ | Specific surface area of Pd-Fe NPs immobilized in membrane ($m^2 \cdot g^{-1}$) |
| $R$ | Pore size of the functionalized membrane |
| $u_0$ | Velocity at center of the pore |

| | |
|---|---|
| $u(r)$ | Velocity at radius r |
| Z | Membrane thickness |
| $\bar{C}$ | Mean concentration at certain axial distance z |
| $(\tau)$ | Residence time |
| CSTR | Continuous stirred-tank reactor |

**Chapter 6**

| | |
|---|---|
| $(k_{cat}/ K_M)$ | Catalytic efficiency |
| LMH | Liter per meter square per hour ($L/m^2$-hr) |

**Chapter 9**

| | |
|---|---|
| $Ø_{pore}$ | Membrane pore volume fraction |
| $Ø_{PVDF}$ | PVDF volume fraction |
| $Ø_{free\ space}$ | Free volume fraction of the membrane |
| $C'$ | Concentration of $Ag^+$ in liquid phase (moles of $Ag^+/m^3$) |
| $q'$ | Concentration of $Ag^+$ in SH-PAA layer (moles of $Ag^+/m^3$) |
| $q_{eq}$ | Maximum concentration of $Ag^+$ in PAA-SH layer for $C'$ (moles of $Ag^+/m^3$) |
| $J_W$ | Membrane water flux (m/s) |
| $t'$ | Time (s) |
| $z'$ | Distance down the membrane thickness (m) |
| $K$ | Mass transfer coefficient of $Ag^+$ into the stationary phase (SH-PAA) |
| γ | Silver-thiol affinity constant |
| $C_0$ | Inlet feed concentration of $Ag^+$ (mol of $Ag^+/m^3$) |
| $q_\infty$ | Maximum $Ag^+$ capture (mol of $Ag/m^3$ of SH-PAA) |
| $L$ | Membrane thickness (m) |
| $T_S$ | Time at which break-through of $Ag^+$ adsorption was observed |

## REFERENCES


1. Werber, J. R.; Osuji, C. O.; Elimelech, M., Materials for Next-Generation Desalination and Water Purification Membranes. *Nat. Rev. Mater.* **2016,** *1*, 16018.

2. Shannon, M. A.; Bohn, P. W.; Elimelech, M.; Georgiadis, J. G.; Marinas, B. J.; Mayes, A. M., Science and Technology for Water Purification in the Coming Decades. *Nature* **2008,** *452* (7185), 301-310.

3. Hankins, N. P.; Singh, R., *Emerging Membrane Technology for Sustainable Water Treatment*. Elsevier: 2016.

4. Escobar, I.; Van der Bruggen, B., *Modern Applications in Membrane Science and Technology*. ACS Publications: 2011.

5. Elimelech, M.; Phillip, W. A., The Future of Seawater Desalination: Energy, Technology, and the Environment. *Science* **2011,** *333* (6043), 712-717.

6. Bhattacharyya, D.; Schäfer, T.; Wickramasinghe, S.; Daunert, S., *Responsive Membranes and Materials*. John Wiley & Sons: West Sussex, United Kingdom, 2012.

7. Park, H. B.; Kamcev, J.; Robeson, L. M.; Elimelech, M.; Freeman, B. D., Maximizing the Right Stuff: The Trade-Off between Membrane Permeability and Selectivity. *Science* **2017,** *356* (6343).

8. Wang, L.; Boutilier, M. S. H.; Kidambi, P. R.; Jang, D.; Hadjiconstantinou, N. G.; Karnik, R., Fundamental Transport Mechanisms, Fabrication and Potential Applications of Nanoporous Atomically Thin Membranes. *Nat. Nanotechnol.* **2017,** *12* (6), 509-522.

9. Zheng, S.; Tu, Q.; Urban, J. J.; Li, S.; Mi, B., Swelling of Graphene Oxide Membranes in Aqueous Solution: Characterization of Interlayer Spacing and Insight into Water Transport Mechanisms. *ACS Nano* **2017,** *11* (6), 6440-6450.

10. Feng, X.; Kawabata, K.; Kaufman, G.; Elimelech, M.; Osuji, C. O., Highly Selective Vertically Aligned Nanopores in Sustainably Derived Polymer Membranes by Molecular Templating. *ACS Nano* **2017,** *11* (4), 3911-3921.

11. Zhang, P.; Li, J.; Lv, L.; Zhao, Y.; Qu, L., Vertically Aligned Graphene Sheets Membrane for Highly Efficient Solar Thermal Generation of Clean Water. *ACS Nano* **2017,** *11* (5), 5087-5093.

12. Howorka, S., Building Membrane Nanopores. *Nat. Nanotechnol.* **2017,** *12* (7), 619-630.

13. Warsinger, D. M.; Chakraborty, S.; Tow, E. W.; Plumlee, M. H.; Bellona, C.; Loutatidou, S.; Karimi, L.; Mikelonis, A. M.; Achilli, A.; Ghassemi, A.; Padhye, L. P.; Snyder, S. A.; Curcio, S.; Vecitis, C. D.; Arafat, H. A.; Lienhard, J. H., A Review of Polymeric Membranes and Processes for Potable Water Reuse. *Prog. Polym. Sci.* **2018,** *81*, 209-237.

14. Van Der Bruggen, B.; Vandecasteele, C.; Van Gestel, T.; Doyen, W.; Leysen, R., A Review of Pressure-Driven Membrane Processes in Wastewater Treatment and Drinking Water Production. *Environ. Prog.* **2003,** *22* (1), 46-56.

15. Xu, J.; Bhattacharyya, D., Fe/Pd Nanoparticle Immobilization in Microfiltration Membrane Pores: Synthesis, Characterization, and Application in the Dechlorination of Polychlorinated Biphenyls. *Ind. Eng. Chem. Res.* **2007,** *46* (8), 2348-2359.

16. Xu, J.; Bhattacharyya, D., Modeling of Fe/Pd Nanoparticle-Based Functionalized Membrane Reactor for PCB Dechlorination at Room Temperature. *J. Phys. Chem. C* **2008,** *112* (25), 9133-9144.

17. Xu, J.; Bhattacharyya, D., Membrane-based Bimetallic Nanoparticles for Environmental Remediation: Synthesis and Reactive Properties. *Environ. Prog. Sustainable Energy* **2005,** *24* (4), 358-366.

18. Xiao, L.; Davenport, D. M.; Ormsbee, L.; Bhattacharyya, D., Polymerization and Functionalization of Membrane Pores for Water Related Applications. *Ind. Eng. Chem. Res.* **2015,** *54* (16), 4174-4182.

19. Xiao, L.; Isner, A.; Waldrop, K.; Saad, A.; Takigawa, D.; Bhattacharyya, D., Development of Bench and Full-Scale Temperature and pH Responsive Functionalized PVDF Membranes with Tunable Properties. *J. Membr. Sci.* **2014,** *457*, 39-49.

20. Smuleac, V.; Bachas, L.; Bhattacharyya, D., Aqueous-Phase Synthesis of PAA in PVDF Membrane Pores for Nanoparticle Synthesis and Dichlorobiphenyl Degradation. *J. Membr. Sci.* **2010,** *346* (2), 310-317.

21. Datta, S.; Cecil, C.; Bhattacharyya, D., Functionalized Membranes by Layer-By-Layer Assembly of Polyelectrolytes and In Situ Polymerization of Acrylic Acid for Applications in Enzymatic Catalysis. *Ind. Eng. Chem. Res.* **2008,** *47* (14), 4586-4597.

22. Ritchie, S. M. C.; Bachas, L. G.; Olin, T.; Sikdar, S. K.; Bhattacharyya, D., Surface Modification of Silica- and Cellulose-Based Microfiltration Membranes with Functional Polyamino Acids for Heavy Metal Sorption. *Langmuir* **1999,** *15* (19), 6346-6357.

23. Ritchie, S. M. C.; Kissick, K. E.; Bachas, L. G.; Sikdar, S. K.; Parikh, C.; Bhattacharyya, D., Polycysteine and Other Polyamino Acid Functionalized Microfiltration Membranes for Heavy Metal Capture. *Environ. Sci. Technol.* **2001,** *35* (15), 3252-3258.

24. Ladhe, A. R.; Frailie, P.; Hua, D.; Darsillo, M.; Bhattacharyya, D., Thiol-Functionalized Silica-Mixed Matrix Membranes for Silver Capture from Aqueous Solutions: Experimental Results and Modeling. *J. Membr. Sci.* **2009,** *326* (2), 460-471.

25. Smuleac, V.; Butterfield, D. A.; Sikdar, S. K.; Varma, R. S.; Bhattacharyya, D., Polythiol-Functionalized Alumina Membranes for Mercury Capture. *J. Membr. Sci.* **2005,** *251* (1), 169-178.

26. Gui, M.; Papp, J. K.; Colburn, A. S.; Meeks, N. D.; Weaver, B.; Wilf, I.; Bhattacharyya, D., Engineered Iron/Iron Oxide Functionalized Membranes for Selenium

and Other Toxic Metal Removal from Power Plant Scrubber Water. *J. Membr. Sci.* **2015,** *488*, 79-91.

27. Gui, M.; Smuleac, V.; Ormsbee, L. E.; Sedlak, D. L.; Bhattacharyya, D., Iron Oxide Nanoparticle Synthesis in Aqueous and Membrane Systems for Oxidative Degradation of Trichloroethylene from Water. *J. Nanopart. Res.* **2012,** *14* (5), 861.

28. Gui, M.; Ormsbee, L. E.; Bhattacharyya, D., Reactive Functionalized Membranes for Polychlorinated Biphenyl Degradation. *Ind. Eng. Chem. Res.* **2013,** *52* (31), 10430-10440.

29. Xu, J. Synthesis and Reactivity of Membrane-supported Bimetallic Nanoparticles for PCB and Trichloroethylene Dechlorination. University of Kentucky, 2007.

30. Datta, S. Functionalized Polymeric Membranes for Bioseparation and Biocatalysis. University of Kentucky, 2007.

31. Bhattacharyya, D.; Ganapathi, S.; Vishwanath, S.; Summers, M.; Butterfield, D. A., Immobilized Enzyme Reactions on Beads and Membranes. In *Biofunctional Membranes*, Butterfield, D. A., Ed. Springer US: Boston, MA, 1996; pp 117-129.

32. Hu, K.; Dickson, J. M., Development and Characterization of Poly(Vinylidene Fluoride)–Poly(Acrylic Acid) Pore-Filled pH-Sensitive Membranes. *J. Membr. Sci.* **2007,** *301* (1-2), 19-28.

33. Hu, K.; Dickson, J., Modelling of the Pore Structure Variation with pH for Pore-Filled pH-Sensitive Poly(Vinylidene Fluoride)–Poly(Acrylic Acid) Membranes. *J. Membr. Sci.* **2008,** *321* (2), 162-171.

34. Hernández, S.; Papp, J. K.; Bhattacharyya, D., Iron-Based Redox Polymerization of Acrylic Acid for Direct Synthesis of Hydrogel/Membranes and Metal Nanoparticles for Water Treatment. *Ind. Eng. Chem. Res.* **2014,** *53* (3), 1130-1142.

35. Wan, H.; Islam, M. S.; Briot, N. J.; Schnobrich, M.; Pacholik, L.; Ormsbee, L.; Bhattacharyya, D., Pd/Fe Nanoparticle Integrated PMAA-PVDF Membranes for Chloro-

Organic Remediation from Synthetic and Site Groundwater. *J. Membr. Sci.* **2020,** *594*, 117454.

36. Smuleac, V.; Varma, R.; Sikdar, S.; Bhattacharyya, D., Green Synthesis of Fe and Fe/Pd Bimetallic Nanoparticles in Membranes for Reductive Degradation of Chlorinated Organics. *J. Membr. Sci.* **2011,** *379* (1–2), 131-137.

37. Wang, X.; Chen, C.; Liu, H.; Ma, J., Preparation and Characterization of PAA/PVDF Membrane-Immobilized Pd/Fe Nanoparticles for Dechlorination of Trichloroacetic Acid. *Water Res.* **2008,** *42* (18), 4656-4664.

38. Xia, Z.; Liu, H.; Wang, S.; Meng, Z.; Ren, N., Preparation and Dechlorination of a Poly(Vinylidene Difluoride)-Grafted Acrylic Acid Film Immobilized with Pd/Fe Bimetallic Nanoparticles for Monochloroacetic Acid. *Chem. Eng. J.* **2012,** *200-202*, 214-223.

39. Wan, H.; Briot, N. J.; Saad, A.; Ormsbee, L.; Bhattacharyya, D., Pore Functionalized PVDF Membranes with In-Situ Synthesized Metal Nanoparticles: Material Characterization, and Toxic Organic Degradation. *J. Membr. Sci.* **2017,** *530*, 147-157.

40. Lin, Y.-H.; Tseng, H.-H.; Wey, M.-Y.; Lin, M.-D., Characteristics, Morphology, and Stabilization Mechanism of PAA250K-Stabilized Bimetal Nanoparticles. *Colloids Surf., A* **2009,** *349* (1-3), 137-144.

41. Han, L.; Qian, L.; Yan, J.; Chen, M., Effects of the Biochar Aromaticity and Molecular Structures of the Chlorinated Organic Compounds on the Adsorption Characteristics. *Environ. Sci. Pollut. Res.* **2017,** *24* (6), 5554-5565.

42. Xin, J.; Tang, F.; Zheng, X.; Shao, H.; Kolditz, O.; Lu, X., Distinct Kinetics and Mechanisms of mZVI Particles Aging in Saline and Fresh Groundwater: $H_2$ Evolution and Surface Passivation. *Water Res.* **2016,** *100*, 80-87.

43. Zhao, X.; Liu, W.; Cai, Z.; Han, B.; Qian, T.; Zhao, D., An Overview of Preparation and Applications of Stabilized Zero-Valent Iron Nanoparticles for Soil and Groundwater Remediation. *Water Res.* **2016,** *100*, 245-266.

44. Sun, Y.; Li, J.; Huang, T.; Guan, X., The Influences of Iron Characteristics, Operating Conditions and Solution Chemistry on Contaminants Removal by Zero-Valent Iron: A review. *Water Res.* **2016,** *100*, 277-295.

45. Crane, R. A.; Scott, T. B., Nanoscale Zero-Valent Iron: Future Prospects for an Emerging Water Treatment Technology. *J. Hazard. Mater.* **2012,** *211–212*, 112-125.

46. O'Carroll, D.; Sleep, B.; Krol, M.; Boparai, H.; Kocur, C., Nanoscale Zero Valent Iron and Bimetallic Particles for Contaminated Site Remediation. *Adv. Water Resour.* **2013,** *51*, 104-122.

47. Yan, W.; Herzing, A. A.; Kiely, C. J.; Zhang, W.-x., Nanoscale Zero-Valent Iron (nZVI): Aspects of the Core-Shell Structure and Reactions with Inorganic Species in Water. *J. Contam. Hydrol.* **2010,** *118* (3–4), 96-104.

48. Li, X.; Sotto, A.; Li, J.; Van der Bruggen, B., Progress and Perspectives for Synthesis of Sustainable Antifouling Composite Membranes Containing In Situ Generated Nanoparticles. *J. Membr. Sci.* **2017,** *524*, 502-528.

49. Greenlee, L. F.; Hooker, S. A., Development of Stabilized Zero Valent Iron Nanoparticles. *Desalin. Water Treat.* **2012,** *37* (1-3), 114-121.

50. Zhang, W.-x.; Wang, C.-B.; Lien, H.-L., Treatment of Chlorinated Organic Contaminants with Nanoscale Bimetallic Particles. *Catal. Today* **1998,** *40* (4), 387-395.

51. Schrick, B.; Blough, J. L.; Jones, A. D.; Mallouk, T. E., Hydrodechlorination of Trichloroethylene to Hydrocarbons Using Bimetallic Nickel−Iron Nanoparticles. *Chem. Mater.* **2002,** *14* (12), 5140-5147.

52. Feng, J.; Lim, T.-T., Pathways and Kinetics of Carbon Tetrachloride and Chloroform Reductions by Nano-scale Fe and Fe/Ni Particles: Comparison with Commercial Micro-scale Fe and Zn. *Chemosphere* **2005,** *59* (9), 1267-1277.

53. Lien, H.-L.; Zhang, W.-X., Nanoscale Pd/Fe Bimetallic Particles: Catalytic Effects of Palladium on Hydrodechlorination. *Appl. Catal., B* **2007,** *77* (1–2), 110-116.

54. He, F.; Zhao, D., Hydrodechlorination of Trichloroethene Using Stabilized Fe-Pd Nanoparticles: Reaction Mechanism and Effects of Stabilizers, Catalysts and Reaction Conditions. *Appl. Catal., B* **2008,** *84* (3–4), 533-540.

55. Tee, Y.-H.; Bachas, L.; Bhattacharyya, D., Degradation of Trichloroethylene by Iron-Based Bimetallic Nanoparticles. *J. Phys. Chem. C* **2009,** *113* (22), 9454-9464.

56. Xiao, L.; Isner, A. B.; Hilt, J. Z.; Bhattacharyya, D., Temperature Responsive Hydrogel with Reactive Nanoparticles. *J. Appl. Polym. Sci.* **2013,** *128* (3), 1804-1814.

57. Hernández, S.; Lei, S.; Rong, W.; Ormsbee, L.; Bhattacharyya, D., Functionalization of Flat Sheet and Hollow Fiber Microfiltration Membranes for Water Applications. *ACS Sustainable Chem. Eng.* **2016,** *4* (3), 907-918.

58. Brena, B. M.; Batista-Viera, F., Immobilization of Enzymes. In *Immobilization of Enzymes and Cells*, Guisan, J. M., Ed. Humana Press: Totowa, NJ, 2006; pp 15-30.

59. Sheldon, R. A.; van Pelt, S., Enzyme Immobilisation in Biocatalysis: Why, What and How. *Chem. Soc. Rev.* **2013,** *42* (15), 6223-6235.

60. Tütem, E.; Apak, R.; Ünal, Ç. F., Adsorptive Removal of Chlorophenols from Water by Bituminous Shale. *Water Res.* **1998,** *32* (8), 2315-2324.

61. Yang, C.; Nuxoll, E. E.; Cussler, E. L., Reactive Barrier Films. *AIChE J.* **2001,** *47* (2), 295-302.

62. Li, X.-q.; Elliott, D. W.; Zhang, W.-x., Zero-Valent Iron Nanoparticles for Abatement of Environmental Pollutants: Materials and Engineering Aspects. *Critical Reviews in Solid State and Materials Sciences* **2006,** *31* (4), 111-122.

63. Hamby, D. M., Site Remediation Techniques Supporting Environmental Restoration Activities—A Review. *Sci. Total Environ.* **1996,** *191* (3), 203-224.

64. Pera-Titus, M.; García-Molina, V.; Baños, M. A.; Giménez, J.; Esplugas, S., Degradation of Chlorophenols by Means of Advanced Oxidation Processes: A General Review. *Appl. Catal., B* **2004,** *47* (4), 219-256.

65. Xu, P.; Yu, B.; Li, F. L.; Cai, X. F.; Ma, C. Q., Microbial Degradation of Sulfur, Nitrogen and Oxygen Heterocycles. *Trends Microbiol.* **2006,** *14* (9), 398-405.

66. Dec, J.; Bollag, J.-M., Use of Enzymes in Bioremediation. In *Pesticide Biotransformation in Plants and Microorganisms*, American Chemical Society: 2000; Vol. 777, pp 182-193.

67. Mohamad, N. R.; Marzuki, N. H. C.; Buang, N. A.; Huyop, F.; Wahab, R. A., An Overview of Technologies for Immobilization of Enzymes and Surface Analysis Techniques for Immobilized Enzymes. *Biotechnol. Biotechnol. Equip.* **2015,** *29* (2), 205-220.

68. Homaei, A. A.; Sariri, R.; Vianello, F.; Stevanato, R., Enzyme Immobilization: An Update. *J. Chem. Biol.* **2013,** *6* (4), 185-205.

69. Madhavi, V.; Lele, S. S., Laccase: Properties and Applications. *BioResources* **2009,** *4* (4), 1694-1717.

70. Roy-Arcand, L.; Archibald, F. S., Direct Dechlorination of Chlorophenolic Compounds by Laccases from Trametes (Coriolus) Versicolor. *Enzyme Microb. Technol.* **1991,** *13* (3), 194-203.

71. Jolivalt, C.; Brenon, S.; Caminade, E.; Mougin, C.; Pontié, M., Immobilization of Laccase from Trametes Versicolor on A Modified PVDF Microfiltration Membrane: Characterization of the Grafted Support and Application in Removing A Phenylurea Pesticide in Wastewater. *J. Membr. Sci.* **2000,** *180* (1), 103-113.

72. Xu, R.; Chi, C.; Li, F.; Zhang, B., Laccase–Polyacrylonitrile Nanofibrous Membrane: Highly Immobilized, Stable, Reusable, and Efficacious for 2,4,6-Trichlorophenol Removal. *ACS Appl. Mater. Interfaces* **2013,** *5* (23), 12554-12560.

73. Chen, Y.; Stemple, B.; Kumar, M.; Wei, N., Cell Surface Display Fungal Laccase as a Renewable Biocatalyst for Degradation of Persistent Micropollutants Bisphenol A and Sulfamethoxazole. *Environ. Sci. Technol.* **2016,** *50* (16), 8799-8808.

74. Liu, G.; Dotzauer, D. M.; Bruening, M. L., Ion-Exchange Membranes Prepared Using Layer-by-Layer Polyelectrolyte Deposition. *J. Membr. Sci.* **2010,** *354* (1–2), 198-205.

75. Dotzauer, D. M.; Dai, J.; Sun, L.; Bruening, M. L., Catalytic Membranes Prepared Using Layer-by-Layer Adsorption of Polyelectrolyte/Metal Nanoparticle Films in Porous Supports. *Nano Lett.* **2006,** *6* (10), 2268-2272.

76. Lewis, S. R.; Datta, S.; Gui, M.; Coker, E. L.; Huggins, F. E.; Daunert, S.; Bachas, L.; Bhattacharyya, D., Reactive Nanostructured Membranes for Water Purification. *Proc. Natl. Acad. Sci. U. S. A.* **2011,** *108* (21), 8577-8582.

77. Moriyama, S.; Noda, A.; Nakanishi, K.; Matsuno, R.; Kamikubo, T., Thermal Stability of Immobilized Glucoamylase Entrapped in Polyacrylamide Gels and Bound to SP-Sephadex C–50. *Agric. Biol. Chem.* **1980,** *44* (9), 2047-2054.

78. Kim, Y. D.; Dordick, J. S.; Clark, D. S., Siloxane-Based Biocatalytic Films and Paints for Use as Reactive Coatings. *Biotechnol. Bioeng.* **2001,** *72* (4), 475-482.

79. Cao, L., Introduction: Immobilized Enzymes: Past, Present and Prospects. In *Carrier-Bound Immobilized Enzymes*, Wiley-VCH Verlag GmbH & Co. KGaA: 2005; pp 1-52.

80. Jochems, P.; Satyawali, Y.; Diels, L.; Dejonghe, W., Enzyme Immobilization on/in Polymeric Membranes: Status, Challenges and Perspectives in Biocatalytic Membrane Reactors (BMRs). *Green Chem.* **2011,** *13* (7), 1609-1623.

81. Ji, Q.; Wang, B.; Tan, J.; Zhu, L.; Li, L., Immobilized Multienzymatic Systems for Catalysis of Cascade Reactions. *Process Biochem.* **2016,** *51* (9), 1193-1203.

82. Jia, F.; Narasimhan, B.; Mallapragada, S., Materials-Based Strategies for Multi-Enzyme Immobilization and Co-Localization: A Review. *Biotechnol. Bioeng.* **2014,** *111* (2), 209-222.

83. Rosini, E.; Allegretti, C.; Melis, R.; Cerioli, L.; Conti, G.; Pollegioni, L.; D'Arrigo, P., Cascade Enzymatic Cleavage of the β-O-4 Linkage in a Lignin Model Compound. *Catal. Sci. Technol.* **2016,** *6* (7), 2195-2205.

84. Lange, H.; Decina, S.; Crestini, C., Oxidative Upgrade of Lignin – Recent Routes Reviewed. *Eur. Polym. J.* **2013,** *49* (6), 1151-1173.

85. Gasser, C. A.; Hommes, G.; Schäffer, A.; Corvini, P. F. X., Multi-Catalysis Reactions: New Prospects and Challenges of Biotechnology to Valorize Lignin. *Appl. Microbiol. Biotechnol.* **2012,** *95* (5), 1115-1134.

86. Bozell, J. J.; Hoberg, J. O.; Dimmel, D. R., Heteropolyacid Catalyzed Oxidation of Lignin and Lignin Models to Benzoquinones. *J. Wood Chem. Technol.* **2000,** *20* (1), 19-41.

87. Khanlari, S.; Dubé, M. A., Effect of pH on Poly(acrylic acid) Solution Polymerization. *J. Macromol. Sci., Part A: Pure Appl.Chem.* **2015,** *52* (8), 587-592.

88. Pandey, M. P.; Kim, C. S., Lignin Depolymerization and Conversion: A Review of Thermochemical Methods. *Chem. Eng. Technol.* **2011,** *34* (1), 29-41.

89. Mayer, A. M.; Staples, R. C., Laccase: New Functions for an Old Enzyme. *Phytochemistry* **2002,** *60* (6), 551-565.

90. Bhunia, A.; Durani, S.; Wangikar, P. P., Horseradish Peroxidase Catalyzed Degradation of Industrially Important Dyes. *Biotechnol. Bioeng.* **2001,** *72* (5), 562-567.

91. Datta, R.; Kelkar, A.; Baraniya, D.; Molaei, A.; Moulick, A.; Meena, R. S.; Formanek, P., Enzymatic Degradation of Lignin in Soil: A Review. *Sustainability* **2017,** *9* (7), 1163.

92. Janusz, G.; Pawlik, A.; Sulej, J.; Świderska-Burek, U.; Jarosz-Wilkołazka, A.; Paszczyński, A., Lignin Degradation: Microorganisms, Enzymes Involved, Genomes Analysis and Evolution. *FEMS Microbiol. Rev.* **2017,** *41* (6), 941-962.

93. Moreira, M. T.; Moldes-Diz, Y.; Feijoo, S.; Eibes, G.; Lema, J. M.; Feijoo, G., Formulation of Laccase Nanobiocatalysts Based on Ionic and Covalent Interactions for the Enhanced Oxidation of Phenolic Compounds. *Appl. Sci.* **2017,** *7* (8), 851.

94. Veitch, N. C., Horseradish Peroxidase: A Modern View of a Classic Enzyme. *Phytochemistry* **2004,** *65* (3), 249-259.

95. Franssen, M. C. R.; Steunenberg, P.; Scott, E. L.; Zuilhof, H.; Sanders, J. P. M., Immobilised Enzymes in Biorenewables Production. *Chem. Soc. Rev.* **2013,** *42* (15), 6491-6533.

96. Crestini, C.; Perazzini, R.; Saladino, R., Oxidative Functionalisation of Lignin by Layer-by-Layer Immobilised Laccases and Laccase Microcapsules. *Appl. Catal., A* **2010,** *372* (2), 115-123.

97. Moeder, M.; Martin, C.; Koeller, G., Degradation of Hydroxylated Compounds Using Laccase and Horseradish Peroxidase Immobilized on Microporous Polypropylene Hollow Fiber Membranes. *J. Membr. Sci.* **2004,** *245* (1), 183-190.

98. Nicell, J. A.; Bewtra, J. K.; Taylor, K. E.; Biswas, N.; St.Pierre, C., Enzyme Catalyzed Polymerization and Precipitation of Aromatic Compounds from Wastewater. *Water Sci. Technol.* **1992,** *25* (3), 157-164.

99. Nicell, J. A.; Bewtra, J. K.; Biswas, N.; Taylor, E., Reactor Development for Peroxidase Catalyzed Polymerization and Precipitation of Phenols from Wastewater. *Water Res.* **1993,** *27* (11), 1629-1639.

100. Islam, M. S.; Hernández, S.; Wan, H.; Ormsbee, L.; Bhattacharyya, D., Role of Membrane Pore Polymerization Conditions for pH Responsive Behavior, Catalytic Metal Nanoparticle Synthesis, and PCB Degradation. *J. Membr. Sci.* **2018,** *555*, 348-361.

101. Hernández, S.; Islam, M. S.; Thompson, S.; Kearschner, M.; Hatakeyama, E.; Malekzadeh, N.; Hoelen, T.; Bhattacharyya, D., Thiol-Functionalized Membranes for Mercury Capture from Water. *Ind. Eng. Chem. Res.* **2020,** *59* (12), 5287-5295.

102. Conde, J.; Dias, J. T.; Grazú, V.; Moros, M.; Baptista, P. V.; de la Fuente, J. M., Revisiting 30 Years of Biofunctionalization and Surface Chemistry of Inorganic Nanoparticles for Nanomedicine. *Front. Chem.* **2014,** *2* (48).

103. Wang, C.; Yan, Q.; Liu, H.-B.; Zhou, X.-H.; Xiao, S.-J., Different EDC/NHS Activation Mechanisms between PAA and PMAA Brushes and the Following Amidation Reactions. *Langmuir* **2011,** *27* (19), 12058-12068.

104. Sam, S.; Touahir, L.; Salvador Andresa, J.; Allongue, P.; Chazalviel, J. N.; Gouget-Laemmel, A. C.; Henry de Villeneuve, C.; Moraillon, A.; Ozanam, F.; Gabouze, N.; Djebbar, S., Semiquantitative Study of the EDC/NHS Activation of Acid Terminal Groups at Modified Porous Silicon Surfaces. *Langmuir* **2010,** *26* (2), 809-814.

105. Gu, B.; Bian, Y.; Miller, C. L.; Dong, W.; Jiang, X.; Liang, L., Mercury Reduction and Complexation by Natural Organic Matter in Anoxic Environments. *Proc. Natl. Acad. Sci. U. S. A.* **2011,** *108* (4), 1479-1483.

106. Schuster, E., The Behavior of Mercury in the Soil with Special Emphasis on Complexation and Adsorption Processes - A Review of the Literature. *Water, Air, Soil Pollut.* **1991,** *56* (1), 667-680.

107. Wagner-döbler, I., Pilot Plant for Bioremediation of Mercury-containing Industrial Wastewater. *Appl. Microbiol. Biotechnol.* **2003,** *62* (2-3), 124-133.

108. Avellan, A.; Stegemeier, J. P.; Gai, K.; Dale, J.; Hsu-Kim, H.; Levard, C.; O'Rear, D.; Hoelen, T. P.; Lowry, G. V., Speciation of Mercury in Selected Areas of the Petroleum Value Chain. *Environ. Sci. Technol.* **2018,** *52* (3), 1655-1664.

109. Besouw, M.; Masereeuw, R.; van den Heuvel, L.; Levtchenko, E., Cysteamine: An Old Drug with New Potential. *Drug Discovery Today* **2013,** *18* (15), 785-792.

110. Gallego-Villar, L.; Hannibal, L.; Häberle, J.; Thöny, B.; Ben-Omran, T.; Nasrallah, G. K.; Dewik, A.-N.; Kruger, W. D.; Blom, H. J., Cysteamine Revisited: Repair of Arginine to Cysteine Mutations. *J. Inherited Metab. Dis.* **2017,** *40* (4), 555-567.

111. Meeks, N. D.; Davis, E.; Jain, M.; Skandan, G.; Bhattacharyya, D., Mercury Removal by Thiol-functionalized Metal Oxide–Carbon Black Sorbent and Mixed-Matrix Membranes. *Environ. Prog. Sustainable Energy* **2013,** *32* (3), 705-714.

112. Arshadi, M.; Mousavinia, F.; Khalafi-Nezhad, A.; Firouzabadi, H.; Abbaspourrad, A., Adsorption of Mercury Ions from Wastewater by a Hyperbranched and Multi-Functionalized Dendrimer Modified Mixed-Oxides Nanoparticles. *J. Colloid Interface Sci.* **2017,** *505*, 293-306.

113. Sun, M.; Cheng, G.; Ge, X.; Chen, M.; Wang, C.; Lou, L.; Xu, X., Aqueous Hg(II) Immobilization by Chitosan Stabilized Magnetic Iron Sulfide Nanoparticles. *Sci. Total Environ.* **2018,** *621*, 1074-1083.

114. Sun, N.; Wen, X.; Yan, C., Adsorption of Mercury Ions from Wastewater Aqueous Solution by Amide Functionalized Cellulose from Sugarcane Bagasse. *Int. J. Biol. Macromol.* **2018,** *108*, 1199-1206.

115. Saraydın, D.; Yıldırım, E. Ş.; Karadağ, E.; Güven, O., Radiation-Synthesized Acrylamide/Crotonic Acid Hydrogels for Selective Mercury (II) Ion Adsorption. *Adv. Polym. Technol* **2018,** *37* (3), 822-829.

116. Bansal, M.; Ram, B.; Chauhan, G. S.; Kaushik, A., L-Cysteine Functionalized Bagasse Cellulose Nnanofibers for Mercury(II) Ions Adsorption. *Int. J. Biol. Macromol.* **2018,** *112*, 728-736.

117. Qin, H.; Xiao, R.; Guo, L.; Meng, J.; Chen, J., Mercury (II) Adsorption from Aqueous Solution using Nitrogen and Sulfur Co-Doped Activated Carbon. *Water Sci. Technol.* **2018,** *2017* (1), 310-318.

118. Deng, S.; Zhang, G.; Liang, S.; Wang, P., Microwave Assisted Preparation of Thio-Functionalized Polyacrylonitrile Fiber for the Selective and Enhanced Adsorption of Mercury and Cadmium from Water. *ACS Sustainable Chem. Eng.* **2017,** *5* (7), 6054-6063.

119. AlOmar, M. K.; Alsaadi, M. A.; Jassam, T. M.; Akib, S.; Ali Hashim, M., Novel Deep Eutectic Solvent-Functionalized Carbon Nanotubes Adsorbent for Mercury Removal from Water. *J. Colloid Interface Sci.* **2017,** *497*, 413-421.

120. Kokkinos, E.; Simeonidis, K.; Pinakidou, F.; Katsikini, M.; Mitrakas, M., Optimization of Tetravalent Manganese Feroxyhyte's Negative Charge Density: A High-Performing Mercury Adsorbent from Drinking Water. *Sci. Total Environ.* **2017,** *574*, 482-489.

121. Ai, K.; Ruan, C.; Shen, M.; Lu, L., $MoS_2$ Nanosheets with Widened Interlayer Spacing for High-Efficiency Removal of Mercury in Aquatic Systems. *Adv. Funct. Mater.* **2016,** *26* (30), 5542-5549.

122. Zhou, J.; Liu, Y.; Zhou, X.; Ren, J.; Zhong, C., Removal of Mercury Ions from Aqueous Solution by Thiourea-Functionalized Magnetic Biosorbent: Preparation and Mechanism Study. *J. Colloid Interface Sci.* **2017,** *507*, 107-118.

123. Dąbrowski, A.; Hubicki, Z.; Podkościelny, P.; Robens, E., Selective Removal of The Heavy Metal Ions from Waters and Industrial Wastewaters by Ion-Exchange Method. *Chemospher* **2004,** *56* (2), 91-106.

124. Huang, L.; Peng, C.; Cheng, Q.; He, M.; Chen, B.; Hu, B., Thiol-Functionalized Magnetic Porous Organic Polymers for Highly Efficient Removal of Mercury. *Ind. Eng. Chem. Res.* **2017,** *56* (46), 13696-13703.

125. Cheng, J.; Li, Y.; Li, L.; Lu, P.; Wang, Q.; He, C., Thiol-/Thioether-Functionalized Porous Organic Polymers for Simultaneous Removal of Mercury(II) Ion and Aromatic Pollutants in Water. *New J. Chem.* **2019,** *43* (20), 7683-7693.

126. Thakur, S.; Das, G.; Raul, P. K.; Karak, N., Green One-Step Approach to Prepare Sulfur/Reduced Graphene Oxide Nanohybrid for Effective Mercury Ions Removal. *J. Phys. Chem. C* **2013,** *117* (15), 7636-7642.

127. Ma, L.; Wang, Q.; Islam, S. M.; Liu, Y.; Ma, S.; Kanatzidis, M. G., Highly Selective and Efficient Removal of Heavy Metals by Layered Double Hydroxide Intercalated with the $MoS_4^{2-}$ Ion. *J. Am. Chem. Soc.* **2016,** *138* (8), 2858-2866.

128. Aguila, B.; Sun, Q.; Perman, J. A.; Earl, L. D.; Abney, C. W.; Elzein, R.; Schlaf, R.; Ma, S., Efficient Mercury Capture Using Functionalized Porous Organic Polymer. *Adv. Mater.* **2017,** *29* (31), 1700665.

129. Bandaru, N. M.; Reta, N.; Dalal, H.; Ellis, A. V.; Shapter, J.; Voelcker, N. H., Enhanced Adsorption of Mercury Ions on Thiol Derivatized Single Wall Carbon Nanotubes. *J. Hazard. Mater.* **2013,** *261*, 534-541.

130. Rudd, N. D.; Wang, H.; Fuentes-Fernandez, E. M. A.; Teat, S. J.; Chen, F.; Hall, G.; Chabal, Y. J.; Li, J., Highly Efficient Luminescent Metal–Organic Framework for the Simultaneous Detection and Removal of Heavy Metals from Water. *ACS Appl. Mater. Interfaces* **2016,** *8* (44), 30294-30303.

131. Gai, K.; Avellan, A.; Hoelen, T. P.; Lopez-Linares, F.; Hatakeyama, E. S.; Lowry, G. V., Impact of Mercury Speciation on Its Removal from Water by Activated Carbon and Organoclay. *Water Res.* **2019,** *157*, 600-609.

132. Li, Z.; Li, M.; Bian, Z.; Kathiraser, Y.; Kawi, S., Design of Highly Stable and Selective Core/Yolk–Shell Nanocatalysts—A Review. *Appl. Catal., B* **2016,** *188*, 324-341.

133. Saha, A.; Bharmoria, P.; Mondal, A.; Ghosh, S. C.; Mahanty, S.; Panda, A. B., Generalized Synthesis and Evaluation of Formation Mechanism of Metal Oxide/Sulphide@C Hollow Spheres. *J. Mater. Chem. A* **2015,** *3* (40), 20297-20304.

134. Nakamura, R.; Matsubayashi, G.; Tsuchiya, H.; Fujimoto, S.; Nakajima, H., Transition in the Nanoporous Structure of Iron Oxides during the Oxidation of Iron Nanoparticles and Nanowires. *Acta Mater.* **2009,** *57* (14), 4261-4266.

135. Wang, B.; Wu, H.; Yu, L.; Xu, R.; Lim, T. T.; Lou, X. W., Template-free Formation of Uniform Urchin-like $\alpha$-FeOOH Hollow Spheres with Superior Capability for Water Treatment. *Adv. Mater.* **2012,** *24* (8), 1111-1116.

136. Zhou, J.; Song, H.; Chen, X.; Zhi, L.; Yang, S.; Huo, J.; Yang, W., Carbon-Encapsulated Metal Oxide Hollow Nanoparticles and Metal Oxide Hollow Nanoparticles: A General Synthesis Strategy and Its Application to Lithium-Ion Batteries. *Chem. Mater.* **2009,** *21* (13), 2935-2940.

137. Riasat, R.; Nie, G., Synthesis and Characterization of Nontoxic Hollow Iron Oxide ($\alpha$-$Fe_2O_3$) Nanoparticles Using a Simple Hydrothermal Strategy. *J. Nanomater.* **2016,** *2016*, 7.

138. Xing, R.; Bhirde, A. A.; Wang, S.; Sun, X.; Liu, G.; Hou, Y.; Chen, X., Hollow Iron Oxide Nanoparticles as Multidrug Resistant Drug Delivery and Imaging Vehicles. *Nano Res.* **2013,** *6* (1), 1-9.

139. Galeano, C.; Meier, J. C.; Soorholtz, M.; Bongard, H.; Baldizzone, C.; Mayrhofer, K. J. J.; Schüth, F., Nitrogen-Doped Hollow Carbon Spheres as a Support for Platinum-Based Electrocatalysts. *ACS Catal.* **2014,** *4* (11), 3856-3868.

140. Wang, Y.; Kong, A.; Chen, X.; Lin, Q.; Feng, P., Efficient Oxygen Electroreduction: Hierarchical Porous Fe–N-doped Hollow Carbon Nanoshells. *ACS Catal.* **2015,** *5* (6), 3887-3893.

141. Titirici, M.-M.; Antonietti, M.; Thomas, A., A Generalized Synthesis of Metal Oxide Hollow Spheres Using a Hydrothermal Approach. *Chem. Mater.* **2006,** *18* (16), 3808-3812.

142. Qu, B.; Zhu, C.; Li, C.; Zhang, X.; Chen, Y., Coupling Hollow $Fe_3O_4$–Fe Nanoparticles with Graphene Sheets for High-Performance Electromagnetic Wave Absorbing Material. *ACS Appl. Mater. Interfaces* **2016,** *8* (6), 3730-3735.

143. Hensley, A. J. R.; Hong, Y.; Zhang, R.; Zhang, H.; Sun, J.; Wang, Y.; McEwen, J.-S., Enhanced $Fe_2O_3$ Reducibility via Surface Modification with Pd: Characterizing the

Synergy within Pd/Fe Catalysts for Hydrodeoxygenation Reactions. *ACS Catal.* **2014,** *4* (10), 3381-3392.

144. You, H.; Zhang, F.; Liu, Z.; Fang, J., Free-Standing Pt–Au Hollow Nanourchins with Enhanced Activity and Stability for Catalytic Methanol Oxidation. *ACS Catal.* **2014,** *4* (9), 2829-2835.

145. Asset, T.; Job, N.; Busby, Y.; Crisci, A.; Martin, V.; Stergiopoulos, V.; Bonnaud, C.; Serov, A.; Atanassov, P.; Chattot, R.; Dubau, L.; Maillard, F., Porous Hollow PtNi/C Electrocatalysts: Carbon Support Considerations To Meet Performance and Stability Requirements. *ACS Catal.* **2018,** *8* (2), 893-903.

146. Sarma, R.; Islam, M. S.; Miller, A.-F.; Bhattacharyya, D., Layer-by-Layer-Assembled Laccase Enzyme on Stimuli-Responsive Membranes for Chloro-Organics Degradation. *ACS Appl. Mater. Interfaces* **2017,** *9* (17), 14858-14867.

147. Hwang, S.; Shao, Q.; Williams, H.; Hilty, C.; Gao, Y. Q., Methanol Strengthens Hydrogen Bonds and Weakens Hydrophobic Interactions in Proteins – A Combined Molecular Dynamics and NMR Study. *J. Phys. Chem. B* **2011,** *115* (20), 6653-6660.

148. Boethling, R. S.; Mackay, D., *Handbook of Property Estimation Methods for Chemicals: Environmental Health Sciences*. CRC Press: Boca Raton, FL, 2000.

149. O'Neil, M., *The Merck Index: An Encyclopedia of Chemicals, Drugs, and Biologicals*. Cambridge, UK, 2013.

150. Riauba, L.; Niaura, G.; Eicher-Lorka, O.; Butkus, E., A Study of Cysteamine Ionization in Solution by Raman Spectroscopy and Theoretical Modeling. *J. Phys. Chem. A* **2006,** *110* (50), 13394-13404.

151. Perrin, D. D.; Dempsey, B.; Serjeant, E. P., *pKa Prediction for Organic Acids and Bases*. Springer: Netherlands, 1981.

152. Laughlin, R. G., Fundamentals of the Zwitterionic Hydrophilic Group. *Langmuir* **1991,** *7* (5), 842-847.

153. Hernández, S.; Saad, A.; Ormsbee, L.; Bhattacharyya, D., Nanocomposite and Responsive Membranes for Water Treatment. In *Emerging Membrane Technology For Sustainable Water Treatment; Hankins, NP, Singh, R., Eds*, Elsevier Science: Cambridge, MA, USA, 2016; pp 389-431.

154. Kadłubowski, S.; Henke, A.; Ulański, P.; Rosiak, J. M.; Bromberg, L.; Hatton, T. A., Hydrogels of Polyvinylpyrrolidone (PVP) and Poly(acrylic acid) (PAA) Synthesized by Photoinduced Crosslinking of Homopolymers. *Polymer* **2007,** *48* (17), 4974-4981.

155. Riccardi, D.; Guo, H.-B.; Parks, J. M.; Gu, B.; Summers, A. O.; Miller, S. M.; Liang, L.; Smith, J. C., Why Mercury Prefers Soft Ligands. *J. Phys. Chem. Lett.* **2013,** *4* (14), 2317-2322.

156. Davenport, D.; Gui, M.; Ormsbee, L.; Bhattacharyya, D., Development of PVDF Membrane Nanocomposites via Various Functionalization Approaches for Environmental Applications. *Polymers* **2016,** *8* (2), 32.

157. Nielsen, L. E., Cross-Linking–Effect on Physical Properties of Polymers. *J. Macromol. Sci., Polym. Rev.* **1969,** *3* (1), 69-103.

158. Kjøniksen, A.-L.; Nyström, B., Effects of Polymer Concentration and Cross-Linking Density on Rheology of Chemically Cross-Linked Poly(vinyl alcohol) Near the Gelation Threshold. *Macromolecules* **1996,** *29* (15), 5215-5222.

159. Zhao, F.; Bi, W.; Zhao, S., Influence of Crosslink Density on Mechanical Properties of Natural Rubber Vulcanizates. *J. Macromol. Sci., Part B: Phys.* **2011,** *50* (7), 1460-1469.

160. Ying, L.; Yu, W. H.; Kang, E. T.; Neoh, K. G., Functional and Surface-Active Membranes from Poly(vinylidene fluoride)-graft-Poly(acrylic acid) Prepared via RAFT-Mediated Graft Copolymerization. *Langmuir* **2004,** *20* (14), 6032-6040.

161. Ouyang, Z.-W.; Chen, E.-C.; Wu, T.-M., Thermal Stability and Magnetic Properties of Polyvinylidene Fluoride/Magnetite Nanocomposites. *Materials* **2015,** *8* (7), 4553-4564.

162. Moharram, M. A.; Khafagi, M. G., Thermal Behavior of Poly(acrylic acid)–Poly(vinyl pyrrolidone) and Poly(acrylic acid)–Metal–Poly(vinyl pyrrolidone) Complexes. *J. Appl. Polym. Sci.* **2006,** *102* (4), 4049-4057.

163. He, F.; Luo, B.; Yuan, S.; Liang, B.; Choong, C.; Pehkonen, S. O., PVDF Film Tethered with RGD-Click-Poly(glycidyl methacrylate) Brushes by Combination of Direct Surface-Initiated ATRP and Click Chemistry for Improved Cytocompatibility. *RSC Adv.* **2014,** *4* (1), 105-117.

164. Kirwan, L. J.; Fawell, P. D.; van Bronswijk, W., In Situ FTIR-ATR Examination of Poly(acrylic acid) Adsorbed onto Hematite at Low pH. *Langmuir* **2003,** *19* (14), 5802-5807.

165. Groll, J.; Ademovic, Z.; Ameringer, T.; Klee, D.; Moeller, M., Comparison of Coatings from Reactive Star Shaped PEG-*stat*-PPG Prepolymers and Grafted Linear PEG for Biological and Medical Applications. *Biomacromolecules* **2005,** *6* (2), 956-962.

166. Zhang, W.; Wahlgren, M.; Sivik, B., Membrane Characterization by the Contact Angle Technique: II. Characterization of UF-Membranes and Comparison Between the Captive Bubble and Sessile Drop as Methods to Obtain Water Contact Angles. *Desalination* **1989,** *72* (3), 263-273.

167. Baek, Y.; Kang, J.; Theato, P.; Yoon, J., Measuring Hydrophilicity of RO Membranes by Contact Angles via Sessile Drop and Captive Bubble Method: A Comparative Study. *Desalination* **2012,** *303*, 23-28.

168. Choi, J.; Rubner, M. F., Influence of the Degree of Ionization on Weak Polyelectrolyte Multilayer Assembly. *Macromolecules* **2005,** *38* (1), 116-124.

169. Lützenkirchen, J.; van Male, J.; Leermakers, F.; Sjöberg, S., Comparison of Various Models to Describe the Charge−pH Dependence of Poly(acrylic acid). *J. Chem. Eng. Data* **2011,** *56* (4), 1602-1612.

170. Swift, T.; Swanson, L.; Geoghegan, M.; Rimmer, S., The pH-Responsive Behaviour of Poly(acrylic acid) in Aqueous Solution is Dependent on Molar Mass. *Soft Matter* **2016,** *12* (9), 2542-2549.

171. Huang, Q.; Shi, X.; Pinto, R. A.; Petersen, E. J.; Weber, W. J., Tunable Synthesis and Immobilization of Zero-Valent Iron Nanoparticles for Environmental Applications. *Environ. Sci. Technol.* **2008,** *42* (23), 8884-8889.

172. He, F.; Zhao, D., Manipulating the Size and Dispersibility of Zerovalent Iron Nanoparticles by Use of Carboxymethyl Cellulose Stabilizers. *Environ. Sci. Technol.* **2007,** *41* (17), 6216-6221.

173. Hadjipanayis, C. G.; Bonder, M. J.; Balakrishnan, S.; Wang, X.; Mao, H.; Hadjipanayis, G. C., Metallic Iron Nanoparticles for MRI Contrast Enhancement and Local Hyperthermia. *Small* **2008,** *4* (11), 1925-1929.

174. Yuvakkumar, R.; Elango, V.; Rajendran, V.; Kannan, N., Preparation and Characterization of Zero Valent Iron Nanoparticles. *Dig. J. Nanomater. Biostruct.* **2011,** *6* (4), 1771-1776.

175. Hudson, R.; Hamasaka, G.; Osako, T.; Yamada, Y. M.; Li, C.-J.; Uozumi, Y.; Moores, A., Highly Efficient Iron (0) Nanoparticle-Catalyzed Hydrogenation in Water in Flow. *Green Chem.* **2013,** *15* (8), 2141-2148.

176. Borchert, H.; Shevchenko, E. V.; Robert, A.; Mekis, I.; Kornowski, A.; Grübel, G.; Weller, H., Determination of Nanocrystal Sizes: A Comparison of TEM, SAXS, and XRD Studies of Highly Monodisperse $CoPt_3$ Particles. *Langmuir* **2005,** *21* (5), 1931-1936.

177. Zhu, B.-W.; Lim, T.-T., Catalytic Reduction of Chlorobenzenes with Pd/Fe Nanoparticles: Reactive Sites, Catalyst Stability, Particle Aging, and Regeneration. *Environ. Sci. Technol.* **2007,** *41* (21), 7523-7529.

178. Phenrat, T.; Saleh, N.; Sirk, K.; Tilton, R. D.; Lowry, G. V., Aggregation and Sedimentation of Aqueous Nanoscale Zerovalent Iron Dispersions. *Environ. Sci. Technol.* **2007,** *41* (1), 284-290.

179. Greenlee, L. F.; Torrey, J. D.; Amaro, R. L.; Shaw, J. M., Kinetics of Zero Valent Iron Nanoparticle Oxidation in Oxygenated Water. *Environ. Sci. Technol*. **2012,** *46* (23), 12913-12920.

180. Islam, M. S.; Rahman, M. M.; Ilias, S., Characterization of Pd–Cu Membranes Fabricated by Surfactant Induced Electroless Plating (SIEP) for Hydrogen Separation. *Int. J. Hydrogen Energy* **2012,** *37* (4), 3477-3490.

181. Choi, H.; Al-Abed, S. R.; Agarwal, S.; Dionysiou, D. D., Synthesis of Reactive Nano-Fe/Pd Bimetallic System-Impregnated Activated Carbon for the Simultaneous Adsorption and Dechlorination of PCBs. *Chem. Mater.* **2008,** *20* (11), 3649-3655.

182. Davis, M. E.; Davis, R. J., *Fundamentals of Chemical Reaction Engineering*. McGraw-Hill: New York, USA, 2003.

183. Chen, N. H., *Process Reactor Design*. Allyn and Bacon: Boston, USA, 1983.

184. Penu, R.; Vasilescu, I.; Eremia, S. A. V.; Gatea, F.; Radu, G.-L.; Litescu, S.-C., Development of a Nanocomposite System and Its Application in Biosensors Construction. *Cent. Eur. J. Chem.* **2013,** *11* (6), 968-978.

185. Zhang, X.; Hua, M.; Lv, L.; Pan, B., Ionic Polymer-Coated Laccase with High Activity and Enhanced Stability: Application in the Decolourisation of Water Containing AO7. *Sci. Rep.* **2015,** *5*, 8253.

186. Spinelli, D.; Fatarella, E.; Di Michele, A.; Pogni, R., Immobilization of Fungal (*Trametes Versicolor*) Laccase onto Amberlite IR-120 H Beads: Optimization and Characterization. *Process Biochem.* **2013,** *48* (2), 218-223.

187. Rother, C.; Nidetzky, B., Enzyme Immobilization by Microencapsulation: Methods, Materials, and Technological Applications. In *Encyclopedia of Industrial Biotechnology*, Flickinger, M. C., Ed. John Wiley & Sons: 2014; pp 1-21.

188. Hu, X.; Ji, H.; Wu, L., Singlet Oxygen Photogeneration and 2,4,6-TCP Photodegradation at Pt/$TiO_2$ Under Visible Light Illumination. *RSC Adv.* **2012,** *2* (32), 12378-12383.

189. Gaitan, I. J.; Medina, S. C.; González, J. C.; Rodríguez, A.; Espejo, Á. J.; Osma, J. F.; Sarria, V.; Alméciga-Díaz, C. J.; Sánchez, O. F., Evaluation of Toxicity and Degradation of a Chlorophenol Mixture by the Laccase Produced by *Trametes Pubescens*. *Bioresour. Technol.* **2011,** *102* (3), 3632-3635.

190. Diez, M. C.; Gallardo, F.; Tortella, G.; Rubilar, O.; Navia, R.; Bornhardt, C., Chlorophenol Degradation in Soil Columns Inoculated with Anthracophyllum Discolor Immobilized on Wheat Grains. *J. Environ. Manage.* **2012,** *95*, S83-S87.

191. Liu, X. Z.; Zhang, Q.; Liang, Y. X.; Zhang, R. F., Biodegradation of 2-Chlorophenol by Laccase Immobilized on Large-Sized Macroporous Silica. *Adv. Mater. Res.* **2014,** *1010-1012*, 830-834.

192. Dai, Y.; Yao, J.; Song, Y.; Liu, X.; Wang, S.; Yuan, Y., Enhanced Performance of Immobilized Laccase in Electrospun Fibrous Membranes by Carbon Nanotubes Modification and Its Application for Bisphenol A removal from water. *J. Hazard. Mater.* **2016,** *317*, 485-493.

193. Li, G.; Nandgaonkar, A. G.; Wang, Q.; Zhang, J.; Krause, W. E.; Wei, Q.; Lucia, L. A., Laccase-Immobilized Bacterial Cellulose/$TiO_2$ Functionalized Composite Membranes: Evaluation for Photo- and Bio-Catalytic Dye Degradation. *J. Membr. Sci.* **2017,** *525*, 89-98.

194. Lin, J.; Fan, L.; Miao, R.; Le, X.; Chen, S.; Zhou, X., Enhancing Catalytic Performance of Laccase via Immobilization on Chitosan/$CeO_2$ Microspheres. *Int. J. Biol. Macromol.* **2015,** *78*, 1-8.

195. Liu, Y.; Zeng, Z.; Zeng, G.; Tang, L.; Pang, Y.; Li, Z.; Liu, C.; Lei, X.; Wu, M.; Ren, P.; Liu, Z.; Chen, M.; Xie, G., Immobilization of Laccase on Magnetic Bimodal

Mesoporous Carbon and the Application in the Removal of Phenolic Compounds. *Bioresour. Technol.* **2012,** *115*, 21-26.

196. Wang, S.; Chen, W.; He, S.; Zhao, Q.; Li, X.; Sun, J.; Jiang, X., Mesosilica-Coated Ultrafine Fibers for Highly Efficient Laccase Encapsulation. *Nanoscale* **2014,** *6* (12), 6468-6472.

197. Wang, Y.; Zhang, D.; He, F. R.; Chen, X. C., Immobilization of Laccase by $Cu^{2+}$ Chelate Affinity Interaction on Surface Modified Magnetic Silica Particles and Its Use for the Removal of Pentachlorophenol. *Chin. Chem. Lett.* **2012,** *23* (2), 197-200.

198. Brissos, V.; Tavares, D.; Sousa, A. C.; Robalo, M. P.; Martins, L. O., Engineering a Bacterial DyP-Type Peroxidase for Enhanced Oxidation of Lignin-Related Phenolics at Alkaline pH. *ACS Catal.* **2017,** *7* (5), 3454-3465.

199. Lončar, N.; Colpa, D. I.; Fraaije, M. W., Exploring the Biocatalytic Potential of a DyP-Type Peroxidase by Profiling the Substrate Acceptance of *Thermobifida Fusca* DyP Peroxidase. *Tetrahedron* **2016,** *72* (46), 7276-7281.

200. Rocha-Martin, J.; Velasco-Lozano, S.; Guisán, J. M.; López-Gallego, F., Oxidation of Phenolic Compounds Catalyzed by Immobilized Multi-Enzyme Systems with Integrated Hydrogen Peroxide Production. *Green Chem.* **2014,** *16* (1), 303-311.

201. Sarma, R.; Islam, M. S.; Running, M.; Bhattacharyya, D., Multienzyme Immobilized Polymeric Membrane Reactor for the Transformation of a Lignin Model Compound. *Polymers* **2018,** *10* (4), 463.

202. Luxbacher, T., Electrokinetics on Polymer Surfaces. In *9th Freiberger Polymertag*, 2009.

203. Luxbacher, T., *The ZETA Guide: Principles of the Streaming Potential Technique*. First ed.; Anton Paar GmbH: Graz, Austria: 2014.

204. AMBERSEP™ GT74 - Product Data Sheet. p AMBERSEP™ GT74 Product Data Sheet.

205. French, R. A.; Jacobson, A. R.; Kim, B.; Isley, S. L.; Penn, R. L.; Baveye, P. C., Influence of Ionic Strength, pH, and Cation Valence on Aggregation Kinetics of Titanium Dioxide Nanoparticles. *Environ. Sci. Technol.* **2009,** *43* (5), 1354-1359.

206. Liu, G.; Cai, Y.; O'Driscoll, N., *Environmental Chemistry and Toxicology of Mercury*. John Wiley & Sons: 2011.

207. Powell, K. J.; Brown, P. L.; Byrne, R. H.; Gajda, T.; Hefter, G.; Sjöberg, S.; Wanner, H., Chemical Speciation of Hg(II) with Environmental Inorganic Ligands. *Aust. J. Chem.* **2004,** *57* (10), 993-1000.

208. Humbert, H.; Gallard, H.; Suty, H.; Croué, J.-P., Natural Organic Matter (NOM) and Pesticides Removal Using a Combination of Ion Exchange Resin and Powdered Activated Carbon (PAC). *Water Res.* **2008,** *42* (6), 1635-1643.

209. Baes, C. F.; Mesmer, R. E., *The Hydrolysis of Cations*. John Wiley & Sons: New York, USA, 1976.

210. Gai, K.; Hoelen, T. P.; Hsu-Kim, H.; Lowry, G. V., Mobility of Four Common Mercury Species in Model and Natural Unsaturated Soils. *Environ. Sci. Technol.* **2016,** *50* (7), 3342-3351.

211. National Primary Drinking Water Regulations. https://www.epa.gov/ground-water-and-drinking-water/national-primary-drinking-water-regulations.

212. Zhang, X.; Wu, T.; Zhang, Y.; Ng, D. H. L.; Zhao, H.; Wang, G., Adsorption of $Hg^{2+}$ by Thiol Functionalized Hollow Mesoporous Silica Microspheres with Magnetic Cores. *RSC Adv.* **2015,** *5* (63), 51446-51453.

213. Wang, W.; Lu, Y.-C.; Huang, H.; Wang, A.-J.; Chen, J.-R.; Feng, J.-J., Solvent-free Synthesis of Sulfur- and Nitrogen-co-doped Fluorescent Carbon Nanoparticles from Glutathione for Highly Selective and Sensitive Detection of Mercury(II) Ions. *Sens. Actuators, B* **2014,** *202*, 741-747.

214. Rahman, M. M.; Islam, M. S.; Rahman, M. A.; Tun, H.; Deshmane, V.; Hossain, T.; Ilias, S., Evaluation and Characterization of Pd-Ag Composite Membrane Fabricated by Surfactant Induced Electroless Plating (SIEP) for Hydrogen Separation. *Sep. Sci. Technol.* **2019,** *54* (13), 2084-2097.

215. Finlayson, B. A., *Introduction to Chemical Engineering Computing*. Second ed.; John Wiley & Sons: 2012.

216. Cussler, E. L., *Diffusion: Mass Transfer in Fluid Systems*. Third ed.; Cambridge University Press: 2009.

217. Southard, M. Z.; Green, D. W., *Perry's Chemical Engineers' Handbook*. Nineth ed.; McGraw-Hill Education: 2018.

218. Wang, Z.; Wang, Z.; Wu, H.; Lou, X. W., Mesoporous Single-crystal $CoSn(OH)_6$ Hollow Structures with Multilevel Interiors. *Sci. Rep.* **2013,** *3* (1), 1391.

219. Yin, Y.; Rioux, R. M.; Erdonmez, C. K.; Hughes, S.; Somorjai, G. A.; Alivisatos, A. P., Formation of Hollow Nanocrystals Through the Nanoscale Kirkendall Effect. *Science* **2004,** *304* (5671), 711-714.

220. Caruso, F., Hollow Capsule Processing through Colloidal Templating and Self-Assembly. *Chem. - Eur. J.* **2000,** *6* (3), 413-419.

221. Zhong, Z.; Yin, Y.; Gates, B.; Xia, Y., Preparation of Mesoscale Hollow Spheres of $TiO_2$ and $SnO_2$ by Templating Against Crystalline Arrays of Polystyrene Beads. *Adv. Mater.* **2000,** *12* (3), 206-209.

222. Yu, C.; Fan, J.; Tian, B.; Zhao, D., Morphology Development of Mesoporous Materials: a Colloidal Phase Separation Mechanism. *Chem. Mater.* **2004,** *16* (5), 889-898.

223. Dong, A.; Ren, N.; Tang, Y.; Wang, Y.; Zhang, Y.; Hua, W.; Gao, Z., General Synthesis of Mesoporous Spheres of Metal Oxides and Phosphates. *J. Am. Chem. Soc.* **2003,** *125* (17), 4976-4977.

224. Azam, A.; Ahmed, A. S.; Oves, M.; Khan, M. S.; Habib, S. S.; Memic, A., Antimicrobial Activity of Metal Oxide Nanoparticles against Gram-positive and Gram-negative Bacteria: A Comparative Study. *Int. J. Nanomed.* **2012,** *7*, 6003-6009.

# VITA

Mohammad Saiful Islam is born in Bangladesh. He completed his B.Sc. in Chemical Engineering from Bangladesh University of Science & Engineering (BUET), Dhaka, Bangladesh in 2004. After working as a process engineer for several years in process industries he pursued his Master's in Science (MS) in Chemical Engineering from North Carolina Agricultural & Technical State University (NCATSU), Greensboro, NC in 2011. After completion of his masters he return to Bangladesh and served as a process manager in a refinery till summer of 2015. In Fall 2015, he joined in the Ph.D. program in chemical engineering at the University of Kentucky.

## Awards

- 2018 Environmental Division Best Graduate Student Paper Award from American Institute of Chemical Engineers (AIChE)
- University of Kentucky Graduate School Travel Awards, 2018

## Publications

- **Islam, M. S.**; Wan, H.; Detisch, M. J.; Khan, M. A.; Bhattacharyya, D., Synthesis of Hollow Nanoparticles Characterization and Application towards Degradation of Chlorinated Organic Compounds. **to be submitted** in July **2020**.
- **Islam, M. S.**; Vogler, R. J; Al Hasnine, S. M. A.; Hatakeyama, E.; Malekzadeh, N.; Hoelen, T.; Bhattacharyya, D., Heavy Metal Removal from Wastewater using Cysteamine Functionalized Membranes. *ACS Omega*, Submitted May **2020**.
- Wan, H.; **Islam, M. S.**; Qian, D.; Ormsbee, L.; Bhattacharyya, D., Reductive Degradation of $CCl_4$ by Sulfidized Fe and Pd-Fe Nanoparticles: Kinetics, Longevity, and Morphology Aspects. *Chem. Eng. J.* **2020,** *394*, 125013.
- Wan, H.; **Islam, M. S**.; Briot, N. J.; Schnobrich, M.; Pacholik, L.; Ormsbee, L.; Bhattacharyya, D., Pd/Fe Nanoparticle Integrated PMAA-PVDF Membranes for Chloro-Organic Remediation from Synthetic and Site Groundwater. *J. Membr. Sci.* **2020,** *594*, 117454.

- Hernández, S.; **Islam, M. S.**; Thompson, S.; Kearschner, M.; Hatakeyama, E.; Malekzadeh, N.; Hoelen, T.; Bhattacharyya, D., Thiol-Functionalized Membranes for Mercury Capture from Water. *Ind. Eng. Chem. Res.* **2020,** *59* (12), 5287-5295.
- Sarma, R.; **Islam, M. S.**; Running, M.; Bhattacharyya, D., Multienzyme Immobilized Polymeric Membrane Reactor for the Transformation of a Lignin Model Compound. *Polymers* **2018,** *10* (4), 463.
- **Islam, M. S.**; Hernández, S.; Wan, H.; Ormsbee, L.; Bhattacharyya, D., Role of Membrane Pore Polymerization Conditions for pH Responsive Behavior, Catalytic Metal Nanoparticle Synthesis, and PCB Degradation. *J. Membr. Sci.* **2018,** *555*, 348-361.
- Sarma, R.; **Islam, M. S.**; Miller, A.-F.; Bhattacharyya, D., Layer-by-Layer-Assembled Laccase Enzyme on Stimuli-Responsive Membranes for Chloro-Organics Degradation. *ACS Appl. Mater. Interfaces* **2017,** *9* (17), 14858-14867.

**Selected Conference Presentations**

- **Islam**, M. S.; Wan, H.; Bhattacharyya, D.; PVDF Membrane Pore Functionalization Approaches with Applications to Pollutant Remediation, **2018 AIChE** Annual Meeting, Pittsburgh, PA, USA.
- **Islam**, M. S.; Wan, H.; Bhattacharyya, D.; Role of Polymerization Conditions for Making pH Responsive Membranes: Effect of Monomer and Cross-Linker on Catalytic Pd-Fe Nanoparticle Synthesis and PCB Degradation, 27$^{th}$ Annual Meeting of North American Membrane Society (**NAMS**), **2018**, Lexington, KY, USA.
- **Islam, M. S.** and Bhattacharyya, D., Optimization of Functionalization and Nanoparticle Loading on pH Responsive Membranes for PCB Degradation, International Congress on Membranes and Membrane Processes (**ICOM 2017**), San Francisco, CA, USA.
- **Islam**, **M. S.**; Hernández, S.; Fugate, C.; Bhattacharyya, D., Effect of Monomer and Cross-Linker Concentration on pH Responsive Functionalized Membranes, **2016 AIChE** Annual Meeting, San Francisco, CA, USA.

……